A Bayesian Approach to Parameter Reconstruction from Surface Electromyographic Signals

Von der Fakultät Mathematik und Physik der Universität Stuttgart und dem SC SimTech zur Erlangung der Würde eines Doktors der Naturwissenschaften (Dr. rer. nat) genehmigte Abhandlung

Vorgelegt von

Anna Rörich

aus Traben-Trarbach

Hauptberichter: Prof. Dr. Dominik Göddeke
1. Mitberichter: Prof. Dr. Oliver Röhrle
2. Mitberichter: Prof. Dr. Lars Grasedyck

Tag der mündlichen Prüfung: 22.07.2021

Institut für Angewandte Analysis und Numerische Simulation der Universität Stuttgart

2021

"Es geht nicht um Perfektion, aber darum besser zu werden – nicht besser als der Rest, sondern besser als du selbst."

Kontrak K. "Kampfgeist 4".
In: *Sie Wollten Wasser Doch Kriegen Benzin.* Track 1-6. BMG, 2019

Abstract

Applying a Bayesian approach to infer the electrical conductivity of a body or body part from surface electromyographic (EMG) signals yields a non-invasive and radiation-free imaging technique. Further, measuring the surface EMG signals that stem from voluntary muscle contractions, there is no need to apply external electrical stimuli to the body. The electrical conductivity provides structural information of the corresponding tissue that is used to estimate whether the tissue has isotropic or anisotropic properties and which is the preferred conducting direction, if applicable. Additionally, changes in the magnitude of the electrical conductivity indicate changes in the tissue material. Together, these properties of the electrical conductivity provide medical images of the examined body part. This imaging process results in an inverse and mathematically ill-posed problem. Including a stochastic model of the inevitable measurement error into the mathematical problem description, the whole system is embedded into a probabilistic framework. Thus, instead of estimating the structure of the examined body part, the probability distribution of the parameters describing the tissue structure given surface EMG measurements, the so-called posterior distribution, is estimated. This Bayesian approach to inverse problems not only yields more information about the quantities of interest than classical regularization approaches, but also has a regularizing effect on the ill-posed problem. Indeed, the Bayesian inverse problem of inferring the tissue structure from surface EMG measurements is proven to be well-posed. This yields the convergence of the inversion algorithm and allows establishing error bounds and thus quantifying the uncertainties in the solution of the inverse EMG problem. Numerically, Markov chain Monte Carlo methods are used to explore the posterior distribution. Accelerations of these sampling methods are achieved by deriving a data-sparse representation of the discretized forward model for all conceivable discretizations of the parameters describing the tissue structure. The resulting approach is not only mathematically well-founded, but also faster by orders of magnitude. Finally, the proposed sampling algorithms are applied to several use cases that are related to clinical applications.

Zusammenfassung

Die Anwendung eines Bayes'schen Ansatzes zur Schätzung der elektrischen Leitfähigkeit eines Körpers oder Körperteils aus elektromyographischen (EMG) Oberflächensignalen ergibt ein nichtinvasives und strahlungsfreies Bildgebungsverfahren. Werden EMG Oberflächensignale gemessen, die von willkürlichen Muskelkontraktionen herrühren, ist es zudem nicht notwendig den Körper externen elektrischen Reizen auszusetzen. Die elektrische Leitfähigkeit liefert strukturelle Informationen des entsprechenden Gewebes, anhand derer berechnet werden kann, ob das Gewebe isotrope oder anisotrope Eigenschaften hat und welches gegebenenfalls die bevorzugte elektrische Fließrichtung ist. Zudem weisen Änderungen in der Größe der elektrischen Leitfähigkeit auf Veränderungen im Gewebematerial hin. Zusammen liefern diese Eigenschaften der elektrischen Leitfähigkeit medizinische Bilder des untersuchten Körperteils. Dieser Abbildungsprozess führt zu einem inversen und mathematisch schlecht gestellten Problem. Durch die Einbeziehung eines stochastischen Modells des unvermeidlichen Messfehlers in das mathematische Model wird das gesamte System in einen stochastischen Kontext gesetzt. Anstatt die Struktur des untersuchten Körperteils zu ermitteln, wird nun die Wahrscheinlichkeitsverteilung der Parameter, die die Gewebestruktur bei gegebenen EMG Oberflächenmessungen beschreiben, die sogenannte Posteriorverteilung, bestimmt. Dieser Bayes'sche Ansatz für inverse Probleme liefert nicht nur mehr Informationen über die gesuchten Größen als klassische Ansätze, sondern hat auch einen regularisierenden Effekt auf das inverse Problem. Tatsächlich wird die Wohlgestelltheit des Bayes'schen inversen Problems, die Gewebestruktur aus EMG Oberflächenmessungen zu bestimmen, bewiesen. Dies liefert die Konvergenz des Inversionsalgorithmus und ermöglicht die Festlegung von Fehlerschranken und damit die Quantifizierung von Unsicherheiten in der Lösung des inversen EMG-Problems. Numerisch werden Markov-Chain-Monte-Carlo-Methoden verwendet um die Posteriorverteilung zu untersuchen. Beschleunigungen dieser Sampling-Methoden werden durch die Herleitung einer datenarmen Repräsentation des Vorwärtsmodells für alle denkbaren Diskretisierungen der die Gewebestruktur beschreibenden Parameter erreicht. Der resultierende Ansatz ist nicht nur mathematisch fundiert, sondern auch um Größenordnungen schneller. Abschließend werden die vorgestellten Sampling-Algorithmen auf mehrere Szenarien angewendet, die sich auf klinische Anwendungen beziehen.

Contents

1. Introduction

We aim at using a Bayesian approach to parameter estimation from surface electromyographic (EMG) signals for medical imaging. The goal of medical imaging techniques is to provide images of the inside of a body or body part to reveal internal structures of the body tissue and to picture the functionality of living organs within the human body. The resulting images and insights then help diagnosing and treating diseases. By inferring parameters from surface EMG measurements we contribute to developing a non-invasive and radiation-free medical imaging technique. In contrast to invasive imaging techniques, non-invasive methods foresee from injecting measuring devices, such as needle electrodes or endoscopes, into the human body.

The history of medical imaging techniques began in 1895 when Wilhelm Conrad Röntgen discovered the X-rays and made the first X-ray photographs of human body parts that revealed inner structures like bones. Nowadays, X-rays are used in non-invasive imaging techniques such as X-ray and computed tomography (CT) scans. Nevertheless, X-ray scans apply harmful ionizing radiation, the X-rays, to the body and the dose and exposure time should be kept as minimal as possible.

In the 1940s, ultrasound was first used to image the human body. Compared to X-ray scans, ultrasonic imaging has the advantage of renouncing the application of ionizing radiation to the body. The application of ultrasonic waves is considered to be harmless within the restrictions made for clinical applications. Ultrasonic imaging is highly suited for examining aqueous and sanguineous organs but has difficulties picturing gaseous organs and organs that are shadowed by bones [24].

In the 1970s and 1980s, magnetic resonance imaging (MRI) was developed. Magnetic resonance imaging uses strong magnetic fields, magnetic field gradients, and radio frequency signals to generate images of the body. For obvious reasons, MRI is not suited for patients with metal medical implants. Like ultrasonic imaging, MRI applies no ionizing radiation to the body, but is often experienced as an unpleasant procedure as undergoing an MRI scan means being inserted into a narrow tube and being exposed to loud noise.

Since the 1980s, also electrical impedance tomography (EIT) is used for medical imag-

ing. EIT applies small alternating currents to electrodes placed on the skin surface and measures the resulting equipotentials at the skin surface. EIT is a non-invasive, radiation- and noise-free medical imaging technique, that infers the conductivity and impedance of the body part under investigation.

The mathematical formulation of inferring the electrical conductivity from surface measurements of electrical potentials, the surface EMG signals, goes back to Alberto Pedro Calderón, see the reprint [8] of his original work. We refer to [54] for a more detailed review of the history and developments of medical imaging.

As with the EIT, we are interested in inferring the electrical conductivity. Instead of applying electrical currents to the body and measuring the resulting equipotentials, we aim at using the connection between muscle contraction and surface EMG measurements that we explain in Section 2.6. Roughly speaking, muscle fibers get stimulated to contract by an electrical stimulus from the spinal cord. This electrical stimulus travels through the muscle fibers and the surrounding tissue like neighboring muscle fibers, fat, bone, tendons, or skin. The resulting fluctuations in the electrical potential of the skin can be measured as surface EMG measurements and contain information about the tissues that they traveled. Thus, by measuring the changes of the surface EMG signals due to the contraction of skeletal muscles, there is no need for applying any electrical stimulus to the body.

The remainder of this chapter is structured as follows. In Section 1.1, we model the electrical conductivity as a mathematical function and explain how to compute medical images from the knowledge of the electrical conductivity of a body or body part. We present the outline of our approach for constructing a radiation-free and non-invasive imaging method in Section 1.2. Finally, Section 1.3 gives an overview of related research areas and aligns our work within the existing research.

1.1. Motivation and Aims

We already formulated the aim of achieving a non-invasive and radiation-free imaging method by inferring the electrical conductivity of a body from surface EMG data. In the following, we discuss why the electrical conductivity is a well-suited parameter for this task and how to compute images from the electrical conductivity.

Electrical conductivity is a measure of the ability of a material to conduct electricity. The SI unit of electrical conductivity is siemens per meter (S/m), where the unit siemens is defined as ampere per volt, i.e., $1\,\mathrm{S} \coloneqq \frac{1\,\mathrm{A}}{1\,\mathrm{V}}$. We model the electrical conductivity of a

three-dimensional body or body part $D \subset \mathbb{R}^3$ as a matrix-valued function $\sigma : D \to \mathbb{R}^{3\times 3}$ with $x \mapsto \sigma(x)$. Here, each matrix entry $(\sigma(x))_{jk}$ quantifies the conductivity of the body at location $x \in D$ in the e_j-e_k-direction for the standard unit vectors $e_j \in \mathbb{R}^3$ with $(e_j)_k = \delta_{jk}$ and $j, k = 1, 2, 3$.

Physically, the electrical conductivity is strictly positive since an electrical conductivity of 0 would correspond to an absolutely insulating material that is so far unknown. Similarly, the electrical conductivity is bounded above since an electrical conductivity of infinity corresponds to a material that shows no resistance to electricity. However, even the best known superconductor has a small but positive electrical resistance. Formalizing our considerations about the boundedness of the conductivity yields $\sigma \in L^\infty(D; \mathbb{R}^{3\times 3})$.

When considering the electrical conductivity for medical imaging, the materials considered are biological tissues, such as muscle, fat, bone, or skin tissue. The electrical conductivity varies significantly between different types of biological tissue, hence, the electrical conductivity contains information about the biological tissue and its structure. Note that the differences in the electrical conductivity of different tissues may lead to discontinuities in σ whenever D contains more than one tissue. Thus, we cannot expect higher regularity from σ than L^∞. In the following, we give some examples of the correspondence between tissue structure and electrical conductivity.

First, we consider a domain of homogeneous, isotropic tissue, i.e., the tissue properties are constant through the domain (homogeneity) and behave equal in each direction (isotropy), such as fat tissue. From the homogeneity of the tissue, we deduce that the electrical conductivity is constant in the domain, i.e., $\sigma(x) = \sigma \in \mathbb{R}^{3\times 3}$. The isotropy of the tissue implies that the electrical conductivity is a diagonal matrix with diagonal entries s, i.e., $\sigma = \operatorname{diag}(s, s, s)$ for some positive value $s \in \mathbb{R}$.

Next, we consider a domain of homogeneous, anisotropic tissue, i.e., the tissue properties are constant through the body or body part D but the tissue behaves different in different directions. Again, we have a constant conductivity $\sigma \in \mathbb{R}^{3\times 3}$, where the entries of σ characterize the anisotropy of the tissue. Exemplarily, we assume that the tissue is highly conducting in e_1- and e_3-direction and less conducting in e_2-direction. The electrical conductivity is then modeled by a diagonal matrix $\sigma = \operatorname{diag}(s', s, s')$ with $0 < s < s' < \infty$.

Note that the two above examples generalize to inhomogeneous tissue by making the electrical conductivity space-dependent, i.e., $\sigma(x) = \operatorname{diag}(s(x), s(x), s(x))$ in the first example and $\sigma(x) = \operatorname{diag}(s'(x), s(x), s'(x))$ in the second example. The most important example of inhomogeneous tissue is a body part that consists of several different

tissues. Even if the properties of each tissue are homogeneous, the composite will have inhomogeneous properties. In clinical applications, changes in the tissue properties may additionally indicate abnormal changes of the tissue, e.g., through cicatrization.

We finally consider an inhomogeneous, anisotropic tissue that has a preferred conducting direction $d \in \mathbb{R}^3$, i.e., a direction in which the tissue is more conductive than in the directions transversal to d. The electrical conductivity of such an inhomogeneous, anisotropic tissue is described through a matrix-valued function $\sigma(x) \in L^\infty(D; \mathbb{R}^{3\times 3})$ as discussed above. Furthermore, the preferred conducting direction d corresponds to the eigenvector belonging to the largest eigenvalue of the conductivity at each point $x \in D$. In this way, we are able to compute the preferred conducting direction of a tissue from its electrical conductivity.

An example for a biological tissue that possesses a preferred conducting direction is skeletal muscle tissue, where the preferred conducting direction coincides with the direction of the muscle fibers. In skeletal muscle tissue, the conductivity in the directions transversal to the muscle fiber direction is much smaller than in longitudinal (muscle fiber) direction. We denote the value of the conductivity in longitudinal direction by s', the value of the conductivity in the transversal directions by s, and define the direction $d_{\mathrm{F}}(x)$ of a muscle fiber in point $x \in D$ through the rotation angles $\alpha(x) = (\alpha_1(x), \alpha_2(x), \alpha_3(x))$ around the e_1-, e_2-, and e_3-axes such that

$$d_{\mathrm{F}}(x) = R_1(\alpha_1(x))R_2(\alpha_2(x))R_3(\alpha_3(x))e_1.$$

Here, $R_1(\alpha_1(x))$, $R_2(\alpha_2(x))$, and $R_3(\alpha_3(x)) \in \mathbb{R}^{3\times 3}$ denote the rotation matrices in three dimensions around the e_1-, e_2-, and e_3-axis. The electrical conductivity of the skeletal muscle tissue in a point $x \in D$ is then given by

$$\sigma(x) = R_1(\alpha_1(x))R_2(\alpha_2(x))R_3(\alpha_3(x))\,\mathrm{diag}(s', s, s)R_3^\top(\alpha_3(x))R_2^\top(\alpha_2(x))R_1^\top(\alpha_1(x)).$$

From the above representation of the electrical conductivity and the strict positivity of the conductivities in the e_1-, e_2-, and e_3-direction, we deduce that the resulting conductivity $\sigma(x)$ is a positive definite matrix for each $x \in D$. Moreover, the rotations imply symmetry of the conductivity σ.

Summarizing, we deduce that areas of similar electrical conductivity are made of the same tissue and that the structure of this tissue is determined by the (an)isotropy of the electrical conductivity. In this way, the electrical conductivity yields information about the tissue structure and is thus well-suited for medical imaging techniques.

1.2. Outline

As discussed above, we pursue the goal of developing a medical imaging method using the relation between the electrical conductivity of biological tissue and surface EMG measurements. Achieving this goal involves several tasks. First, a model that describes the behavior of EMG signals for a given electrical conductivity, the forward model, is needed. Such a model describes the evolution and propagation of EMG signals, which includes chemical reactions, electrical ion flows, and mechanical reactions of the tissue due to these ion flows.

Second, an algorithm that inverts the forward model, i.e., that searches for the electrical conductivity that yields computed surface EMG data "close" to the clinical measurements has to be defined. Care must be taken when defining such an algorithm, since the mentioned inversion of the forward model leads to an ill-posed problem. Special techniques from the field of inverse problems are needed to regularize the ill-posed problem and thus guarantee the existence of well-behaved solutions.

The third and probably most crucial task consists of proving the convergence of the inversion algorithm, establishing error bounds and therewith providing tools for quantifying the uncertainties in the solutions of the inverse problem, i.e., of the estimated electrical conductivities.

The last, but not less important, step is to conduct all necessary computations in reasonable time to provide a competitive algorithm.

We achieve our postulated goal by combining aspects from biomechanics, optimization, especially from the theory of inverse problems, and probability and tensor theory. Chapter 2 summarizes all relevant mathematical and electrophysiological fundamentals from the mentioned areas. In contrast to the above description, we begin with the general theory of inverse problems, stochastic, and tensors before specifying the forward model that describes the evolution and propagation of surface EMG signals.

More precisely, we begin with an introduction to inverse problems and classical solution techniques in Section 2.1. The Bayesian approach that we will consider throughout this thesis is another approach to inverse problems that builds on probability theory. Roughly speaking, the idea consists of including a probabilistic model of the inevitable measurement error into the forward model and regarding the whole model as probabilistic. The task of finding the probability distribution of the parameters of interest given measurements is then called the Bayesian formulation of the inverse problem. We give an overview of the aspects of probability theory needed to apply the Bayesian approach

for solving inverse problems in Section 2.2. For solving Bayesian inverse problems numerically, sampling strategies have been developed. We focus on Markov chain Monte Carlo sampling methods that we introduce in Section 2.3. Building on the derived theory, we discuss the Bayesian approach to inverse problems in Section 2.4 and adapt the introduced Markov chain Monte Carlo methods to sample from the probability distribution of the parameters of interest, given measurements. These sampling strategies, however, include solving the forward problem for many parameters, which is computationally demanding. In Section 2.5, we introduce low-rank tensor formats to achieve a data-sparse and fast-to-evaluate representation of the forward problem and thus accelerate the sampling process. Concluding Chapter 2, we introduce the model of the electrophysiological behavior of biological tissue, especially skeletal muscle tissue, that describes the evolution, propagation, and measuring of EMG data in Section 2.6.

In Chapter 3, we present our implementation of the forward surface EMG model that is based on the KerMor software package[1]. We roughly sketch the structure of the original implementation before we present our modifications and extensions that aim at making the code flexible enough to handle arbitrary space-dependent conductivities and thus be suited for inversion.

In Chapter 4 we state the deterministic and probabilistic forward and the Bayesian inverse EMG problem and prove and discuss their well-posedness. We will see that the well-posedness of the forward problems is indeed crucial for proving the well-posedness of the Bayesian inverse EMG problem and thus worth being discussed. For defining the Bayesian inverse problem, we model the inevitable measurement error and include it into the forward EMG model as mentioned above. Searching for the probability distribution of the parameters of interest given EMG measurement data then defines the Bayesian inverse EMG problem. Recalling our discussion from Section 1.1, we establish the electrical conductivity of the investigated body part as the parameter of interest. Concluding Chapter 4 we deduce error bounds for the solution of the Bayesian inverse EMG problem with respect to discretizations of the forward EMG problem and the probabilistic conductivities from the well-posedness results.

In Chapter 5 we adapt the sampling strategies introduced in Section 2.3 to sample from the probability distribution of the electrical conductivity given EMG measurement data. We validate and quantify the performance of our sampling algorithm in several parameter studies and notice that solving the forward EMG problem is computationally demanding and makes up a high percentage of the runtime. Thus, solving the

[1] `https://www.morepas.org/software/kermor/index.html`

forward EMG problem in each step of the sampling algorithm is impractical when a high number of proposals needs to be drawn until the sampling algorithm converges. For accelerating the sampling process, we use a low-rank tensor representation of the parameter-dependent forward EMG problem. Doing so enables us to precompute the solution of the forward EMG problem on a discrete parameter grid, store the solutions in a data-sparse format, and evaluate this tensor solution in each step of the sampling algorithm. Our parameter studies show that evaluating the precomputed tensor solution in each step of the sampling algorithm is much faster than solving the forward EMG problem and, nevertheless, accurate.

In Chapter 6 we apply our sampling algorithm to several use cases that are related to clinical applications. First, we quantify the influence of an additional layer of surrounding tissue on the inferability of the magnitudes of the electrical conductivity of the underlying muscle. Second, we generalize this scenario to inferring the structure of electrically active tissue and examine the suitability of our sampling algorithm for inferring the muscle fiber direction and conductivity magnitudes simultaneously. Moreover, we quantify the influence of a layer of surrounding tissue on the inferability of the muscle fiber direction and conductivity magnitudes. Third, we investigate a scenario of two muscles lying on top of each other. This scenario introduces additional model parameters, namely the thickness of the two muscles and the conductivity magnitudes and rotation angle of the second muscle. Inferring these parameters, we start with inferring only the thickness of the muscles and increase the number of parameters until inferring all model parameters simultaneously.

Finally, we summarize our contributions in Chapter 7 and give several ideas for future research.

1.3. State of the Art

In the following, we give a brief overview on existing work done in the areas of EMG modeling, imaging methods using surface EMG measurements and the corresponding inverse problems, sampling algorithms, and the use of low-rank tensor formats for accelerating costly computations.

1.3.1. EMG and Modeling

A complex multi-scale multi-physics model of the evolution and propagation of EMG signals in skeletal muscle was developed in [48, 74, 87]. Reducing the computational cost of these forward models, model order reduction was successfully applied in [29, 75]. Here, the key ingredients for the order reduction was Galerkin projection via proper orthogonal decomposition and application of the discrete empirical interpolation method to the nonlinear source term of the EMG model.

Surface EMG has various applications in medical fields such as neurophysiology, ergonomics and occupational medicine, proctology and obstetrics, movement and gait analysis, musculoskeletal physical therapy, exercise physiology and sports, and for man-machine interfacing in rehabilitation technologies [70, Chapters 12-20]. The usual task of inverse problems arising in these fields is source localization of the electrical stimuli [10, 21, 22, 67, 71].

The imaging method that developed from the use of surface EMG measurements is the EIT mentioned in the introduction to Chapter 1. EIT is most frequently used for continuous assessment of the respiratory status [68]. The resulting inverse problem uses Dirichlet-to-Neumann and Neumann-to-Dirichlet maps that represent the connection between transmitted and received data [6]. We emphasize that the electrodes placed on the skin surface are split into transmitting and receiving electrodes in EIT thus reducing the number of measuring electrodes.

In contrast, we aim at measuring the surface EMG signals that result from voluntary muscle contraction, which renders the use of transmitting electrodes redundant.

1.3.2. Regularization of Inverse Problems

Tikhonov-type regularization was used in [36, 106] to infer the electrical conductivity of biological tissue (cardiac and skeletal muscle tissue respectively) from EMG measurements. Moreover, in [106] model order reduction was used to construct a surrogate of the EMG model and thus accelerate the inversion.

A difference to our Bayesian approach is that the regularization methods used in [36, 106] neglect the inevitable measurement error. Moreover, we forebear from using surrogates but rely on exact and nevertheless faster-to-evaluate representations of the EMG model for accelerating the inversion.

Although the Bayesian approach has been used successfully in many scientific areas such as geosciences [85], to our knowledge, there is no work applying a Bayesian ap-

proach to the inverse problem of inferring the electrical conductivity from surface EMG measurements.

Bayes' theorem, the fundamental ingredient of the Bayesian approach to inverse problems, was formulated in the function-space setting in [17, 99].

1.3.3. Calculating the Posterior

There has been a lot of progress in designing improved algorithms for ensuring the applicability of the Bayesian approach to computationally demanding models. The approaches for improving these algorithms can roughly be divided into three groups: one group that focuses on accelerating the evaluation of computationally demanding forward models during the sampling process, a second group that focuses on efficient sampling, and a third group that improves Quasi-Monte Carlo and direct integration algorithms. A brief overview can be found in [94].

Surrogates

In [50] a method based on polynomial chaos expansions was used to construct a surrogate of the forward problem. Stochastic collocation methods, based on generalized polynomial chaos, were used in [69] to construct a polynomial approximation of the forward solution over the support of the prior distribution. This approximation then yielded a surrogate posterior probability density that could be evaluated repeatedly at minimal computational cost.

In [82] a Gaussian process emulator was used to construct a surrogate of the forward problem. This surrogate was adaptively improved by iteratively selecting the training points for the Gaussian process emulator.

In contrast to the above mentioned global surrogates, local approximations of the forward model were used in Markov chain Monte Carlo methods to accelerate the sampling process in [12]. These local approximations can be either polynomial or Gaussian process approximations. The resulting sampling algorithm was proven to still sample from the exact posterior distribution.

Sampling

In [40] delayed rejection [102] and adaptive sampling [39, 41] were combined and the ergodicity of the resulting Markov chain was proven. The idea of delayed rejection is to

retry rejected samples, while adaptive sampling updates the proposal strategy in each iteration with the full information cumulated so far.

Another approach of improving the sampling process is to use Hamiltonian dynamics to guide the sampling process, resulting in Hamiltonian Markov chain Monte Carlo methods [77].

Adapting the ideas of multigrid methods to sampling algorithms, multilevel Monte Carlo algorithms were introduced [49]. In [92] quasi Monte Carlo methods and multilevel Monte Carlo methods were used to accelerate the convergence of the sampling algorithm. Further, in [20] a hierarchical multilevel Markov chain Monte Carlo algorithm was developed and applied to subsurface flow in porous media.

A family of Markov chain Monte Carlo samplers that can adapt to the particular structure of a posterior distribution over functions, the dimension-independent likelihood-informed Markov chain Monte Carlo, was introduced in [15]. This dimension-independent likelihood-informed Markov chain Monte Carlo was combined with a multilevel Markov chain Monte Carlo in [14].

Quantifying the convergence of Markov chain Monte Carlo methods, [105] established dimension-independent bounds on the Monte Carlo error of Markov chain Monte Carlo sampling for non-Gaussian prior measures.

Combining the advantages of surrogates and advanced sampling techniques, a sparse, parametric and deterministic generalized polynomial chaos surrogate of the forward model and a multi-level Markov chain Monte Carlo strategy, were used in [50]. Here, the multi-level Markov chain Monte Carlo strategy utilizes sampling from a multi-level discretization of the posterior and the forward model. Furthermore, in [84] Gaussian process surrogates were combined with hybrid Monte Carlo methods [27] for avoiding expensive evaluations of the underlying forward model.

Markov chain Monte Carlo methods for functions were introduced in [13, 17, 90, 99]. Especially the Metropolis-Hastings algorithm, preconditioned Crank-Nicolson, and sequential Monte Carlo methods were generalized to infinite dimensions.

Quasi-Monte Carlo and Integration

In contrast to Markov chain Monte Carlo methods, Quasi-Monte Carlo methods use low-discrepancy sequences for numerical integration. An overview of recent developments of Quasi-Monte Carlo methods, i.e., equal-weight rules for the approximate evaluation of high-dimensional integrals, is given in [19]. We give some examples in the following.

A class of adaptive, deterministic sparse tensor Smolyak quadrature schemes for the ef-

ficient approximate numerical evaluation of expectations under the posterior is designed and analyzed in [93]. Further, in [94] numerical sampling methods, which are robust with respect to the size of the observational noise, based on a Laplace approximation of the posterior were proposed. For computing infinite-dimensional integrals with respect to the posterior distribution in the context of Bayesian inverse problems with Gaussian priors, a Hessian-based adaptive sparse quadrature was introduced in [11].

1.3.4. Tensor Approaches

In the last few years, low-rank tensor methods were examined in the context of Bayesian inverse problems. In [23] low-rank tensor formats were used to compute a surrogate of the target distribution. There, the target distribution was directly approximated using a generalization of the cross approximation.

Furthermore, low-rank tensor formats were applied in [28] to develop a sampling-free approach to Bayesian inversion with an explicit polynomial representation of the parameter densities, based on an affine-parametric representation of a linear forward model.

Moreover, in [33] low-rank tensor formats were used to calculate time-marginal distributions of continuous-time Markov chains that describe the evolving genotype of a tumor progression model.

In order to distinguish our work from the aforementioned works we, again, emphasize that we extend the theoretical findings from [17, 99] to yield the well-posedness of the Bayesian inverse EMG problem of inferring the electrical conductivity from surface EMG measurements. Further, we combine an exact low-rank tensor representation of the forward EMG model with the infinite-dimensional Metropolis-Hastings algorithm for accelerating the sampling process.

2. Fundamentals

Generally speaking, the medical imaging methods introduced in Chapter 1 can be interpreted mathematically as the task of inferring *parameters* $\boldsymbol{p}^* \in \boldsymbol{\mathcal{J}}$ from given *measurements* or *data* $\phi^* \in Y$, where $\boldsymbol{p}^*$ and ϕ^* are connected through a so-called *forward* or *observation operator* $\mathcal{G} : \boldsymbol{\mathcal{J}} \to Y$ that maps $\boldsymbol{p} \mapsto \phi$ with $\phi^* = \mathcal{G}(\boldsymbol{p}^*)$. Further, we call $\boldsymbol{\mathcal{J}}$ the *parameter space* or *space of admissible parameters* and Y the *measurement space*. Usually, the measurements are finite dimensional. In this case, $Y = \mathbb{R}^{N_\mathrm{M}}$, where $N_\mathrm{M} \in \mathbb{N}$ is the number of measurements. The general problem of inferring $\boldsymbol{p}^*$ from ϕ^* is called *inverse problem*. We give a brief introduction to inverse problems and an overview on classical solution techniques in Section 2.1.

Beside these classical solution methods, there is the Bayesian approach to inverse problems that is based on a stochastic formulation of inverse problems. Since we aim at applying a Bayesian approach to the inverse problem introduced in Section 1.1, we summarize the stochastic definitions and results that build the theoretical framework for the Bayesian approach of solving inverse problems in Section 2.2.

For solving Bayesian inverse problems numerically, sampling strategies have been developed. We give an introduction to Markov chain Monte Carlo sampling in Section 2.3.

Building on the derived theory, we discuss the Bayesian approach to inverse problems and a sampling algorithm adapted to the inverse problem setting in Section 2.4.

The sampling strategies introduced in Section 2.3, however, include solving the parameter-dependent *forward problem* of computing ϕ for given parameters $\boldsymbol{p}$ through $\phi = \mathcal{G}(\boldsymbol{p})$ for many parameters, which can be computationally demanding. In Section 2.5, we introduce low-rank tensor formats to achieve a data-sparse and fast-to-evaluate representation of $\mathcal{G}(\boldsymbol{p})$.

Finally, in Section 2.6 we introduce the model of the electrophysiological behavior of biological tissue, especially skeletal muscle tissue, that describes the evolution, propagation, and measuring of EMG data. This model defines the forward and inverse EMG problem that we study in Chapters 4, 5, and 6.

2.1. Inverse Problems

Besides the inverse EMG problem, which was motivated in Section 1.1 and will be discussed further in Section 4.3, inverse problems appear in various real-world applications and fields of research, such as medicine, physical chemistry, geophysics, astronomy, and material sciences. We name some applications and categories of inverse problems in the following. For a more detailed overview, we refer to [30].

There is, for example, the wide field of medical imaging techniques. These include established methods of computerized tomography, magnetic resonance imaging, and ultrasound, which all aim at recovering the density of a material or body part from method-specific measurements, here X-rays, radio frequency signals, and ultrasound.

Another wide field of inverse problems is signal and image processing, where the focus lies, e.g., on reconstructing missing fragments of images or on deblurring of blurred parts of images. We mention image processing in astronomy that was established after the launch of the NASA/ESA Hubble Space Telescope in early 1990 [1]. Launched to provide diffraction limited (high spatial resolution) images, it was quickly discovered that the images send back to Earth were flawed due to a manufacturing error in the main mirror of the telescope. This incident led to a high acceptance of image restoration techniques in astronomy and thus, even after the Hubble Space Telescope was repaired in late 1993, image processing techniques remained an important tool in astronomy [30].

An often quoted and discussed example for inverse problems in physics is heat conduction, where researchers are interested in determining the temperature of an object or a specific point in space at a past time from actual measurements of the temperature of that body or point, or even from temperature measurements in other spatial points. Another inverse problem in heat conduction is to determine thermal parameters, such as the thermal conductivity.

The latter inverse problem is one example for the broad field of *parameter identification* or *reconstruction* that aims at estimating parameters, such as material parameters, that cannot be measured directly from measurements of related quantities. The inverse problem of inferring the electrical conductivity from surface EMG measurements, introduced in Section 1.1, also falls into this category of inverse problems.

2.1.1. Classical Regularization Methods

We consider the abstract inverse problem of finding a parameter or state of interest $\boldsymbol{p}^* \in \boldsymbol{\mathcal{J}}$ from data or measurements $\phi^* \in Y$ that are connected through a forward map

$\mathcal{G} : \boldsymbol{\mathcal{J}} \to Y$ with $\mathcal{G}(\boldsymbol{p}) = \phi$ for some spaces $\boldsymbol{\mathcal{J}}, Y$ as introduced in the beginning of this chapter, see Page 13. From a mathematical point of view, the inverse problem of calculating $\boldsymbol{p}^*$ for given ϕ^* consists of inverting the forward map $\mathcal{G}$. This inverse problem is *well-posed* in the sense of Hadamard [44], if the following conditions hold:

1. *Existence:* For each admissible $\phi \in Y$ there exists a parameter $\boldsymbol{p} \in \boldsymbol{\mathcal{J}}$ such that $\mathcal{G}(\boldsymbol{p}) = \phi$.

2. *Uniqueness:* For each admissible $\phi \in Y$ the parameter $\boldsymbol{p} \in \boldsymbol{\mathcal{J}}$ with $\mathcal{G}(\boldsymbol{p}) = \phi$ is unique.

3. *Stability:* The parameters $\boldsymbol{p} \in \boldsymbol{\mathcal{J}}$ with $\mathcal{G}(\boldsymbol{p}) = \phi$ depend continuously on the data $\phi \in Y$.

If one of the above conditions is violated, the problem is called *ill-posed*. The examples of inverse problems that we gave before are all ill-posed. In parameter reconstruction tasks, the ill-posedness is usually caused by the underdetermined task of inferring continuous, i.e., infinite-dimensional, parameters from finite measurements of some related quantity. Furthermore, the forward map does not need to be injective.

For an example of the uniqueness issues that may occur when dealing with inverse problems, imagine measuring the temperature of a pot of soup on a stove at a certain time, where we are interested in the temperature of the soup at a past time. The measured temperature might now be achieved from heating the soup, i.e., the temperature of the soup at the past time was lower than the measured temperature. On the other hand, the soup might have been boiling before and cooled to the measured temperature, i.e., the temperature of the soup at the past time was higher then the measured temperature. Another possible scenario is that the temperature of the soup was kept constant over time.

Unfortunately, most inverse problems are ill-posed. Hence, the question arises how to ensure uniqueness of the solution and in general well-posedness of the inverse problem. These considerations lead to *regularization techniques*.

The main goal of regularization methods is the restoration of stability of the solution with respect to the data [30, Chapter 3]. The idea of *classical regularization methods* is to achieve well-posedness by adding information or assumptions about the solution or the physical system to the problem description. Over the last decades a large number of regularization methods have been developed. We mention some classical regularization approaches below. Good overviews can be found in [30] and [55].

Starting our overview on classical regularization methods, we summarize the *Tikhonov regularization* method, see also [103]. For an introduction to the well-posedness of Tikhonov-regularized inverse problems we refer to [30, Chapters 5 and 10]. The Tikhonov regularization is widely used, especially for parameter estimation problems.

The idea of the Tikhonov regularization method is to add a *regularization term* $\|\boldsymbol{p} - \hat{\boldsymbol{p}}\|^2$ to the least squares formulation of the inverse problem, i.e., the aim is to solve the optimization problem

$$\min_{\boldsymbol{p} \in \mathcal{J}} \|\mathcal{G}(\boldsymbol{p}) - \phi^*\|^2 + \alpha_{\mathrm{R}} \|\boldsymbol{p} - \hat{\boldsymbol{p}}\|^2 \tag{2.1}$$

for data $\phi^* \in Y$. Here $\hat{\boldsymbol{p}}$ describes a desired or expected state of the underlying physical system, e.g., equilibrium. While $\hat{\boldsymbol{p}} = \boldsymbol{0}$ is often used in the linear case, this choice has no special meaning in the nonlinear case such that $\hat{\boldsymbol{p}}$ comprises other a-priori knowledge about the solution. The *regularization parameter* $\alpha_{\mathrm{R}} > 0$ controls the influence of the regularization term. If α_{R} tends to infinity, $\boldsymbol{p}$ will tend to the expected state $\hat{\boldsymbol{p}}$, and if α_{R} tends to 0, $\boldsymbol{p}$ will be mainly determined by the forward map $\mathcal{G}$ and the problem will again become ill-posed.

A closer look at the regularized least-squares problem (2.1) reveals another free component of the Tikhonov regularization method, namely the choice of a specific norm. Hence, strategies how to choose the regularization parameter and the norm are needed. In case $\mathcal{G}$ is linear there are a-posteriori parameter selection methods which minimize the error $\left\|\boldsymbol{p}^\alpha - \boldsymbol{p}^\dagger\right\|$ between the Tikhonov-regularized solution $\boldsymbol{p}^\alpha \coloneqq \arg\min_{\boldsymbol{p} \in \mathcal{J}} \|\mathcal{G}(\boldsymbol{p}) - \phi^*\|^2 + \alpha_{\mathrm{R}} \|\boldsymbol{p} - \hat{\boldsymbol{p}}\|^2$ and the solution $\boldsymbol{p}^\dagger = \mathcal{G}^\dagger \phi^*$ with $\mathcal{G}^\dagger$ denoting the pseudo-inverse of $\mathcal{G}$, cf. [30, Chapter 4] and the references therein. Such parameter selection methods do also exist for the nonlinear case but require restrictive assumptions on $\mathcal{G}$.

In practice, heuristic parameter selection methods, such as the L-curve method introduced in [65] and further advocated in [45], are used. We refer to the introduction in [30, Section 4.5] and the summary in [35] for an overview on heuristic parameter selection methods.

Two well-known specific Tikhonov regularizations are the *maximum entropy regularization*, which solves the regularized problem

$$\min_{\boldsymbol{p} \in \mathcal{J}} \|\mathcal{G}(\boldsymbol{p}) - \phi^*\|^2 + \alpha_{\mathrm{R}} \int_{t_0}^{t_1} \boldsymbol{p}(t) \log\left(\frac{\boldsymbol{p}(t)}{\hat{\boldsymbol{p}}(t)}\right) \mathrm{d}t$$

for a time-dependent parameter $\boldsymbol{p}(t)$ on an interval (t_0, t_1) and $\hat{\boldsymbol{p}} > 0$ as before, and the

total variation regularization, which solves the regularized problem

$$\min_{\boldsymbol{p}\in\boldsymbol{\mathcal{J}}} \|\mathcal{G}(\boldsymbol{p}) - \phi^*\|^2 + \alpha_{\mathrm{R}} \int_{t_0}^{t_1} \|\nabla \boldsymbol{p}(t)\|_2 \mathrm{d}t$$

again for a time-dependent parameter $\boldsymbol{p}(t)$. The latter is frequently used in image reconstruction as it enhances sharp features in $\boldsymbol{p}$. The drawback of the total variation regularization is that the regularization term is not differentiable due to the nondifferentiability of the Euclidean norm $\|\cdot\|_2$ at 0. Thus, derivative-free optimization algorithms have to be used. We refer to [104, Chapter 8] for a discussion of the total variation regularization.

A related regularization ansatz is the *regularization with differential operators* that searches for the solution of the optimization problem

$$\min_{\boldsymbol{p}\in\boldsymbol{\mathcal{J}}} \|\mathcal{G}(\boldsymbol{p}) - \phi^*\|^2 + \alpha_{\mathrm{R}} \|\mathcal{Q}(\boldsymbol{p})\|^2$$

with $\mathcal{Q}$ denoting any differential operator. This regularization is used, for example, in spline smoothing with $\mathcal{Q}$ being the second derivative operator.

Contrarily to regularization methods that add extra information to the model as described above, there are regularization methods that regularize ill-posed problems by leaving out information. One category of those methods is *regularization by projection*. The general framework was developed in 1977 [76]. The field of regularization by projection comprises regularization through finite-dimensional approximations such as discretization, collocation, and Ritz-Galerkin approximations.

A similar idea is to use the regularizing effect of terminating iterative processes early, which leads to *iterative regularization methods* [4, 56]. These regularization methods include the (nonlinear) Landweber iterations, which are based on fixed-point equations, the CGNE method, which applies the Conjugate Gradient method to the Normal Equations of the ill-posed problem, and Newton-type methods like the Levenberg-Marquardt method.

Tikhonov-type regularization methods and approximation-based regularization methods both share the presence of free regularization parameters, be it the choice of α_{R} in the Tikhonov-type regularizations or some discretization or truncation parameters in the approximation-based methods. In both cases, care must be taken to balance the accuracy of the (regularized) model and the stability of the (regularized) solution. This is one major drawback of the classical regularization techniques. Another drawback of

the Tikhonov-type regularization methods is the need of additional information about the solution.

We highlight that the above formulations of classical regularization methods completely neglect any measurement error. Stochastic models of the measurement error can nevertheless be included into the classical regularization techniques. However, a more natural approach of incorporating measurement errors into inverse problem formulations is the Bayesian approach that is introduced in Section 2.4. The necessary stochastic knowledge to formulate Bayesian inverse problems is summarized in the next section.

2.2. Stochastic Fundamentals

This section is dedicated to a brief overview of the stochastic definitions, theorems and concepts needed to develop the theory of Bayesian inverse problems. In Section 2.2.1 we start with a summary on measures and measurable spaces and continue by defining probability measures and probability spaces. Next, we introduce random variables and random functions in Section 2.2.2, together with Bayes' theorem. Finally, in Section 2.2.3, we give an introduction to Markov chains, which are substantial to the sampling algorithms for solving Bayesian inverse problems that we will introduce in Section 2.3.

2.2.1. Measures and Measurable Spaces

Let Y be any space or set, $\mathcal{A}$ be a σ-algebra of subsets of Y and $\mu : \mathcal{A} \to [0, \infty]$ be a measure on the measurable space $(Y, \mathcal{A})$. A measure space $(Y, \mathcal{A}, \mu)$ is called *complete* if $\mathcal{A}$ is the collection of all μ-measurable subsets of Y, i.e., $\mathcal{A} = \{S \subset Y \mid \mu(S') = \mu(S' \cap S) + \mu(S' \cap (Y \setminus S)$ for each $S' \subset Y\}$, cf. [2, Definition 10.34]. This definition is equivalent to $\mathcal{A}$ containing all μ-negligible subsets of Y, cf. [7, Definition 2.1.41].

We say that a property holds *μ-almost everywhere* (μ-a.e.) if there exists a set $S \subset \mathcal{A}$ with $\mu(S) = 0$ such that the property holds for all $y \in Y \setminus S$.

A measure μ on a measurable space $(Y, \mathcal{A})$ is called *σ-finite*, if there exists a sequence $\{S_j\}_{j=1}^{\infty} \subset \mathcal{A}$ such that $\mu(S_j) < \infty$ for all $j = 1, \ldots, \infty$ and $\bigcup_{j=1}^{\infty} S_j = Y$, cf. [7, Definition 2.1.32]. Further, a measure μ on a measurable space $(Y, \mathcal{A})$ is *of bounded variation* if

$$\sup \left\{ \sum_{j=1}^{n} |\mu(S_j)| \mid \{S_1, \ldots, S_n\} \text{ is a partition of } Y \right\} < \infty,$$

where $\{S_1, \ldots, S_n\}$ is a partition of Y for some $n \in \mathbb{N}$ if S_j are pairwise disjoint subsets of Y and $\bigcup_{j=1}^{n} S_j = Y$, compare [2, Section 10.10].

Let μ, μ' be two measures on a σ-algebra $\mathcal{A}$ of subsets of some space Y. Then μ, μ' are *mutually singular*, if there exists $S \in \mathcal{A}$ with $\mu(S) = 0$ and $\mu'(Y \setminus S) = 0$, cf. [59, Definition 7.30]. Further, μ' is *absolutely continuous* with respect to μ if $\mu'(S) = 0$ for all $S \in \mathcal{A}$ with $\mu(S) = 0$, and we write $\mu' \ll \mu$, cf. [59, Definition 7.30]. This definition allows us to state the *Radon-Nikodym theorem* as in. [2, Theorem 13.18].

Theorem 2.2.1 (Radon-Nikodym Theorem). *Let $(Y, \mathcal{A}, \mu)$ be a σ-finite complete measure space and μ' be a signed measure of bounded variation that is absolutely continuous with respect to the measure μ. Then there exists a (μ-almost everywhere) unique μ-integrable function $f : Y \to [0, \infty)$ satisfying*

$$\mu'(S) = \int_S f \mathrm{d}\mu$$

for each $S \in \mathcal{A}$. The function f is often called the Radon-Nikodym derivative *of μ' with respect to μ and is then written as $f = \frac{\mathrm{d}\mu'}{\mathrm{d}\mu}$.*

Using the definition of the Radon-Nikodym derivative, we define a metric on measures for quantifying their distance. Following [17, Chapter 4] and [50], we use the *Hellinger metric*.

Definition 2.2.2 (Hellinger Metric). *Let $(Y, \mathcal{A})$ be a measurable space and μ, μ' be measures on Y that are absolutely continuous with respect to a common reference measure ν. The* Hellinger metric *of μ and μ' is defined as*

$$d_{Hell}(\mu, \mu') \coloneqq \sqrt{\frac{1}{2} \int_Y \left(\sqrt{\frac{\mathrm{d}\mu}{\mathrm{d}\nu}} - \sqrt{\frac{\mathrm{d}\mu'}{\mathrm{d}\nu}} \right)^2 \mathrm{d}\nu}.$$

Subsequently, we will use the notion of measures to define random variables and probability measures. For doing so, we need the definition of (strongly) measurable functions. We call a function $f : Y \to Y'$ that maps from a measurable space $(Y, \mathcal{A})$ to a Banach space Y' *strongly measurable* if there exists a sequence of simple functions $f_j : Y \to Y'$ such that $\lim_{j \to \infty} f_j = f$ pointwise on Y. If Y' is separable, f is strongly measurable if and only if f is measurable, cf. [53, Section 1.1].

A well-known property of measures that will help us proving measurability in Chapter 4 is the following, see, e.g., [59, Theorem 1.88]:

Lemma 2.2.3. *Let $(Y, \mathcal{A})$ be a Borel measurable topological space and $f \in C^0(Y; \mathbb{R})$ for some measure μ on $(Y, \mathcal{A})$. Then f is a μ-measurable function.*

Moreover, we define the *(Lebesgue-)Bochner spaces* according to [53, Definition 1.2.15] as follows: Given a measure space $(Y, \mathcal{A}, \mu)$, a Banach space $(Y', \|\cdot\|_{Y'})$ and a natural number $1 \leq q < \infty$, the Lebesgue-Bochner space $L^q(Y; Y')$ is defined as the linear space of all (equivalence classes of) strongly μ-measurable functions $g : Y \to Y'$ for which $\int_Y \|g\|_{Y'}^q \mathrm{d}\mu < \infty$. Further, $L^\infty(Y; Y')$ is defined as the linear space of all (equivalence classes of) strongly μ-measurable functions $g : Y \to Y'$ for which there exists a real number $r \geq 0$ such that $\mu\{\|g\|_{Y'} > r\} = 0$. The Lebesgue-Bochner spaces are Banach spaces when endowed with the norms

$$\|g\|_{L^q(Y;Y')} \coloneqq \left(\int_Y \|g(y)\|_{Y'}^q \mathrm{d}\mu(y) \right)^{1/q} < \infty, \quad 1 \leq q < \infty \text{ or}$$
$$\|g\|_{L^\infty(Y;Y')} \coloneqq \operatorname*{ess\,sup}_{y \in Y} \|g(y)\|_{Y'} < \infty.$$

Having defined the basic concepts of measure theory, we proceed with the definition of probability measures and spaces.

We call a measure space $(Y, \mathcal{A}, \mu)$ a *probability space* with *probability measure* μ if $\mu(Y) = 1$. We denote a complete probability space by $(\Omega, \mathcal{A}, \mu)$, and call Ω the *sample space* and $\mathcal{A}$ the *event space*. Further, we say that a property holds *μ-almost surely* (μ-a.s.) if there exists a set $S \subset \mathcal{A}$ with $\mu(S) = 0$ such that the property holds for all $y \in Y \setminus S$.

Throughout this thesis, we will be concerned with product probability measures, more precisely we will define probability measures on infinite product spaces. The *Kolmogorov extension theorem*, cf. [2, Section 15.6], [7, Theorem 5.1.7], proves the existence of such probability measures.

For understanding the Kolmogorov extension theorem, we need the definition of the pushforward of a measure. Let thus $(Y, \mathcal{A})$ and $(Y', \mathcal{A}')$ be measurable space, μ be a measure on Y, and $f : Y \to Y'$ be a measurable map. According to [17, Section 7.2.1], the *pushforward* $\mu' \coloneqq f^\# \mu$ of μ under the map f defines a measure on Y' and is defined by $\mu'(S) \coloneqq \mu(f^{-1}(S))$ for all $S \in \mathcal{A}'$.

We now state the Kolmogorov extension theorem as in [17, Theorem 7.4]:

Theorem 2.2.4 (Kolmogorov Extension Theorem). *Let Y be a Polish space, i.e., a separable completely metrizable topological space, and S be an arbitrary set. Assume that, for any finite subset $S' \subset S$, we are given a probability measure $\mu_{S'}$ on the finite*

product space $Y^{S'} \coloneqq \bigtimes_{j\in S'} Y$. *Assume further that the family of measures* $\{\mu_{S'}\}$ *is consistent in the sense that if* $S'' \subset S'$ *and* $\mathrm{pr}_{S',S''} : Y^{S'} \to Y^{S''}$ *denotes the natural projection map, then the pushforward of the measure* $\mu_{S'}$ *under the natural projection* $\mathrm{pr}_{S',S''}$ *fulfills* $\mathrm{pr}^{\#}_{S',S''}\,\mu_{S'} = \mu_{S''}$.

Then there exists a unique probability measure μ *on* Y^S *endowed with the product* σ*-algebra and the property that* $\mathrm{pr}^{\#}_{S,S'}\,\mu = \mu_{S'}$ *for all finite* $S' \subset S$.

As an example for the above theorem, we construct a product measure on the infinite product space $\mathbb{R}^\infty \coloneqq \bigtimes_{k=1}^{\infty} \mathbb{R}$. Let μ_0 denote a probability measure on $\mathbb{R}$ and define $\mu_S \coloneqq \bigotimes_{j\in S} \mu_0$ for every finite set $S \subset \mathbb{R}^\infty$. Then, according to Theorem 2.2.4, $\mu \coloneqq \bigotimes_{j=1}^{\infty} \mu_0$ is a probability measure on $\mathbb{R}^\infty$.

2.2.2. Random Variables

Following [59, Definition 1.102], we define a *random variable* as a measurable mapping $\mathfrak{X} : \Omega \to Y$ between a complete probability space $(\Omega, \mathcal{A}, \mu)$ and a measurable space $(Y, \mathcal{A}')$. Generalizing this definition, we define a *random function* or *stochastic process* as a family of random variables $\{\mathfrak{X}(\omega, \iota)\}$, ι lying in some index set $\mathcal{I}$ such that $\mathfrak{X}(\omega, \iota)$ is a random variable defined on the sample space Ω for each fixed $\iota \in \mathcal{I}$ and $\mathfrak{X}(\omega, \iota)$ is a function on the index set $\mathcal{I}$ for each fixed $\omega \in \Omega$, cf. [26, Section 2.1]. In case that $\mathcal{I} \subset \mathbb{R}^d$ and $Y = \mathbb{R}^n$ for $d, n \in \mathbb{N}$, we call $\mathfrak{X}(\omega, \iota)$ a *random field*, because $\mathfrak{X}(\omega, \iota)$ is a vector field for each fixed $\omega \in \Omega$.

We briefly outline the construction of random functions with specific properties. Precisely, we construct random functions $\mathfrak{f} : \Omega \times D \to \mathbb{R}^{n\times n}$ such that $\mathfrak{f}(\omega, \cdot) \in L^\infty(D; \mathbb{R}^{n\times n})$ for each $\omega \in \Omega$, a domain $D \subset \mathbb{R}^d$, i.e., a connected and open subset of $\mathbb{R}^d$, and $n, d \in \mathbb{N}$. Random functions of this class will be needed in Section 4.2.1. We follow the approach of [17, Section 2.1] and start with a basis representation of a deterministic function $f : D \to \mathbb{R}^{n\times n}$ of the form

$$f(x) = m(x) + \sum_{j=1}^{\infty} \varsigma_j \varphi_j(x)$$

with coefficients $\varsigma_j \in \mathbb{R}$, for $j = 1, \ldots, \infty$ and we assume that the functions $m, \varphi_j \in L^\infty(D; \mathbb{R}^{n\times n})$. Further, we normalize the basis $\{\varphi_j\}_{j=1}^{\infty}$ such that $\|\varphi_j\|_{L^\infty(D)} = 1$ for all $j = 1, \ldots, \infty$. By randomizing the coefficients ς_j in the way that $\varsigma_j = \gamma_j \zeta_j(\omega)$ for

$j = 1, \dots, \infty$, the deterministic function becomes probabilistic, indicated by $\mathfrak{f}$:

$$\mathfrak{f}(\omega, x) = m(x) + \sum_{j=1}^{\infty} \gamma_j \zeta_j(\omega) \varphi_j(x)$$

We choose $\gamma \coloneqq \{\gamma_j\}_{j=1}^{\infty} \in \ell^1$ and the random sequence $\zeta \coloneqq \{\zeta_j\}_{j=1}^{\infty}$ to be identically independent distributed (i.i.d.) with ζ_1 being distributed according to the uniform distribution on $[-1, 1]$ denoted by $U([-1, 1])$, i.e., $\zeta_1 \sim U([-1, 1])$. Here, $\ell^1 \coloneqq \{\{y_j\}_{j=1}^{\infty} \in \mathbb{R}^{\mathbb{N}} \mid \sum_{j=1}^{\infty} |y_j| < \infty\}$ denotes the space of all absolutely summable sequences in $\mathbb{R}^{\mathbb{N}}$. Note that scaling the random coefficients ζ to be uniformly distributed on $[-1, 1]$ also includes scaling the coefficients γ such that $\varsigma_j = \gamma_j \zeta_j(\omega)$ still holds for $j = 1, \dots, \infty$. We further assume that there exist constants $m_{\min}, m_{\max}, \delta > 0$ such that

$$\begin{aligned} 0 < m_{\min} \leq \operatorname*{ess\,inf}_{x \in D} m(x) \leq m(x) \leq \operatorname*{ess\,sup}_{x \in D} m(x) \leq m_{\max} < \infty, \\ \|\gamma\|_{\ell^1} = \frac{\delta}{1+\delta} m_{\min} \end{aligned}$$

and define the closure of the linear span of the functions $m, \varphi_j,\ j = 1, \dots, \infty$, with respect to $\|\cdot\|_{L^\infty(D)}$ as $\mathcal{J}_{\mathfrak{f}}$. Then the space $(\mathcal{J}_{\mathfrak{f}}, \|\cdot\|_{L^\infty(D)})$ is a separable Banach space [17, Section 2.2]. Furthermore, for $\mathfrak{f}^{N_{\text{trunc}}}(\omega, x) \coloneqq m(x) + \sum_{j=1}^{N} \gamma_j \zeta_j(\omega) \varphi_j(x)$, the sequence $\{\mathfrak{f}^{N_{\text{trunc}}}\}_{N_{\text{trunc}}=1}^{\infty}$ is Cauchy in $\mathcal{J}_{\mathfrak{f}}$ with limiting function $\mathfrak{f}$ and

$$\frac{1}{1+\delta} m_{\min} \leq \mathfrak{f}(\omega, x) \leq m_{\max} + \frac{\delta}{1+\delta} m_{\min} \quad \text{a.e. and a.s.}$$

From the above inequalities we see the boundedness of $\|\mathfrak{f}(\omega, \cdot)\|_{L^\infty(D)}$ for almost each $\omega \in \Omega$, i.e., $\mathfrak{f} \in L^\infty(D; \mathbb{R}^{n \times n})$ almost surely. For a proof of this argument we refer to [17, Theorem 2.1].

We interpret $\zeta = \{\zeta_j\}_{j=1}^{\infty}$ as an element of the probability space $(\mathbb{R}^\infty, \mathcal{B}(\mathbb{R}^\infty), \mu)$, where $\mathcal{B}(\mathbb{R}^\infty)$ denotes the Borel σ-algebra on $\mathbb{R}^\infty$ and μ is the measure defined in the example following Theorem 2.2.4. We further define the mapping $f' : \mathbb{R}^\infty \to \mathcal{J}_{\mathfrak{f}}$ with $\zeta \mapsto f'(\zeta) \coloneqq \mathfrak{f}(\omega, x) = m(x) + \sum_{j=1}^{\infty} \gamma_j \zeta_j(\omega) \varphi_j(x)$. Using this definition we are able to define a measure on $\mathcal{J}_{\mathfrak{f}}$ as the pushforward of μ under the map f', which means we define $\rho_0 \coloneqq f'^{\#}\mu$. Compare the above construction of ρ_0 with the Kolmogorv extension theorem 2.2.4 and the example thereafter. The measure ρ_0 is a probability measure on $\mathcal{J}_{\mathfrak{f}}$, i.e., $\rho_0(\mathcal{J}_{\mathfrak{f}}) = 1$. Due to the separability of $\mathcal{J}_{\mathfrak{f}}$ it is natural to use the Borel σ-algebra to define the probability space $(\mathcal{J}_{\mathfrak{f}}, \mathcal{B}(\mathcal{J}_{\mathfrak{f}}), \rho_0)$ [17, Section 2.6]. We will come back to

this probability space in Section 4.2.1 and move on with defining properties of random variables and functions.

The *expectation* of a random function $\mathfrak{X} : \Omega \times \mathcal{I} \to \mathbb{R}$ that is defined on a probability space $(\Omega, \mathcal{A}, \mu)$ and an index set $\mathcal{I}$ is defined as

$$\bar{\mathfrak{X}}(\iota) \coloneqq \mathbb{E}(\mathfrak{X}(\omega, \iota)) \coloneqq \int_\Omega \mathfrak{X}(\omega, \iota) \mathrm{d}\mu(\omega) \in \mathbb{R} \text{ for all } \iota \in \mathcal{I}$$

and the *covariance* is given by

$$\begin{aligned} \mathrm{cov}_{\mathfrak{X}}(\iota, \iota') &\coloneqq \mathbb{E}\left((\mathfrak{X}(\omega, \iota) - \bar{\mathfrak{X}}(\iota))(\mathfrak{X}(\omega, \iota') - \bar{\mathfrak{X}}(\iota'))\right) \\ &= \int_\Omega (\mathfrak{X}(\omega, \iota) - \bar{\mathfrak{X}}(\iota))(\mathfrak{X}(\omega, \iota') - \bar{\mathfrak{X}}(\iota')) \mathrm{d}\mu(\omega) \in \mathbb{R} \text{ for all } \iota, \iota' \in \mathcal{I}, \end{aligned}$$

see, e.g., [59, Definition 5.1], [26, Section 1.3.1]. For $\iota = \iota'$, the covariance becomes the *variance*

$$\mathrm{var}(\mathfrak{X})(\iota) \coloneqq \mathrm{cov}_{\mathfrak{X}}(\iota, \iota) = \mathbb{E}\left((\mathfrak{X}(\omega, \iota) - \bar{\mathfrak{X}}(\iota))^2\right) \in \mathbb{R} \text{ for all } \iota \in \mathcal{I}.$$

Two random variables, functions or fields are called *uncorrelated* if their covariance equals zero for all $\iota, \iota' \in \mathcal{I}$. Note that the covariance being equal to zero is equivalent to $\mathbb{E}(\mathfrak{X}(\omega, \iota)\mathfrak{X}(\omega, \iota')) = \mathbb{E}(\mathfrak{X}(\omega, \iota))\mathbb{E}(\mathfrak{X}(\omega, \iota'))$. This equality for the expectations is implied by a stronger property, the independence. For defining the independence we need the concept of conditional probability.

Let $(\Omega, \mathcal{A}, \mu)$ be a probability space. Following [59, Definition 8.2], we define the *conditional probability* of $S \in \mathcal{A}$ given $S' \in \mathcal{A}$ through

$$\mu(S \mid S') \coloneqq \begin{cases} \frac{\mu(S \cap S')}{\mu(S')} & \text{if } \mu(S') > 0, \\ 0 & \text{otherwise} \end{cases}$$

and say that two events $S, S' \in \mathcal{A}$ with probabilities $\mu(S), \mu(S') > 0$ are *independent* if

$$\mu(S \mid S') = \mu(S) \quad \text{or equivalently} \quad \mu(S' \mid S) = \mu(S').$$

Further, a finite set of $n \in \mathbb{N}$ events $\{S_j\}_{j=1}^n$ is *(mutually) independent*, see, e.g., [7, Definition 1.2.3], if every event is independent of any intersection of the other events,

i.e., if and only if for every $k \leq n$ and for every $\{S'_j\}_{j=1}^k \subset \{S_j\}_{j=1}^n$

$$\mu\left(\bigcap_{j=1}^{k} S'_j\right) = \prod_{j=1}^{k} \mu(S'_i)$$

holds. Conditional probabilities are further characterized by the Bayes theorem that was introduced in the second half of the 18th century by Thomas Bayes [5].

Theorem 2.2.5 (Bayes Theorem). *Let $(\Omega, \mathcal{A}, \mu)$ be a probability space and $S, S' \in \mathcal{A}$ with $\mu(S') > 0$. Then*

$$\mu(S \mid S') = \frac{\mu(S' \mid S)\mu(S)}{\mu(S')}.$$

2.2.3. Markov Chains

A *Markov process* is a stochastic process for which the state of the system at any future time depends only on the present state.

A good first insight into Markov chains in finite dimensions is offered by Norris [79]. A more general approach to Markov processes that is based on the notion of Markov transitions instead of Markov kernels is given by Aliprantis and Border [2, Chapters 19, 20]. For a brief introduction to Markov chains in the function space inverse problem setting, we refer to [17, Chapter 5].

We introduce the notion of a stochastic or Markov kernel and a filtration to specify the definition of a Markov process, cf. [59, Definition 9.9]. Let $\mathcal{I}$ be an index set. We call a family $(\mathcal{F}_\iota)_{\iota\in\mathcal{I}}$ of σ-algebras $\mathcal{F}_\iota$ a *filtration* if $\mathcal{F}_{\iota'} \subset \mathcal{F}_\iota$ for all $\iota, \iota' \in \mathcal{I}$ with $\iota' \leq \iota$. The filtration $(\mathcal{F}_\iota = \sigma(\mathfrak{X}(\cdot, \iota'), \iota' \leq \iota))_{\iota\in\mathcal{I}} =: \sigma(\mathfrak{X})$, with $\sigma(\cdot)$ denoting a σ-algebra of the indicated set, is called the *natural filtration* of a stochastic process $\mathfrak{X}$ defined over the index set $\mathcal{I}$. A filtration $(\mathcal{F}_\iota)_{\iota\in\mathcal{I}}$ represents the behavior of a stochastic process $\mathfrak{X}$ until time $\iota \in \mathcal{I}$ and thus allows for defining the independence of the current state of a stochastic process from its past states.

For a stochastic process $\mathfrak{X} = \{\mathfrak{X}(\cdot, \iota)\}_{\iota\in\mathcal{I}}$ with index set $\mathcal{I}$ and *state space* $(Y, \mathcal{A}, \mu)$ we define the probability measure $\mu_y(\mathfrak{X} \in S) \coloneqq \mu(\mathfrak{X} \in S \mid \mathfrak{X}(\cdot, 0) = y)$ for each $y \in Y$ and $S \in \mathcal{A}^{\mathcal{I}}$ with the product σ-algebra $\mathcal{A}^{\mathcal{I}} \coloneqq \bigotimes_{\iota\in\mathcal{I}} \mathcal{A}$.

Further, for two measurable spaces $(Y, \mathcal{A}), (Y', \mathcal{A}')$ we define a *stochastic* or *Markov kernel* to be a mapping $K : Y \times \mathcal{A}' \to [0, \infty]$ that satisfies the following two conditions: First, for each $S \in \mathcal{A}'$ the mapping $y \mapsto K(y, S)$ is a measurable function and, second, for each $y \in Y$ the mapping $S \mapsto K(y, S)$ is a probability measure [59, Definition 8.25].

The latter property implies that a Markov kernel is a mapping $K : Y \times \mathcal{A}' \to [0,1]$. The finite dimensional equivalent of a stochastic kernel is a stochastic matrix, i.e., a matrix $R \in \mathbb{R}^{n \times n}$ for some $n \in \mathbb{N}$, where the sum of each row and each column of R equals 1.

Using the above definitions, we define a Markov process following [59, Definition 17.3].

Definition 2.2.6 (Markov Process). *Let $\mathcal{I}$ be any index set and without loss of generality $0 \in \mathcal{I}$, $(\Omega, \mathcal{A}, \mu)$ be a probability space, and $(Y, \mathcal{A}')$ be a measurable space. A stochastic process $\mathfrak{X} = \{\mathfrak{X}(\cdot, \iota)\}_{\iota \in \mathcal{I}}$ with filtration $(\mathcal{F}_\iota)_{\iota \in \mathcal{I}}$ is called a* Markov process *in $(\Omega, \mathcal{A})$ with distribution $(\mu_y)_{y \in Y}$ if:*

(i) For each $y \in Y$, $\mathfrak{X}$ is a stochastic process on $(\Omega, \mathcal{A}, \mu_y)$ with $\mu_y(\mathfrak{X}(\cdot, 0) = y) = 1$.

(ii) The mapping $K : Y \times \mathcal{A}'^{\mathcal{I}} \to [0,1]$ with $(y, S) \mapsto K(y, S) \coloneqq \mu_y(\mathfrak{X} \in S)$ is a Markov kernel.

(iii) For all $S \in \mathcal{A}'$, $y \in Y$ and $\iota, \iota' \in \mathcal{I}$ with $\iota' = \iota + t$ for some increment t the Markov property

$$\mu_y(\mathfrak{X}(\cdot, \iota') \in S \mid \mathcal{F}_\iota) = K_{\iota'}(\mathfrak{X}(\cdot, \iota), S) \quad \mu_y\text{-a.s.}$$

holds. Here, the stochastic kernel of transition probabilities of $\mathfrak{X}$ after an increment t is defined as $K_{\iota'} : Y \times \mathcal{A}' \to [0,1]$ with $K_{\iota'}(y, S) \coloneqq K(y, \{y' \in Y^{\mathcal{I}} : y'(\iota) \in S\}) = \mu_y(\mathfrak{X}(\cdot, \iota') \in S)$ with the product space $Y^{\mathcal{I}} \coloneqq \bigtimes_{\iota \in \mathcal{I}} Y$.

We call $\mathfrak{X}$ a *Markov chain* if $\mathfrak{X}$ is a Markov process with index set $\mathcal{I} = \mathbb{N}_0$. In examples, the Markov processes and Markov chains are often indexed by time, such that the increment t in the above Definition can be interpreted as the passing of some time span.

A well-known example of a Markov chain is the *random walk*. We illustrate the one-dimensional random walk using the example of a drunk man walking on a straight street. The man starts his walk at time $\iota = 0$ in position y_0, i.e., $\mathfrak{X}(\iota = 0) = y_0$. With each step the drunk takes, he decides to either go down or up the street with equal probability, i.e., $\mathbb{P}(\mathfrak{X}(\iota = j+1) = y_{j+1} \mid \mathfrak{X}(\iota = j) = y_j) = \mathbb{P}(\mathfrak{X}(\iota = j+1) = y_{j-1} \mid \mathfrak{X}(\iota = j) = y_j) = \frac{1}{2}$, where $\mathbb{P}$ denotes the probability of the indexed event. Obviously, the position of the drunken man at a certain time $\iota = j + 1$ does only depend on the position of the drunken man at the previous time $\iota = j$. This property of Markov processes corresponds to property (iii) in Definition 2.2.6 and is often referred to as *memorylessness*.

A Markov process with kernel K on $(Y \times \mathcal{A})$ is said to be *invariant* with respect to a nonzero signed or σ-finite measure μ if

$$\mu(S) = \int_Y \mu(\mathrm{d}y) K(y, S)$$

for all $S \in \mathcal{A}$, compare [18, Section 2.4]. The measure μ fulfilling the above equation is called the *invariant* or *stationary* distribution of the Markov process. A criterion that implies invariance and is often easier to verify is reversibility, cf. [17, Definition 5.1]. We call a Markov process, as defined above, *reversible* if the measure $\mu \otimes K$ on $\mathcal{A} \otimes \mathcal{A}$ is symmetric, i.e.,

$$\int_S \mu(\mathrm{d}y) K(y, S') = \int_{S'} \mu(\mathrm{d}y') K(y', S) \tag{2.2}$$

for all $(S, S') \in \mathcal{A} \otimes \mathcal{A}$ and integration parameters y, y'. The above equation is sometimes also called *detailed balance*.

The convergence or long run behavior of Markov processes is examined by ergodic theory. We refer to [25, Chapter 5] and [2, Chapters 19, 20] for an introduction to ergodic theory of Markov chains. Roughly speaking, a μ-ergodic Markov process statistically represents the probability measure μ, i.e., the expectation and other statistical quantities of the Markov process correspond with the respective quantities of the probability distribution μ. Furthermore, a Markov process is μ-ergodic if the Markov process is invariant with respect to μ and some additional properties hold. Precisely, [2, Theorem 19.25] says that ergodic measures can be found as the extreme points of the set of invariant measures and [2, Corollary 19.26] guarantees that every continuous Markov transition on a compact metrizable space admits ergodic measures. The latter result can directly be transferred to the notion of Markov kernels. We deduce that a Markov chain that is invariant with respect to a measure μ is well-suited to represent the statistical behavior of this measure μ. The Markov chain Monte Carlo methods for sampling from a given probability distribution μ, introduced in the following section, build on this property of invariant measures of Markov processes.

2.3. Markov Chain Monte Carlo Methods

Markov chain Monte Carlo (MCMC) methods are a class of algorithms for sampling from (high-dimensional) probability distributions such as the posterior distributions that arise

in Bayesian inversion as we will see in Section 2.4. The essential ingredient of MCMC methods is the construction of a Markov chain, see Definition 2.2.6, that is invariant with respect to the desired probability distribution, see our discussion at the end of Section 2.2.3. For a general introduction to finite-dimensional MCMC methods, we refer to [79].

Monte Carlo methods or randomized simulations, as they were often called in the beginning, were developed by Stanislaw Ulam and John von Neumann in the late 1940s and enabled sampling from the uniform and many other standard distributions. Extending the Monte Carlo concept to more general distributions that arise, e.g., from physical models, von Neumann introduced the *acceptance-rejection sampling*.

The idea of acceptance-rejection sampling is to propose a sample according to some proposal distribution and accept the sample if it is "good enough" while rejecting it otherwise. The fidelity of the proposed samples is measured by an *acceptance strategy*. One major advantage of acceptance-rejection algorithms is their ability to sample from distributions whose normalizing constants are unknown or intractable, which is common in computational statistics. This simple method is, however, not well-suited for sampling from high-dimensional distributions due to the curse of dimensionality [86].

To overcome this drawback, Markov chains were brought into play. The idea of MCMC methods is to construct Markov chains that have the desired distribution as their stationary distribution and then sample from the Markov chain instead of sampling from the desired distribution itself. The core problem of this idea is to find such a Markov chain.

In 1953, Metropolis solved this problem and introduced his *Metropolis algorithm* to sample from the Boltzmann distribution [72]. In 1970, Hastings generalized the Metropolis algorithm to form the *Metropolis-Hastings algorithm*, which became the probably most famous and simplest MCMC method [47]. Further developments of MCMC methods are, e.g., simulated annealing that was introduced by Kirkpatrick et al. in 1983, cf. [57], and the Gibbs sampling that was developed in 1984 by Geman and Geman [32] for digital image reconstruction based on a Bayesian approach to estimate the maximum of the posterior distribution. Geman and Geman also proved convergence of their approach. Furthermore, Tierney uses Markov chains for exploring posterior distributions and also showed some convergence results in 1994 [101] and Diaconis generalized the Metropolis algorithm to higher-dimensional Lipschitz domains [18].

For more details about the developments of MCMC methods, we refer to [86]. Throughout this thesis we focus on the Metropolis-Hastings algorithm and thus introduce this

algorithm in more detail in the following. We present the idea of the Metropolis-Hastings algorithm in finite-dimensional state spaces following [79].

Throughout this section, we consider a stochastic process $\{\mathfrak{X}(\omega,\iota)\}_{\iota\in\mathcal{I}}$ on a probability space $(\Omega,\mathcal{A},\mu)$ and indexed by a countable index set $\mathcal{I}$ with $\mathfrak{X}(\cdot,\iota):\Omega\to Y'$ for some state space Y'. We interpret such a stochastic process $\{\mathfrak{X}(\omega,\iota)\}_{\iota\in\mathcal{I}}$ as a random variable $\{\mathfrak{X}(\omega,\iota)\}_{\iota\in\mathcal{I}}:\Omega\to(Y')^{\mathcal{I}}=\bigtimes_{\iota\in\mathcal{I}}Y'$ with state space in product form. For finite index sets $\mathcal{I}$ and finite sets Y_ι with $\iota\in\mathcal{I}$, we generalize the above idea by defining the product form state space $Y\coloneqq\bigtimes_{\iota\in\mathcal{I}}Y_\iota$. Thus, $\mathfrak{X}\coloneqq\{\mathfrak{X}(\cdot,\iota)\}_{\iota\in\mathcal{I}}$ with $\mathfrak{X}(\cdot,\iota)\in Y_\iota$ for all $\iota\in\mathcal{I}$ denotes a random variable with values in the state space $Y=\bigtimes_{\iota\in\mathcal{I}}Y_\iota$. Let further μ denote the distribution of $\mathfrak{X}$ from which we wish to draw samples.

As stated above, the basic idea of MCMC methods, and thus of the Metropolis-Hastings algorithm, is to construct a Markov chain $(\mathfrak{M}_j)_{j\geq0}$ that has μ as its invariant distribution, since simulating a Markov chain is easier than simulating μ itself. This is due to the fact that the state space Y as defined above is in product form, i.e., each component $\mathfrak{M}_0(\cdot,\iota)$ is a random variable in Y_ι and thereby $\mathfrak{M}_{j+1}(\cdot,\iota)$ is a random variable with values in Y_ι according to a distribution determined by $\mathfrak{M}_j$. In other words, we sample random variables in Y_ι instead of the much larger space Y. Under suitable assumptions, the distribution of $\mathfrak{M}_j$ converges to μ as $j\to\infty$, see, e.g., [79, Sections 1.8, 3.6].

To obtain a Markov chain that has μ as its invariant distribution we construct the transition probabilities of going from state indexed by j to state indexed by k at time ι of the Markov chain, denoted by $P_{jk}(\iota)$, such that they fulfill the finite-dimensional detailed balance equation

$$\mu_jP_{jk}(\iota)=\mu_kP_{kj}(\iota)$$

for all states indexed by j,k. Given any stochastic matrix $R(\iota)$, the transition matrix $P(\iota)$ satisfies detailed balance if

$$\begin{aligned}\mu_jP_{jk}(\iota)&=(\mu_jR_{jk}(\iota))\wedge(\mu_kR_{kj}(\iota))\quad\text{for } j\neq k,\\ P_{jj}(\iota)&=1-\sum_{k\neq j}P_{jk}(\iota)\geq0.\end{aligned}$$

Further choosing the stochastic matrix R to be symmetric, i.e., $R_{jk}(\iota)=R_{kj}(\iota)$ for all

states indexed by j, k, the formula for the transition probabilities becomes

$$P_{jk}(\iota) = (\left(\frac{\mu_k}{\mu_j}\right) \wedge 1) R_{jk}(\iota), \quad \text{for } j \neq k,$$

assuming $\mu_j > 0$. The acceptance-rejection algorithm that uses a Markov chain with transition probabilities determined as above is the Metropolis-Hastings algorithm, as shown in Algorithm 2.3.1. The acceptance strategy in Algorithm 2.3.1 is $a(j,k) := (\frac{\mu_k}{\mu_j}) \wedge 1$. In practice, a stopping criterion, such as a maximal number of proposals to be drawn, has to be added to Algorithm 2.3.1.

Algorithm 2.3.1 Prototypical Metropolis Hastings algorithm

Input: initial guess $\mathfrak{M}_0 \in Y$, proposal distribution K_{p}
Output: Markov chain $\mathfrak{M}$ with transition matrix P

1: set $j = 0$
2: propose $\mathfrak{M}_k \sim K_{\mathrm{p}jk}$
3: $\mathfrak{M}_{j+1} = \mathfrak{M}_k$ with probability $a(j,k)$, independently of $(\mathfrak{M}_j, \mathfrak{M}_k)$ or
   $\mathfrak{M}_{j+1} = \mathfrak{M}_j$ with probability $1 - a(j,k)$
4: $j = j + 1$, return to step 2

2.4. The Bayesian Approach to Inverse Problems

The main idea of the Bayesian approach for solving inverse problems is to model the measured data and parameters as stochastic quantities and examine their statistical behavior.

As the name Bayesian approach suggests, this approach goes back to Bayes' theorem, as first stated in [5] in 1763, and Bayesian statistics. Even though the field of Bayesian statistics was early seen as a generalization of the classical statistics, Bayesian statistics remained highly controversial until the late 20th century. We refer to [66] for an overview on the history of Bayesian statistics. We will see this generalization aspect in the treatment of inverse problems when drawing a connection between the Bayesian approach and the Tikhonov regularization.

The Bayesian approach to inverse problems was first developed in finite dimensional spaces and it took until the 21st century that a function space, i.e., an infinite dimensional, approach for Bayesian inverse problems was derived [99]. Non-stationary Bayesian inverse problems that occur, e.g., in monitoring the heart by measurements of the magnetic fields outside the body over time, are discussed in [55]. This kind of

problems lead to Bayesian filtering methods, such as Kalman and particle filters.

The basic ingredient for defining the Bayesian formulation of inverse problems is to explicitly add a model of the inevitable measurement error to the forward model $\mathcal{G}(\boldsymbol{p}) = \phi$ as introduced in the beginning of Chapter 2. The measurement error is, however, usually unknown deterministically, but its stochastic properties may be known from experiments. Therefore, the measurement error is modeled as a stochastic quantity η on a complete probability space $(\Omega, \mathcal{A}, \mu)$, see Section 2.2.1, and is then added to the forward model as additive noise. In the inverse setting we thus search for a parameter $\boldsymbol{p}^* \in \boldsymbol{\mathcal{J}}$ that fulfills the equation

$$\mathcal{G}(\boldsymbol{p}^*) + \eta = \phi^*$$

for given data ϕ^*. Obviously, the above equation implies that the unknown parameter $\boldsymbol{p}^*$ is a random variable too, and we write $\boldsymbol{p}^* = \boldsymbol{p}^*(\omega)$ to emphasize this randomness.

A naive approach for solving the above stochastic problem is to fix $\omega \in \Omega$ and to apply any of the classical regularization techniques from Section 2.1.1 to solve the equation $\mathcal{G}(\boldsymbol{p}^*(\omega)) + \eta(\omega) = \phi^*$. We thus obtain one specific instance of the random variable $\boldsymbol{p}^*$. Clearly, knowing this single instance $\boldsymbol{p}^*(\omega)$ is meaningless if we are interested in the overall behavior of the stochastic parameter $\boldsymbol{p}^*$.

In Section 2.4.1, we state Bayes' theorem to compute the conditional probability distribution of parameters $\boldsymbol{p}$ given data ϕ^* and thus quantify the behavior of the probabilistic parameter $\boldsymbol{p}$ given ϕ^*. For sampling from a general probability distribution, we introduced the Metropolis-Hastings algorithm in Section 2.3. We adapt this sampling strategy to sample from the conditioned probability distribution of $\boldsymbol{p}$ given ϕ^* and extend the finite-dimensional setting of Section 2.3 to the infinite-dimensional Banach space setting in Section 2.4.2.

2.4.1. Bayes' Theorem in the Inverse Problem Setting

For calculating the conditional probability distribution of the parameter $\boldsymbol{p}$ given data ϕ^*, we use Bayes' theorem. If the spaces $\boldsymbol{\mathcal{J}}$ and Y are finite-dimensional and μ is a measure on $\boldsymbol{\mathcal{J}}$, Bayes' theorem 2.2.5 is applicable and we obtain

$$\mu(\boldsymbol{p} \mid \phi^*) = \frac{\mu(\phi^* \mid \boldsymbol{p})\mu(\boldsymbol{p})}{\mu(\phi^*)},$$

assuming $\mu(\phi^*) > 0$. We call $\boldsymbol{\rho}_0(\boldsymbol{p}) \coloneqq \mu(\boldsymbol{p})$ the *prior distribution* or short *prior*. It describes the a-priori knowledge or belief about the parameter $\boldsymbol{p}$. Further, we call the conditional probability $L(\boldsymbol{p}, \phi^*) \coloneqq \mu(\phi^* \mid \boldsymbol{p})$ the *likelihood function* or short *likelihood*. It describes the interrelation between the data ϕ^* and the unknown parameter $\boldsymbol{p}$. Furthermore, we call $\boldsymbol{\rho}_{\phi^*}(\boldsymbol{p}) \coloneqq \mu(\boldsymbol{p} \mid \phi^*)$ the *posterior distribution* or short *posterior* of $\boldsymbol{p}$ given ϕ^*. It describes the behavior of the unknown parameter $\boldsymbol{p}$ dependent on the measurements ϕ^* and thus is the solution of the Bayesian inverse problem. The *scaling factor* $Z \coloneqq \mu(\phi^*)$ is often intractable and treated as a proportionality constant. Applying the above definitions we, reach the proportionality

$$\boldsymbol{\rho}_{\phi^*}(\boldsymbol{p}) \propto L(\boldsymbol{p}, \phi^*)\boldsymbol{\rho}_0(\boldsymbol{p})$$

that describes the general Bayesian setting. This formula can be understood as going from a construction of the joint probability distribution on unknown parameters and data, i.e., the likelihood function, to the conditional distribution of the unknown parameters given data, i.e., the posterior [17, Section 3.1].

Bayes' theorem in the inverse problem setting was further generalized to inverse problems in function spaces in [17, Section 3.2] and [99, Chapter 2]. Let thus $\boldsymbol{\mathcal{J}}, Y$ be separable Banach spaces, the forward map $\mathcal{G} : \boldsymbol{\mathcal{J}} \to Y$ be measurable, and the noise η be independent of $\boldsymbol{p}$ with η distributed according to some distribution ρ_{noise}, i.e., $\eta \sim \rho_{\text{noise}}$. Further, let $\boldsymbol{\rho}_0$ denote the prior on $\boldsymbol{\mathcal{J}}$, $L(\boldsymbol{p}, \phi^*)$ denote the measure of ϕ^* given $\boldsymbol{p}$, and $\Phi : \boldsymbol{\mathcal{J}} \times Y \to \mathbb{R}$ be a potential that fulfills

$$\frac{\mathrm{d}L(\boldsymbol{p}, \cdot)}{\mathrm{d}\rho_{\text{noise}}}(\phi) = \exp\big(-\Phi(\boldsymbol{p}, \phi)\big). \tag{2.3}$$

Finally, the product measures ν_0 and $\nu_{\boldsymbol{p}}$ are defined as

$$\nu_0(\mathrm{d}\boldsymbol{p}, \mathrm{d}\phi) \coloneqq \boldsymbol{\rho}_0(\mathrm{d}\boldsymbol{p}) \otimes \rho_{\text{noise}}(\mathrm{d}\phi), \tag{2.4}$$

$$\nu_{\boldsymbol{p}}(\mathrm{d}\boldsymbol{p}, \mathrm{d}\phi) \coloneqq \boldsymbol{\rho}_{\phi^*}(\mathrm{d}\boldsymbol{p}) \otimes L(\boldsymbol{p}, \mathrm{d}\phi). \tag{2.5}$$

Within this setting Bayes' theorem reads as follows.

Theorem 2.4.1 (Infinite-dimensional Bayes Theorem). *Assume that the potential $\Phi : \boldsymbol{\mathcal{J}} \times Y \to \mathbb{R}$ is ν_0-measurable and that for measurements $\phi^* \in Y$*

$$Z \coloneqq \int_{\boldsymbol{\mathcal{J}}} \exp\big(-\Phi(\boldsymbol{p}, \phi^*)\big)\boldsymbol{\rho}_0(\mathrm{d}\boldsymbol{p}) > 0 \quad \rho_{noise}\text{-a.s.} \tag{2.6}$$

Then the conditional distribution of $\boldsymbol{p}$ *given* ϕ^* *exists under* $\nu_{\boldsymbol{p}}$*, and is denoted by* $\boldsymbol{\rho}_{\phi^*}$*. Furthermore, the posterior is absolutely continuous with respect to the prior, i.e.,* $\boldsymbol{\rho}_{\phi^*} \ll \boldsymbol{\rho}_0$*, and for* $\phi^* \in Y$

$$\frac{\mathrm{d}\boldsymbol{\rho}_{\phi^*}}{\mathrm{d}\boldsymbol{\rho}_0}(\boldsymbol{p}) = \frac{1}{Z} \exp\big(-\Phi(\boldsymbol{p}, \phi^*)\big) \quad \nu_{\boldsymbol{p}}\text{-a.s.}$$

For a proof see [17, Theorem 3.4].

Note that properties that hold almost surely and are build into the prior will be inherited by the posterior due to the absolute continuity of the posterior with respect to the prior. More precisely, almost sure properties could only be changed by data if the data contained an infinite amount of information, which is unnatural in most applications.

We highlight that Bayes' theorem for separable Banach spaces as cited above also holds for measurable spaces as long as all other assumptions are fulfilled [50].

Summarizing, we see that solving a Bayesian inverse problem comprises modeling the prior $\boldsymbol{\rho}_0(\boldsymbol{p})$, calculating the likelihood $L(\boldsymbol{p}, \phi^*)$, and developing methods to explore the posterior $\boldsymbol{\rho}_{\phi^*}(\boldsymbol{p})$. We briefly discuss each of these three steps, following the description in [55, Section 3.1].

Modeling the Prior Distribution

Modeling the prior distribution is typically the most crucial step in Bayesian inversion. Finding an appropriate prior means quantifying the expected behavior of or qualitative knowledge about the unknown parameter and thus transferring it into the framework of probability distributions. At the same time, care must be taken that the prior is not too restrictive or informative if the behavior of the unknown parameter is barely known.

We forbear from discussing the subtleties of prior modeling and mention the wide class of Gaussian priors that are based on Gaussian distributions, and the impulse priors, such as the ℓ^1 prior, the Cauchy density, the entropy density, and the lognormal density. Further, a rich class of prior distributions can be derived from the theory of Markov random fields, e.g., the total variation density. Furthermore, there are so-called sample-based densities where the prior is build from huge data sets of the unknown. For an overview on prior modeling we refer to [80] and [81, Chapter 3].

Calculating the Likelihood Function

The likelihood function is mainly determined by the measurement error model, i.e., by the stochastic properties of the noise η. Recall that we denoted the distribution of η by ρ_{noise}.

In the above introduction to Bayesian inversion we used an additive noise model, i.e., $\mathcal{G}(\boldsymbol{p}) + \eta = \phi$. If we additionally assume that η is mutually independent of the unknown parameter $\boldsymbol{p}$, the likelihood function emerges from shifting the density of ϕ^* by $\mathcal{G}(\boldsymbol{p})$, i.e.,

$$L(\boldsymbol{p}, \phi^*) = \rho_{\text{noise}}(\phi^* - \mathcal{G}(\boldsymbol{p})).$$

Note that ρ_{noise} can be any continuous probability distribution. When dropping the assumption of mutual independence of η and $\boldsymbol{p}$, the likelihood function is given by

$$L(\boldsymbol{p}, \phi^*) = \rho_{\text{noise}}(\phi^* - \mathcal{G}(\boldsymbol{p}) \mid \boldsymbol{p}).$$

A more complex noise model can be achieved by using mutually independent multiplicative noise, i.e., $\mathcal{G}(\boldsymbol{p})\eta = \phi$. This model emerges from describing incomplete knowledge of the forward model. For an overview on more elaborate noise models we refer to [64], and to [52, Section 1.4] for a detailed discussion on the concept of noise and error.

It is clear, that the case of additive and mutually independent noise is desirable from a computational point of view, as the likelihood can then be computed easily.

Exploring the Posterior Distribution

We assume for the moment that the posterior distribution is known and summarize several point, spread, and interval estimators to extract information from this posterior. For the numerical approximation of the posterior we have introduced MCMC methods in Section 2.3.

Point estimators aim at calculating one value that represents the posterior in an optimal way. We give three examples. The *maximum a posteriori* or short *MAP estimator*

$$\boldsymbol{p}_{\text{MAP}} \coloneqq \arg\max_{\boldsymbol{p} \in \mathcal{J}} \boldsymbol{\rho}_{\phi^*}(\boldsymbol{p})$$

calculates the most probable value of the unknown. The MAP estimator might be meaningful whenever the distribution is narrow and unimodal, while it is less informative when

dealing with multimodal distributions. In [17, Chapter 4.5] it is shown that searching for the MAP estimator leads to the same optimization problem as classical Tikhonov regularization methods with specific norms and regularization parameters. This relation between Tikhonov regularization and finding the MAP estimator implies that calculating the MAP estimator suffers from the same problems of uniqueness as the classical approaches, see the explanation in [99, Section 2.2].

The *conditional mean estimator*

$$\boldsymbol{p}_{\mathrm{CM}} \coloneqq \mathbb{E}\{\boldsymbol{p} \mid \phi^*\} = \int_{\boldsymbol{\mathcal{J}}} \boldsymbol{p}\boldsymbol{\rho}_{\phi^*}(\boldsymbol{p})\mathrm{d}\boldsymbol{p}$$

calculates the expected value of the posterior, compare to the definition of the expectation in Section 2.2.2, and can be used to help interpreting the MAP estimator.

The *maximum likelihood* or short *ML estimator*

$$\boldsymbol{p}_{\mathrm{ML}} \coloneqq \arg\max_{\boldsymbol{p}\in\boldsymbol{\mathcal{J}}} L(\boldsymbol{p}, \phi^*)$$

searches for the value of the unknown parameter that is most likely to produce the measured data. The ML estimator is called a non-Bayesian estimator as it is independent of the posterior distribution. In [99, Section 2.2] it is shown that calculating the ML estimator is equivalent to solving the classical least squares formulation of the inverse problem without regularization.

An example for a spread estimator is the *conditional covariance estimator*

$$\mathrm{cov}(\boldsymbol{p} \mid \phi^*) \coloneqq \int_{\boldsymbol{\mathcal{J}}} (\boldsymbol{p} - \boldsymbol{p}_{\mathrm{CM}})(\boldsymbol{p} - \boldsymbol{p}_{\mathrm{CM}})^\top \boldsymbol{\rho}_{\phi^*}(\boldsymbol{p})\mathrm{d}\boldsymbol{p} \in \mathbb{R}^{n\times n},$$

compare to the definition of the covariance in Section 2.2.2, that can be used to further improve the interpretation of the MAP and conditional mean estimators.

In contrast to point and spread estimators, *interval estimators* aim at calculating an interval that contains the unknown parameter with a certain probability. An example is the *Bayesian credibility set* S_p that is defined for any $q \in (0, 100)$ by

$$\mathbb{P}(S_p \mid \phi^*) = \int_{S_p} \boldsymbol{\rho}_{\phi^*}(\boldsymbol{p})\mathrm{d}\boldsymbol{p} \overset{!}{=} \frac{q}{100}, \quad \boldsymbol{\rho}_{\phi^*}(\boldsymbol{p})\big|_{\boldsymbol{p}\in\partial S_p} = \mathrm{const.}$$

The boundary of S_p is an equiprobability hypersurface enclosing $q\,\%$ of the mass of the posterior distribution.

As suggested at the beginning of this section, we have seen that the Bayesian approach to inverse problems yields a generalization of the classical regularization techniques in the sense that some point estimators of the posterior distribution lead to classical regularization methods. We deduce that the posterior distribution contains richer information about the behavior of the unknown parameter than classical regularization methods would be able to give.

2.4.2. Metropolis-Hastings Algorithm for Bayesian Inversion

We construct a Metropolis-Hastings algorithm to sample from the posterior distribution that is the solution of the above general Bayesian inverse problem, cf. [17, Chapter 5] for more details. Therefore, we focus on Metropolis-Hastings algorithms that make sense in infinite dimensions in order to construct algorithms that will perform well under refinement of finite dimensional approximations.

Let $\boldsymbol{\mathcal{J}}$ be a separable Banach space with Borel σ-algebra $\mathcal{B}(\boldsymbol{\mathcal{J}})$, and let the potential $\Phi : \boldsymbol{\mathcal{J}} \times Y \to \mathbb{R}$ with $\frac{\mathrm{d}L(\boldsymbol{p},\cdot)}{\mathrm{d}\rho_{\text{noise}}}(\phi^*) = \exp\big(-\Phi(\boldsymbol{p},\phi^*)\big)$ and the scaling factor $Z = \int_{\boldsymbol{\mathcal{J}}} \exp\big(-\Phi(\boldsymbol{p},\phi^*)\big)\boldsymbol{\rho}_0(\mathrm{d}\boldsymbol{p})$ be as above.

As in the finite dimensional case, see Section 2.3, we are looking for Markov chains that have a desired distribution, here $\boldsymbol{\rho}_{\phi^*}$, as their invariant distribution. Again, we use the detailed balance equation to construct a transition kernel K of such a $\boldsymbol{\rho}_{\phi^*}$-invariant Markov chain. A Markov chain on a separable Banach space $\boldsymbol{\mathcal{J}}$ satisfies detailed balance if

$$\boldsymbol{\rho}_{\phi^*}(\mathrm{d}\boldsymbol{p})K(\boldsymbol{p},\mathrm{d}\boldsymbol{p}') = \boldsymbol{\rho}_{\phi^*}(\mathrm{d}\boldsymbol{p}')K(\boldsymbol{p}',\mathrm{d}\boldsymbol{p}) \tag{2.7}$$

holds, when both sides are understood as measures on $(\boldsymbol{\mathcal{J}} \times \boldsymbol{\mathcal{J}}, \mathcal{B}(\boldsymbol{\mathcal{J}}) \otimes \mathcal{B}(\boldsymbol{\mathcal{J}}))$, compare to the definition of symmetry of measures in Equation (2.2).

Algorithm 2.3.1 directly transfers to the infinite dimensional case with the proposal distribution being defined through a kernel K_{p} and the Markov kernel K, taking the place of the transition matrix P. We see from Algorithm 2.3.1 that there are two possibilities to control the Markov chain, namely the proposal kernel K_{p} and the acceptance probability $a : \boldsymbol{\mathcal{J}} \times \boldsymbol{\mathcal{J}} \to [0,1]$. The following theorem tells us how to choose these two quantities in order to achieve a Markov chain with invariant distribution $\boldsymbol{\rho}_{\phi^*}$.

Theorem 2.4.2. *Let $\Phi(\boldsymbol{p};\cdot) : \boldsymbol{\mathcal{J}} \to \mathbb{R}$ be bounded on bounded subsets of $\boldsymbol{\mathcal{J}}$ and $\frac{\mathrm{d}\boldsymbol{\rho}_{\phi^*}}{\mathrm{d}\boldsymbol{\rho}_0}(\boldsymbol{p}) = \frac{1}{Z}\exp(-\Phi(\boldsymbol{p}))$. If the proposal kernel K_p is reversible with respect to the prior $\boldsymbol{\rho}_0$, i.e., if Equation (2.7) holds for K_p and $\boldsymbol{\rho}_0$, Algorithm 2.3.1 produces a Markov*

chain that is reversible with respect to $\boldsymbol{\rho}_{\phi^*}$ *if*

$$a(\boldsymbol{p}, \boldsymbol{p}') = \min\{1, \exp(\Phi(\boldsymbol{p}) - \Phi(\boldsymbol{p}'))\}.$$

For a proof of Theorem 2.4.2 we refer to [17, Theorem 5.8].

Note that the acceptance probability is defined through the Radon-Nikodym derivatives, see Theorem 2.2.1, between the posteriors for $\boldsymbol{p}$ and $\boldsymbol{p}'$ and the prior $\boldsymbol{\rho}_0$ in Theorem 2.4.2. Because measures in infinite dimensions tend to be mutually singular, most finite-dimensional Metropolis-Hastings algorithms are meaningless in the infinite-dimensional setting.

Note further that even though Theorem 2.4.2 fully specifies the acceptance probability a, it leaves the choice of the proposal kernel K_p open as long as it is reversible with respect to the prior. Choosing K_p to be the prior, i.e., $K_\mathrm{p}(\boldsymbol{p}, \mathrm{d}\boldsymbol{p}') = \boldsymbol{\rho}_0(\mathrm{d}\boldsymbol{p}')$, prior reversibility is obviously given. The resulting algorithm is called *independence sampler* and tends to work well whenever the potential Φ only varies slightly depending on the evaluation point. In the case that Φ changes significantly, proposals that are more local with respect to the evaluation point are needed, such as the proposals generated by the pCN method that is based on Gaussian priors, compare [17, Section 5.2].

Applying a sampling algorithm that is defined in infinite dimensional spaces to sample from the posterior distribution $\boldsymbol{\rho}_{\phi^*}$ of parameters $\boldsymbol{p}$ given data ϕ^* yields the convergence of the algorithm under refinement of discretizations of the parameter space and the underlying forward problem $\mathcal{G}(\boldsymbol{p}) = \phi$. On the other hand, Metropolis-Hastings algorithms and especially the independence sampler show slow convergence in practice, such that a high number of samples needs to be drawn, cf. [101, Section 2.3.3] and the numerical experiments in Section 5.2. Drawing a new sample includes evaluating the acceptance probability and thus the potential Φ. In most applications the evaluation of the potential includes solving the forward problem for the proposed parameter, which is often computationally expensive, compare to Chapter 5.

2.5. Low-rank Tensor Formats

In this section, we introduce low-rank tensor formats as a tool to represent parameter-dependent linear systems and their solutions for all parameter combinations data-sparse. Such parameter-dependent linear systems occur, e.g., when discretizing parameter-dependent forward problems $\mathcal{G} : \boldsymbol{\mathcal{J}} \to Y$ with $\mathcal{G}(\boldsymbol{p}) = \phi$. For an example, see Section 3.2.4.

We refer to [60] for a comprehensive and accessible introduction to tensors, tensor formats and tensor decompositions. The following summary is based on work that has previously been published in [88] by the author of this thesis and co-workers.

For motivating low-rank tensor formats, we consider the arbitrary linear, parameter-dependent problem $A(\boldsymbol{p})\phi(\boldsymbol{p}) = b$ for a linear and parameter-dependent operator $A = A(\boldsymbol{p})$, a parameter-independent right-hand side b, and $d \in \mathbb{N}$ parameters $\boldsymbol{p} = (\boldsymbol{p}^{(1)}, \ldots, \boldsymbol{p}^{(d)})$. Discretizing the parameters such that each parameter $\boldsymbol{p}^{(j)}$ is allowed to take n_j different discrete values $\boldsymbol{p}^{(j)}(1), \ldots, \boldsymbol{p}^{(j)}(n_j)$ for all $j = 1, \ldots, d$ and solving the linear, parameter-dependent problem

$$A((\boldsymbol{p}^{(1)}(k_1), \ldots, \boldsymbol{p}^{(d)}(k_d))\phi((\boldsymbol{p}^{(1)}(k_1), \ldots, \boldsymbol{p}^{(d)}(k_d)) = b \tag{2.8}$$

for each parameter combination, i.e., for all $k_j = 1, \ldots, n_j$ and $j = 1, \ldots, d$ yields $\prod_{j=1}^{d} n_j$ solution vectors.

Obviously, if d or n_j, for $j = 1, \ldots, d$, are large, solving the parameter-dependent linear system given by Equation (2.8) for all parameter combinations and storing the $\prod_{j=1}^{d} n_j$ solution vectors is infeasible. Rewriting the linear system (2.8), we aim at using the underlying linear structure of the system to achieve a data-sparse representation.

Exemplifying the ansatz, we set $d = 1$ and consider solving the scaled equation $\boldsymbol{p}(k_1)A\phi(\boldsymbol{p}(k_1)) = b$ for a single parameter $\boldsymbol{p}$ taking the $n_1 \in \mathbb{N}$ values $\boldsymbol{p}(1), \ldots, \boldsymbol{p}(n_1)$, some operator A, and a right-hand side b. Solving the scaled problem for all $\boldsymbol{p}(k_1)$ is equivalent to solving

$$\begin{pmatrix} \boldsymbol{p}(1)A & 0 & \ldots & 0 \\ 0 & \boldsymbol{p}(2)A & \ddots & \vdots \\ \vdots & \ddots & \ddots & 0 \\ 0 & \ldots & 0 & \boldsymbol{p}(n_1)A \end{pmatrix} \begin{pmatrix} \phi(\boldsymbol{p}(1)) \\ \phi(\boldsymbol{p}(2)) \\ \vdots \\ \phi(\boldsymbol{p}(n_1)) \end{pmatrix} = \begin{pmatrix} b \\ b \\ \vdots \\ b \end{pmatrix}. \tag{2.9}$$

We rewrite this possibly huge system of equations using the Kronecker product and achieve

$$\left(\operatorname{diag}(\boldsymbol{p}(1), \boldsymbol{p}(2), \ldots, \boldsymbol{p}(n_1)) \otimes A\right) \phi(\boldsymbol{p}(1), \boldsymbol{p}(2), \ldots, \boldsymbol{p}(n_1)) = (1, \ldots, 1)^{\top} \otimes b.$$

Obviously, the above representation is data-sparse compared to the representation in Equation (2.9).

We define the *CANDECOMP/PARAFAC (CP) representation*[1] that is a generalization of the above representation and was first introduced in 1970 [9, 46].

Definition 2.5.1 (CP Representation and CP Decomposition). *Let $\mathcal{I}_k$ with $|\mathcal{I}_k| = n_k$ for all* modes *$k \in \mathcal{D} \coloneqq \{1, \dots, d\}$ and the* dimension *d, and $\mathcal{I} \coloneqq \bigtimes_{k=1}^{d} \mathcal{I}_k$ be index sets. A* CP representation *of a tensor $\mathbf{B} \in \mathbb{R}^{\mathcal{I}}$, with* representation rank *$r \in \mathbb{N}_0$, is defined as*

$$\mathbf{B} = \sum_{j=1}^{r} \bigotimes_{k=1}^{d} b_j^{(k)} \qquad \text{with } b_j^{(k)} \in \mathbb{R}^{\mathcal{I}_k}. \tag{2.10}$$

The minimal r, such that (2.10) *holds, is called the* CP rank *of $\mathbf{B}$ and in this case* (2.10) *is called the* CP decomposition *of $\mathbf{B}$. Tensors of rank* 1*, i.e., tensors of the form $\bigotimes_{k=1}^{d} b^{(k)}$, are called* elementary tensors*.*

We estimate the storage cost of a tensor in the CP format, i.e., in the form (2.10), to be $\mathcal{O}(r \sum_{k=1}^{d} |\mathcal{I}_k|) \approx \mathcal{O}(rdn)$ with $n \coloneqq \max_{k \in \mathcal{D}} n_k$. Recall that the cost for storing the full tensor is $\mathcal{O}(\prod_{k=1}^{d} |\mathcal{I}_k|) \approx \mathcal{O}(n^d)$. Thus, in case the representation rank r is small, a tensor in CP format is immediately data-sparse.

Therefore, it is desirable to use low-rank tensor formats to represent linear, parameter-dependent problems $A(\boldsymbol{p})\phi(\boldsymbol{p}) = b$. Computing the solutions of the above linear, parameter-dependent problem when the operator $A(\boldsymbol{p})$ and the right-hand side b are represented in low-rank tensor formats, means solving linear systems within low-rank tensor formats. Direct solvers that calculate the inverse of an operator with rank $r > 1$ are, however, unknown as illustrated by the following example.

Consider a CP operator $\mathbf{A}$ of dimension 1 and rank 2, i.e., $\mathbf{A} = A_1 + A_2$, with matrices $A_1, A_2 \in \mathbb{R}^{n \times n}$ for some $n \in \mathbb{N}$. Finding a direct inverse of $\mathbf{A}$ in the CP format means finding matrices C_j and F_j such that $\mathbf{A}^{-1} = (A_1 + A_2)^{-1} = \sum_{j=1}^{r} C_j^{-1} + F_j^{-1}$ for some rank $r \in \mathbb{N}$. Since such a property is unknown even for the sum of matrices [73] it is also unknown for the more general case of tensors.

Consequently, linear systems in the CP format are solved using iterative solvers. Unfortunately, the arithmetic operations performed when applying iterative solvers within low-rank tensor formats often lead to an increase of the representation rank.

Consider, exemplarily, a CP operator $\mathbf{A} = \sum_{j=1}^{3} A_j^{(1)} \otimes A_j^{(2)}$ of dimension 2 and rank 3, and a CP vector $\mathbf{x} = \sum_{k=1}^{2} x_k^{(1)} \otimes x_k^{(2)}$ of dimension 2 and rank 2. Then, the application of $\mathbf{A}$ to $\mathbf{x}$ yields $\mathbf{A}\mathbf{x} = (\sum_{j=1}^{3} A_j^{(1)} \otimes A_j^{(2)})(\sum_{k=1}^{2} x_k^{(1)} \otimes x_k^{(2)}) = \sum_{j=1}^{3} \sum_{k=1}^{2} A_j^{(1)} x_k^{(1)} \otimes$

[1] The abbreviation CANDECOMP stands for canonical decomposition and PARAFAC for parallel factors.

$A_j^{(2)} x_k^{(2)} = \sum_{l=1}^{6} y_l^{(1)} \otimes y_l^{(2)}$ with $y_l^{(i)} \coloneqq A_j^{(i)} x_k^{(i)}$ for $l = j + 3(k-1)$ and $i = 1, 2$. Thus, $\mathbf{Ax}$ is a CP vector of representation rank 6 $(= 2 \cdot 3)$.

The above example shows the need of a *truncation* of CP tensors of a certain rank to a lower rank, i.e., an approximation of a CP tensor of a certain rank with a CP tensor of a lower rank. Since the set of CP tensors of rank r is not closed, the approximation of a CP tensor of rank r is an ill-posed problem [98]. To overcome this drawback, we use the *hierarchical Tucker* format for representing and computing the solution of parameter-dependent linear systems.

The hierarchical Tucker format was first introduced in [43] and further analyzed in [37]. The general idea of the hierarchical Tucker format is to define a hierarchy among the modes $\mathcal{D} = \{1, \ldots, d\}$, compare [37, Definition 3.1].

Definition 2.5.2 (Dimension Tree). *A* dimension tree $\mathcal{T}$ *for dimension* $d \in \mathbb{N}$ *is a binary tree with nodes labeled by non-empty subsets of the modes* $\mathcal{D}$*. Its* root *is labeled with* $\mathcal{D}$ *and each node* $w \in \mathcal{T}$ *satisfies one of the following conditions:*

(i) w *is a* leaf *of* $\mathcal{T}$ *and is labeled with a single-element subset* $z = \{j\} \subseteq \mathcal{D}$*. We call the set of all leaves* $\mathcal{L}(\mathcal{T})$*.*

(ii) $w \in \mathcal{I}(\mathcal{T}) \coloneqq \mathcal{T} \setminus \mathcal{L}(\mathcal{T})$ *is an* inner node *of* $\mathcal{T}$ *and has exactly two children* $w_1, w_2 \in \mathcal{T}$*, for which the corresponding labels* z, z_1, $z_2 \subseteq \mathcal{D}$ *with* z, z_1, $z_2 \neq \emptyset$ *fulfill* $z = z_1 \dot{\cup} z_2$*.*

We will identify a node w *with its label* z *and therefore also write* $z \in \mathcal{T}$*.*

Figure 2.1 shows an example of a dimension tree for $d = 3$. Each node $w \in \mathcal{T}$ represents a non-empty subset $z \subseteq \mathcal{D}$ of the modes. Using the labeling of the dimension trees, we define the *matricization* of a tensor for each node as in [37, Definition 3.3].

Definition 2.5.3 (Matricization and Vectorization). *Let* $\mathbf{B} \in \mathbb{R}^{\mathcal{I}}$*,* $z \subseteq \mathcal{D}$ *with* $z \neq \emptyset$*, and* $g \coloneqq \mathcal{D} \setminus z$ *with* $\mathcal{I}_z \coloneqq \bigtimes_{l \in z} \mathcal{I}_l$ *and* $\mathcal{I}_g \coloneqq \bigtimes_{l \in g} \mathcal{I}_l$*. The* matricization $\mathbf{B}^{(z)} \in \mathbb{R}^{\mathcal{I}_z \times \mathcal{I}_g}$ *of* $\mathbf{B}$ *corresponding to* z *is defined through* $\mathbf{B}^{(z)}[(j_k)_{k \in z}, (j_k)_{k \in g}] \coloneqq \mathbf{B}[j_1, \ldots, j_d]$ *for all* $j = (j_k)_{k \in \mathcal{D}}$*. In particular,* $\mathbf{B}^{(\mathcal{D})} \in \mathbb{R}^{|\mathcal{I}|}$ *and we call* $\mathrm{vec}(\mathbf{B}) \coloneqq \mathbf{B}^{(\mathcal{D})}$ *the* vectorization *of* $\mathbf{B}$*.*

A matricization can be interpreted as an unfolding of the tensor along the indicated dimensions as illustrated in Figure 2.2. Based on the concept of matricizations we define the *hierarchical Tucker rank* as in [37, Definition 3.4].

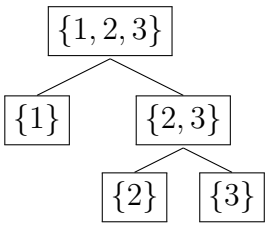

Figure 2.1.: Dimension tree for dimension $d = 3$

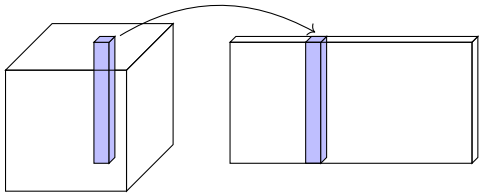

Figure 2.2.: Visual representation of a matricization

Definition 2.5.4 (Hierarchical Tucker Rank). *Let* $\mathbf{B} \in \mathbb{R}^{\mathcal{I}}$ *and* $\mathcal{T}$ *be a dimension tree and let* $r_z \coloneqq \operatorname{rank}(\mathbf{B}^{(z)})$ *denote the matrix rank of the matricization* $\mathbf{B}^{(z)}$ *for all* $z \in \mathcal{T}$*. Then, the* hierarchical Tucker rank *of* $\mathbf{B}$ *is defined as* $\operatorname{rank}_{\mathcal{T}}(\mathbf{B}) \coloneqq (r_z)_{z\in\mathcal{T}}$*. The set of tensors with hierarchical Tucker rank node-wise bounded by* $(r_z)_{z\in\mathcal{T}}$ *is defined as* $\mathcal{H}\text{-Tucker}(\mathcal{T}, (r_z)_{z\in\mathcal{T}}) \coloneqq \{\mathbf{B} \in \mathbb{R}^{\mathcal{I}} \mid \operatorname{rank}(\mathbf{B}^{(z)}) \leq r_z \text{ for all } z \in \mathcal{T}\}$.

By construction, the *nestedness property*

$$\begin{aligned} &\operatorname{span}\{\mathbf{B}^{(z)}[\cdot, j] \mid 1 \leq j \leq r_z\} \subseteq \\ &\quad \operatorname{span}\{\mathbf{B}^{(z_1)}[\cdot, j_1] \otimes \mathbf{B}^{(z_2)}[\cdot, j_2] \mid 1 \leq j_k \leq r_{z_k}, k = 1, 2\} \end{aligned} \tag{2.11}$$

holds for all $z \in \mathcal{I}(\mathcal{T})$ with children $z_1, z_2 \in \mathcal{T}$.

Further, we call a *frame tree* (a family of matrices) $(U_z)_{z\in\mathcal{T}}$ with *frames* $U_z = (U_z[\cdot, 1]|\dots|U_z[\cdot, r_z]) \in \mathbb{R}^{\mathcal{I}_z \times r_z}$ a *generator* of a tensor $\mathbf{B}$, if $\operatorname{range}(\mathbf{B}^{(z)}) \subseteq \operatorname{range}(U_z)$ holds for all $z \in \mathcal{T}$.

The frame tree $(U_z)_{z\in\mathcal{T}}$ is called *nested*, if $U_z[\cdot, j] \in \operatorname{span}\{U_{z_1}[\cdot, j_1] \otimes U_{z_2}[\cdot, j_2] | 1 \leq j_k \leq r_{z_k}, k = 1, 2\}$ holds for all $z \in \mathcal{I}(\mathcal{T})$ with z_1, z_2 children of z and for all $j \in \{1, \dots, r_z\}$.

If U_g is the matrix that contains column by column a basis of $\operatorname{range}(\mathbf{B}^{(g)})$ for labels $g \in \{z, z_1, z_2\}$, then there exist coefficients $B_z[j, j_1, j_2] \in \mathbb{R}$ such that $U_z[\cdot, j] = \sum_{j_1=1}^{r_{z_1}} \sum_{j_2=1}^{r_{z_2}} B_z[j, j_1, j_2](U_{z_1}[\cdot, j_1] \otimes U_{z_2}[\cdot, j_2])$. We call the corresponding tensor $B_z \in \mathbb{R}^{r_z \times r_{z_1} \times r_{z_2}}$ *transfer tensor*.

Thus, by providing the transfer tensors B_z for all $z \in \mathcal{I}(\mathcal{T})$ and the frames U_z for all $z \in \mathcal{L}(\mathcal{T})$ we have another representation of a tensor $\mathbf{B}$, cf. [37, Definition 3.6]. For computing the matrices U_z for $z \in \mathcal{T}$, the singular value decomposition can be applied to the corresponding matricizations $\mathbf{B}^{(z)}$.

Definition 2.5.5 (Hierarchical Tucker Format). *Let* $\mathbf{B} \in \mathbb{R}^{\mathcal{I}}$*,* $\mathcal{T}$ *be a dimension tree,* $r_z \in \mathbb{N}$ *for all* $z \in \mathcal{T}$ *with* $r_{\mathcal{D}} = 1$*,* $(U_z)_{z\in\mathcal{L}(\mathcal{T})}$ *be a nested generator of* $\mathbf{B}$ *with* $U_z \in \mathbb{R}^{\mathcal{I}_z \times r_z}$*, and* $(B_z)_{z\in\mathcal{I}(\mathcal{T})}$ *be the corresponding transfer tensors. Then, we call*

$((U_z)_{z\in\mathcal{L}(\mathcal{T})}, (B_z)_{z\in\mathcal{I}(\mathcal{T})})$ *a* hierarchical Tucker representation *of* $\mathbf{B}$. *The vector* $(r_z)_{z\in\mathcal{T}}$ *is called* representation rank.

The memory required to store a hierarchical Tucker representation of a tensor $\mathbf{B} \in \mathbb{R}^{\mathcal{I}}$ with dimension tree $\mathcal{T}$ and representation rank $(r_z)_{z\in\mathcal{T}}$ is of order $\mathcal{O}(rdn + r^3 d)$ for $n = \max_{j\in\mathcal{D}} |\mathcal{I}_j|$ and $r = \max_{z\in\mathcal{T}} r_z$ [37, Lemma 3.7].

Recall that we introduced the hierarchical Tucker format because the truncation of a tensor in CP format of a certain rank down to a tensor in CP format with lower rank is an ill-posed problem. The existence of such a truncation method of a tensor $\mathbf{B} \in \mathcal{H}\text{-Tucker}(\mathcal{T}, (r_z)_{z\in\mathcal{T}})$ down to lower rank $(r'_z)_{z\in\mathcal{T}}$ with an arithmetic cost in $\mathcal{O}(r^2 dn + r^4 d)$ was proven in [37]. For a tensor $\mathbf{B} \in \mathcal{H}\text{-Tucker}(\mathcal{T}, (r_z)_{z\in\mathcal{T}})$ we define the truncation as the following operator:

$$\begin{aligned}\text{truncate} : \mathcal{H}\text{-Tucker}(\mathcal{T}, (r_z)_{z\in\mathcal{T}}) &\to \mathcal{H}\text{-Tucker}(\mathcal{T}, (r'_z)_{z\in\mathcal{T}}) \text{ with} \\ \mathbf{B} &\mapsto \mathbf{B}' \coloneqq \text{truncate}(\mathbf{B})\end{aligned}$$

According to [62], the resulting approximation $\mathbf{B}' \in \mathcal{H}\text{-Tucker}(\mathcal{T}, (r'_z)_{z\in\mathcal{T}})$ fulfills the quasi-optimal error estimate

$$\|\mathbf{B} - \mathbf{B}'\| \leq \sqrt{2d-3} \inf_{\mathbf{C}\in\mathcal{H}\text{-Tucker}(\mathcal{T},(r'_z)_{z\in\mathcal{T}})} \|\mathbf{B} - \mathbf{C}\|.$$

For details about the practical realization of the truncation, we refer to [62] and Section 3.2.4. Moreover, a CP representation of a tensor with CP rank r can be transferred into a hierarchical Tucker representation with rank node-wise bounded by r [42, Theorem 11.17].

For solving parameter-dependent linear problems in the hierarchical Tucker format, we introduce the preconditioned conjugate gradients (PCG) method in Algorithm 2.5.1, compare to [62, Algorithm 2], and to the standard PCG algorithm for parameter-independent linear systems [91, Algorithm 9.1]. Here, $\langle\cdot,\cdot\rangle_2$ denotes the Euclidean scalar product and we write the iteration indices as subscripts in brackets to avoid confusion with the matricization. Furthermore, a precondictioner $\mathbf{M}$ with CP rank 1 is chosen such that the inverse $\mathbf{M}^{-1}$ can directly be calculated [60, Section 2.6].

The PCG method in Algorithm 2.5.1 approximates the solution of a parameter-dependent linear system numerically within the hierarchical Tucker format if $\mathbf{A}$ is positive definite and symmetric. Furthermore, Algorithm 2.5.1 converges if the truncation error is small enough as was proven in [38, Lemma 5].

Algorithm 2.5.1 Preconditioned conjugate gradients method with truncation

Input: Operator $\mathbf{A}$, right-hand side $\mathbf{b}$, preconditioner $\mathbf{M}$ with CP rank 1, initial guess $\boldsymbol{\phi}_{(0)}$ in the hierarchical Tucker format
Output: Approximate solution $\boldsymbol{\phi}$ of $\mathbf{A}\boldsymbol{\phi} = \mathbf{b}$ in the hierarchical Tucker format

$\mathbf{R}_{(0)} = \text{truncate}\left(\mathbf{b} - \mathbf{A}\boldsymbol{\phi}_{(0)}\right)$
$\mathbf{Z}_{(0)} = \mathbf{M}^{-1}\mathbf{R}_{(0)}$
$\mathbf{P}_{(0)} = \mathbf{Z}_{(0)}$
$\mathbf{Q}_{(0)} = \text{truncate}\left(\mathbf{A}\mathbf{P}_{(0)}\right)$
$k = 0$
while $\frac{\|\mathbf{R}_{(k)}\|}{\|\mathbf{b}\|} > \varepsilon$ **and** $k < k_{\max}$ **do**
  $\boldsymbol{\phi}_{(k+1)} = \text{truncate}\left(\boldsymbol{\phi}_{(k)} + \frac{\langle \mathbf{R}_{(k)}, \mathbf{P}_{(k)} \rangle_2}{\langle \mathbf{Q}_{(k)}, \mathbf{P}_{(k)} \rangle_2} \mathbf{P}_{(k)}\right)$
  $\mathbf{R}_{(k+1)} = \text{truncate}\left(\mathbf{b} - \mathbf{A}\boldsymbol{\phi}_{(k+1)}\right)$
  $\mathbf{Z}_{(k+1)} = \mathbf{M}^{-1}\mathbf{R}_{(k+1)}$
  $\mathbf{P}_{(k+1)} = \text{truncate}\left(\mathbf{Z}_{(k+1)} - \frac{\langle \mathbf{Q}_{(k)}, \mathbf{Z}_{(k+1)} \rangle_2}{\langle \mathbf{Q}_{(k)}, \mathbf{P}_{(k)} \rangle_2} \mathbf{P}_{(k)}\right)$
  $\mathbf{Q}_{(k+1)} = \text{truncate}\left(\mathbf{A}\mathbf{P}_{(k+1)}\right)$
  $k = k + 1$
end while

Algorithm 2.5.1 comprises additions and inner products of two tensors in the hierarchical Tucker format, which have an arithmetic cost in $\mathcal{O}(dnr^2 + dr^4)$, the application of an operator, which has an arithmetic cost in $\mathcal{O}(dn^2r)$, and the evaluation of an entry of the represented tensor, which has an arithmetic cost in $\mathcal{O}(dr^3)$. For small rank r most of the operations needed for the PCG method scale linearly in the dimension d and the mode size n, thus yielding an efficient method for solving parameter-dependent linear systems in low-rank tensor formats.

Finding conditions that guarantee the existence of a low-rank approximation for a given tensor, such as the solution $\phi(\boldsymbol{p})$ of the parameter-dependent problem $A(\boldsymbol{p})\phi(\boldsymbol{p}) = b$, is a research topic of its own and goes beyond the scope of this thesis. We refer to [3, 16, 63] for further details and assume that the solution of the parameter-dependent forward problem indeed has a low-rank approximation. For the forward EMG problem that we introduce in the next section, this claim is backed up by the numerical experiments in Section 3.2.4.

2.6. A Model of Surface Electromyographic Data

As stated in Section 1.1, we are interested in inferring the structure of biological tissue from surface EMG measurements. Recall, that surface EMG measurements are the changes of the electrical potential of the skin measured by electrodes placed on the skin surface. These changes of the electrical potential of the skin result from the propagation of the electrical signals, that stimulate skeletal muscles to contract, through the skeletal muscle and all kinds of tissue filling the space between the excitation site and the measuring electrodes. Hence, some knowledge on the evolution and propagation of EMG signals through biological tissue is necessary. In this section, we present a model of the electrical behavior of skeletal muscles and the tissue that surrounds the skeletal muscles. Note that the presented model can be extended by a model of force generation and the corresponding continuum mechanics, i.e., by a model of the contractions of skeletal muscles. This goes beyond the scope of this thesis and we refer to [74] and the references therein for further information.

A skeletal muscle consists of multiple fascicles, i.e., of multiple bundles of muscle cells, see Figure 2.3. The muscle cells are usually called *muscle fibers* because of their long and thin cylindrical shape. The muscle fibers are composed of so-called myofibrils that are able to react to electrical stimuli from the spinal cord via contraction. Apart from the grouping of muscle fibers into muscle fiber bundles, muscle fibers are grouped functionally into *motor units*. Motor units are independent of the grouping of the muscle fibers to fascicles and contain the muscle fibers that are stimulated simultaneously with the same stimulus from the spinal cord. As depicted in Figure 2.3 each muscle fiber bundle usually consists of muscle fibers of multiple motor units.

The electrical behavior of a muscle fiber under stimulation is modeled in Section 2.6.1. Following the structure of skeletal muscles, we assemble a skeletal muscle from muscle fibers in Section 2.6.2. Moreover, we introduce the bidomain model that describes the electrical behavior of electrically active biological tissue, such as a skeletal muscle, in Section 2.6.3. Afterwards, the focus moves to a simplification of the bidomain model that describes the propagation of electrical signals through electrically passive tissue, such as fat, skin, and bone tissue in Section 2.6.4. Completing the model of EMG data, we describe the process of measuring surface EMG data and define the forward EMG problem.

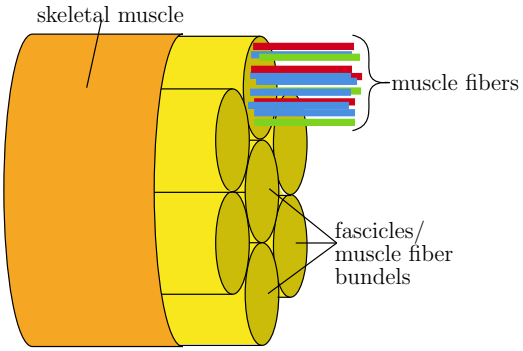

Figure 2.3.: Sketch of a skeletal muscle, where muscle fibers in the same color belong to one motor unit

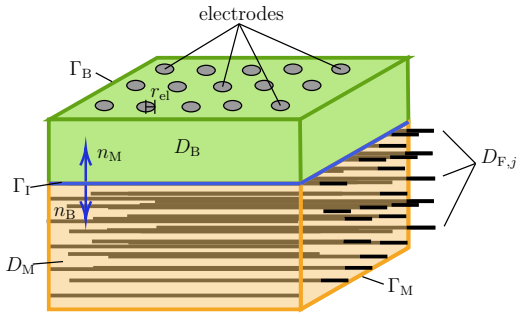

Figure 2.4.: Sketch of skeletal muscle with muscle fibers, surrounding tissue, and measuring electrodes

2.6.1. Chemo-electrical Model of a Muscle Fiber

As stated above, each muscle fiber belonging to the same motor unit receives the same electrical stimulus at the same time through the so-called *motor neurons*. We assume that muscle fibers are stimulated by their motor neuron only and do not receive any electrical signal from the surrounding muscle fibers [87]. Therefore it is realistic to use isolated one-dimensional models to describe the electrical behavior of each single muscle fiber $D_{F,j}$, for $j = 1, \ldots, N_{MF}$, and N_{MF} the number of muscle fibers, as depicted in Figure 2.4.

An electrical stimulus from the spinal cord changes the electrical potentials of the innervated muscle fibers. More precisely, the properties of the muscle fiber membranes of the innervated muscle fibers change due to the electrical stimulus and allow ions to pass the membrane. This in return leads to changes in the muscle fiber membrane potential that describes the difference in the extracellular and intracellular potentials. The changes of the muscle fiber membrane potential are often called *(muscle fiber) action potentials* (APs).

Several established models exist to describe the chemo-electrical behavior of muscle fibers and the propagation of APs along them. The range varies from simple heuristic models to complex physically motivated ones. The more simple models consist of few algebraic equations to fit the muscle fiber action potential shape while models of tens of coupled ordinary differential equations define the other side of the complexity spectrum. In the following, we describe the model of Rosenfalck et al. and the more complex model developed by Hodgkin and Huxley in the 1960s. The idea of the Hodgkin-Huxley model can further be extended to include more complex chemo-electro-mechanical relations.

Doing so results in one of the most complex models, the model by Shorten et al. that is explained in [97]. The above mentioned extension of our model to include muscle contraction is based on this model by Shorten et al., compare [74] and [48, Section 4.3.1].

Rosenfalck Model

The *Rosenfalck model* was first published by Rosenfalck et al. in 1969 [89] and models the characteristic shape of muscle fiber APs using the algebraic equation

$$v_{\mathrm{m},j}(s_{\mathrm{F},j}) = c_{\mathrm{R},1} s_{\mathrm{F},j}^3 \exp(-c_{\mathrm{R},2} s_{\mathrm{F},j}) - c_{\mathrm{R},3}, \qquad s_{\mathrm{F},j} \in D_{\mathrm{F},j},\ j = 1, \ldots, N_{\mathrm{MF}} \tag{2.12}$$

for each muscle fiber $D_{\mathrm{F},j}$, $j = 1, \ldots, N_{\mathrm{MF}}$. The model parameters $c_{\mathrm{R},j} \in \mathbb{R}, j = 1, 2, 3$, can, for example, be estimated from recordings of action potentials.

The Rosenfalck model is often used because of its explicit form that allows to evaluate the model easily.

The modeled AP shape is shown in Figure 2.5 for several parameter sets. As reference configuration we used the parameter combination that is implemented in the software package KerMor, compare Chapter 3. There, $c_{\mathrm{R},1} = 84 \cdot (3.1)^3 = 2502.444$, $c_{\mathrm{R},2} = 3.1$, and $c_{\mathrm{R},3} = 80$.

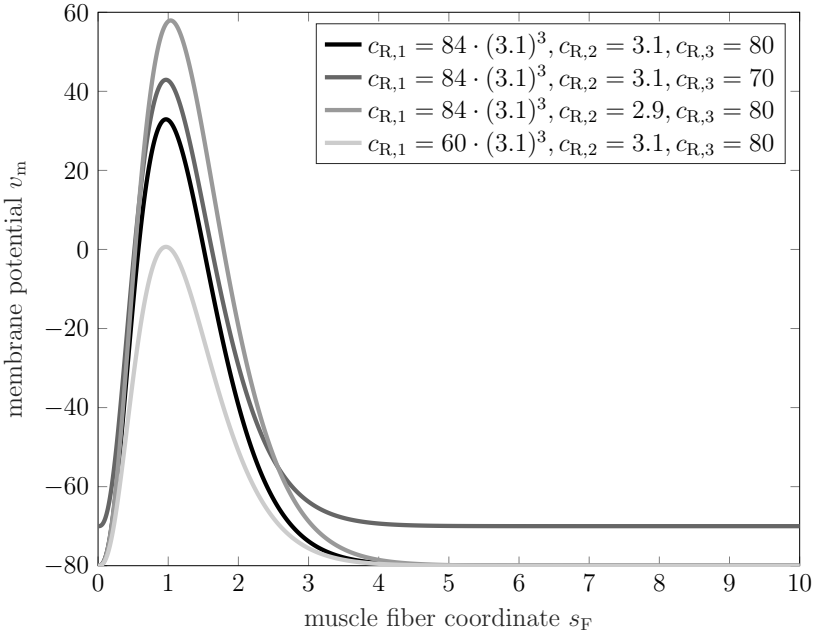

Figure 2.5.: Influence of the model parameters $c_{\mathrm{R},j}, j = 1, 2, 3$ on the AP shape in the Rosenfalck model

We see from Figure 2.5 that $c_{\mathrm{R},3}$ can be interpreted as the negative minimal or resting membrane potential while $c_{\mathrm{R},1}$ and $c_{\mathrm{R},2}$ influence the width and height of the peak. Overall the modeled AP shapes resemble the shapes known from electrocardiograms.

Hodgkin-Huxley Model

In 1952 Hodgkin and Huxley published a more complex model of the electro-physiology of muscle fibers [51]. The *Hodgkin-Huxley model* is based on a series of electro-physiological experiments on the squid giant axon in the late 1940s and early 1950s. In 1963 Hodgkin and Huxley were awarded the Nobel Prize in Physiology and Medicine for their research.

The novelty of their approach was to describe the electrical behavior of muscle fibers by an electrically equivalent circuit. In such a substitute electrical circuit, capacitors model the charge storage capacity of the cell membrane, resistors model the ion channels embedded in the cell membrane, and batteries model the electro-chemical potentials established by differing intra- and extracellular ion concentrations. The substitute electrical circuit used by Hodgkin and Huxley is shown in Figure 2.6. Modelling the proper-

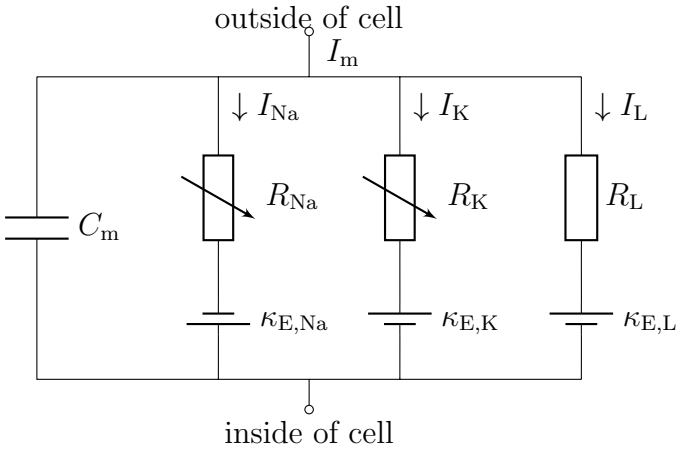

Figure 2.6.: Substitute electrical circuit of the Hodgkin-Huxley model following [51]

ties of this substitute electrical circuit leads to a system of coupled ordinary differential equations.

We start with the law of capacitance that reads

$$C_{\mathrm{m},j}\partial_t v_{\mathrm{m},j} = I_{\mathrm{m},j}.$$

Here, $C_{\mathrm{m},j}$ is the membrane capacitance and $v_{\mathrm{m},j}$ is the membrane potential of the j^{th} muscle fiber. Further, the total current flow $I_{\mathrm{m},j}$ across the muscle fiber cell membrane

is assumed to be the difference of a stimulating current $I_{\text{stim},j}$ and an ionic current $I_{\text{ion},j}$, i.e., $I_{\text{m},j} = I_{\text{stim},j} - I_{\text{ion},j}$:

$$\partial_t v_{\text{m},j} = \frac{1}{C_{\text{m},j}}(I_{\text{stim},j} - I_{\text{ion},j}) \tag{2.13}$$

From now on, we neglect the index j of the muscle fiber on the ionic current for ease of notation. We further subdivide the ionic current into a sodium current I_{Na}, a potassium current I_{K} and a leakage current I_{L}. The leakage current represents the current flow due to the natural permeability of the cell membrane, e.g., with respect to chloride ions. Each ionic current I_j with $j \in \{\text{Na}, \text{K}, \text{L}\}$ is described through the difference of an equilibrium potential $\kappa_{\text{E},j}$ and the membrane potential weighted by the ion specific conductance $\kappa_{\text{g},j}$. The ionic current is thus modeled by

$$I_{\text{ion}} = \kappa_{\text{g,Na}}(v_{\text{m}} - \kappa_{\text{E,Na}}) + \kappa_{\text{g,K}}(v_{\text{m}} - \kappa_{\text{E,K}}) + c_{\text{g,L}}(v_{\text{m}} - \kappa_{\text{E,L}}).$$

Note that the leakage conductance is assumed to be constant and thus denoted by $c_{\text{g,L}}$.

The membrane conductance with respect to sodium and potassium ions is modeled with the help of so called gates. These gates can either be in the permissive state, allowing ions to pass the membrane, or in the non-permissive state. We denote the probability of an individual gate being in the permissive state by λ_k and use transition rates α_k, β_k to describe the likelihood of a gate to switch from a permissive to a non-permissive state and vice versa. The transition rates change depending on the membrane potential v_{m}. Formalizing the above descriptions, we have

$$\partial_t \lambda_k = \alpha_k(v_{\text{m}})(1 - \lambda_k) - \beta_k(v_{\text{m}})\lambda_k, \quad k \in \{\text{Na}, \text{K}, \text{L}\}.$$

As stated above, Hodgkin and Huxley considered three types of gates, namely sodium, potassium, and leakage gates, and we denote them by $G_l, l = 1, 2, 3$. Their influence on the ionic conductivities is modeled as follows:

$$\kappa_{\text{g,Na}} = c_{\text{g,Na}} \prod_k \lambda_k = c_{\text{g,Na}} G_1^3 G_3,$$
$$\kappa_{\text{g,K}} = c_{\text{g,K}} \prod_k \lambda_k = c_{\text{g,K}} G_2^4$$

Here, the factors $c_{\text{g,Na}}$ and $c_{\text{g,K}}$ are constants.

Completing the Hodgkin-Huxley model, the transition rates α_k, β_k are fitted using the

general ansatz

$$\vartheta(v_{\mathrm{m}}) = \frac{c_{\vartheta,1} + c_{\vartheta,2} v_{\mathrm{m}}}{c_{\vartheta,3} + c_{\vartheta,4} \exp\left(\frac{v_{\mathrm{m}} + c_{\vartheta,5}}{c_{\vartheta,6}}\right)}$$

for $\vartheta \in \{\alpha_k, \beta_k\}$ and model constants $c_{\vartheta,l}$, for $l = 1, \ldots, 6$.

The resulting system of equations comprises four ordinary differential equations and eight algebraic equations for each muscle fiber. We abstain from explicitly stating this overall system of equations and refer to [78] and the original publication [51] for further details.

2.6.2. Assembling a Skeletal Muscle Model from Muscle Fiber Models

In contradiction to our assumption that muscle fibers can be treated as one-dimensional objects, muscle fibers are not one-dimensional in nature. Additionally, bundles of bundles of muscle fibers form skeletal muscles and the latter should clearly be modeled as three-dimensional objects. Hence, the questions arise how to assemble a three-dimensional skeletal muscle from one-dimensional muscle fibers and how to transfer the one-dimensional muscle fiber membrane potentials $v_{\mathrm{m},j}$ to a quantity, that can be propagated through the three-dimensional muscle.

We suggest the following procedure: We start with placing each muscle fiber $D_{\mathrm{F},j}$ into the three-dimensional space. Therefore, we assign a starting point $y_{\mathrm{F},j} \in \mathbb{R}^3$ and a direction $d_{\mathrm{F},j} : D_{\mathrm{M}} \to \mathbb{R}^3$ with $\|d_{\mathrm{F},j}(x)\|_2 = 1$ for all $x \in D_{\mathrm{M}}$ to every muscle fiber $D_{\mathrm{F},j}$ for $j = 1, \ldots, N_{\mathrm{MF}}$. The directions $d_{\mathrm{F},j}$ will in the following often be called *muscle fiber directions* and may depend on the position in space as indicated above. The space-dependence allows us to consider curved muscle fibers as illustrated in Figure 2.7. The embedding

$$x_{\mathrm{F},j} = y_{\mathrm{F},j} + s_{\mathrm{F},j} d_{\mathrm{F},j} \in D_{\mathrm{M}} \subset \mathbb{R}^3, \quad s_{\mathrm{F},j} \in D_{\mathrm{F},j}, j = 1, \ldots, N_{\mathrm{MF}}$$

of a one-dimensional muscle fiber into the three-dimensional space is depicted in Figure 2.8. Multiplying this equation with $d_{\mathrm{F},j}^{\top}$ from the left yields the relation

$$s_{\mathrm{F},j} = d_{\mathrm{F},j}^{\top}(x_{\mathrm{F},j} - y_{\mathrm{F},j}), \quad j = 1, \ldots, N_{\mathrm{MF}} \tag{2.14}$$

that allows rewriting the muscle fiber membrane potentials from Section 2.6.1 in terms of

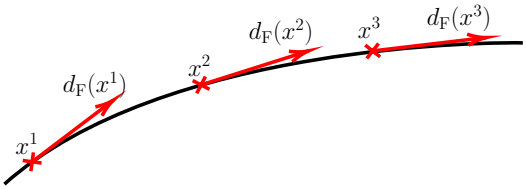

Figure 2.7.: Change of the muscle fiber direction in points $x^1, x^2, x^3 \in D_M$ of a curved muscle fiber

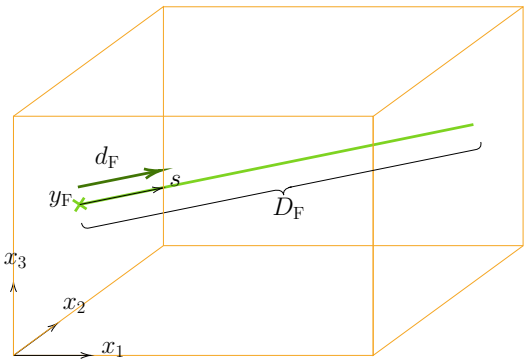

Figure 2.8.: Embedding of a one-dimensional muscle fiber into the three-dimensional space

the three-dimensional variables $x_{F,j}$, i.e., $v_{m,j}(s_{F,j}) = v_{m,j}(x_{F,j}) = v_{m,j}(d_{F,j}^\top(x_{F,j} - y_{F,j}))$.

Our next step is to fill the space between the N_{MF} one-dimensional muscle fibers $D_{F,j} \subset D_M$ for $j = 1, \ldots, N_{MF}$ to generate the muscle D_M. We use a smoothing operator $\mathcal{S}$ that blows up the muscle fibers in transversal fiber direction and thus achieve $D_M = \cup_{j=1}^{N_{MF}} \mathcal{S}(D_{F,j})$. In terms of the membrane potential, this relation translates to

$$V_m(x) = \sum_{j=1}^{N_{MF}} \mathcal{S}(v_{m,j})(x). \tag{2.15}$$

The smoothing operator that is used throughout the numerical experiments is a composition of an orthogonal projection and the Gaussian smoothing kernel $\mathcal{K}_\alpha : \mathbb{R}^3 \to \mathbb{R}$ with

$$\mathcal{K}_\alpha(y) := \exp\left(-\frac{\alpha}{2}\|y\|^2\right) \tag{2.16}$$

and a smoothing parameter $\alpha > 0$. More precisely, we project a three-dimensional muscle point $x \in D_M$ onto the nearest muscle fiber $D_{F,j}$, calculate the membrane potential at this point, and afterwards weight the outcome according to the distance of x to the muscle fiber using the Gaussian smoothing kernel (2.16). We thus have

$$\mathcal{S}(v_{m,j})(x) = v_{m,j}(d_{F,j}^\top(\mathrm{pr}_j(x) - y_{F,j}))\exp\left(-\frac{\alpha}{2}\left\|x - \mathrm{pr}_j(x)\right\|^2\right) \tag{2.17}$$

with the orthogonal projection

$$\mathrm{pr}_j(x) \coloneqq y_{\mathrm{F},j} + \left((x - y_{\mathrm{F},j})^\top d_{\mathrm{F},j}\right) d_{\mathrm{F},j} \tag{2.18}$$

of a body point $x \in D_{\mathrm{M}}$ onto a muscle fiber $D_{\mathrm{F},j}$ with starting point $y_{\mathrm{F},j}$ and muscle fiber direction $d_{\mathrm{F},j}$. The membrane potential in Equation (2.15) thus lives on the three-dimensional muscle domain D_{M} and can be propagated through the muscle tissue.

For remarks on how the muscle fiber embedding is done in practice and how to treat space-dependent muscle fiber directions, we refer to Sections 3.2.1to 3.2.3.

2.6.3. Propagation of Electrical Signals through Skeletal Muscle Tissue

Within this section, we model the propagation of the membrane potential V_{m} through the muscle domain D_{M}. As discussed in Section 2.6.1, the membrane potential is the difference between the intra- and extracellular potentials. We denote the intra- and extracellular potentials by ϕ_{i} and ϕ_{e} and thus get $V_{\mathrm{m}} = \phi_{\mathrm{i}} - \phi_{\mathrm{e}}$.

Simplifying the geometry, we assume that every point $x \in D_{\mathrm{M}}$ possesses both intra- and extracellular properties. Consequently, V_{m}, ϕ_{i}, and ϕ_{e} are defined on the whole muscle domain D_{M}, i.e., there is no division into intra- and extracellular domains. This assumption is the main ingredient of the *bidomain model* that was first introduced in 1969 [95] and is successfully used in cardiology to model the electrical behavior of cardiac muscle [83, Chapter 5]. This bidomain ansatz was adapted for modeling the electrical behavior of skeletal muscles in [87].

The bidomain equation

$$\nabla \cdot ((\sigma_{\mathrm{i}} + \sigma_{\mathrm{e}})\nabla\phi_{\mathrm{e}}) = -\nabla \cdot (\sigma_{\mathrm{i}}\nabla V_{\mathrm{m}}) \quad \text{in } D_{\mathrm{M}} \tag{2.19}$$

describes the interaction between the membrane potential V_{m} and the extracellular potential ϕ_{e} and thus the propagation of muscle fiber APs through the skeletal muscle D_{M} [74]. Here, σ_{i} and σ_{e} denote the conductivity of the intra- and extracellular tissue and V_{m} is the membrane potential that can be calculated as described in Section 2.6.1. Recall that we modeled the electrical conductivity as a function in L^∞ in Section 1.1. We thus have $\sigma_{\mathrm{i}}, \sigma_{\mathrm{e}} \in L^\infty(D_{\mathrm{M}}; \mathbb{R}^{3\times 3})$.

We see that the bidomain equation consists of two diffusion terms: one that describes the diffusion of the extracellular potential with diffusion coefficient $\sigma_{\mathrm{i}} + \sigma_{\mathrm{e}}$ on the left-

hand side and another one that describes the diffusion of the membrane potential with diffusion coefficient σ_i on the right-hand side. Recall that the membrane potential V_m is time-dependent as described in the Rosenfalck and Hodgkin-Huxley models in Section 2.6.1. Hence, given the conductivities σ_i and σ_e and the membrane potential, the (time-dependent) extracellular potential ϕ_e is described by a simple diffusive process.

2.6.4. Propagation of Electrical Signals through Electrically Inactive Tissue

Biological tissue that reacts passively to electrical stimuli is called electrically inactive. In contrast to electrically active tissue like the muscle tissue discussed in the previous section, the chemical, electrical, and mechanical properties of electrically inactive tissues remain unchanged under electrical stimulation such that electrical stimuli simply get propagated through the material. Examples of electrically inactive tissues are bone, skin, fat, tendon, and other connective tissues. Usually, skeletal muscles are surrounded by this kind of tissue. Remember that our aim is to model the changes in the electrical potential at the skin surface and thus to model surface EMG measurements. Hence, we need to extend the model of the propagation of electrical signals through skeletal muscle tissue to also incorporate the propagation of electrical signals through electrically inactive tissue.

Similar to the muscle tissue case, the propagation of the electrical potential through the *surrounding tissue* D_B is a diffusive process and thus described by the generalized Laplace equation

$$\nabla \cdot (\sigma_0 \nabla \phi_0) = 0 \qquad \text{in } D_\mathrm{B}. \tag{2.20}$$

Here, $\sigma_0 \in L^\infty(D_\mathrm{B}; \mathbb{R}^{3\times 3})$ denotes the electrical conductivity of the tissue D_B and ϕ_0 its electrical potential. In contrast to the bidomain equation, there is no source term on the right-hand side of equation (2.20). This is due to the lack of electrical sources in the electrically inactive tissue.

The propagation of the electrical potential is ensured by the two coupling conditions

$$\phi_\mathrm{e} = \phi_0 \qquad \text{on } \Gamma_\mathrm{I}, \tag{2.21a}$$

$$(\sigma_\mathrm{e} \nabla \phi_\mathrm{e}) \cdot n_\mathrm{M} = -(\sigma_0 \nabla \phi_0) \cdot n_\mathrm{B} \qquad \text{on } \Gamma_\mathrm{I}, \tag{2.21b}$$

where the abbreviation $\Gamma_\mathrm{I} \coloneqq \partial D_\mathrm{M} \cap \partial D_\mathrm{B}$ is used to denote the interface between muscle

tissue and the surrounding tissue. Moreover, we define the outer body boundary $\Gamma_{\mathrm{B}} \coloneqq \partial D_{\mathrm{B}} \setminus \Gamma_{\mathrm{I}}$ and the outer muscle boundary $\Gamma_{\mathrm{M}} \coloneqq \partial D_{\mathrm{M}} \setminus \Gamma_{\mathrm{I}}$. The outer normal vectors at these boundaries are denoted by n_{B} and n_{M}, see Figure 2.4.

Equation (2.21a) guarantees that the extracellular potential ϕ_{e} and the potential ϕ_0 in the surrounding tissue are equal on the interface Γ_{I}, and thus models the propagation of the electrical potential from the muscle to the surrounding tissue. Equation (2.21b) additionally ensures the continuity of the current flow across the interface Γ_{I}.

We complete the model of the evolution and propagation of APs through biological tissue with the following no-flow boundary conditions:

$$(\sigma_{\mathrm{i}} \nabla \phi_{\mathrm{i}}) \cdot n_{\mathrm{M}} = 0 \qquad \text{on } \partial D_{\mathrm{M}}, \tag{2.22a}$$

$$(\sigma_0 \nabla \phi_0) \cdot n_{\mathrm{B}} = 0 \qquad \text{on } \Gamma_{\mathrm{B}}, \tag{2.22b}$$

$$(\sigma_{\mathrm{e}} \nabla \phi_{\mathrm{e}}) \cdot n_{\mathrm{M}} = 0 \qquad \text{on } \Gamma_{\mathrm{M}} \tag{2.22c}$$

We have Equation (2.22a) to ensure that there is no current flowing out of the intracellular muscle region, modeling the insulation of the muscle fibers as discussed in Section 2.6.1. Further, Equation (2.22b) incorporates the no-flow condition for the outer boundary of the surrounding tissue, meaning no current can flow over the outer skin boundary. Finally, Condition (2.22c) is posed to ensure a no-flow condition in computational scenarios where the muscle region D_M is not fully covered by surrounding tissue. This happens in numerical examples where only parts of muscles are modeled to simplify the geometry and to limit the computational complexity, cf. Chapters 3, 5, and 6.

Obviously, imposing no-flow boundary conditions on each boundary leads to mathematical ill-posedness of the model. For reaching mathematical well-posedness and solvability of the forward EMG model, the zero-mean condition

$$\int_{D_{\mathrm{M}}} \phi_{\mathrm{e}} + \int_{D_{\mathrm{B}}} \phi_0 = 0 \tag{2.23}$$

is introduced. Using the abbreviations $D \coloneqq D_{\mathrm{M}} \cup D_{\mathrm{B}}$ and

$$\phi \coloneqq \phi_{\mathrm{e}} \mathbb{1}_{D_{\mathrm{M}}} + \phi_0 \mathbb{1}_{D_{\mathrm{B}}} \tag{2.24}$$

Equation (2.23) reads $\int_D \phi = 0$. Here, $\mathbb{1}$ denotes the characteristic function of the indicated domain. Note that the domain D specified above is one specific example of the arbitrary domain D considered in Section 1.1.

2.6.5. Measuring Surface EMG Signals

Summarizing the previous sections, we find that electrical signals are evoked by a stimulus from the spinal cord that influences the chemo-electrical behavior of the innervated muscle fibers. These electrical fluctuations travel along the muscle fibers as muscle fiber APs (Equation (2.12)), propagate through the muscle (Equation (2.19)) and surrounding tissue (Equation (2.20)), and accumulate to the electrical signals that can be measured at the skin surface by electrodes.

We place N_{M} electrodes with radius $r_{\mathrm{el}} > 0$ at measuring points $x_{\mathrm{m},j} \in \partial D$ for $j = 1, \ldots, N_{\mathrm{M}}$ at the domain boundary as depicted in Figure 2.4. Note that, whenever D_{M} is completely surrounded by surrounding tissue D_{B}, the domain boundary is $\partial D = \partial D_{\mathrm{M}}$. In clinical applications this is always the case and thus $\phi(\partial D) = \phi_0(\partial D)$. However, to reduce the computational domain or for validation of the model, body parts or even a single skeletal muscle without surrounding tissue can be investigated. In this setting, the measuring electrodes may be placed directly at the muscle surface, i.e., $\phi(\partial D) = \phi_{\mathrm{e}}(\partial D)$. We emphasize that the latter scenario is not applicable to the clinical setting but enables the numerical validation of the model.

We model the EMG measuring process as the integral mean of the surface potential $\phi(\partial D)$ underneath the electrodes that are centered at the measuring points $\mathbb{x} := (x_{\mathrm{m},j})_{j=1}^{N_{\mathrm{M}}} \in \mathbb{R}^{3\times N_{\mathrm{M}}}$:

$$\phi_{\mathbb{x}} := \phi(\mathbb{x}) := \frac{1}{\pi r_{\mathrm{el}}^2} \Big(\int_{B_{r_{\mathrm{el}}}(x_{\mathrm{m},j}) \cap \partial D} \phi(x) \mathrm{d}x \Big)_{j=1}^{N_{\mathrm{M}}} \in \mathbb{R}^{N_{\mathrm{M}}} \tag{2.25}$$

Here, $B_{r_{\mathrm{el}}}(x_{\mathrm{m},j})$ denotes the ball in $\mathbb{R}^3$ with radius r_{el} around the center $x_{\mathrm{m},j}$.

We emphasize that for our theoretical investigations in Chapter 4 any bounded operator that maps ϕ to $\phi_{\mathbb{x}} \in \mathbb{R}^{N_{\mathrm{M}}}$ is allowed. Other approaches to model the measuring process could be to use the maximum value of ϕ in $B_{r_{\mathrm{el}}}(x_{\mathrm{m},j}) \cap \partial D$ to define $\phi_{\mathbb{x}}$ or to take $\phi_{\mathbb{x}} := (\phi(x_{\mathrm{m},j}))_{j=1}^{N_{\mathrm{M}}}$. For remarks on the numerical treatment of the measuring process we refer to Section 3.2.

Combining all the above models, we specify the *deterministic forward EMG problem* through the forward map

$$\mathcal{G} : (L^\infty(D; \mathbb{R}^{3\times 3}))^3 \to \mathbb{R}^{N_{\mathrm{M}}} \quad \text{with} \quad \boldsymbol{\sigma} := (\sigma_{\mathrm{i}}, \sigma_{\mathrm{e}}, \sigma_0) \mapsto \phi_{\mathbb{x}}, \tag{2.26}$$

which maps a given triple $(\sigma_{\mathrm{i}}, \sigma_{\mathrm{e}}, \sigma_0)$ of conductivities to surface EMG measurements $\phi_{\mathbb{x}}$. Note that the conductivities $\sigma_{\mathrm{i}}, \sigma_{\mathrm{e}}$ and σ_0 are artificially set to zero outside their natural

domains D_{M} and D_{B} such that they are defined on the whole domain D. In the following, we call the triple $\boldsymbol{\sigma} = (\sigma_{\mathrm{i}}, \sigma_{\mathrm{e}}, \sigma_0)$ the *global conductivity*.

Compared to the general forward problem introduced in the beginning of Chapter 2, we have specified the forward operator $\mathcal{G}$ to represent the forward EMG model and the parameters $\boldsymbol{p}$ to be the global conductivity $\boldsymbol{\sigma}$. Furthermore, we set the parameter space $\boldsymbol{\mathcal{J}} = (L^\infty(D; \mathbb{R}^{3\times 3}))^3$ and the space of measurements $Y = \mathbb{R}^{N_{\mathrm{M}}}$.

3. Implementation of the Forward EMG Model

Our implementation of the forward EMG model introduced in Section 2.6 is based on the forward EMG model implemented in the KerMor framework[1]. KerMor is a software package implemented in MATLAB. We roughly sketch the structure of the KerMor forward EMG model in Section 3.1. Then, we present our modifications of and extensions to the KerMor forward EMG model, in Section 3.2. In detail, we decouple the discretization of the muscle domain D_{M} from the number of muscle fibers N_{MF} and extend the model to allow for non-diagonal, space-dependent conductivity tensors. Moreover, we use the `htucker` toolbox [61] to implement a low-rank tensor representation of the forward EMG problem. Summarizing the modified KerMor package, we present our standard settings for the forward EMG model in Section 3.3.

3.1. Status Quo

There are basically three steps to set up a forward EMG model in the KerMor framework:

1. A geometry that describes the computational domain needs to be defined.
2. The discretization is defined by choosing a discretization grid size.
3. A muscle fiber AP model has to be chosen.

The muscle domain D_{M} is considered to be a cuboid, where the length of the cuboid's edges in cm can be specified by the user. Note that the forward EMG model is independent of the position of the cubiod in space. The cuboid is thus assumed to have its origin at $(0, 0, 0)$ and its edges are assumed to be aligned with the standard unit vectors e_1, e_2, and $e_3 \in \mathbb{R}^3$. Within the KerMor framework, the cuboid geometry is specified as `geo=[length_1, length_2, length_3]`. An additional layer of surrounding tissue of a

[1] `https://www.morepas.org/software/kermor/index.html`

given thickness θ in cm can be added in e_3-direction by adding a fourth entry to the geometry, i.e., `geo=[length_1, length_2, length_3, θ]`. The edges of the domain D then have lengths `length_1` cm×`length_2` cm×(`length_3`+θ) cm.

There are two models available for the electrophysiology of the muscle fibers, the Rosenfalck model, see Section 2.6.1, and the model of Shorten et al. [97]. The muscle fiber potential is computed for $N_t = 101$ time steps spanning the time interval $[t_0, t_1] = [0, 100]$ in milliseconds. Both the number of time steps and the time interval are hard-coded into the KerMor framework and we thus take them as fixed parameters.

The Rosenfalck model can simply be evaluated at the discrete time steps and no time-stepping scheme is needed. To see where the time enters the Rosenfalck model, we rewrite Equation (2.12) using the AP velocities u_j and the relation $s_{\mathrm{F},j} = u_j t$ for $t \in [t_0, t_1] \subset \mathbb{R}$:

$$v_{\mathrm{m},j}(t) = c_{\mathrm{R},1}(u_j t)^3 \exp(-c_{\mathrm{R},2} u_j t) - c_{\mathrm{R},3}, \qquad t \in [t_{0,j}, t_{1,j}],\ j = 1, \ldots, N_{\mathrm{MF}}$$

For the discrete time steps $t_k = kh_t$ with a given time step size h_t (in the KerMor framework $h_t = 1\,\mathrm{ms}$) the above equation reads

$$(v^{\mathrm{h}}_{\mathrm{m},j})_k = c_{\mathrm{R},1}(u_j t_k)^3 \exp(-c_{\mathrm{R},2} u_j t_k) - c_{\mathrm{R},3}, \qquad k = 0, \ldots, N_t,\ j = 1, \ldots, N_{\mathrm{MF}}. \quad (3.1)$$

The Shorten model comprises several ODEs and is thus solved using a time stepping scheme. The default time stepping scheme implemented in KerMor is MATLAB's `ode23` solver, i.e., the explicit Runge-Kutta (2,3) pair of Bogacki and Shampine, cf. [96] and the references therein for further information.

In the original KerMor implementation, the propagation of the electrical potential through the muscle domain is modeled by the bidomain equation, as described in Section 2.6.3, for the constant extracellular conductivity $\sigma_{\mathrm{e}} = \mathrm{diag}(6.7, 6.7, 6.7)$ in mS/cm and the constant intracellular conductivity $\sigma_{\mathrm{i}} = \mathrm{diag}(8.93, 0.893, 0.893)$ in mS/cm. The propagation of the electrical potential through the surrounding tissue is modeled by a generalized Laplace equation, as described in Section 2.6.4, for a constant conductivity $\sigma_0 = \mathrm{diag}(4.0, 4.0, 4.0)$ in mS/cm. Note that the above conductivity matrices are hard-coded into the KerMor package.

The domain is discretized using central finite differences of second order with equidistant grid size h_x in all three spatial directions. The muscle fibers are assumed to lie on the finite difference grid edges that are parallel to the e_1-axis. Furthermore, the muscle fibers are discretized such that the muscle fiber grid points equal the grid points of the three-

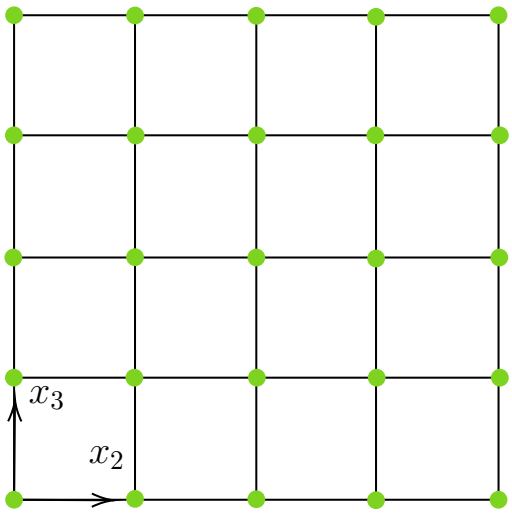

(a) Assembly of muscle fibers (green) according to the muscle grid (black)

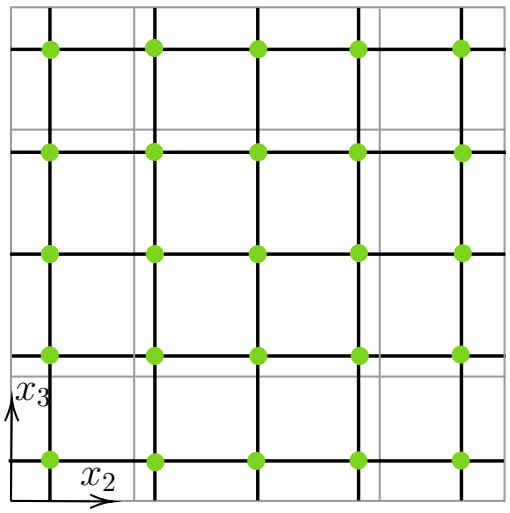

(b) Assembly of $N_{\mathrm{MF}} = 25$ muscle fibers (green) according to a muscle fiber grid (black), muscle grid in gray

Figure 3.1.: Illustration of the assembly of muscle fibers that are parallel to e_1

dimensional muscle domain as illustrated in Figure 3.1a. Hence, the three-dimensional membrane potential V_{m} at the muscle domain grid points equals the corresponding muscle fiber membrane potentials $v_{\mathrm{m},j}$ at these grid points.

In this way, the coupling between muscle fibers, their discretization, and the muscle domain discretization simplifies the assembling process described in Section 2.6.2. On the other hand, we see that the number of muscle fibers in the above model equals the number of grid points in the e_2-e_3-plane. Note that, e.g., in the biceps brachii, the number of muscle fibers is $N_{\mathrm{MF}} \approx 250\,000$ [58]. The described dependency between the model, i.e., the number of muscle fibers in the muscle, and the muscle domain grid size, is obviously undesirable and is resolved in Section 3.2.1.

The resulting discrete system of linear equations is solved using MATLAB's build-in QR-decomposition. Finally, the surface EMG data is generated as the finite difference solution of the discretized forward EMG problem at the surface grid points, i.e., by extracting the corresponding values from the solution vector.

3.2. Modifications and Extensions

We extend the KerMor forward model described in Section 3.1 as follows:

First, we resolve the connection of the number of muscle fibers and the three-dimen-

sional discretization and introduce a one-dimensional discretization of the muscle fibers that is independent of the three-dimensional discretization in Section 3.2.1. Additionally, we show the influence of the newly introduced parameters `N_MF` (number of muscle fibers) and `N_MFGP` (number of muscle fiber grid points) on the computed surface EMG data.

Second, in Section 3.2.2, we allow the muscle fiber direction to be an arbitrary vector $d_{\mathrm{F}} \in \mathbb{R}^3$ with $\|d_{\mathrm{F}}\| = 1$ instead of assuming $d_{\mathrm{F}} = e_1$ as before. This implies a generalization of the muscle fiber assembling routine to arbitrary muscle fiber directions. Further, we discussed already in Section 1.1 that the intracellular conductivity is a positive definite and symmetric matrix that is determined by the muscle fiber direction and the magnitudes of the longitudinal and transversal condictivities. Thus, introducing arbitrary muscle fiber directions means allowing arbitrary positive definite, symmetric intracellular conductivity matrices. We emphasize, that the conductivity matrices and muscle fiber directions are still assumed to be constant throughout their corresponding domain.

Third, in Section 3.2.3, we allow the intracellular conductivity to be space-dependent. This leads to a change in the discretization and includes solving a 3×3 eigenvalue problem in each muscle fiber grid point to compute the muscle fiber direction.

Fourth, in Section 3.2.4, we derive an affine representation of the discrete operator of the forward EMG problem and derive a low-rank tensor format representation of the operator and the right-hand side of the forward EMG problem for arbitrary but fixed muscle fiber directions. We use the `htucker` toolbox [61] to include this low-rank tensor representation of the forward EMG model into the KerMor framework.

3.2.1. Muscle Fibers

For resolving the coupling of the number of muscle fibers and the discretization of the three-dimensional muscle domain D_{M}, we introduce two new parameters: the number of muscle fibers $\texttt{N\_MF} \in \mathbb{N}^2$, which represents the number of muscle fibers to be put in e_2- and e_3-direction, and the number of muscle fiber grid points $\texttt{N\_MFGP} \in \mathbb{N}$.

Both quantities influence the computation of the membrane potential V_{m}. Before, the muscle fiber grid points coincided with the three-dimensional muscle domain grid points, see Figure 3.1a, such that the discrete muscle fiber action potentials were simply written into the corresponding entries of the three-dimensional membrane potential. Having different grids for muscle fibers and the muscle domain, as depicted in Figure 3.1b, this practice becomes infeasible. Instead, we use the combination of smoothing and projection introduced in Section 2.6.2 to accumulate the muscle fiber membrane potential

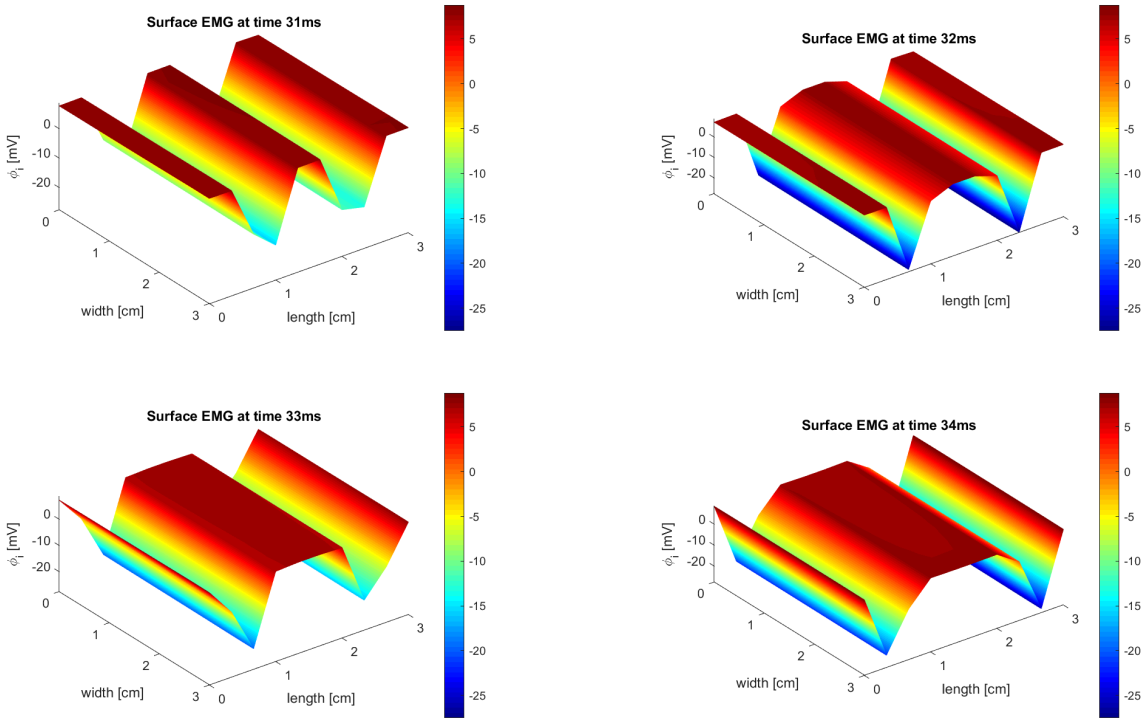

Figure 3.2.: Computed surface EMG signals at time steps $t = 31\,\text{ms}, t = 32\,\text{ms}, t = 33\,\text{ms}, t = 34\,\text{ms}$ in the setting of Section 3.2.1 for $h_x = \frac{1}{3}$

of each muscle fiber grid point to the nearest muscle domain grid point and weight the muscle fiber membrane potential according to the distance between the corresponding muscle fiber and muscle domain grid point. The weighting is done using the Gaussian smoothing kernel (2.16) with smoothing parameter $\alpha = 10$, such that the influence of the muscle fiber action potential on the membrane potential is high when muscle fiber grid point and muscle domain grid point are close and decreases rapidly with increasing distance.

We consider the following example: For the muscle domain `geo=[3,3,1]` with grid size $h_x = \frac{1}{3}$ and 100×100 muscle fibers with 100 muscle fiber grid points, we compute the surface EMG data from muscle fiber action potentials that are computed by the Rosenfalck model. The computed surface EMG data at times $t = 31\,\text{ms}$, $t = 32\,\text{ms}$, $t = 33\,\text{ms}$, and $t = 34\,\text{ms}$ is shown in Figure 3.2. Since the e_1-axis represents the muscle fiber direction, we see two wave fronts, i.e., the accumulated muscle fiber APs, traveling along the e_1-axis. As the stimulus is introduced in the middle of the muscle fibers, the wave fronts are symmetric and spread outwards from the points with $x_1 = 1.5$. We conduct the same experiment with spatial grid size $h_x = \frac{1}{12}$ and show the computed surface EMG data at times $t = 31\,\text{ms}$, $t = 32\,\text{ms}$, $t = 33\,\text{ms}$, and $t = 34\,\text{ms}$ in Figure 3.3.

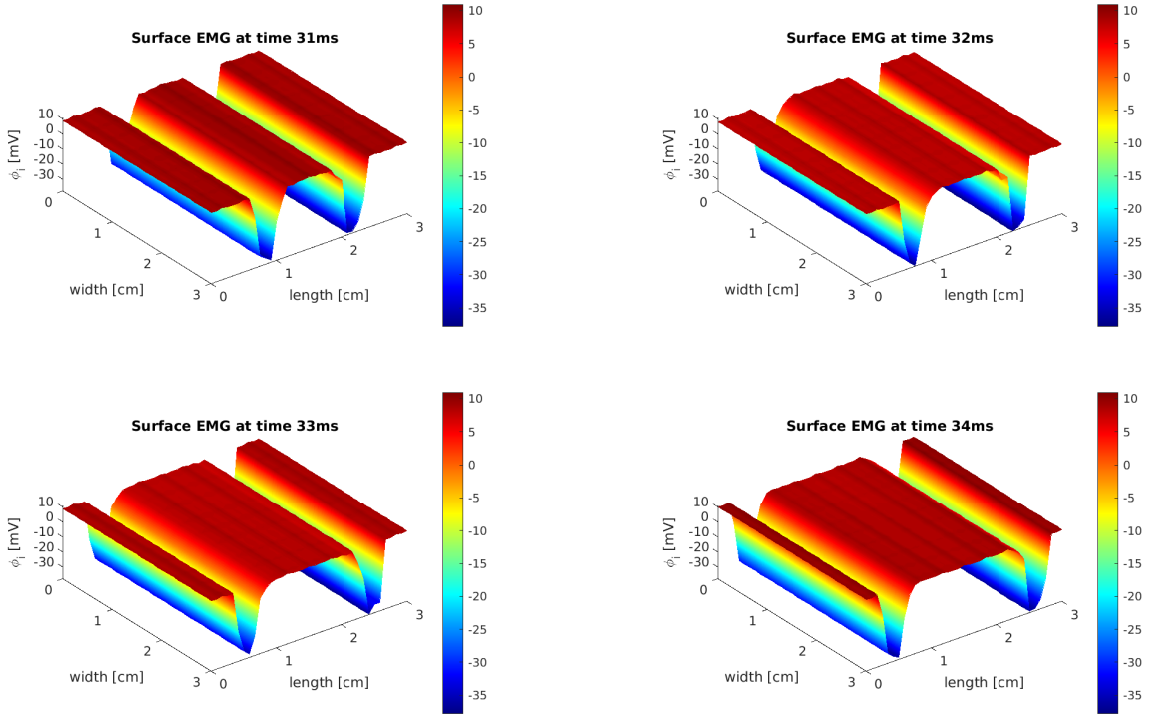

Figure 3.3.: Computed surface EMG signals at time steps $t = 31\,\text{ms}, t = 32\,\text{ms}, t = 33\,\text{ms}, t = 34\,\text{ms}$ in the setting of Section 3.2.1 for $h_x = \frac{1}{12}$

We see the same quantitative behavior of the two wave fronts evolving from the points with $x_1 = 1.5$. Moreover, the peaks of the wave fronts appear to be narrower and to have higher amplitudes compared to the wave fronts for $h_x = \frac{1}{3}$ in Figure 3.2. This is due to the finer discretization that represents the wave fronts more accurate and captures the peaks more precisely. The shapes of the peaks in Figure 3.3 correspond to the shapes of the Rosenfalck model depicted in Figure 2.5.

In the following, we test the influence of the newly introduced quantities. Therefore, we consider the above example and fix all parameters but the number of muscle fiber grid points `N_MFGP` and the number of muscle fibers `N_MF`. We vary the number of muscle fibers to be `N_MF=[j,j]` for $j \in \{10, 20, 30, 40, 50, 100\}$ and the number of muscle fiber grid points to be `N_MFGP=k` for $k \in \{10, 20, 30, 40, 50, 100\}$. Note that the actual number of muscle fibers is thus $N_{\text{MF}} = j^2$.

In Table 3.1 we show the infinity norm of the difference between the computed surface EMG data $\phi_{\mathbb{x}}^{100,100}$ for 100×100 muscle fibers with 100 muscle fiber grid points and the computed surface EMG data $\left\|\phi_{\mathbb{x}}^{j,k} - \phi_{\mathbb{x}}^{100,100}\right\|_\infty$ for $j, k \in \{10, 20, 30, 40, 50, 100\}$. The decay of the error in Table 3.1 with increasing number of muscle fibers implies that the number of muscle fibers has high impact on the computed surface EMG data.

Table 3.1.: Infinity norm of the error of computed surface EMG data for varying number of muscle fibers N_MF and number of muscle fiber grid points N_MFGP in the setting of Section 3.2.1 for $h_x = \frac{1}{3}$

N_MF/N_MFGP	10.00	20.00	30.00	40.00	50.00	100.00
$[10, 10]$	39.43	27.26	19.04	11.35	11.41	2.10
$[20, 20]$	39.38	26.46	19.20	10.23	10.45	0.79
$[30, 30]$	39.14	26.13	19.21	9.94	10.23	0.53
$[40, 40]$	38.94	25.73	19.24	9.49	9.99	0.26
$[50, 50]$	39.08	25.91	19.30	9.69	10.18	0.35
$[100, 100]$	38.85	25.64	19.27	9.38	9.97	0.0

Table 3.2.: Infinity norm of the error of computed surface EMG data for varying number of muscle fibers N_MF and number of muscle fiber grid points N_MFGP in the setting of Section 3.2.1 for $h_x = \frac{1}{12}$

N_MF/N_MFGP	10.00	20.00	30.00	40.00	50.00	100.00
$[10, 10]$	69.67	66.16	59.63	53.94	40.66	37.96
$[20, 20]$	69.61	63.73	55.75	48.75	35.51	25.28
$[30, 30]$	72.24	63.50	54.12	46.19	31.99	18.12
$[40, 40]$	71.85	61.92	51.71	43.59	29.09	0.21
$[50, 50]$	71.84	61.92	51.72	43.60	29.05	0.20
$[100, 100]$	71.78	61.87	51.67	43.57	29.02	0.0

An acceptable error below one is only achieved when the number of muscle fibers is $N_{\mathrm{MF}} = 100$ and when using at least $20 \times 20 = 400$ muscle fibers.

We rerun the same experiment for spatial grid size $h_x = \frac{1}{12}$ to reduce the influence of the spatial discretization error on the results. Again, we calculate the infinity norm of the difference between the computed surface EMG data $\phi_{\mathrm{x}}^{100,100}$ for 100×100 muscle fibers with 100 muscle fiber grid points and the computed surface EMG data $\left\|\phi_{\mathrm{x}}^{j,k} - \phi_{\mathrm{x}}^{100,100}\right\|_\infty$ for $j, k \in \{10, 20, 30, 40, 50, 100\}$. The results are shown in Table 3.2.

We see that choosing a finer spatial grid size and thus a finer resolution of the solution increases the error. Comparing this behavior to the influence of the spatial grid size on the computed surface EMG data, see Figures 3.2 and 3.3, this behavior is explained by the more prominent peaks of the wave fronts. The errors shown in Table 3.2 indicate that using $40 \times 40 = 1600$ muscle fibers yields a reasonable error. Further, the error does not decrease significantly when choosing $50 \times 50 = 2500$ muscle fibers. Moreover, increasing the number of muscle fibers implies evaluating the Rosenfalck model more often. We deduce that choosing N_MFGP= 100 and N_MF= $[40, 40]$ yields acceptable errors

and reasonable computation times.

3.2.2. Muscle Fiber Direction

We extend the KerMor forward EMG model from the previous section by allowing arbitrary muscle fiber directions, i.e., $d_\mathrm{F} \in \mathbb{R}$ with $\|d_\mathrm{F}\| = 1$ arbitrary. Note that we still assume that all muscle fibers have the same constant direction, which means that all muscle fibers are modeled as parallel straight lines. Nevertheless, these muscle fibers are allowed to have a non-zero angle with the muscle surface as depicted in Figure 3.4. Such muscle fibers that have a constant angle with respect to the muscle boundary occur in *pennate skeletal muscles* such as the rectus femoris or the deltoid muscle. We refer to [31] for a discussion on different fiber architectures and the resulting properties.

Taking into account such sloping muscle fibers, we need to rethink the distribution of muscle fibers within the muscle domain. We explain the muscle fiber distribution using a two-dimensional example. A sketch of this scenario is given in Figure 3.4. The

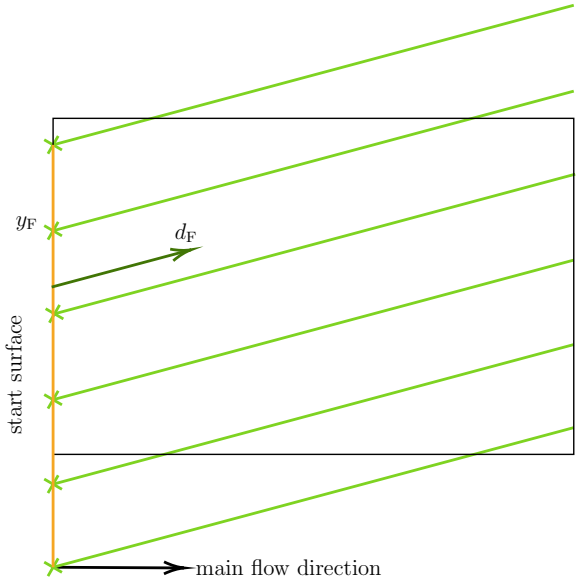

Figure 3.4.: Assembly of rotated muscle fibers (light green) in 2d

extension to three dimensions is straight forward as indicated by the terms in brackets in the following description. In order to equidistantly place j (in 3d: $j \times j$) muscle fibers with direction d_F into the muscle domain D_M we pursue the following four steps:

1. Determine the *main flow direction* being the unit vector e_j that fulfills $e_j^\top d_\mathrm{F} \geq e_k^\top d_\mathrm{F}$ for $k = 1, 2$ (in 3d: $k = 1, 2, 3$). In our two-dimensional example from Figure 3.4,

the main flow direction is e_1. Note that in case two directions have the same influence on the muscle fiber direction, i.e., the muscle fiber has an angle of 45° with the e_1-axis in the one-dimensional case, the smallest index is chosen to indicate the main flow direction. The same procedure is used in the three-dimensional setting.

2. Define the *extended start surface*, indicated in orange in Figure 3.4, as the one-dimensional line (in 3d: two-dimensional surface) on which to place the muscle fiber starting points. The start surface is perpendicular to the main flow direction and the extension is calculated such that the whole muscle domain is covered by muscle fibers, using simple geometric relations.

3. Place j muscle fiber starting points equidistantly on the start surface (in 3d: in each direction of the start surface), and define the muscle fibers as the straight lines starting in these muscle fiber starting points and having direction d_{F}, as indicated in dark green in Figure 3.4. Obviously, these muscle fibers are also defined outside the muscle domain. Hence, our last step is to

4. cut the muscle fibers at their intersections with the muscle domain boundary.

The muscle fiber membrane potentials are then computed and transferred to the three-dimensional membrane potential as described in Section 3.2.1.

We show the influence of a change in the muscle fiber direction on the computed surface EMG data at time $t = 31\,\mathrm{ms}$ in Figure 3.5 for spatial grid size $h_x = \frac{1}{3}$ and for $h_x = \frac{1}{12}$ in Figure 3.6 to examine the influence of the spatial grid size. The computations are conducted in the setting of Section 3.2.1 with `N_MF=[100,100]` and `N_MFGP=100`. Furthermore, we choose $\sigma_{\mathrm{i}}^* = \mathrm{diag}(8.93, 0.893, 0.893)$ for the reference configuration shown in Figures 3.5a and 3.6a.

We define the other muscle fiber directions by rotating the first unit vector e_1 by the angles $\alpha_1 = (0, 0, \frac{\pi}{2})$, $\alpha_2 = (0, 0, \frac{\pi}{4})$, and $\alpha_3 = (\frac{\pi}{6}, \frac{\pi}{7}, \frac{\pi}{8})$, i.e., we have

$$d_{\mathrm{F}}(\alpha_j) = R_1(\alpha_{j,1})R_2(\alpha_{j,2})R_3(\alpha_{j,3})e_1$$

with the rotation matrices

$$R_1(\alpha_1) \coloneqq \begin{pmatrix} 1 & 0 & 0 \\ 0 & \cos(\alpha_1) & -\sin(\alpha_1) \\ 0 & \sin(\alpha_1) & \cos(\alpha_1) \end{pmatrix},$$

$$R_2(\alpha_2) \coloneqq \begin{pmatrix} \cos(\alpha_2) & 0 & \sin(\alpha_2) \\ 0 & 1 & 0 \\ -\sin(\alpha_2) & 0 & \cos(\alpha_2) \end{pmatrix}, \text{ and}$$
$$R_3(\alpha_3) \coloneqq \begin{pmatrix} \cos(\alpha_3) & -\sin(\alpha_3) & 0 \\ \sin(\alpha_3) & \cos(\alpha_3) & 0 \\ 0 & 0 & 1 \end{pmatrix}. \tag{3.2}$$

Following this approach, we construct the corresponding intracellular conductivities by

$$\sigma_{\mathrm{i}}(\alpha_j) = R_1(\alpha_{j,1})R_2(\alpha_{j,2})R_3(\alpha_{j,3})\sigma_{\mathrm{i}}^* R_3^\top(\alpha_{j,3})R_2^\top(\alpha_{j,2})R_1^\top(\alpha_{j,1}).$$

Short calculation shows that $d_{\mathrm{F}}(\alpha_1) = e_2$ and thus $\sigma_{\mathrm{i}}(\alpha_1)$ is a diagonal matrix where the largest value is the second diagonal entry. The second angle yields $d_{\mathrm{F}}(\alpha_2) = (\frac{1}{\sqrt{2}}, \frac{1}{\sqrt{2}}, 0)$, meaning the muscle fibers are aligned parallel to the diagonal of the e_1-e_2-plane. Finally, we construct a 'random' direction, corresponding to a dense, symmetric, and positive definite intracellular conductivity matrix, using α_3.

As the muscle fiber direction indicates the travel direction of the muscle fiber action potentials, we see, in Figures 3.5 and 3.6, that the computed surface EMG data depends strongly on the muscle fiber direction. More precisely, the AP wave fronts propagate along the muscle fiber directions. In contrast to the other muscle fiber directions, $d_{\mathrm{F}}(\alpha_3)$ is no longer parallel to the muscle surface resulting in the asymmetric behavior of the computed surface EMG data in Figures 3.5d and 3.6d. Again, we see that using the spatial grid size $h_x = \frac{1}{3}$ we are able to capture the qualitative behavior of the surface EMG data but we are unable to capture the exact height and width of the wave fronts.

3.2.3. Space-dependent Conductivities

We further generalize the KerMor model from Section 3.2.2 to allow for intracellular conductivities that vary in space, i.e., $\sigma_{\mathrm{i}} = \sigma_{\mathrm{i}}(x)$ for $x \in D_{\mathrm{M}}$. Recall that, according to our discussion in Section 1.1, a space-dependent intracellular conductivity $\sigma_{\mathrm{i}}(x)$ introduces a space-dependent muscle fiber direction, i.e., $d_{\mathrm{F}} = d_{\mathrm{F}}(x)$. In terms of the muscle fiber directions, this enables the modeling of bent muscle fibers or overlaying muscles. We emphasize that the intracellular conductivity has to be specified in such a way that it introduces non-intersecting muscle fibers since two physical muscle fibers cannot occupy the same spatial point at the same time. Exemplifying the space-dependence of the conductivity, we discuss a model of two muscles lying on top of each other at the

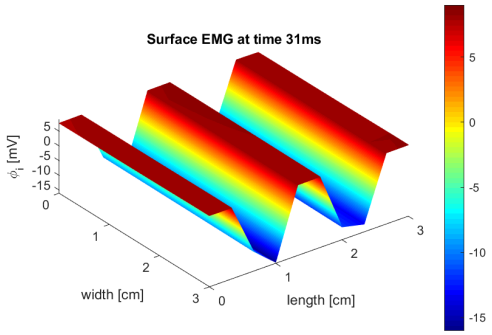

(a) Computed surface EMG data for σ_{i}^{*}

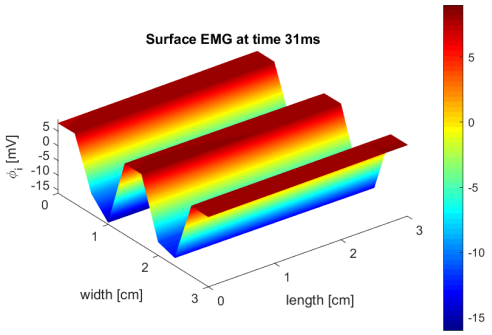

(b) Computed surface EMG data for $\sigma_{\mathrm{i}}(\alpha_1)$

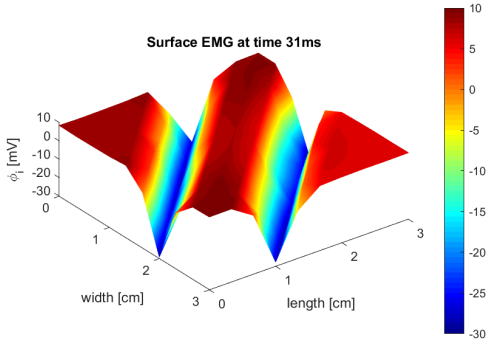

(c) Computed surface EMG data for $\sigma_{\mathrm{i}}(\alpha_2)$

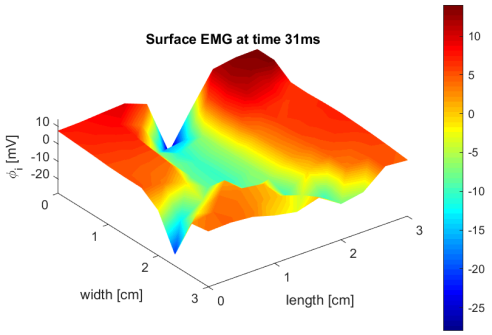

(d) Computed surface EMG data for $\sigma_{\mathrm{i}}(\alpha_3)$

Figure 3.5.: Influence of number of muscle fibers on the computed surface EMG data in the setting of Section 3.2.2 and $h_x = \frac{1}{3}$

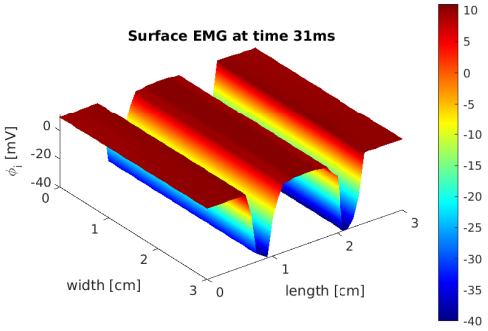

(a) Computed surface EMG data for σ_i^*

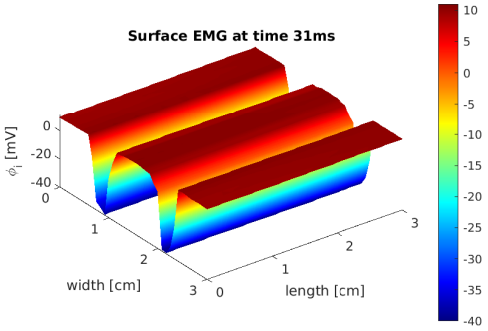

(b) Computed surface EMG data for $\sigma_i(\alpha_1)$

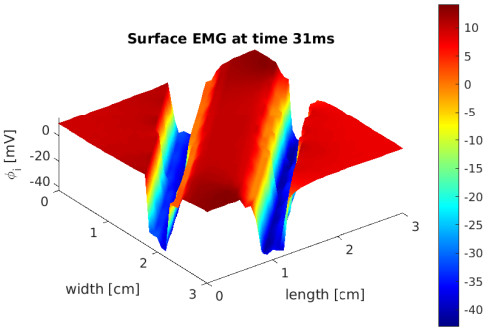

(c) Computed surface EMG data for $\sigma_i(\alpha_2)$

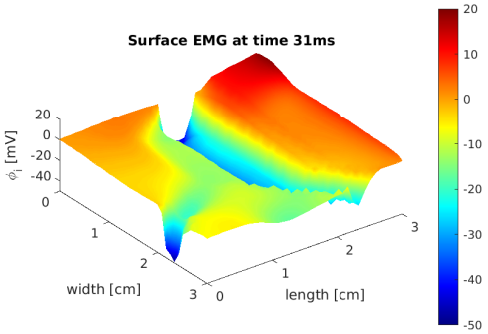

(d) Computed surface EMG data for $\sigma_i(\alpha_3)$

Figure 3.6.: Influence of number of muscle fibers on the computed surface EMG data in the setting of Section 3.2.2 and $h_x = \frac{1}{12}$

end of this section and in Section 6.3 in the inverse setting.

The assumption that the intracellular conductivity is space-dependent leads to a 're-discretization' of the problem. For simplicity and to follow the existing discretization of the KerMor package, we assume that the spatial grid size h_x is equal in each direction. We denote the $N_\mathrm{h} \coloneqq N_{\mathrm{h},1}N_{\mathrm{h},2}N_{\mathrm{h},3} \in \mathbb{N}$ grid points by $(x_{j_1}, x_{j_2}, x_{j_3})$ for $j_k = 0, \dots, N_{\mathrm{h},k}$ and $k = 1, 2, 3$, and a conductivity σ at grid point $(x_{j_1}, x_{j_2}, x_{j_3})$ by σ_{j_1,j_2,j_3}. A three-dimensional second-order consistent stencil for

$$B\phi \coloneqq \nabla \cdot (\sigma(x)\nabla\phi(x)) = \sum_{j=1}^{3} \frac{\partial}{\partial x_j}\left(\sigma(x)\frac{\partial}{\partial x_j}\phi(x)\right) \tag{3.3}$$

is then given by

$$\begin{bmatrix} 0 & 0 & 0 \\ 0 & \frac{\sigma_{j,j,j-1}+\sigma_{j,j,j}}{2h_x^2} & 0 \\ 0 & 0 & 0 \end{bmatrix} \text{ in the first plane, in the second plane by}$$

$$\begin{bmatrix} 0 & \frac{\sigma_{j,j-1,j}+\sigma_{j,j,j}}{2h_x^2} & 0 \\ \frac{\sigma_{j-1,j,j}+\sigma_{j,j,j}}{2h_x^2} & -\frac{\sigma_{j-1,j,j}+\sigma_{j,j-1,j}+\sigma_{j,j,j-1}+6\sigma_{j,j,j}+\sigma_{j,j,j+1}+\sigma_{j,j+1,j}+\sigma_{j+1,j,j}}{2h_x^2} & \frac{\sigma_{j,j,j}+\sigma_{j+1,j,j}}{2h_x^2} \\ 0 & \frac{\sigma_{j,j,j}+\sigma_{j,j+1,j}}{2h_x^2} & 0 \end{bmatrix},$$

$$\text{and by } \begin{bmatrix} 0 & 0 & 0 \\ 0 & \frac{\sigma_{j,j,j}+\sigma_{j,j,j+1}}{2h_x^2} & 0 \\ 0 & 0 & 0 \end{bmatrix} \text{ in the third plane.} \tag{3.4}$$

This stencil easily follows from the one-dimensional second-order consistent stencil

$$\frac{1}{h_x^2}\begin{bmatrix} \frac{\sigma_{j-1}+\sigma_j}{2} & -\frac{\sigma_{j-1}+2\sigma_j+\sigma_{j+1}}{2} & \frac{\sigma_j+\sigma_{j+1}}{2} \end{bmatrix}$$

using the Kronecker product structure of (3.3). The above one-dimensional stencil follows from Taylor's theorem and equating the coefficients of

$$\begin{aligned} (B\phi)_j &= \left(\frac{\partial}{\partial x}\sigma(x_j)\frac{\partial}{\partial x}\phi_j + \sigma(x_j)\frac{\partial^2}{\partial x^2}\phi_j\right) \quad \text{and} \\ (B^\mathrm{h}\phi^\mathrm{h})_j &= \frac{1}{h_x^2}\left(-\tilde{\sigma}_j\phi_{j-1} + (\tilde{\sigma}_j + \tilde{\sigma}_{j+1})\phi_j - \tilde{\sigma}_{j+1}\phi_{j+1}\right). \end{aligned}$$

From the relation between intracellular conductivity and muscle fiber direction, it is obvious that the muscle fiber directions $d_{\mathrm{F},j} = d_{\mathrm{F},j}(x)$ are space-dependent too for

$j = 1, \ldots, N_{\mathrm{MF}}$. Thus, apart from the operator of the forward EMG model described in Section 2.6, also the right-hand side and especially the assembling process of the muscle fibers as described in Section 3.2.2 is affected by a spatially varying intracellular conductivity. More precisely, in point 3 of our assembling routine, we have defined the muscle fibers as straight lines starting in the muscle fiber starting points and pointing in the muscle fiber direction. This procedure has to be adapted to a spatially varying muscle fiber direction.

From an implementational point of view this means that, when assembling the muscle fibers, the muscle fiber direction needs to be computed in every muscle fiber grid point $x^{\mathrm{h}}_{\mathrm{F},j}$. Recall that the muscle fiber direction can be computed as the eigenvector belonging to the maximal eigenvalue of the intracellular conductivity at any point $x^{\mathrm{h}}_{\mathrm{F},j}$, as discussed in Section 1.1. A muscle fiber can thus be assembled into the muscle domain by starting at the start surface, evaluating the intracellular conductivity at the starting point, computing the muscle fiber direction in the starting point, doing a step with the muscle fiber grid size in the computed direction, evaluating the intracellular conductivity at the new point and so on. Note that, in this way, we define the muscle fiber grid points iteratively. Using such an implementation, one has to be careful to choose the intracellular conductivity $\sigma_{\mathrm{i}}(x)$ such that the discrete muscle fibers do not intersect at any point.

Exemplarily, we implemented the scenario of two skeletal muscles lying on top of each other as depicted in Figure 3.7. We begin with the setting of Section 3.2.1 and assume

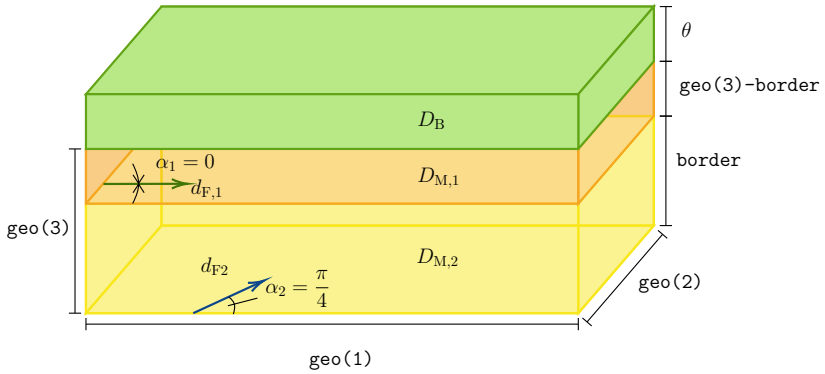

Figure 3.7.: Two-muscle scenario with layer of surrounding tissue of thickness θ

that the intracellular conductivity is constant in each muscle and that the muscle fibers are aligned with the e_1-e_2-plane, i.e., we only allow rotations around the e_3-axis. The intracellular conductivity of such a muscle composite of two muscles can be modeled by a conductivity of which the magnitudes and rotation angles change at the bound-

ary between the two muscles. In the example depicted in Figure 3.7, the intracellular conductivity is given by

$$\sigma_{\mathrm{i}}(x) = \begin{cases} \sigma_{\mathrm{i}}(\alpha_1) & x_3 > \texttt{border}, \\ \sigma_{\mathrm{i}}(\alpha_2) & \text{otherwise}, \end{cases} \tag{3.5}$$

where `border` denotes the height of the lower muscle. Further, the intracellular conductivities $\sigma_{\mathrm{i}}(\alpha_j)$ are defined as the rotation around the e_3-axis of the intracellular conductivity $\sigma_{\mathrm{i}} = \mathrm{diag}(8.93, 0.893, 0.893)$, i.e., $\sigma_{\mathrm{i}}(\alpha_j) \coloneqq R_3(\alpha_j)\sigma_{\mathrm{i}}R_3^\top(\alpha_j)$. Furthermore, we specify the number of muscle fibers in each muscle part to be `N_MF = [100,50]` with `N_MFGP = 100` and neglect the surrounding tissue, i.e., we set $\theta = 0$. We discuss the case $\theta > 0$ in Section 6.3. The computed surface EMG data for the two muscle scenario with angles $\alpha_1 = 0$ and $\alpha_2 = \frac{\pi}{4}$ and `border=2/3` is shown in Figure 3.8 for $h_x = \frac{1}{3}$ and in Figure 3.9 for $h_x = \frac{1}{12}$. Compared to the computed surface EMG data for the one muscle setting in Figures 3.2 and 3.3, we clearly see the influence of the changed setting. Furthermore, we observe a significant difference for the different spatial discretization grid sizes. While the wave fronts for $h_x = \frac{1}{3}$ in Figure 3.8 still appear smooth due to the coarse grid, we see that the surface EMG signal varies significantly for $h_x = \frac{1}{12}$ due to the superposition of the two muscles. The two muscle scenario is further investigated in the Bayesian inverse setting in Section 6.3.

3.2.4. Tensor Representation of the Forward EMG Problem

We derive a low-rank tensor representation of the discrete forward EMG operator using its affine structure. This is joint work with Tim A. Werthmann and has previously been published in [88]. The affine structure of the discrete forward operator can be seen when discretizing Equation (3.3) using the stencil defined in Equation (3.4), see Section 3.2.3. Using the linearity of (3.4) yields the affine representation of the discrete forward operator B that is given by

$$\begin{aligned} &\frac{\sigma_{j,j-1,j}}{h_x^2} M_{j,j-1,j} + \frac{\sigma_{j,j,j+1}}{h_x^2} M_{j,j,j+1} + \frac{\sigma_{j-1,j,j}}{h_x^2} M_{j-1,j,j} \\ &\qquad + \frac{\sigma_{j,j,j}}{h_x^2} M_{j,j,j} + \frac{\sigma_{j+1,j,j}}{h_x^2} M_{j+1,j,j} + \frac{\sigma_{j,j,j-1}}{h_x^2} M_{j,j,j-1} + \frac{\sigma_{j,j+1,j}}{h_x^2} M_{j,j+1,j}. \end{aligned}$$

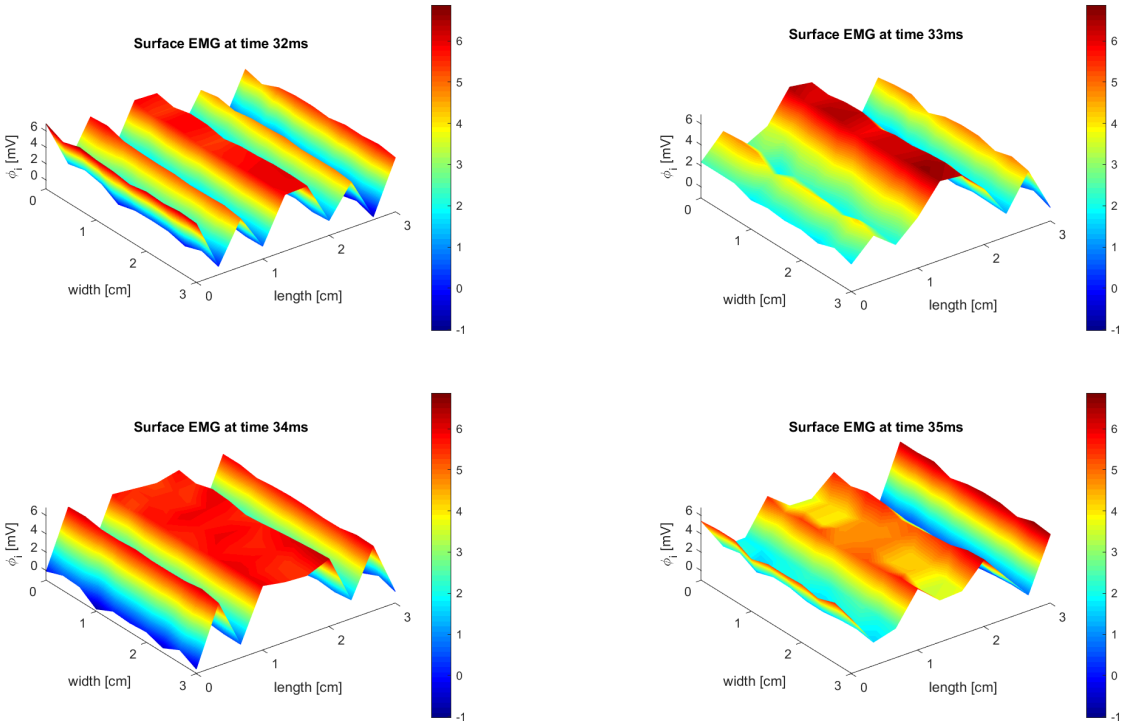

Figure 3.8.: Computed surface EMG data at time steps $t = 31\,\text{ms}, t = 32\,\text{ms}, t = 33\,\text{ms}, t = 34\,\text{ms}$ as described in Section 3.2.3 for $h_x = \frac{1}{3}$

Here, the stencil in the first plane is given by

$$M^{(:,:,1)}_{j,j-1,j} = M^{(:,:,1)}_{j,j,j+1} = M^{(:,:,1)}_{j-1,j,j} = M^{(:,:,1)}_{j,j,j} = M^{(:,:,1)}_{j+1,j,j} = \begin{bmatrix} 0 & 0 & 0 \\ 0 & 0 & 0 \\ 0 & 0 & 0 \end{bmatrix},$$

$$M^{(:,:,1)}_{j,j,j-1} = \begin{bmatrix} 0 & 0 & 0 \\ 0 & \frac{1}{2} & 0 \\ 0 & 0 & 0 \end{bmatrix}, M^{(:,:,1)}_{j,j-1,j} = \begin{bmatrix} 0 & 0 & 0 \\ 0 & 0 & 0 \\ 0 & 0 & 0 \end{bmatrix},$$

in the second plane by

$$M^{(:,:,2)}_{j,j-1,j} = \begin{bmatrix} 0 & \frac{1}{2} & 0 \\ 0 & -\frac{1}{2} & 0 \\ 0 & 0 & 0 \end{bmatrix}, \quad M^{(:,:,2)}_{j,j,j+1} = \begin{bmatrix} 0 & 0 & 0 \\ 0 & -\frac{1}{2} & 0 \\ 0 & 0 & 0 \end{bmatrix},$$

$$M^{(:,:,2)}_{j-1,j,j} = \begin{bmatrix} 0 & 0 & 0 \\ \frac{1}{2} & -\frac{1}{2} & 0 \\ 0 & 0 & 0 \end{bmatrix}, \quad M^{(:,:,2)}_{j,j,j} = \begin{bmatrix} 0 & \frac{1}{2} & 0 \\ \frac{1}{2} & -3 & \frac{1}{2} \\ 0 & \frac{1}{2} & 0 \end{bmatrix}, \quad M^{(:,:,2)}_{j+1,j,j} = \begin{bmatrix} 0 & 0 & 0 \\ 0 & -\frac{1}{2} & \frac{1}{2} \\ 0 & 0 & 0 \end{bmatrix},$$

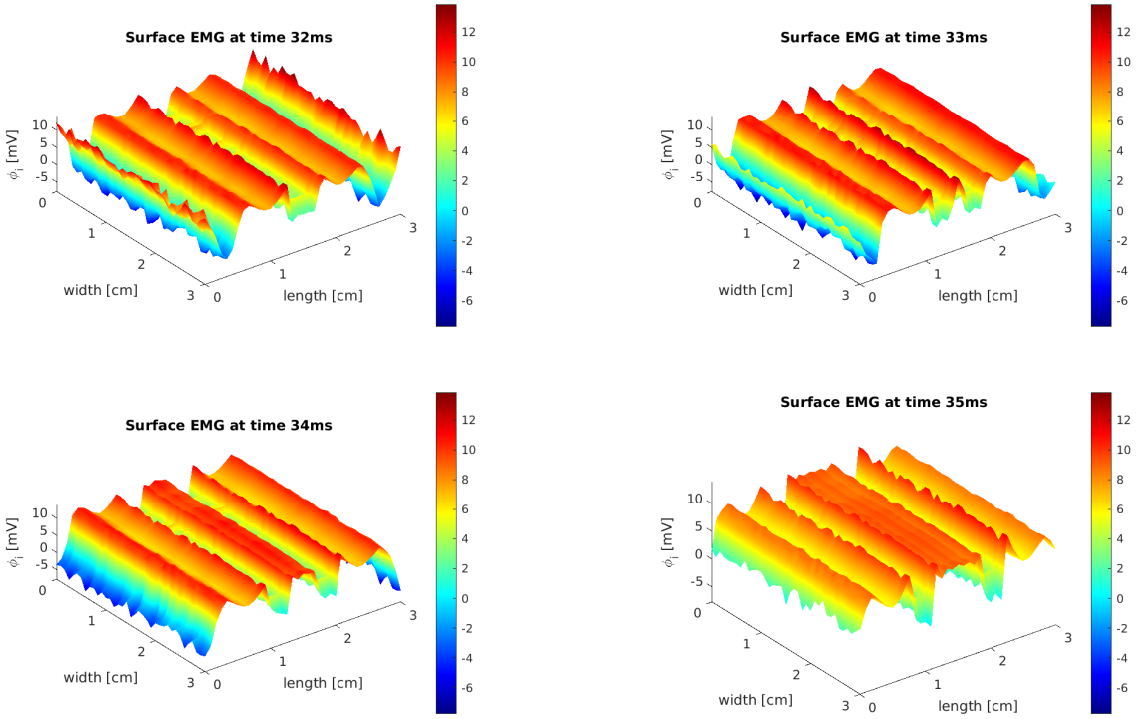

Figure 3.9.: Computed surface EMG data at time steps $t = 31\,\text{ms}, t = 32\,\text{ms}, t = 33\,\text{ms}, t = 34\,\text{ms}$ as described in Section 3.2.3 for $h_x = \frac{1}{12}$

$$M^{(:,:,2)}_{j,j,j-1} = \begin{bmatrix} 0 & 0 & 0 \\ 0 & -\frac{1}{2} & 0 \\ 0 & 0 & 0 \end{bmatrix}, \qquad M^{(:,:,2)}_{j,j-1,j} = \begin{bmatrix} 0 & 0 & 0 \\ 0 & -\frac{1}{2} & 0 \\ 0 & \frac{1}{2} & 0 \end{bmatrix},$$

and in the third plane by

$$M^{(:,:,3)}_{j,j-1,j} = \begin{bmatrix} 0 & 0 & 0 \\ 0 & 0 & 0 \\ 0 & 0 & 0 \end{bmatrix}, M^{(:,:,3)}_{j,j,j+1} = \begin{bmatrix} 0 & 0 & 0 \\ 0 & \frac{1}{2} & 0 \\ 0 & 0 & 0 \end{bmatrix},$$

$$M^{(:,:,3)}_{j-1,j,j} = M^{(:,:,3)}_{j,j,j} = M^{(:,:,3)}_{j+1,j,j} = M^{(:,:,3)}_{j,j,j-1} = M^{(:,:,3)}_{j,j-1,j} = \begin{bmatrix} 0 & 0 & 0 \\ 0 & 0 & 0 \\ 0 & 0 & 0 \end{bmatrix}.$$

Let $A^{\text{h}}_{\sigma_\text{e}}$ denote the discrete operator given by Equation (3.4) for constant $\sigma = \sigma_\text{e} \in \mathbb{R}^{3\times 3}$ and let $A^{\text{h}}_{j_1,j_2,j_3}$ denote the discrete operator given by the stencil M_{j_1,j_2,j_3} from above. Then, the discrete operator A^{h} of the left-hand side operator A of the bidomain

equation (2.19) with

$$A\phi_{\mathrm{e}} \coloneqq \nabla \cdot ((\sigma_{\mathrm{i}}(x) + \sigma_{\mathrm{e}})\nabla\phi_{\mathrm{e}}(x)) = \nabla \cdot (\sigma_{\mathrm{e}}\nabla\phi_{\mathrm{e}}(x)) + \nabla \cdot (\sigma_{\mathrm{i}}(x)\nabla\phi_{\mathrm{e}}(x))$$

is given by

$$A^{\mathrm{h}} \coloneqq A^{\mathrm{h}}_{\sigma_{\mathrm{e}}} + \sum_{j_1=1}^{N_{\mathrm{h},1}} \sum_{j_2=1}^{N_{\mathrm{h},2}} \sum_{j_3=1}^{N_{\mathrm{h},3}} \sigma_{j_1,j_2,j_3} A^{\mathrm{h}}_{j_1,j_2,j_3}.$$

We clearly see the difference in the discretization for the space-independent extracellular conductivity σ_{e} and the space-dependent intracellular conductivity σ_{i}.

For deriving a CP representation of the above discrete parameter-dependent forward EMG problem, we place the above considerations into the general framework of parameter-dependent linear systems introduced in Section 2.5. Using the vectorization, see Definition 2.5.3, we define $A^{\mathrm{h},(k)} \coloneqq \mathrm{vec}(A^{\mathrm{h}}_{j_1,j_2,j_3})$ and the parameters $\boldsymbol{p}^{(k)} \coloneqq \mathrm{vec}(\sigma_{j_1,j_2,j_3})$ for $k = 1, \ldots, d$. Here d is the number of parameters.

For specifying the above definitions, recall that the matrix-valued intracellular conductivity σ_{i} is symmetric. After spatial discretization, the matrix entries of σ_{i} in each discrete point, i.e., of σ_{j_1,j_2,j_3}, remain as the free parameters. Using a row-wise numbering we thus have the vectorization of the space-discrete $(1,1)$ entry of σ_{i} as the first parameter $\boldsymbol{p}^{(1)}$, the vectorization of the space-discrete $(1,2)$ entry of σ_{i} as the second parameter $\boldsymbol{p}^{(2)}$, and so on. Note that we skip the entries $(2,1), (3,1)$, and $(3,2)$ since they are defined through the entries $(1,2), (1,3)$, and $(2,3)$ due to the symmetry of σ_{i}. The above procedure leads to $d = 6$ parameters.

We further set $A^{\mathrm{h},(0)} \coloneqq A^{\mathrm{h}}_{\sigma_{\mathrm{e}}}$. Together, this yields a parameter-dependent affine structure of the form

$$A^{\mathrm{h}}(\boldsymbol{p}) \coloneqq A^{\mathrm{h},(0)} + \sum_{k=1}^{6} \boldsymbol{p}^{(k)} A^{\mathrm{h},(k)}$$

with $\boldsymbol{p} = (\boldsymbol{p}^{(1)}, \ldots, \boldsymbol{p}^{(6)})$, and where each $A^{\mathrm{h},(k)}$ is constant, i.e., $A^{\mathrm{h},(k)}$ is parameter-independent.

Next, we discretize the parameters $\boldsymbol{p} = (\boldsymbol{p}^{(1)}, \ldots, \boldsymbol{p}^{(6)})$. Thus, we allow each parameter $\boldsymbol{p}^{(k)}$, $k = 1, \ldots, 6$, to take $N_{\boldsymbol{p},k} \in \mathbb{N}$ different values $\boldsymbol{p}^{\mathrm{h},(k)}(j)$ with $j = 1, \ldots, N_{\boldsymbol{p},k}$. Writing the above parameter-dependent linear operator for all discrete parameters leads

to a large block-diagonal system, compare with Equation (2.9), with the operator

$$\mathbf{A} \coloneqq \operatorname{blkdiag}\left(A_1^{(0)}, \ldots, A_{N_{\boldsymbol{p}}}^{(0)}\right) \coloneqq \begin{pmatrix} A_1^{(0)} & 0 & \ldots & 0 \\ 0 & A_2^{(0)} & \ddots & \vdots \\ \vdots & \ddots & \ddots & 0 \\ 0 & \ldots & 0 & A_{N_{\boldsymbol{p}}^*}^{(0)} \end{pmatrix}.$$

Here, the j^{th} diagonal block is given by $A_j^{(0)} = A^{\mathrm{h},(0)} + \sum_{k=1}^{6} \boldsymbol{p}^{\mathrm{h},(k)}(j) A^{\mathrm{h},(k)}$ and $N_{\boldsymbol{p}}^* \coloneqq \max_{k=1,\ldots,6} N_{\boldsymbol{p},k}$. The memory requirement to store $\mathbf{A}$, however, grows exponentially in the number $N_{\boldsymbol{p}} \coloneqq \prod_{k=1,\ldots,6} N_{\boldsymbol{p},k}$ of parameter grid points and thus, even for a moderate number of parameters such as $d = 6$ in our case and moderate $N_{\boldsymbol{p},k}$, a classical representation of our problem is infeasible, see our discussion in Section 2.5.

We follow the idea used to reformulate our example parameter-dependent linear system defined in Equation (2.9) to become data-sparse in Section 2.5. Using the notation $A_j^{(l)} \coloneqq \sum_{k=l}^{6} \boldsymbol{p}^{\mathrm{h},(k)}(j) A^{\mathrm{h},(k)}$ for $l = 1, \ldots, 6$, we thus obtain

$$\begin{aligned}
\mathbf{A} &= \operatorname{blkdiag}\left(A^{\mathrm{h},(0)} + A_1^{(1)}, A^{\mathrm{h},(0)} + A_2^{(1)}, \ldots, A^{\mathrm{h},(0)} + A_{N_{\boldsymbol{p}}}^{(1)}\right) \\
&= \operatorname{blkdiag}\left(A^{\mathrm{h},(0)}, A^{\mathrm{h},(0)}, \ldots, A^{\mathrm{h},(0)}\right) \\
&\quad + \operatorname{blkdiag}\left(\boldsymbol{p}^{\mathrm{h},(1)}(1) A^{\mathrm{h},(1)}, \boldsymbol{p}^{\mathrm{h},(1)}(2) A^{\mathrm{h},(1)}, \ldots, \boldsymbol{p}^{\mathrm{h},(1)}(N_{\boldsymbol{p},1}) A^{\mathrm{h},(1)}\right) \\
&\quad + \operatorname{blkdiag}\left(A_1^{(2)}, A_2^{(2)}, \ldots, A_{N_{\boldsymbol{p}}}^{(2)}\right) \\
&= \operatorname{Id}_{N_{\boldsymbol{p},6}} \otimes \cdots \otimes \operatorname{Id}_{N_{\boldsymbol{p},2}} \otimes \operatorname{Id}_{N_{\boldsymbol{p},1}} \otimes A^{(0)} \\
&\quad + \operatorname{Id}_{N_{\boldsymbol{p},6}} \otimes \cdots \otimes \operatorname{Id}_{N_{\boldsymbol{p},2}} \otimes \operatorname{diag}\left(\boldsymbol{p}^{\mathrm{h},(1)}\right) \otimes A^{\mathrm{h},(1)} \\
&\quad + \ldots \\
&\quad + \operatorname{diag}\left(\boldsymbol{p}^{\mathrm{h},(6)}\right) \otimes \cdots \otimes \operatorname{Id}_{N_{\boldsymbol{p},2}} \otimes \operatorname{Id}_{N_{\boldsymbol{p},1}} \otimes A^{\mathrm{h},(6)}.
\end{aligned}$$

Recalling the CP representation from Definition 2.5.1, the above considerations lead to the data-sparse CP representation

$$\mathbf{A} = \sum_{k=0}^{6} \bigotimes_{j=0}^{6} A^{*,(k)}(j)$$

of the parameter-dependent operator A, where

$$A^{*,(k)}(j) = \begin{cases} A^{\mathrm{h},(j)} & \text{if } j = 6, \\ \mathrm{diag}\left(\boldsymbol{p}^{\mathrm{h},(j)}\right) & \text{if } j + k = 6 \text{ and } k \neq 0, \\ \mathrm{Id}_{n_{6-k}} & \text{otherwise} \end{cases}$$

with discrete parameters $\boldsymbol{p}^{\mathrm{h},(j)} = (\boldsymbol{p}^{\mathrm{h},(j)}(1), \ldots, \boldsymbol{p}^{\mathrm{h},(j)}(N_{\boldsymbol{p},j}))$. Due to the linearity of the operator with respect to the intracellular conductivity, the above CP representation holds for arbitrary space-dependent intracellular conductivities.

Contrarily, the right-hand side $b \coloneqq -\nabla \cdot (\sigma_{\mathrm{i}} \nabla V_{\mathrm{m}})$ of the bidomain equation (2.19) depends nonlinearly on spatial changes of the intracellular conductivity as these changes correspond to changes in the muscle fiber direction and thus in the membrane potential V_{m}. We will quantify this issue further in Section 5.1, see the discussion around Figure 5.2. In case the muscle fiber direction is known, e.g., through one of the imaging techniques discussed in Chapter 1, and fixed, a CP representation $\mathbf{b}$ of the right-hand side of the bidomain equation (2.19) similar to the above CP representation of the operator can be achieved. This setting corresponds to fixing the rotation angles and thus leaves the three conductivity magnitudes as free parameters.

Note that these CP representations of the operator and the right-hand side (in the case of fixed rotation angles) are exact representations.

The question arises whether we can prove that the tensor solution $\boldsymbol{\phi}(\boldsymbol{p})$ of the parameter-dependent forward EMG problem of finding $\boldsymbol{\phi}(\boldsymbol{p})$ such that $\mathbf{A}(\boldsymbol{p})\boldsymbol{\phi}(\boldsymbol{p}) = \mathbf{b}(\boldsymbol{p})$ has a low-rank approximation. As discussed in Section 2.5, general criterions for guarantying the existence of a low-rank representation of $\boldsymbol{\phi}$ are unknown. Thus, we assume that the solution of the parameter-dependent forward EMG problem has a low-rank approximation.

Furthermore, we represent $\mathbf{A}(\boldsymbol{p})$ and $\mathbf{b}(\boldsymbol{p})$ using the hierarchical Tucker format, see Definition 2.5.5, and use the preconditioned conjugate gradients method with truncation as introduced in Algorithm 2.5.1 to approximate the solution $\boldsymbol{\phi}(\boldsymbol{p})$ of $\mathbf{A}(\boldsymbol{p})\boldsymbol{\phi}(\boldsymbol{p}) = \mathbf{b}(\boldsymbol{p})$ in the hierarchical Tucker format.

For justification of the assumption that $\boldsymbol{\phi}(\boldsymbol{p})$ has low rank, we examine the rank of $\boldsymbol{\phi}(\boldsymbol{p})$ in the setting that we will use in the inverse case, see Chapters 5 and 6. We refer to [88] for the same experiment in a different setting and highlight that both lead to similar results.

We specify the forward EMG model by choosing the geometry `geo=[3,3,1]` and

setting $h_x = \frac{1}{3}$, `N_MF=40`, `N_MFGP=[100,100]`, and $\sigma_e = \mathrm{diag}(6.7, 6.7, 6.7)$. Furthermore, we set $\boldsymbol{p} \coloneqq (\sigma_{i,11}, \sigma_{i,22}, \sigma_{i,33})$ and aim at calculating the EMG data for each $\boldsymbol{p}$ in the parameter space $\boldsymbol{\mathcal{J}} \coloneqq [6, 10] \times (0, 4] \times (0, 4]$. We discretize the parameter space $\boldsymbol{\mathcal{J}}$ with grid size $h_{\boldsymbol{p}} = 0.001$ and compute $A^{h,(0)}$ using the conductivity at the midpoint of the resulting grid, i.e., for $\boldsymbol{p} = (8, 2, 2)$. For handling the time-dependency in the right-hand side, we solve the corresponding linear system for all time steps simultaneously.

We define the solution tensor as follows: We set the first dimension of the tensor to correspond to the spatial dimension, i.e., the first dimension is $(3 \cdot \frac{1}{h_x} + 1)(3 \cdot \frac{1}{h_x} + 1)(1 \cdot \frac{1}{h_x} + 1) = 400$. The second dimension of the tensor corresponds to the time steps and thus is $101 = N_t$. The third dimension of the tensor corresponds to the longitudinal intracellular conductivity magnitude and thus is $(10-6)\frac{1}{h_{\boldsymbol{p}}}+1 = (10-6)\cdot 1000+1 = 4001$, while the fourth and fifth dimension of the tensor, which correspond to the second and third (transversal) intracellular conductivity magnitudes, are of size $(4 - h_{\boldsymbol{p}})\frac{1}{h_{\boldsymbol{p}}} + 1 = 4 \cdot 1000 = 4000$. This leads to a tensor solution $\boldsymbol{\phi}$ of size $400 \times 101 \times 4001 \times 4000 \times 4000$. Note that the surface of the muscle cuboid has $(3 \cdot 3 + 1)(3 \cdot 3 + 1) = 100$ spatial nodes. Extracting the electrical potential at the surface grid points, i.e., evaluating the tensor solution $\boldsymbol{\phi}$ at the surface grid points, we would thus remain with a surface EMG tensor of size $100 \times 101 \times 4001 \times 4000 \times 4000$.

Moreover, for the PCG algorithm 2.5.1, we specify the maximal number of iterations $N_{\mathrm{CG}} = 15$ and the tolerance for the residual norm $\varepsilon = 1 \times 10^{-4}$. Further, we truncate to a relative accuracy of 1×10^{-6} using the `truncate` routine of the `htucker` toolbox. The relative accuracy guarantees that $\|\mathbf{B} - \mathrm{truncate}(\mathbf{B})\| \leq 1 \times 10^{-6}\|\mathrm{truncate}(\mathbf{B})\|$. The actual truncation rank thus depends on the chosen relative accuracy. We refer to [62] for a detailed description of the truncation routine. We choose the preconditioner $\mathbf{M} \coloneqq \mathrm{Id}_{n_d} \otimes \cdots \otimes \mathrm{Id}_{n_1} \otimes A^{h,(0)}$. Note that, according to [62], the choice of the low-rank tensor preconditioner has little influence on the convergence behavior and run time of the PCG algorithm.

Having specified all necessary parameters, we show a logarithmic-linear plot of the relative singular values for the corresponding matricizations, see Definition 2.5.3, of the tensor solution $\boldsymbol{\phi}$ in Figure 3.10. The plot of the singular values was computed using the `plot_sv` function of the `htucker` toolbox [61]. We observe that the rank of the matricization corresponding to the labels $\{3\}$, $\{4\}$, and $\{5\}$, which correspond to the parameter space, is 5. We also see that the rank of the matricization corresponding to the label $\{2\}$ is 60. Recall that the second dimension of the tensor corresponds to the time. The rank of the matricization corresponding to the label $\{1\}$ is 330. This

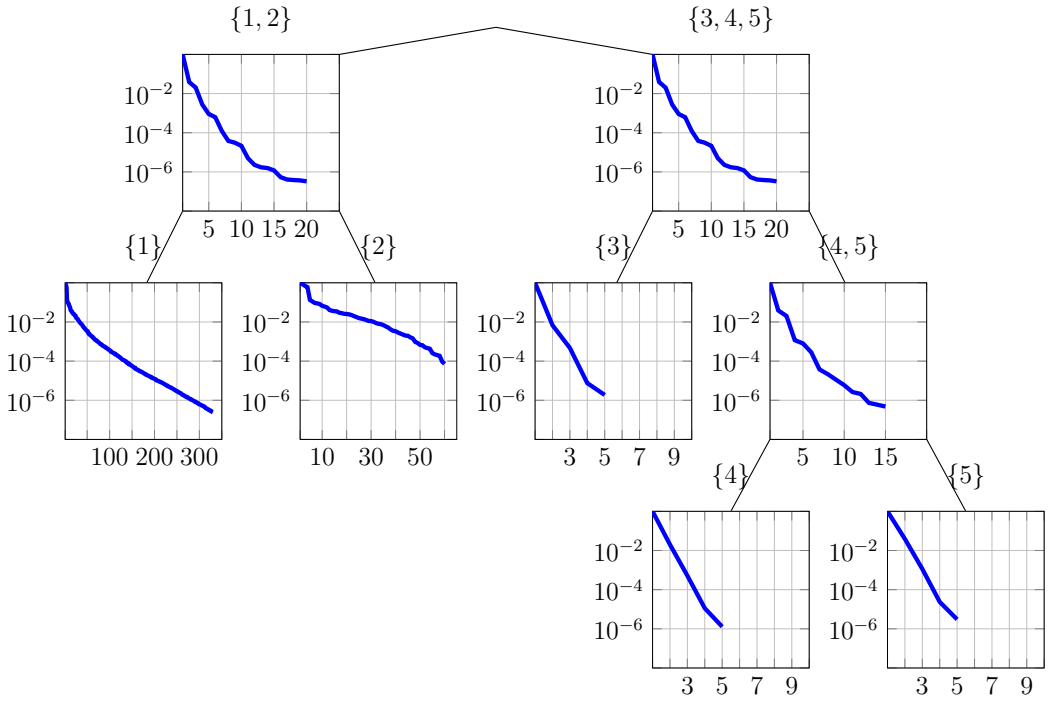

Figure 3.10.: Relative singular values of the corresponding matricization of the low-rank solution of the forward EMG problem described in Section 3.2.4

matricization separates the spatial dimension $\{1\}$ and the time dimension $\{2\}$. Recall that the right-hand side of the bidomain equation (2.19), which is determined by the muscle fiber membrane potential through Equations (2.12) and (2.15), changes over time, see our discussion at the end of Section 2.6.3. Thus, each time step yields a different right-hand side, which explains the high rank of the matricization corresponding to the label $\{1\}$.

For further justification of the assumption that the tensor solution $\boldsymbol{\phi}$ has low rank, we show the rank of the matricizations of $\boldsymbol{\phi}$ for the spatial discretization grid size $h_x = \frac{1}{3}$ and $h_x = \frac{1}{12}$ for the three conductivities $\sigma_{\mathrm{i}}^{*,1} = (8.93, 0.893, 0.893)$, $\sigma_{\mathrm{i}}^{*,2} = (0.893, 8.93, 0.893)$, and $\sigma_{\mathrm{i}}^{*,3} = (0.893, 0.893, 8.93)$ and $\alpha^* = (0, 0, 0)$ in Table 3.3. We observe, that the rank of the tensor solution $\boldsymbol{\phi}$ is independent of the spatial grid size h_x. We highlight, that the rank of the matricizations with respect to the labels $\{3\}$, $\{4\}$, and $\{5\}$, i.e., with respect to the dimensions representing the parameter space, remains low throughout all the settings because of the observed affine structure.

Recall that storing the solutions $\phi(\boldsymbol{p}^{\mathrm{h}})$ for all parameter combinations $\boldsymbol{p}^{\mathrm{h}}$ is infeasible unless using low-rank tensor representations. In the above example, using low-rank tensor formats we reduce the theoretical storage cost of 2.07×10^{10} MB for the full

Table 3.3.: Acceptance rate κ_a of the SA for inferring the rotation angles for 1000 drawn samples, noise level $\xi = 0.1$ and varying sampling radius r_s in the setting of Section 3.3

	$h_x = \frac{1}{3}$			$h_x = \frac{1}{12}$		
label	$\sigma^{*,1}$	$\sigma^{*,2}$	$\sigma^{*,3}$	$\sigma^{*,1}$	$\sigma^{*,2}$	$\sigma^{*,3}$
$\{1\}$	330	330	155	330	330	155
$\{2\}$	60	60	40	60	60	40
$\{3\}$	5	5	5	5	5	5
$\{4\}$	5	5	5	5	5	5
$\{5\}$	5	5	5	5	5	5

tensor, calculated for the above $400 \times 101 \times 4001 \times 4000 \times 4000$ tensor counting the storage cost for one entry as 64 bit, to 4.77 MB needed by MATLAB to store the actually calculated tensor solution $\boldsymbol{\phi}$.

Moreover, we discussed in Section 2.5 that the evaluation of a tensor in hierarchical Tucker format, such as the tensor solution $\boldsymbol{\phi}$, is cheap in the sense that the cost is of order $\mathcal{O}(dr^3)$ if the hierarchical Tucker rank is node-wise bounded by r and d denotes the dimension. In the above example, the maximum tensor rank in the dimensions $3, 4$ and 5 referring to the parameter space is 5 and we have $d = 3$ parameters. Using the resulting low-rank tensor representation to evaluate the forward EMG problem will lead to a tremendous speedup of the sampling algorithms used to solve the Bayesian inverse EMG problem in Chapter 5.

3.3. Standard Settings for the Forward EMG Model

Summarizing Sections 3.1 and 3.2, we set the following standard settings of the generalized forward EMG model to be used within the inversion algorithms in Chapters 5 and 6.

We compute all experiments on the muscle cuboid defined through `geo=[3,3,1]`, i.e., we neglect any surrounding tissue unless stated explicitly.

The standard spatial grid size for the muscle cuboid is $h_x = \frac{1}{3}$. In accordance with Tables 3.1 and 3.2 and to weight computational costs against accuracy, we choose `N_MFGP=100` and we insert `N_MF =[40,40]` muscle fibers. We compute surface EMG data on the time interval $[t_0, t_1] = [0, 100]$ ms with time step size $h_t = 1$ ms.

We use the Rosenfalck model to describe the electrophysiology of the muscle fibers,

since the Rosenfalck model is also investigated theoretically in Section 4.1. The Rosenfalck parameters are chosen to be $c_{\mathrm{R},1} = 84 \cdot (3.1)^3 = 2502.444, c_{\mathrm{R},2} = 3.1$, and $c_{\mathrm{R},3} = 80$, compare to Figure 2.5 in Section 2.6.1 for the meaning of the Rosenfalck parameters.

Finally, we set the extracellular conductivity to be a constant diagonal matrix throughout the whole muscle cuboid with $\sigma_{\mathrm{e}} = \mathrm{diag}(6.7, 6.7, 6.7)$. As reference values of the intracellular conductivity we use the diagonal and constant matrices $\sigma_{\mathrm{i}}^{*,1} = (8.93, 0.893, 0.893)$, $\sigma_{\mathrm{i}}^{*,2} = (0.893, 8.93, 0.893)$, and $\sigma_{\mathrm{i}}^{*,3} = (0.893, 0.893, 8.93)$ and we set the rotation angles $\alpha^* = (0, 0, 0)$. Together, we have the three reference parameters $\boldsymbol{p}^{*,j} = (\sigma_{\mathrm{i}}^{*,j}, \alpha^*)$ for $j = 1, 2, 3$.

Using low-rank tensor representations of the parameter-dependent forward EMG problem, we use the PCG algorithm 2.5.1 with $N_{\mathrm{CG}} = 15$ and $\varepsilon = 1 \times 10^{-4}$. Furthermore, we truncate to a relative accuracy of 1×10^{-6} and use the preconditioner $\mathbf{M} \coloneqq \mathrm{Id}_{n_d} \otimes \cdots \otimes \mathrm{Id}_{n_1} \otimes A^{\mathrm{h},(0)}$, see Section 3.2.4.

4. Theoretical Results

Throughout this chapter we state the deterministic and probabilistic forward and the Bayesian inverse EMG problem and prove and discuss their well-posedness in the sense of Hadamard, see Section 2.1.1. We will see that the well-posedness of the forward problems is indeed crucial for proving the well-posedness of the Bayesian inverse EMG problem and thus worth being discussed.

In Section 4.1.1 we begin with deriving the weak formulation of the deterministic forward EMG problem (2.26) that was introduced in Section 2.6. Based on the weak formulation of the deterministic forward EMG problem, we will prove the well-posedness of the deterministic forward problem in Section 4.1.2.

We continue with modeling the inevitable measurement error to formulate the probabilistic forward EMG problem in Section 4.2.1 and the Bayesian inverse EMG problem in Section 4.3.1. We recommend to compare this procedure of defining the Bayesian inverse EMG problem to the general introduction of Bayesian inversion in Section 2.4.

The well-posedness of the probabilistic forward EMG problem is proved in Section 4.2.2. The well-posedness of the deterministic and probabilistic forward EMG problem builds the foundation of the proof of well-posedness of the Bayesian inverse EMG problem that we conduct in Section 4.3.2.

Finally, in Section 4.4 we deduce error bounds for the solution of the Bayesian inverse EMG problem with respect to a discretization of the forward EMG problem and the probabilistic conductivities from the well-posedness results.

4.1. Deterministic Forward EMG Problem

Recall that the deterministic forward EMG problem is encapsulated in the forward operator $\mathcal{G}$ as defined in Equation (2.26). It comprises the evolution of APs in the muscle fibers according to the Rosenfalck model (2.12)

$$v_{\mathrm{m},j}(s_{\mathrm{F},j}) = c_{\mathrm{R},1} s_{\mathrm{F},j}^3 \exp(-c_{\mathrm{R},2} s_{\mathrm{F},j}) - c_{\mathrm{R},3}, \qquad s_{\mathrm{F},j} \in D_{\mathrm{F},j},\ j = 1, \dots, N_{\mathrm{MF}}$$

or according to the Hodgkin-Huxley model (2.13)

$$\begin{aligned}\partial_t v_{\mathrm{m},j} &= \frac{1}{C_{\mathrm{m},j}}(I_{\mathrm{stim}} - I_{\mathrm{ion}}), \qquad j = 1, \dots, N_{\mathrm{MF}} \\ &= \frac{1}{C_{\mathrm{m},j}}(I_{\mathrm{stim}} - (\kappa_{\mathrm{g,Na}}(v_{\mathrm{m},j} - \kappa_{\mathrm{E,Na}}) + \kappa_{\mathrm{g,K}}(v_{\mathrm{m},j} - \kappa_{\mathrm{E,K}}) + c_{\mathrm{g,L}}(v_{\mathrm{m},j} - \kappa_{\mathrm{E,L}}))),\end{aligned}$$

the application of the smoothing operator (2.15)

$$V_{\mathrm{m}}(x) = \sum_{j=1}^{N_{\mathrm{MF}}} \mathcal{S}(v_{\mathrm{m},j})(x),$$

the propagation of the resulting three-dimensional APs through muscle and surrounding tissue according to Equations (2.19) and (2.20)

$$\begin{aligned}\nabla \cdot ((\sigma_{\mathrm{i}} + \sigma_{\mathrm{e}})\nabla\phi_{\mathrm{e}}) &= -\nabla \cdot (\sigma_{\mathrm{i}}\nabla V_{\mathrm{m}}) && \text{in } D_{\mathrm{M}} \\ \nabla \cdot (\sigma_0 \nabla\phi_0) &= 0 && \text{in } D_{\mathrm{B}},\end{aligned}$$

and the evaluation of the electrical potential at the skin surface according to (2.25)

$$\phi_{\mathbb{x}} = \phi(\mathbb{x}) = \frac{1}{\pi r_{\mathrm{el}}^2}\Big(\int_{B_{r_{\mathrm{el}}}(x_{\mathrm{m},j}) \cap \partial D} \phi(x)\mathrm{d}x\Big)_{j=1}^{N_{\mathrm{M}}} \in \mathbb{R}^{N_{\mathrm{M}}}.$$

Additionally, the coupling, boundary, and zero-mean conditions, Equations (2.21), (2.22) and (2.23),

$$\begin{aligned}\phi_{\mathrm{e}} &= \phi_0 && \text{on } \Gamma_{\mathrm{I}}, \\ (\sigma_{\mathrm{e}}\nabla\phi_{\mathrm{e}}) \cdot n_{\mathrm{M}} &= -(\sigma_0\nabla\phi_0) \cdot n_{\mathrm{B}} && \text{on } \Gamma_{\mathrm{I}}, \\ (\sigma_{\mathrm{i}}\nabla V_{\mathrm{m}}) \cdot n_{\mathrm{M}} &= -(\sigma_{\mathrm{i}}\nabla\phi_{\mathrm{e}}) \cdot n_{\mathrm{M}} && \text{on } \partial D_{\mathrm{M}}, \\ (\sigma_0\nabla\phi_0) \cdot n_{\mathrm{B}} &= 0 && \text{on } \Gamma_{\mathrm{B}}, \\ (\sigma_{\mathrm{e}}\nabla\phi_{\mathrm{e}}) \cdot n_{\mathrm{M}} &= 0 && \text{on } \Gamma_{\mathrm{M}}, \\ \int_{D_{\mathrm{M}}} \phi_{\mathrm{e}} + \int_{D_{\mathrm{B}}} \phi_0 &= 0\end{aligned}$$

yield the physical and mathematical well-posedness of the problem.

We prove the mathematical well-posedness in Section 4.1.2 after deriving the weak formulation of the above summarized deterministic forward EMG problem in Section 4.1.1.

4.1.1. Weak Formulation

Completing our description of the deterministic forward EMG problem as summarized above, we derive its weak formulation. The weak formulation forms the basis of our theoretical framework, i.e., of the well-posedness of the Bayesian inverse EMG problem, see Sections 4.1.2, 4.2.2, and 4.3.2.

We denote the Sobolev space of square integrable functions having square integrable weak first derivatives by $H^{1,2}$. For functions $v = \mathbb{1}_{D_\mathrm{M}} v_\mathrm{e} + \mathbb{1}_{D_\mathrm{B}} v_0$ as in (2.24) we define the solution space

$$V \coloneqq \left\{ v \mid v_\mathrm{e} \in H^{1,2}(D_\mathrm{M}; \mathbb{R}), v_0 \in H^{1,2}(D_\mathrm{B}; \mathbb{R}), v_\mathrm{e} = v_0 \text{ on } \Gamma_\mathrm{I}, \int_D v = 0 \right\}$$

as the space of all functions $v = \mathbb{1}_{D_\mathrm{M}} v_\mathrm{e} + \mathbb{1}_{D_\mathrm{B}} v_0$ that are in $H^{1,2}(D; \mathbb{R})$, equal on the boundary Γ_I, and additionally fulfill the zero-mean condition. Note that the coupling condition (2.21a) and the zero-mean condition (2.23) have been incorporated into the solution space that indeed is a vector space. We will see that all other coupling and boundary conditions can be included into the weak formulation itself.

Further, the solution space is equipped with the V-norm

$$\|v\|_V \coloneqq \|\nabla v_\mathrm{e}\|_{L^2(D_\mathrm{M})} + \|\nabla v_0\|_{L^2(D_\mathrm{B})},$$

where $\|\cdot\|_{L^2}$ denotes the Lebesgue norm on the indicated domain. Note that the sum of Sobolev seminorms is a proper norm on V due to the integral zero-mean and the coupling condition. It easily follows that the V-norm fulfills the inequality

$$\frac{1}{2}\|v\|_V^2 \leq \|\nabla v_\mathrm{e}\|_{L^2(D_\mathrm{M})}^2 + \|\nabla v_0\|_{L^2(D_\mathrm{B})}^2 \tag{4.1}$$

for all functions $v \in V$.

Furthermore, we define the infinity norm of the global conductivity $\boldsymbol{\sigma} \in (L^\infty(D; \mathbb{R}^{3\times 3}))^3$ through

$$\|\boldsymbol{\sigma}\|_\infty \coloneqq \max(\|\sigma_\mathrm{i}\|_\infty, \|\sigma_\mathrm{e}\|_\infty, \|\sigma_0\|_\infty)$$

using the infinity norm of the conductivities $\sigma_\mathrm{i}, \sigma_\mathrm{e}$ and σ_0 that is defined as

$$\|\sigma_j\|_\infty \coloneqq \operatorname*{ess\,sup}_{x \in D} \max_{k,l=1,2,3} |(\sigma_j)_{kl}(x)|$$

for $j \in \{\mathrm{i}, \mathrm{e}, 0\}$, compare to the definition of the Lebesgue-Bochner spaces in Section 2.2.1.

Following the standard derivation of weak formulations, namely multiplying Equations (2.19) and (2.20) by a test function $v \in V$, integrating over the domain D, shifting derivatives using integration by parts, and inserting the corresponding coupling and boundary conditions, we see that a weak solution $\phi \in V$ of the deterministic forward EMG problem (2.26) must fulfill

$$\int_{D_\mathrm{M}} \big((\sigma_\mathrm{i} + \sigma_\mathrm{e})\nabla\phi_\mathrm{e}\big) \cdot \nabla v_\mathrm{e} + \int_{D_\mathrm{B}} (\sigma_0 \nabla\phi_0) \cdot \nabla v_0 = -\int_{D_\mathrm{M}} (\sigma_\mathrm{i} \nabla V_\mathrm{m}) \cdot \nabla v_\mathrm{e} \tag{4.2}$$

for all test functions $v \in V$. Assuming that $D \subset \mathbb{R}^3$ is open with Lipschitz boundary, the trace of the solution ϕ of Equation (4.2) exists in $L^2(\partial D; \mathbb{R})$. Thus, the evaluation operator (2.25) is well defined for the solution of the weak formulation (4.2). For ease of notation, the application of the trace operator to the weak solution ϕ is not indicated by any additional notation.

We redefine the forward operator $\mathcal{G}$ from Equation (2.26) to map a given global conductivity $\boldsymbol{\sigma} \in (L^\infty(D; \mathbb{R}^{3\times3}))^3$ to the evaluation $\phi_{\mathbb{x}} \in \mathbb{R}^{N_\mathrm{M}}$ of the trace of the weak solution of Equation (4.2). As it will always be clear from the context, whether the strong or weak forward operator is meant, we do not use any additional notation. Furthermore, we define the bilinear form $a_{\boldsymbol{\sigma}} : V \times V \to \mathbb{R}$ through

$$a_{\boldsymbol{\sigma}}(\phi, v) \coloneqq \int_{D_\mathrm{M}} \big((\sigma_\mathrm{i} + \sigma_\mathrm{e})\nabla\phi_\mathrm{e}\big) \cdot \nabla v_\mathrm{e} + \int_{D_\mathrm{B}} (\sigma_0 \nabla\phi_0) \cdot \nabla v_0$$

and the linear form $\ell_{\boldsymbol{\sigma}} : V \to \mathbb{R}$ through

$$\ell_{\boldsymbol{\sigma}}(v) \coloneqq -\int_{D_\mathrm{M}} (\sigma_\mathrm{i} \nabla V_\mathrm{m}) \cdot \nabla v_\mathrm{e}$$

such that a solution $\phi \in V$ of equation (4.2) fulfills

$$a_{\boldsymbol{\sigma}}(\phi, v) = \ell_{\boldsymbol{\sigma}}(v) \quad \text{for all } v \in V.$$

Summarizing the above considerations, the weak deterministic forward problem reads as follows.

Definition 4.1.1 (Weak Deterministic Forward EMG Problem). *For given global conductivity $\boldsymbol{\sigma} \in (L^\infty(D; \mathbb{R}^{3\times3}))^3$ find the EMG data $\phi_{\mathbb{x}} \in \mathbb{R}^{N_M}$ at measuring points*

$\mathbb{x} \in \mathbb{R}^{3\times N_M}$, *such that* $\phi \in V$ *solves* $a_{\boldsymbol{\sigma}}(\phi, v) = \ell_{\boldsymbol{\sigma}}(v)$ *for all* $v \in V$. *Using the forward operator notation, we compute* $\phi_{\mathbb{x}} = \mathcal{G}(\boldsymbol{\sigma})$.

4.1.2. Well-posedness

Within the setting of Section 4.1.1 we prove the well-posedness of the deterministic forward EMG problem for both the Rosenfalck and the Hodgkin-Huxley model of the muscle fiber AP evolution.

Lemma 4.1.2. *For each given global conductivity* $\boldsymbol{\sigma} \in (L^\infty(D;\mathbb{R}^{3\times 3}))^3$ *there exists a unique solution* $\phi \in V$ *fulfilling* $a_{\boldsymbol{\sigma}}(\phi, v) = \ell_{\boldsymbol{\sigma}}(v)$ *for all* $v \in V$ *and*

$$\sup_{\boldsymbol{\sigma}\in(L^\infty(D,\mathbb{R}^{3\times 3}))^3} \|\phi(\boldsymbol{\sigma})\|_V \leq 2\frac{\|\sigma_i\|_\infty}{\sigma_{min}}\|\nabla V_m\|_{L^2(D_M)}. \tag{4.3}$$

Here, the global minimal conductivity $\sigma_{min} := \big(\sigma_{ie,min}, \sigma_{0,min}\big)$ *is defined as the minimum of the local minimal conductivities* $\sigma_{ie,min} := \operatorname*{ess\,inf}_{x\in D_M} \min_{k,l=1,2,3}(\sigma_i(x)+\sigma_e(x))_{k,l}$ *and* $\sigma_{0,min} := \operatorname*{ess\,inf}_{x\in D_B} \min_{k,l=1,2,3}(\sigma_0(x))_{k,l}$.

Proof. We proceed in two steps.

1. The existence and uniqueness of a solution $\phi \in V$ to Equation (4.2) follows directly from the Lax-Milgram theorem, i.e., from the coercivity and boundedness of the bilinear form $a_{\boldsymbol{\sigma}}$.

   For seeing the coercivity, we calculate

$$\begin{aligned} a_{\boldsymbol{\sigma}}(\phi,\phi) &= \int_{D_\mathrm{M}} \big((\sigma_\mathrm{i}+\sigma_\mathrm{e})\nabla\phi_\mathrm{e}\big)\cdot\nabla\phi_\mathrm{e} + \int_{D_\mathrm{B}} (\sigma_0\nabla\phi_0)\cdot\nabla\phi_0 \\ &\geq \sigma_{\mathrm{ie,min}}\int_{D_\mathrm{M}} \nabla\phi_\mathrm{e}\cdot\nabla\phi_\mathrm{e} + \sigma_{0,\mathrm{min}}\int_{D_\mathrm{B}} \nabla\phi_0\cdot\nabla\phi_0 \\ &= \sigma_{\mathrm{ie,min}}\|\nabla\phi_\mathrm{e}\|^2_{L^2(D_\mathrm{M})} + \sigma_{0,\mathrm{min}}\|\nabla\phi_0\|^2_{L^2(D_\mathrm{M})} \\ &\geq \sigma_{\min}\big(\|\nabla\phi_\mathrm{e}\|^2_{L^2(D_\mathrm{M})} + \|\nabla\phi_0\|^2_{L^2(D_\mathrm{M})}\big) \\ &\overset{(4.1)}{\geq} \frac{1}{2}\sigma_{\min}\|\phi\|^2_V. \end{aligned} \tag{4.4}$$

The boundedness of $a_{\boldsymbol{\sigma}}$ follows from

$$\begin{aligned}|a_{\boldsymbol{\sigma}}(\phi, v)| &\leq \int_{D_{\mathrm{M}}} \left|\left((\sigma_{\mathrm{i}} + \sigma_{\mathrm{e}})\nabla\phi_{\mathrm{e}}\right) \cdot \nabla v_{\mathrm{e}}\right| + \int_{D_{\mathrm{B}}} \left|(\sigma_0 \nabla\phi_0) \cdot \nabla v_0\right| \\ &\overset{\mathrm{HI}}{\leq} \|\sigma_{\mathrm{i}} + \sigma_{\mathrm{e}}\|_\infty \|\nabla\phi_{\mathrm{e}}\|_{L^2(D_{\mathrm{M}})} \|\nabla v_{\mathrm{e}}\|_{L^2(D_{\mathrm{M}})} + \|\sigma_0\|_\infty \|\nabla\phi_0\|_{L^2(D_{\mathrm{B}})} \|\nabla v_0\|_{L^2(D_{\mathrm{B}})} \\ &\leq 2\max\{\|\sigma_{\mathrm{i}} + \sigma_{\mathrm{e}}\|_\infty, \|\sigma_0\|_\infty\} \|\phi\|_V \|v\|_V,\end{aligned}$$

where HI indicates the use of Hölder's inequality. Having proved the coercivity and boundedness of a_ϕ, Lax-Milgram's theorem is applicable.

2. Let $\boldsymbol{\sigma} \in (L^\infty(D; \mathbb{R}^{3\times 3}))^3$ be arbitrary but fixed. We prove the boundedness of $\phi(\boldsymbol{\sigma})$ by testing the weak formulation with the solution itself and using standard estimates, such as Hölder's inequality. For the linear form $\ell_{\boldsymbol{\sigma}}$ we get

$$\begin{aligned}\ell_{\boldsymbol{\sigma}}(\phi) &= -\int_{D_{\mathrm{M}}} (\sigma_{\mathrm{i}} \nabla V_{\mathrm{m}}) \cdot \nabla\phi_{\mathrm{e}} \\ &\leq \int_{D_{\mathrm{M}}} |(\sigma_{\mathrm{i}} \nabla V_{\mathrm{m}}) \cdot \nabla\phi_{\mathrm{e}}| \\ &\overset{\mathrm{HI}}{\leq} \|\sigma_{\mathrm{i}}\|_\infty \|\nabla V_{\mathrm{m}}\|_{L^2(D_{\mathrm{M}})} \|\nabla\phi_{\mathrm{e}}\|_{L^2(D_{\mathrm{M}})} \\ &\leq \|\sigma_{\mathrm{i}}\|_\infty \|\nabla V_{\mathrm{m}}\|_{L^2(D_{\mathrm{M}})} \|\phi\|_V. \end{aligned} \tag{4.5}$$

Combining estimate (4.5) with the coercivity (4.4) and canceling out $\|\phi\|_V$ yields the desired boundedness of $\phi(\boldsymbol{\sigma})$. □

Note that from the Rosenfalck model (2.12) it easily follows that

$$\|\nabla V_{\mathrm{m}}\|_{L^2(D_{\mathrm{M}})} \leq c_{\mathrm{R}} \tag{4.6}$$

for some constant $c_{\mathrm{R}} > 0$. This constant is independent of the solution ϕ and the conductivity $\boldsymbol{\sigma}$ and depends only on the heuristically known model parameters $c_{\mathrm{R},j}, j = 1, 2, 3$. We thus end up with the boundedness of the solution ϕ.

A uniform bound on $\|\nabla V_{\mathrm{m}}\|_{L^2(D_{\mathrm{M}})}$ can also be deduced for the more complex Hodgkin-Huxley model, introduced in Section 2.6.1, as the following lemma shows.

Lemma 4.1.3. *Let $V_m = \sum_{j=1}^{N_{MF}} \mathcal{S}(v_{m,j})$ be the membrane potential achieved by smoothing and adding the muscle fiber membrane potentials $v_{m,j}$ that are the solutions of the Hodgkin-Huxley differential equations* (2.13) *using the smoothing operator $\mathcal{S}$ and or-*

thogonal projection pr *as defined in Equations* (2.15) *and* (2.18)*. Then there exists a constant* $c_{HH} > 0$ *such that*

$$\|\nabla V_m\|_{L^2(D_M)} \leq c_{HH}. \tag{4.7}$$

Note that even if we restricted ourselves to a specific smoothing operator, the proof works for any bounded smoothing operator.

Proof. We first rewrite the gradient of V_m with respect to the three-dimensional spatial variable x as

$$\nabla_x V_\mathrm{m}(x) = \sum_{j=1}^{N_\mathrm{MF}} \nabla_x \left(v_{\mathrm{m},j}(\mathrm{pr}_j(x)) \exp\left(-\frac{\alpha}{2}\left\|x - \mathrm{pr}_j(x)\right\|^2\right)\right).$$

To apply the product rule, we calculate the gradient of both $v_{\mathrm{m},j}$ and the exponential term, and denote the finite AP velocity by $u_j \coloneqq \frac{\mathrm{d}s_{\mathrm{F},j}}{\mathrm{d}t}$:

$$\begin{aligned}\nabla_x \left(v_{\mathrm{m},j}(\mathrm{pr}_j(x))\right) &= \left(\nabla_x v_{\mathrm{m},j}\right)(\mathrm{pr}_j(x))\nabla_x \mathrm{pr}_j(x) = \nabla_x(s_{\mathrm{F},j})\underbrace{\frac{\mathrm{d}t}{\mathrm{d}s_{\mathrm{F},j}}}_{=u_j^{-1}}\partial_t v_{\mathrm{m},j}(t)\nabla_x \mathrm{pr}_j(x)\\ &= d_{\mathrm{F},j}^\top u_j^{-1}\partial_t v_{\mathrm{m},j}(t) d_{\mathrm{F},j} d_{\mathrm{F},j}^\top = u_j^{-1}\partial_t v_{\mathrm{m},j}(t) d_{\mathrm{F},j}, \qquad j = 1,\dots,N_\mathrm{MF}\end{aligned}$$

Here, we have used that the gradient of the muscle fiber coordinate, see Equation (2.14), with respect to x simplifies to $\nabla_x s_{\mathrm{F},j} = \nabla_x(d_{\mathrm{F},j}^\top(x - y_{\mathrm{F},j})) = d_{\mathrm{F},j}^\top$. For the exponential term we get

$$\nabla_x \left(\exp\left(-\frac{\alpha}{2}\left\|x - \mathrm{pr}_j(x)\right\|^2\right)\right) = -\alpha \exp\left(-\frac{\alpha}{2}\left\|x - \mathrm{pr}_j(x)\right\|^2\right)\left(x - \mathrm{pr}_j(x)\right)^\top \left(\mathrm{Id} - d_{\mathrm{F},j} d_{\mathrm{F},j}^\top\right).$$

Putting both equations together and inserting the Hodgkin-Huxley ODE for $\partial_t v_{\mathrm{m},j}$ into the spatial derivative of the muscle fiber membrane potential, we end up with

$$\begin{aligned}\nabla_x V_\mathrm{m}(x) = \quad & \sum_{j=1}^{N_\mathrm{MF}} u_j^{-1}\frac{1}{C_{\mathrm{m},j}}(I_\mathrm{stim} + \kappa_{\mathrm{g,Na}}\kappa_{\mathrm{E,Na}} + \kappa_{\mathrm{g,K}}\kappa_{\mathrm{E,K}} + c_{\mathrm{g,L}}\kappa_{\mathrm{E,L}}) d_{\mathrm{F},j}\\ & \cdot \exp\left(-\frac{\alpha}{2}\left\|x - \mathrm{pr}_j(x)\right\|^2\right)\\ & - \sum_{j=1}^{N_\mathrm{MF}}\left[u_j^{-1}\frac{1}{C_{\mathrm{m},j}}(\kappa_{\mathrm{g,Na}} + \kappa_{\mathrm{g,K}} + c_{\mathrm{g,L}}) d_{\mathrm{F},j} \exp\left(-\frac{\alpha}{2}\left\|x - \mathrm{pr}_j(x)\right\|^2\right)\right.\end{aligned}$$

$$+ \alpha \exp\left(-\frac{\alpha}{2}\left\|x - \mathrm{pr}_j(x)\right\|^2\right)(x - \mathrm{pr}_j(x))^\top \left(\mathrm{Id} - d_{\mathrm{F},j} d_{\mathrm{F},j}^\top\right)\Big] v_{\mathrm{m},j}(\mathrm{pr}_j(x)).$$

We define the first term in the above equation as $f_j(x)$ and look at the norm of $\nabla_x V_\mathrm{m}(x)$:

$$\begin{aligned}
\|\nabla_x V_\mathrm{m}\|_{L^2(D_\mathrm{M})} \leq & N_\mathrm{MF}|D_\mathrm{M}| \max_{j=1,\dots,N_\mathrm{MF}} \|f_j\|_\infty \\
& + \sum_{j=1}^{N_\mathrm{MF}} \underbrace{(|c_{\mathrm{g,Na}}| + |c_{\mathrm{g,K}}| + |c_{\mathrm{g,L}}|) \left\| u_j^{-1} \frac{1}{C_{\mathrm{m},j}} d_{\mathrm{F},j} \exp\left(-\frac{\alpha}{2}\left\|x - \mathrm{pr}_j(x)\right\|^2\right)\right\|_\infty}_{\leq c_1} \\
& \cdot \|v_{\mathrm{m},j}\|_{L^2(D_{\mathrm{F},j})} \\
& + \sum_{j=1}^{N_\mathrm{MF}} \underbrace{\left\|\alpha \exp\left(-\frac{\alpha}{2}\left\|x - \mathrm{pr}_j(x)\right\|^2\right)(x - \mathrm{pr}_j(x))^\top \left(\mathrm{Id} - d_{\mathrm{F},j} d_{\mathrm{F},j}^\top\right)\right\|_\infty}_{\leq c_2} \\
& \cdot \|v_{\mathrm{m},j}\|_{L^2(D_{\mathrm{F},j})}
\end{aligned}$$

Here, we made use of the probabilities λ_k of an individual gate being in the permissive state being lower or equal 1, such that $\|\kappa_{\mathrm{g},k}\|_\infty = |c_{\mathrm{g},k}|$, cf. Section 2.6.1. Note further that the exponential term is bounded on a bounded domain so that we can bound the infinity norms in the second and third term by constants c_1 and c_2. This shortens notations and we achieve

$$\|\nabla_x V_\mathrm{m}\|_{L^2(D_\mathrm{M})} \leq N_\mathrm{MF}|D_\mathrm{M}| \max_{j=1,\dots,N_\mathrm{MF}} \|f_j\|_\infty + (c_1 + c_2) \sum_{j=1}^{N_\mathrm{MF}} \|v_{\mathrm{m},j}\|_{L^2(D_{\mathrm{F},j})}.$$

We see that the gradient of V_m is bounded if the muscle fiber membrane potentials $v_{\mathrm{m},j}$ are bounded. To prove the latter, we use a corollary from Grönwall's inequality for linearly bounded ordinary differential equations that yields the boundedness of the solution of an initial value problem $\partial_t y = F(t, y)$ with $y(t_0) = y_0$ if F is continuous and there exist continuous and integrable functions f, f' such that

$$\|F(t, y)\| \leq f(t) + f'(t)\|y\|.$$

We emphasize that f' indicates a function different from f and is not to be confused with the derivative of f that would be denoted by $\partial_t f$. In this context we have $F : (t_0, t_1) \times \mathbb{R} \to \mathbb{R}$ with

$$F(t, v_{\mathrm{m},j}) = \frac{1}{C_{\mathrm{m},j}}(I_\mathrm{stim} - \kappa_{\mathrm{g,Na}}(v_{\mathrm{m},j} - \kappa_{\mathrm{E,Na}}) - \kappa_{\mathrm{g,K}}(v_{\mathrm{m},j} - \kappa_{\mathrm{E,K}}) - c_{\mathrm{g,L}}(v_{\mathrm{m},j} - \kappa_{\mathrm{E,L}})).$$

Hence, the norm of F is bounded by

$$\begin{aligned}\|F(t, v_{\mathrm{m},j})\| =& \left\| \frac{1}{C_{\mathrm{m},j}} (I_{\mathrm{stim}} + \kappa_{\mathrm{g,Na}}\kappa_{\mathrm{E,Na}} + \kappa_{\mathrm{g,K}}\kappa_{\mathrm{E,K}} + c_{\mathrm{g,L}}\kappa_{\mathrm{E,L}} - (\kappa_{\mathrm{g,Na}} + \kappa_{\mathrm{g,K}} + c_{\mathrm{g,L}})v_{\mathrm{m},j}) \right\| \\ \leq & \underbrace{\frac{1}{|C_{\mathrm{m},j}|} (\|I_{\mathrm{stim}}\| + |c_{\mathrm{g,Na}}|\|\kappa_{\mathrm{E,Na}}\| + |c_{\mathrm{g,K}}|\|\kappa_{\mathrm{E,K}}\| + |c_{\mathrm{g,L}}|\|\kappa_{\mathrm{E,L}}\|)}_{=:f(t)} \\ & + \underbrace{\frac{1}{|C_{\mathrm{m},j}|} (|c_{\mathrm{g,Na}}| + |c_{\mathrm{g,K}}| + |c_{\mathrm{g,L}}|)}_{=:f'(t)} \|v_{\mathrm{m},j}\|_{L^2(D_{\mathrm{F},j})}\end{aligned}$$

and we get the boundedness of $v_{\mathrm{m},j}$ and thus of ∇V_{m} from Grönwall's inequality as stated before. □

We conclude that the L^2-norm of the gradient of the membrane potential V_{m} is bounded for the two models considered here. Estimates (4.6) and (4.7) are summarized to read

$$\|\nabla V_{\mathrm{m}}\|_{L^2(D_{\mathrm{M}})} \leq c_V \tag{4.8}$$

for some $c_V > 0$.

With the help of Lemma 4.1.2 we are able to show that the solution ϕ of $a_{\boldsymbol{\sigma}}(\phi, v) = \ell_{\boldsymbol{\sigma}}(v)$ is Lipschitz continuous with respect to the global conductivity $\boldsymbol{\sigma}$. This Lipschitz continuity is a desirable property for two reasons. First, it induces the well-posedness of the forward problem. Second, the Lipschitz continuity will later be helpful to prove error bounds for the discretized probabilistic forward EMG problem and the well-posedness of the Bayesian inverse EMG problem.

Lemma 4.1.4. *Let $\boldsymbol{\sigma} \in (L^\infty(D; \mathbb{R}^{3\times 3}))^3$ be given and $\phi \in V$ denote the unique electric potential that fulfills $a_{\boldsymbol{\sigma}}(\phi, v) = \ell_{\boldsymbol{\sigma}}(v)$ for all $v \in V$. Then the unique solution ϕ is Lipschitz continuous with respect to $\boldsymbol{\sigma}$, i.e., for all $\boldsymbol{\sigma}, \boldsymbol{\sigma}' \in (L^\infty(D; \mathbb{R}^{3\times 3}))^3$ there exists a constant $c_{L,\boldsymbol{\sigma}} > 0$ such that*

$$\|\phi(\boldsymbol{\sigma}) - \phi(\boldsymbol{\sigma}')\|_V \leq c_{L,\boldsymbol{\sigma}} \|\boldsymbol{\sigma} - \boldsymbol{\sigma}'\|_\infty.$$

Proof. The lemma is clear for $\boldsymbol{\sigma} = \boldsymbol{\sigma}'$. Let thus $\boldsymbol{\sigma}, \boldsymbol{\sigma}' \in (L^\infty(D; \mathbb{R}^{3\times 3}))^3$ with $\boldsymbol{\sigma} \neq \boldsymbol{\sigma}'$ be arbitrary but fixed and $\phi \coloneqq \phi(\boldsymbol{\sigma}), \phi' \coloneqq \phi(\boldsymbol{\sigma}')$ be the solutions of the weak

formulation (4.2) for $\boldsymbol{\sigma}$ and $\boldsymbol{\sigma}'$. Hence, ϕ solves

$$\int_{D_\mathrm{M}} \big((\sigma_\mathrm{i}+\sigma_\mathrm{e})\nabla\phi_\mathrm{e}\big)\cdot\nabla v_\mathrm{e} + \int_{D_\mathrm{B}} (\sigma_0\nabla\phi_0)\cdot\nabla v_0 = -\int_{D_\mathrm{M}} (\sigma_\mathrm{i}\nabla V_\mathrm{m})\cdot\nabla v_\mathrm{e} \quad \text{for all } v\in V \tag{4.9}$$

and ϕ' solves

$$\int_{D_\mathrm{M}} \big((\sigma'_\mathrm{i}+\sigma'_\mathrm{e})\nabla\phi'_\mathrm{e}\big)\cdot\nabla v_\mathrm{e} + \int_{D_\mathrm{B}} (\sigma'_0\nabla\phi'_0)\cdot\nabla v_0 = -\int_{D_\mathrm{M}} (\sigma'_\mathrm{i}\nabla V_\mathrm{m})\cdot\nabla v_\mathrm{e} \quad \text{for all } v\in V. \tag{4.10}$$

By subtracting Equation (4.10) from Equation (4.9) and testing the result with $v=\phi-\phi'$ we achieve

$$\begin{aligned}\int_{D_\mathrm{M}} \big((\sigma_\mathrm{i}+\sigma_\mathrm{e})\nabla\phi_\mathrm{e} - (\sigma'_\mathrm{i}+\sigma'_\mathrm{e})\nabla\phi'_\mathrm{e}\big)\cdot(\nabla\phi_\mathrm{e}-\nabla\phi'_\mathrm{e}) + \int_{D_\mathrm{B}} (\sigma_0\nabla\phi_0-\sigma'_0\nabla\phi'_0)\cdot(\nabla\phi_0-\nabla\phi'_0)\\ = -\int_{D_M} \big((\sigma_\mathrm{i}-\sigma'_\mathrm{i})\nabla V_\mathrm{m}\big)\cdot(\nabla\phi_\mathrm{e}-\nabla\phi'_\mathrm{e}).\end{aligned} \tag{4.11}$$

First, we take a closer look at the right-hand side of Equation (4.11) and calculate

$$\begin{aligned}-\int_{D_\mathrm{M}} \big((\sigma_\mathrm{i}-\sigma'_\mathrm{i})\nabla V_\mathrm{m}\big)\cdot(\nabla\phi_\mathrm{e}-\nabla\phi'_\mathrm{e}) &\le \|\sigma_\mathrm{i}-\sigma'_\mathrm{i}\|_\infty \|\nabla V_\mathrm{m}\|_{L^2(D_\mathrm{M})} \|\nabla\phi_\mathrm{e}-\nabla\phi'_\mathrm{e}\|_{L^2(D_\mathrm{M})}\\ &\le \|\sigma_\mathrm{i}-\sigma'_\mathrm{i}\|_\infty \|\nabla V_\mathrm{m}\|_{L^2(D_\mathrm{M})} \|\phi-\phi'\|_V.\end{aligned} \tag{4.12}$$

In a next step, we modify the left-hand side of Equation (4.11) by adding $\pm((\sigma'_\mathrm{i}+\sigma'_\mathrm{e})\nabla\phi_\mathrm{e})\cdot(\nabla\phi_\mathrm{e}-\nabla\phi'_\mathrm{e})$ to the first integral and $\pm(\sigma'_0\nabla\phi_0)\cdot(\nabla\phi_0-\nabla\phi'_0)$ to the second integral to obtain

$$\begin{aligned}&\int_{D_\mathrm{M}} \big((\sigma_\mathrm{i}+\sigma_\mathrm{e})\nabla\phi_\mathrm{e} - (\sigma'_\mathrm{i}+\sigma'_\mathrm{e})\nabla\phi'_\mathrm{e}\big)\cdot(\nabla\phi_\mathrm{e}-\nabla\phi'_\mathrm{e})\\ &\quad + \int_{D_\mathrm{B}} (\sigma_0\nabla\phi_0-\sigma'_0\nabla\phi'_0)\cdot(\nabla\phi_0-\nabla\phi'_0)\\ =\ &\int_{D_\mathrm{M}} \Big(\big((\sigma_\mathrm{i}+\sigma_\mathrm{e})-(\sigma'_\mathrm{i}+\sigma'_\mathrm{e})\big)\nabla\phi_\mathrm{e}\Big)\cdot(\nabla\phi_\mathrm{e}-\nabla\phi'_\mathrm{e})\\ &\quad + \int_{D_\mathrm{M}} \big((\sigma'_\mathrm{i}+\sigma'_\mathrm{e}))(\nabla\phi_\mathrm{e}-\nabla\phi'_\mathrm{e})\big)\cdot(\nabla\phi_\mathrm{e}-\nabla\phi'_\mathrm{e})\\ &\quad + \int_{D_\mathrm{B}} \big((\sigma_0-\sigma'_0)\nabla\phi_0\big)\cdot(\nabla\phi_0-\nabla\phi'_0)\end{aligned}$$

$$
\begin{aligned}
&+ \int_{D_\mathrm{B}} \big(\sigma_0'(\nabla\phi_0 - \nabla\phi_0')\big) \cdot (\nabla\phi_0 - \nabla\phi_0') \\
\geq\ & \int_{D_\mathrm{M}} \Big(\big((\sigma_\mathrm{i} + \sigma_\mathrm{e}) - (\sigma_\mathrm{i}' + \sigma_\mathrm{e}')\big)\nabla\phi_\mathrm{e}\Big) \cdot (\nabla\phi_\mathrm{e} - \nabla\phi_\mathrm{e}') \\
&+ \int_{D_\mathrm{B}} \big((\sigma_0 - \sigma_0')\nabla\phi_0\big) \cdot (\nabla\phi_0 - \nabla\phi_0') \\
&+ \sigma_{\min}'\big(\|\nabla\phi_\mathrm{e} - \nabla\phi_\mathrm{e}'\|^2_{L^2(D_\mathrm{M})} + \|\nabla\phi_0 - \nabla\phi_0'\|^2_{L^2(D_\mathrm{B})}\big) \\
\overset{(4.1)}{\geq}\ & \int_{D_\mathrm{M}} \Big(\big((\sigma_\mathrm{i} + \sigma_\mathrm{e}) - (\sigma_\mathrm{i}' + \sigma_\mathrm{e}')\big)\nabla\phi_\mathrm{e}\Big) \cdot (\nabla\phi_\mathrm{e} - \nabla\phi_\mathrm{e}') \\
&+ \int_{D_\mathrm{B}} \big((\sigma_0 - \sigma_0')\nabla\phi_0\big) \cdot (\nabla\phi_0 - \nabla\phi_0') \\
&+ \frac{1}{2}\sigma_{\min}'\|\phi - \phi'\|_V^2. \qquad (4.13)
\end{aligned}
$$

Here, the global minimal conductivity $\sigma_{\min}'$ is defined as in Lemma 4.1.2. Combining Equations (4.12) and (4.13) yields the estimate

$$
\begin{aligned}
\frac{1}{2}\sigma_{\min}'\|\phi - \phi'\|_V^2 \leq\ & \|\sigma_\mathrm{i} - \sigma_\mathrm{i}'\|_\infty \|\nabla V_\mathrm{m}\|_{L^2(D_\mathrm{M})}\|\phi - \phi'\|_V \\
&- \int_{D_\mathrm{M}} \Big(\big((\sigma_\mathrm{i} + \sigma_\mathrm{e}) - (\sigma_\mathrm{i}' + \sigma_\mathrm{e}')\big)\nabla\phi_\mathrm{e}\Big) \cdot (\nabla\phi_\mathrm{e} - \nabla\phi_\mathrm{e}') \\
&- \int_{D_\mathrm{B}} \big((\sigma_0 - \sigma_0')\nabla\phi_0\big) \cdot (\nabla\phi_0 - \nabla\phi_0').
\end{aligned}
$$

We continue using Hölder's inequality and the boundedness (4.3) of the solution ϕ:

$$
\begin{aligned}
\frac{1}{2}\sigma_{\min}^2\|\phi - \phi'\|_V^2 \overset{\mathrm{HI}}{\leq}\ & \|\sigma_\mathrm{i} - \sigma_\mathrm{i}'\|_\infty \|\nabla V_\mathrm{m}\|_{L^2(D_\mathrm{M})}\|\phi - \phi'\|_V \\
&+ \|(\sigma_\mathrm{i} + \sigma_\mathrm{e}) - (\sigma_\mathrm{i}' + \sigma_\mathrm{e}')\|_\infty \|\phi\|_V \|\phi - \phi'\|_V \\
&+ \|\sigma_0 - \sigma_0'\|_\infty \|\phi\|_V \|\phi - \phi'\|_V \\
\overset{(4.3)}{\leq}\ & \|\sigma_\mathrm{i} - \sigma_\mathrm{i}'\|_\infty \|\nabla V_\mathrm{m}\|_{L^2(D_\mathrm{M})}\|\phi - \phi'\|_V \\
&+ \|(\sigma_\mathrm{i} + \sigma_\mathrm{e}) - (\sigma_\mathrm{i}' + \sigma_\mathrm{e}')\|_\infty 2\frac{\|\sigma_\mathrm{i}\|_\infty}{\sigma_{\min}} \|\nabla V_\mathrm{m}\|_{L^2(D_\mathrm{M})}\|\phi - \phi'\|_V \\
&+ \|\sigma_0 - \sigma_0'\|_\infty 2\frac{\|\sigma_\mathrm{i}\|_\infty}{\sigma_{\min}} \|\nabla V_\mathrm{m}\|_{L^2(D_\mathrm{M})}\|\phi - \phi'\|_V
\end{aligned}
$$

By canceling out $\|\phi - \phi'\|_V$ and using the triangle inequality (TI) and the boundedness

of $\|\nabla V_\mathrm{m}\|_{L^2(D_\mathrm{M})}$ we see

$$\begin{aligned}\frac{1}{2}\sigma'_{\min}\|\phi-\phi'\|_V &\overset{\mathrm{TI}}{\leq} \|\sigma_\mathrm{i}-\sigma'_\mathrm{i}\|_\infty\|\nabla V_\mathrm{m}\|_{L^2(D_\mathrm{M})}\\ &\quad+2\frac{\|\sigma_\mathrm{i}\|_\infty}{\sigma_{\min}}\big(\|\sigma_\mathrm{i}-\sigma'_\mathrm{i}\|_\infty+\|\sigma_\mathrm{e}-\sigma'_\mathrm{e}\|_\infty\big)\|\nabla V_\mathrm{m}\|_{L^2(D_\mathrm{M})}\\ &\quad+2\frac{\|\sigma_\mathrm{i}\|_\infty}{\sigma_{\min}}\|\sigma_0-\sigma'_0\|_\infty\|\nabla V_\mathrm{m}\|_{L^2(D_\mathrm{M})}\\ &\overset{(4.8)}{\leq}\Big(1+6\frac{\|\sigma_\mathrm{i}\|_\infty}{\sigma_{\min}}\Big)c_\mathrm{V}\|\boldsymbol{\sigma}-\boldsymbol{\sigma}'\|_\infty.\end{aligned}$$

Hence, $\|\phi-\phi'\|_V \leq c_{\mathrm{L},\boldsymbol{\sigma}}\|\boldsymbol{\sigma}-\boldsymbol{\sigma}'\|_\infty$ with $c_{\mathrm{L},\boldsymbol{\sigma}} \coloneqq \frac{2}{\sigma'_{\min}}\Big(1+6\frac{\|\sigma_\mathrm{i}\|_\infty}{\sigma_{\min}}\Big)c_\mathrm{V}$. □

The Lipschitz continuity of the forward operator $\mathcal{G}$ with respect to $\boldsymbol{\sigma}$ easily follows from the above lemma as shown in the following corollary.

Corollary 4.1.5. *For each given global conductivity $\boldsymbol{\sigma} \in (L^\infty(D;\mathbb{R}^{3\times3}))^3$ the forward operator $\mathcal{G} : (L^\infty(D;\mathbb{R}^{3\times3}))^3 \to \mathbb{R}^{N_M}$ is Lipschitz continuous with respect to $\boldsymbol{\sigma}$, i.e., for all $\boldsymbol{\sigma},\boldsymbol{\sigma}' \in (L^\infty(D;\mathbb{R}^{3\times3}))^3$ there exists a constant $c'_{L,\boldsymbol{\sigma}} > 0$ such that*

$$\|\mathcal{G}(\boldsymbol{\sigma})-\mathcal{G}(\boldsymbol{\sigma}')\|_{\mathbb{R}^{N_M}} \leq c'_{L,\boldsymbol{\sigma}}\|\boldsymbol{\sigma}-\boldsymbol{\sigma}'\|_\infty.$$

Proof. The Lipschitz continuity is clear for $\boldsymbol{\sigma}=\boldsymbol{\sigma}'$. For $\boldsymbol{\sigma}\neq\boldsymbol{\sigma}' \in (L^\infty(D;\mathbb{R}^{3\times3}))^3$ we use the definition of the evaluation operator (2.25) and estimate

$$\begin{aligned}\|\mathcal{G}(\boldsymbol{\sigma})-\mathcal{G}(\boldsymbol{\sigma}')\|^2_{\mathbb{R}^{N_\mathrm{M}}} &= \left\|\frac{1}{\pi r_\mathrm{el}^2}\left(\int_{B_{r_\mathrm{el}}(x_{\mathrm{m},j})\cap\partial D}\phi(x,\boldsymbol{\sigma})-\phi(x,\boldsymbol{\sigma}')\mathrm{d}x\right)_{j=1}^{N_\mathrm{M}}\right\|^2_{\mathbb{R}^{N_\mathrm{M}}}\\ &= \sum_{j=1}^{N_\mathrm{M}}\left(\frac{1}{\pi r_\mathrm{el}^2}\right)^2\left|\int_{B_{r_\mathrm{el}}(x_{\mathrm{m},j})\cap\partial D}\phi(x,\boldsymbol{\sigma})-\phi(x,\boldsymbol{\sigma}')\mathrm{d}x\right|^2\\ &\overset{\mathrm{HI}}{\leq} N_\mathrm{M}\left(\frac{1}{\pi r_\mathrm{el}^2}\right)^2|D|^2\|\phi(\boldsymbol{\sigma})-\phi(\boldsymbol{\sigma}')\|^2_{L^2(\partial D)}\\ &\leq N_\mathrm{M}\left(\frac{1}{\pi r_\mathrm{el}^2}\right)^2|D|^2\|\phi(\boldsymbol{\sigma})-\phi(\boldsymbol{\sigma}')\|^2_{L^2(D)}\\ &\leq N_\mathrm{M}\left(\frac{1}{\pi r_\mathrm{el}^2}\right)^2|D|^2\|\phi(\boldsymbol{\sigma})-\phi(\boldsymbol{\sigma}')\|^2_{V}.\end{aligned}$$

Taking the square root, applying Lemma 4.1.4 and defining $c'_{\mathrm{L},\boldsymbol{\sigma}} \coloneqq \frac{\sqrt{N_\mathrm{M}}}{\pi r_\mathrm{el}^2}|D|c_{\mathrm{L},\boldsymbol{\sigma}}$, we see the desired Lipschitz continuity. □

Similar considerations prove the boundedness of the forward operator $\mathcal{G}$:

Corollary 4.1.6. *The forward operator* $\mathcal{G} : (L^\infty(D;\mathbb{R}^{3\times3}))^3 \to \mathbb{R}^{N_M}$ *is bounded, i.e., there exists a constant* $0 < c_b < \infty$ *such that*

$$\|\mathcal{G}\| = \sup_{\boldsymbol{\sigma}\in(L^\infty(D;\mathbb{R}^{3\times3}))^3\setminus\mathbf{0}} \frac{\|\mathcal{G}(\boldsymbol{\sigma})\|_{\mathbb{R}^{N_M}}}{\|\boldsymbol{\sigma}\|_\infty} \leq c_b < \infty.$$

Proof. Since the global conductivity is bounded from below and above, it is sufficient to show the boundedness of $\|\mathcal{G}(\boldsymbol{\sigma})\|_{\mathbb{R}^{N_\mathrm{M}}}$. Following the procedure of the proof of Corollary 4.1.5 we achieve

$$\begin{aligned}
\|\mathcal{G}(\boldsymbol{\sigma})\|_{\mathbb{R}^{N_\mathrm{M}}} &\leq \frac{\sqrt{N_\mathrm{M}}}{\pi r_\mathrm{el}^2}|D|\|\phi\|_V \\
&\overset{(4.3)}{\leq} 2\frac{\sqrt{N_\mathrm{M}}|D|\|\sigma_\mathrm{i}\|_\infty}{\pi r_\mathrm{el}^2\sigma_\mathrm{min}}\|\nabla V_\mathrm{m}\|_{L^2(D_\mathrm{M})} \\
&\overset{(4.8)}{\leq} 2\frac{\sqrt{N_\mathrm{M}}|D|\|\sigma_\mathrm{i}\|_\infty}{\pi r_\mathrm{el}^2\sigma_\mathrm{min}}c_V < \infty.
\end{aligned}$$

□

4.2. Probabilistic Forward EMG Problem

Adding a stochastic model of the inevitable measurement error to the forward EMG problem is the basic idea of the Bayesian approach to inverse problems and leads to the probabilistic forward EMG problem, cf. Section 2.4. We model the measurement error and define the probabilistic forward EMG problem in Section 4.2.1. In Section 4.2.2, we prove the well-posedness of the probabilistic forward EMG problem.

4.2.1. Modeling the Measurement Error and Problem Formulation

As stated in Section 2.4, the measurement error is not known deterministically. Thus, we model the measurement error as a stochastic quantity $\eta : \Omega \to \mathbb{R}^{N_\mathrm{M}}$ for a complete probability space $(\Omega, \mathcal{A}, \mu)$, see Section 2.2.1 for the definition of a complete probability space.

We assume that the measurement error is additive and normally distributed with zero mean and covariance matrix $\Xi = \mathrm{diag}(\xi, \ldots, \xi) \in \mathbb{R}^{N_\mathrm{M}\times N_\mathrm{M}}$, and write $\eta \sim N(0, \Xi)$. For justification of the assumption that the measurement error is normally distributed, we briefly summarize the argument in [100, Section 10.5]: First, the measurement error is assumed to be caused by $N_\mathrm{err} \in \mathbb{N}$ independent sources, e.g., by effects of parallax or

reaction time. Further, each source is assumed to shift the measurements by the same quantity $\varepsilon_{\text{err}} > 0$, where a shift of $-\varepsilon_{\text{err}}$ is equally likely as a shift of $+\varepsilon_{\text{err}}$. Adding up the error sources yields a binomial distribution that is known to tend to a normal distribution in the limiting case $N_{\text{err}} \to \infty$.

Adding the normally distributed measurement error η to the forward operator as in Definition 4.1.1 yields the model of probabilistic EMG data

$$\phi_{\mathbb{x},\text{p}}(\omega) \coloneqq \phi_{\mathbb{x}} + \eta(\omega) = \mathcal{G}(\boldsymbol{\sigma}) + \eta(\omega) \in \mathbb{R}^{N_{\text{M}}} \tag{4.14}$$

for all $\omega \in \Omega$ and $\phi_{\mathbb{x}}$ denoting the evaluation of the membrane potential at measuring points $\mathbb{x}$ according to (2.25). Note that $\phi_{\mathbb{x},\text{p}} = \phi_{\mathbb{x},\text{p}}(\omega)$ is a random variable.

Solving equation (4.14) for the global conductivity $\boldsymbol{\sigma}$, as it is the case in the inverse problem setting, shows that also $\boldsymbol{\sigma}$ is a random variable.

In Section 2.2, we constructed random functions that are in L^∞ almost surely through series expansions with random coefficients. We follow this approach and write the random conductivities $\sigma_{\text{i}}, \sigma_{\text{e}}$ and σ_0 as series expansions

$$\sigma_j(x,\omega) = m_j(x) + \sum_{k=1}^{\infty} \gamma_{j,k} T_{j,k}(\omega) \varphi_k(x) \tag{4.15}$$

for the index $j \in \{\text{i},\text{e},0\}$. Further, we choose the functions $m_j, \varphi_k \in L^\infty(D;\mathbb{R}^{3\times 3})$ with $\|\varphi_k\|_{L^\infty} = 1$ for all $k = 1,\dots,\infty$, the coefficients $\gamma_j \coloneqq \{\gamma_{j,k}\}_{k=1}^{\infty} \in \ell^1$ and the random sequences $T_j \coloneqq \{T_{j,k}\}_{k=1}^{\infty}$ to be i.i.d. with $T_{j,1} \sim U([-1,1])$. Furthermore, we pose the following assumption.

Assumption 4.2.1. *For $j \in \{i,e,0\}$ there exist constants $\delta_j > 0$ and $m_{min,j} > 0$ satisfying $0 < m_{min,j} \leq \operatorname{ess\,inf}_{x\in D} m_j(x)$ such that*

$$\|\gamma_j\|_{\ell^1} = \frac{\delta_j}{1+\delta_j} m_{min,j}.$$

Note that Assumption 4.2.1 ensures the convergence of the series defined in (4.15) and the boundedness of σ_j for $j \in \{\text{i},\text{e},0\}$.

As in Section 2.2, the closure $\mathcal{J}_j$ of the linear span of the functions m_j, φ_k for $k = 1,\dots,\infty$ with respect to the norm $\|\cdot\|_\infty$ on $L^\infty(D;\mathbb{R}^{3\times 3})$ is a separable Banach space for $j \in \{\text{i},\text{e},0\}$ and $\sigma_j \in L^\infty(D;\mathbb{R}^{3\times 3})$ $\rho_{0,j}$-almost surely. Here, $\rho_{0,j}$ is the probability measure as constructed in Section 2.2 using the Kolmogorov extension theorem 2.2.4 and $(\mathcal{J}_j, \mathcal{B}(\mathcal{J}_j), \rho_{0,j})$ is a probability space. We define the global parameter space $\boldsymbol{\mathcal{J}}_{\boldsymbol{\sigma}} \coloneqq$

$\mathcal{J}_\mathrm{i} \times \mathcal{J}_\mathrm{e} \times \mathcal{J}_0$, the product Borel σ-algebra $\mathcal{B}_{\boldsymbol{\sigma}} \coloneqq \mathcal{B}(\mathcal{J}_\mathrm{i}) \otimes \mathcal{B}(\mathcal{J}_\mathrm{e}) \otimes \mathcal{B}(\mathcal{J}_0)$ of the Borel σ-algebras $\mathcal{B}(\mathcal{J}_\mathrm{i})$ of $\mathcal{J}_\mathrm{i}$ for $j \in \{\mathrm{i}, \mathrm{e}, 0\}$, and the product measure $\boldsymbol{\rho}_0 \coloneqq \rho_{0,\mathrm{i}} \otimes \rho_{0,\mathrm{e}} \otimes \rho_{0,0}$ such that $\boldsymbol{\sigma} \in \boldsymbol{\mathcal{J}}_{\boldsymbol{\sigma}}$ and $(\boldsymbol{\mathcal{J}}_{\boldsymbol{\sigma}}, \mathcal{B}_{\boldsymbol{\sigma}}, \boldsymbol{\rho}_0)$ is a probability space.

Note that the treatment of the randomness simplifies significantly when the conductivities are constant, see our previously published results in [88].

In the following, we collect the random sequences T_j in the sequence $\boldsymbol{T} \coloneqq (T_\mathrm{i}, T_\mathrm{e}, T_0)$ and define the product spaces $\mathcal{J} \coloneqq \bigtimes_{k=1}^{\infty}[-1, 1]$ and $\boldsymbol{\mathcal{J}}_{\boldsymbol{T}} \coloneqq \mathcal{J} \times \mathcal{J} \times \mathcal{J}$ such that $T_j \in \mathcal{J}$ for $j \in \{\mathrm{i}, \mathrm{e}, 0\}$ and $\boldsymbol{T} \in \boldsymbol{\mathcal{J}}_{\boldsymbol{T}}$.

We emphasize that through the relation

$$\mathcal{G}(\boldsymbol{\sigma}(\omega)) = \mathcal{G}\Big(\big(m_j(x) + \sum_{k=1}^{\infty} \gamma_{j,k} T_{j,k}(\omega)\varphi_k(x)\big)_{j\in\{\mathrm{i},\mathrm{e},0\}}\Big) = \mathcal{G}(\boldsymbol{T}(\omega))$$

the forward operator can be interpreted to either map random global conductivities $\boldsymbol{\sigma}$ or the random coefficients $\boldsymbol{T}$ to computed surface EMG data $\phi_{\mathbb{x}}$. We thus use the general notion of parameters $\boldsymbol{p} \in \boldsymbol{\mathcal{J}}_{\boldsymbol{p}}$ from now on, where $\boldsymbol{p} = \boldsymbol{\sigma}$ or $\boldsymbol{p} = \boldsymbol{T}$. Whenever it is relevant to distinguish between the two cases, we highlight the difference.

Following the above discussion, we redefine the forward operator to map the parameters $\boldsymbol{p}$ to the probabilistic EMG data $\phi_{\mathbb{x}}$, i.e.,

$$\mathcal{G} : \boldsymbol{\mathcal{J}}_{\boldsymbol{p}} \to \mathbb{R}^{N_\mathrm{M}} \quad \text{with} \quad \boldsymbol{p} \mapsto \phi_{\mathbb{x}} \tag{4.16}$$

for $\boldsymbol{p} = \boldsymbol{\sigma}$ or $\boldsymbol{p} = \boldsymbol{T}$. The probabilistic forward problem then reads:

Definition 4.2.2 (Probabilistic Forward EMG Problem). *For given parameters $\boldsymbol{p} \in \boldsymbol{\mathcal{J}}_{\boldsymbol{p}}$ compute the noisy probabilistic surface EMG data*

$$\phi_{\mathbb{x},p} = \mathcal{G}(\boldsymbol{p}) + \eta. \tag{4.17}$$

4.2.2. Well-posedness

The well-posedness of the probabilistic forward EMG problem 4.2.2 includes the existence of a solution $\phi \in V$ fulfilling Equation (4.2) for all parameters $\boldsymbol{p}$ as well as the continuous dependence of $\mathcal{G}$ on the parameters $\boldsymbol{p} \in \boldsymbol{\mathcal{J}}_{\boldsymbol{p}}$.

Lemma 4.2.3. *Let Assumption 4.2.1 hold. For each given global conductivity $\boldsymbol{\sigma} \in \boldsymbol{\mathcal{J}}_{\boldsymbol{\sigma}}$ there exists a unique solution $\phi \in V$ fulfilling $a_{\boldsymbol{\sigma}}(\phi, v) = \ell_{\boldsymbol{\sigma}}(v)$ for all $v \in V$ almost*

surely. Furthermore, there exists a constant $c_{L,\boldsymbol{\sigma}} > 0$ *such that for all* $\boldsymbol{\sigma}, \boldsymbol{\sigma}' \in \boldsymbol{\mathcal{J}}_{\boldsymbol{\sigma}}$

$$\|\phi(\boldsymbol{\sigma}) - \phi(\boldsymbol{\sigma}')\|_V \leq c_{L,\boldsymbol{\sigma}} \|\boldsymbol{\sigma} - \boldsymbol{\sigma}'\|_\infty \quad a.s.$$

Proof. Assumption 4.2.1 implies the existence of positive constants $m_{\min,j}, m_{\max,j} > 0$ with $m_{\min,j} \leq \operatorname{ess\,inf}_{x\in D} m_j(x)$ and $\operatorname{ess\,sup}_{x\in D} m_j(x) \leq m_{\max,j}$ such that

$$0 < \frac{1}{1+\delta_j} m_{\min,j} \leq \sigma_j(x) \leq m_{\max,j} + \frac{\delta_j}{1+\delta_j} m_{\min,j} < \infty$$

holds almost surely for all $x \in D$, see our discussion in Section 2.2.2. Furthermore, σ is strongly measurable as a measurable function on a separable space, as stated in Section 2.2.1. Thus, the existence of a unique solution of $a_{\boldsymbol{\sigma}}(\phi, v) = \ell_{\boldsymbol{\sigma}}(v)$ follows from Lax-Milgram's theorem.

The Lipschitz continuity then follows directly from the Lipschitz continuity of the solution of the deterministic forward EMG problem as proven in Lemma 4.1.4. □

Similar to the deterministic case, the Lipschitz continuity of the forward operator with respect to the global conductivity follows and we have:

Corollary 4.2.4. *Let Assumption 4.2.1 hold. Then the forward operator* $\mathcal{G} : \boldsymbol{\mathcal{J}}_{\boldsymbol{\sigma}} \to \mathbb{R}^{N_M}$ *is Lipschitz continuous with respect to* $\boldsymbol{\sigma}$ *almost surely, i.e., for all* $\boldsymbol{\sigma}, \boldsymbol{\sigma}' \in \boldsymbol{\mathcal{J}}_{\boldsymbol{\sigma}}$ *there exists a constant* $c'_{L,\boldsymbol{\sigma}} > 0$ *such that*

$$\|\mathcal{G}(\boldsymbol{\sigma}) - \mathcal{G}(\boldsymbol{\sigma}')\|_{\mathbb{R}^{N_M}} \leq c'_{L,\boldsymbol{\sigma}} \|\boldsymbol{\sigma} - \boldsymbol{\sigma}'\|_\infty \quad a.s.$$

The Lipschitz continuity of the forward operator can be extended to the random coefficients $\boldsymbol{T}$. Therefore, following the definition of the infinity norm for the global conductivity we define the infinity norm for $\boldsymbol{T} \in \boldsymbol{\mathcal{J}}_T$ by

$$\begin{aligned} \|\boldsymbol{T}\|_\infty &:= \max(\|T_\mathrm{i}\|_\infty, \|T_\mathrm{e}\|_\infty, \|T_0\|_\infty), \\ \|T_j\|_\infty &:= \sup_{m\geq 1} |T_{j,m}|, \quad j \in \{\mathrm{i}, \mathrm{e}, 0\}. \end{aligned}$$

We now deduce the Lipschitz continuity of the forward operator $\mathcal{G}$ with respect to $\boldsymbol{T}$ from Corollaries 4.2.4 and 4.1.5 using the definition of the global conductivity through the series expansions (4.15).

Corollary 4.2.5. *Let Assumption 4.2.1 hold. Then the forward operator* $\mathcal{G} : \boldsymbol{\mathcal{J}}_{\boldsymbol{T}} \to \mathbb{R}^{N_M}$ *is Lipschitz continuous with respect to* $\boldsymbol{T}$ *almost surely, i.e., for all* $\boldsymbol{T}, \boldsymbol{T}' \in \boldsymbol{\mathcal{J}}_{\boldsymbol{T}}$ *there*

exists a constant $c'_{L,\boldsymbol{T}} > 0$ *such that*

$$\|\mathcal{G}(\boldsymbol{T}) - \mathcal{G}(\boldsymbol{T}')\|_{\mathbb{R}^{N_M}} \leq c'_{L,\boldsymbol{T}} \|\boldsymbol{T} - \boldsymbol{T}'\|_\infty \quad a.s.$$

Proof. The result is clear for $\boldsymbol{T} = \boldsymbol{T}' \in \boldsymbol{\mathcal{J}}_{\boldsymbol{T}}$. Let thus $\boldsymbol{T} \neq \boldsymbol{T}' \in \boldsymbol{\mathcal{J}}_{\boldsymbol{T}}$ and define $\boldsymbol{\sigma} \coloneqq \boldsymbol{\sigma}(\boldsymbol{T}), \boldsymbol{\sigma}' \coloneqq \boldsymbol{\sigma}'(\boldsymbol{T}')$ through the series expansions (4.15).

From Corollary 4.2.4, we already have the existence of a constant $c'_{\mathrm{L},\boldsymbol{\sigma}} > 0$ such that

$$\|\mathcal{G}(\boldsymbol{\sigma}) - \mathcal{G}(\boldsymbol{\sigma}')\|_{\mathbb{R}^{N_\mathrm{M}}} \leq c'_{\mathrm{L},\boldsymbol{\sigma}} \|\boldsymbol{\sigma} - \boldsymbol{\sigma}'\|_\infty \quad a.s.$$

Consequently the remaining task is to find a constant $c_{\mathrm{L},\boldsymbol{T}} > 0$ such that

$$\|\boldsymbol{\sigma} - \boldsymbol{\sigma}'\|_\infty \leq c_{\mathrm{L},\boldsymbol{T}} \|\boldsymbol{T} - \boldsymbol{T}'\|_\infty \quad a.s.$$

Subtracting the series expansions of $\boldsymbol{\sigma}'$ from the series expansions of $\boldsymbol{\sigma}$ yields

$$\sigma_j - \sigma'_j = \sum_{m=1}^{\infty} \gamma_{j,m} \big(T_{j,m} - T'_{j,m}\big) \varphi_m(x)$$

for $j \in \{\mathrm{i}, \mathrm{e}, 0\}$. For estimating the infinity norm of the above difference we use that $\|\varphi_m\|_\infty = 1$ for all $m \in \mathbb{N}$ and get

$$\begin{aligned}
\big\|\sigma_j - \sigma'_j\big\|_\infty &= \operatorname*{ess\,sup}_{x \in D} \max_{k,l=1,2,3} \Big| \sum_{m=1}^{\infty} \gamma_{j,m} \big(T_{j,m} - T'_{j,m}\big) \varphi_m(x) \Big|_{kl} \\
&\leq \Big| \sum_{m=1}^{\infty} \gamma_{j,m} \big(T_{j,m} - T'_{j,m}\big) \Big| \\
&\leq \sup_{m \geq 1} |T_{j,m} - T'_{j,m}| \sum_{m=1}^{\infty} |\gamma_{j,m}| \\
&\overset{\text{Assumption}}{\underset{4.2.1}{\leq}} \frac{\delta_j}{1+\delta_j} m_{\min,j} \sup_{m \geq 1} |T_{j,m} - T'_{j,m}| \\
&= \frac{\delta_j}{1+\delta_j} m_{\min,j} \big\|T_{j,m} - T'_{j,m}\big\|_\infty. \qquad (4.18)
\end{aligned}$$

Using the definitions of the infinity norm for $\boldsymbol{\sigma}$ and $\boldsymbol{T}$, we see that

$$\|\boldsymbol{\sigma} - \boldsymbol{\sigma}'\|_\infty \leq c_{\mathrm{L},\boldsymbol{T}} \|\boldsymbol{T} - \boldsymbol{T}'\|_\infty$$

with $c_{\mathrm{L},\boldsymbol{T}} \coloneqq \max_{j \in \{\mathrm{i},\mathrm{e},0\}} \frac{\delta_j}{1+\delta_j} m_{\min,j}$. Setting $c'_{\mathrm{L},\boldsymbol{T}} \coloneqq c_{\mathrm{L},\boldsymbol{\sigma}} c_{\mathrm{L},\boldsymbol{T}}$ we end up with the Lipschitz

continuity of the forward operator $\mathcal{G}$ with respect to $\boldsymbol{T}$:

$$\|\mathcal{G}(\boldsymbol{T}) - \mathcal{G}(\boldsymbol{T}')\|_V \leq c'_{\mathrm{L},\boldsymbol{T}} \|\boldsymbol{T} - \boldsymbol{T}'\|_\infty \qquad \square$$

Summarizing this section, we deduce that the forward operator of the probabilistic forward EMG problem as defined in Definition 4.2.2 is Lipschitz continuous with respect to $\boldsymbol{p}$ for both, $\boldsymbol{p} = \boldsymbol{\sigma}$ and $\boldsymbol{p} = \boldsymbol{T}$.

4.3. Bayesian Inverse EMG Problem

The definition and the proof of the well-posedness of the Bayesian inverse EMG problem of finding the distribution of parameters $\boldsymbol{p}$ given EMG measurement data ϕ_{EMG} uses Bayes' theorem for the function space setting, see Theorem 2.4.1. We follow the four steps of applying Bayes' theorem outlined in [17, Remark 3.5]:

1. Define a suitable prior measure $\boldsymbol{\rho}_0$ and noise measure ρ_{noise} whose independent product forms the reference measure ν_0 with $\nu_0(\mathrm{d}\boldsymbol{p}, \mathrm{d}\phi_{\mathrm{EMG}}) = \boldsymbol{\rho}_0(\mathrm{d}\boldsymbol{p}) \otimes \rho_{\mathrm{noise}}(\mathrm{d}\phi_{\mathrm{EMG}})$ as in (2.4).

2. Determine the potential Φ such that $\frac{\mathrm{d}L(\boldsymbol{p},\cdot)}{\mathrm{d}\rho_{\mathrm{noise}}}(\phi_{\mathrm{EMG}}) = \exp(-\Phi(\boldsymbol{p}; \phi_{\mathrm{EMG}}))$ as in (2.3).

3. Show that the potential Φ is ν_0-measurable.

4. Show that the scaling factor $Z = \int_{\boldsymbol{\mathcal{J}}} \exp\big(-\Phi(\boldsymbol{p}; \phi_{\mathrm{EMG}})\big) \boldsymbol{\rho}_0(\mathrm{d}\boldsymbol{p}) > 0$ almost surely with respect to ϕ_{EMG}, see (2.6).

In Section 4.3.1 we discuss the first two steps, defining the Bayesian inverse EMG problem. Afterwards, we address the last two steps, which yield the well-posedness of the Bayesian inverse EMG problem in Section 4.3.2.

4.3.1. Problem Formulation

Before defining a suitable prior, noise measure, or potential as mentioned above, we define the parameters to be inferred and the spaces they live in. Remember that we formulated the probabilistic froward EMG problem for both $\boldsymbol{p} = \boldsymbol{\sigma}$ and $\boldsymbol{p} = \boldsymbol{T}$ in Section 4.2.2. Hence, the inverse EMG problem can either be formulated as searching for $\boldsymbol{\sigma} \in \boldsymbol{\mathcal{J}}_{\boldsymbol{\sigma}}$ such that $\mathcal{G}(\boldsymbol{\sigma}) + \eta = \phi_{\mathrm{EMG}}$ or as searching for $\boldsymbol{T} \in \boldsymbol{\mathcal{J}}_T$ such that $\mathcal{G}(\boldsymbol{T}) + \eta = \phi_{\mathrm{EMG}}$.

In the forward setting, the properties of the latter formulation followed from those of the former and the same will hold for the inverse setting, as we will see in Section 4.3.2. We have constructed the probability space $(\boldsymbol{\mathcal{J}}_{\boldsymbol{\sigma}}, \mathcal{B}_{\boldsymbol{\sigma}}, \boldsymbol{\rho}_0)$ for the case $\boldsymbol{p} = \boldsymbol{\sigma}$ in Section 4.2.1.

In case $\boldsymbol{p} = \boldsymbol{T}$ we equip $\mathcal{J} = \bigtimes_{k=1}^{\infty}[-1,1]$ with the product σ-algebra $\mathcal{B}(\mathcal{J}) \coloneqq \bigotimes_{k=1}^{\infty}\mathcal{B}([-1,1])$, where $\mathcal{B}([-1,1])$ is the Borel σ-algebra on $[-1,1]$. Subsequently, the product probability measure

$$\rho_{0,T} \coloneqq \bigotimes_{k=1}^{\infty} \mathrm{d}\mu_k$$

is defined on the measurable space $(\mathcal{J}, \mathcal{B}(\mathcal{J}))$ with $\mathrm{d}\mu_k$ being the normalized Lebesgue measure on $[-1,1]$ as in [50, 92]. Note that $\rho_{0,T}$ is the probability law of the random variables $T_j = \left(T_{j,k}\right)_{k=1}^{\infty}$ since the $T_{j,k}(\omega)$ are assumed to be independent and uniformly distributed on $[-1,1]$.

Moreover, we equip $\boldsymbol{\mathcal{J}}_T \coloneqq \mathcal{J} \times \mathcal{J} \times \mathcal{J}$ with the product σ-algebra $\mathcal{B}_{\boldsymbol{T}} \coloneqq \mathcal{B}(\mathcal{J}) \otimes \mathcal{B}(\mathcal{J}) \otimes \mathcal{B}(\mathcal{J})$ and finally define the prior $\boldsymbol{\rho}_0 \coloneqq \rho_{0,T} \otimes \rho_{0,T} \otimes \rho_{0,T}$ that describes the behavior of $\boldsymbol{T}$ prior to having any knowledge from measurements. As in the case $\boldsymbol{p} = \boldsymbol{\sigma}$, the measure space $(\boldsymbol{\mathcal{J}}_{\boldsymbol{T}}, \mathcal{B}_{\boldsymbol{T}}, \boldsymbol{\rho}_0)$ is a probability space and we write $(\boldsymbol{\mathcal{J}}_{\boldsymbol{p}}, \mathcal{B}_{\boldsymbol{p}}, \boldsymbol{\rho}_0)$ whenever both choices of parameters are valid.

The definition of the prior $\boldsymbol{\rho}_0$ enables us to formulate the *Bayesian inverse EMG problem*.

Definition 4.3.1 (Bayesian Inverse EMG Problem). *For a given prior measure $\boldsymbol{\rho}_0$ and measurements $\phi_{EMG} \in \mathbb{R}^{N_M}$ find the posterior measure $\boldsymbol{\rho}_{\phi_{EMG}}$ of parameters $\boldsymbol{p}$ given EMG measurements ϕ_{EMG}.*

Finishing step one on our way to applying Bayes' theorem to solve the Bayesian inverse EMG problem 4.3.1, we recall that we modeled the measurement error η to be normally distributed with zero mean and covariance Ξ in Section 4.2.1. Hence, ρ_{noise} is the measure with distribution $N(0,\Xi)$ and we have

$$\nu_0(\mathrm{d}\boldsymbol{p}, \mathrm{d}\phi_{\text{EMG}}) = \boldsymbol{\rho}_0(\mathrm{d}\boldsymbol{p}) \otimes \rho_{\text{noise}}(\mathrm{d}\phi_{\text{EMG}}) \tag{4.19}$$

for the reference measure ν_0. According to [17, Section 3.4.2], the use of other statistical assumptions on η is a straightforward extension of the theory whenever η has a smooth density on $\mathbb{R}^{N_{\text{M}}}$.

The potential Φ is defined via the likelihood $L(\boldsymbol{p}, \phi_{\text{EMG}})$ of EMG measurements ϕ_{EMG} given the unknown parameters $\boldsymbol{p}$ for $\boldsymbol{p} = \boldsymbol{\sigma}$ or $\boldsymbol{p} = \boldsymbol{T}$. Since $\phi_{\text{EMG}} = \mathcal{G}(\boldsymbol{p}) + \eta$ with $\eta \sim N(0, \Xi)$, we deduce that

$$\phi_{\text{EMG}} | \boldsymbol{p} \sim N(\mathcal{G}(\boldsymbol{p}), \Xi)$$

and thus $L(\boldsymbol{p}, \cdot)$ is the measure with distribution $N(\mathcal{G}(\boldsymbol{p}), \Xi)$. We compute the product measure

$$\nu_{\boldsymbol{p}}(\mathrm{d}\boldsymbol{p}, \mathrm{d}\phi_{\text{EMG}}) = \boldsymbol{\rho}_0(\mathrm{d}\boldsymbol{p}) \otimes L(\boldsymbol{p}, \mathrm{d}\phi_{\text{EMG}}) \tag{4.20}$$

as defined in Equation (2.5). Inserting the above findings into Equation (2.3), it easily follows that the potential $\Phi : \boldsymbol{\mathcal{J}}_{\boldsymbol{p}} \times \mathbb{R}^{N_{\text{M}}} \to \mathbb{R}$ defined by

$$\Phi(\boldsymbol{p}, \phi_{\text{EMG}}) \coloneqq \frac{1}{2} \|\phi_{\text{EMG}} - \mathcal{G}(\boldsymbol{p})\|_{\Xi}^2 - \frac{1}{2} \|\phi_{\text{EMG}}\|_{\Xi}^2 \tag{4.21}$$

satisfies

$$\frac{\mathrm{d}L(\boldsymbol{p}, \cdot)}{\mathrm{d}\rho_{\text{noise}}}(\phi_{\text{EMG}}) = \exp(-\Phi(\boldsymbol{p}, \phi_{\text{EMG}}))$$

as required in condition (2.3). Here the Ξ-norm is defined as $\|y\|_{\Xi} \coloneqq \left\|\Xi^{-1/2} y\right\|_{\mathbb{R}^{N_{\text{M}}}}$.

Given the potential Φ, we define the scaling factor Z according to (2.6) as

$$Z \coloneqq \int_{\boldsymbol{\mathcal{J}}_{\boldsymbol{p}}} \exp\big(-\Phi(\boldsymbol{p}, \phi_{\text{EMG}})\big) \boldsymbol{\rho}_0(\mathrm{d}\boldsymbol{p}).$$

This completes the setup for applying Bayes' theorem to solve the Bayesian inverse EMG problem 4.3.1.

4.3.2. Well-posedness

Recall that $(\boldsymbol{\mathcal{J}}_{\boldsymbol{p}}, \mathcal{B}_{\boldsymbol{p}}, \boldsymbol{\rho}_0)$ is a probability space and thus a measurable space for both $\boldsymbol{p} = \boldsymbol{\sigma}$ and $\boldsymbol{p} = \boldsymbol{T}$. Hence, we are allowed to apply Bayes' theorem for measurable spaces, as indicated in a remark following Theorem 2.4.1, to prove the existence of a solution of the Bayesian inverse EMG problem 4.3.1.

The remaining steps are the proof of the measurability of the potential Φ, as defined in (4.21), with respect to the reference measure ν_0 and the positivity of the scaling factor Z. The next theorem summarizes both.

Theorem 4.3.2. *Let Assumption 4.2.1 hold and* $\Phi : \boldsymbol{\mathcal{J}}_{\boldsymbol{p}} \times \mathbb{R}^{N_M} \to \mathbb{R}$ *be as in* (4.21). *Then for* $\boldsymbol{p} = \boldsymbol{\sigma}$ *or* $\boldsymbol{p} = \boldsymbol{T}$

1. *the scaling factor* Z *is positive, i.e.,*

$$Z = \int_{\boldsymbol{\mathcal{J}}_{\boldsymbol{p}}} \exp\big(-\Phi(\boldsymbol{p}, \phi_{EMG})\big)\boldsymbol{\rho}_0(\mathrm{d}\boldsymbol{p}) > 0 \qquad \rho_{noise}\text{-a.s.},$$

2. *the potential* $\Phi : \boldsymbol{\mathcal{J}}_{\boldsymbol{p}} \times \mathbb{R}^{N_M} \to \mathbb{R}$ *as defined in* (4.21) *is* ν_0*-measurable, and*

3. *the conditional distribution* $\boldsymbol{\rho}_{\phi_{EMG}}$ *exists with* $\boldsymbol{\rho}_{\phi_{EMG}} \ll \boldsymbol{\rho}_0$*, and for* $\phi_{EMG} \in \mathbb{R}^{N_M}$

$$\frac{\mathrm{d}\boldsymbol{\rho}_{\phi_{EMG}}}{\mathrm{d}\boldsymbol{\rho}_0}(\boldsymbol{p}) = \frac{1}{Z}\exp\big(-\Phi(\boldsymbol{p}, \phi_{EMG})\big) \quad \nu_{\boldsymbol{p}}\text{-a.s.}$$

Here, ν_0 *and* $\nu_{\boldsymbol{p}}$ *are the product measures defined in Equations* (4.19) *and* (4.20).

Proof. Recapitulating Section 2.2 we find that part 1 and 2 of Theorem 4.3.2 are the required assumptions of Theorem 2.4.1. From Theorem 2.4.1, part 3 follows directly once part 1 and 2 are proven.

1. From the properties of the exponential function, it follows that the scaling factor $Z = \int_{\boldsymbol{\mathcal{J}}_{\boldsymbol{p}}} \exp\big(-\Phi(\boldsymbol{p}, \phi_{\mathrm{EMG}})\big)\boldsymbol{\rho}_0(\mathrm{d}\boldsymbol{p})$ is strictly positive as long as the potential Φ is bounded. Applying the triangle inequality, this corresponds to the forward operator being bounded, which we have proved in Corollary 4.1.6.

2. We split the proof of the ν_0-measurability of the potential Φ into two parts. More precisely, we need to show that a) Φ is $\boldsymbol{\rho}_{\phi_{\mathrm{EMG}}}$-measurable in $\boldsymbol{p}$ and b) ρ_{noise}-measurable in ϕ_{EMG}. These measurabilities follow from the Lipschitz continuity of the corresponding mappings and we thus aim at proving that Φ is Lipschitz continuous with respect to $\boldsymbol{p}$ and Lipschitz continuous with respect to ϕ_{EMG}. We note that the Lipschitz continuity of Φ follows from the corresponding Lipschitz continuity of the forward map $\mathcal{G}$ that we have proved in Sections 4.1.2 and 4.2.2. In this way, we deduce properties of the inverse problem from properties of the forward problem, subsequently justifying the work spent to prove the well-posedness of the forward EMG problem.

   a) Let $\boldsymbol{p}, \boldsymbol{p}' \in \boldsymbol{\mathcal{J}}_{\boldsymbol{p}}$. The Lipschitz continuity is clear for $\boldsymbol{p} = \boldsymbol{p}'$. For $\boldsymbol{p} \neq \boldsymbol{p}'$ and

the scalar product $\langle\cdot,\cdot\rangle_\Xi \coloneqq \langle \Xi^{-\frac{1}{2}}\cdot, \Xi^{-\frac{1}{2}}\cdot\rangle$ we calculate

$$\begin{aligned}
|\Phi(\boldsymbol{p}) - \Phi(\boldsymbol{p}')| = \;& \frac{1}{2}\left| \|\phi_{\mathrm{EMG}} - \mathcal{G}(\boldsymbol{p})\|_\Xi^2 - \|\phi_{\mathrm{EMG}} - \mathcal{G}(\boldsymbol{p}')\|_\Xi^2 \right| \\
= \;& \frac{1}{2}\left| \langle \mathcal{G}(\boldsymbol{p}), \mathcal{G}(\boldsymbol{p})\rangle_\Xi - \langle \mathcal{G}(\boldsymbol{p}'), \mathcal{G}(\boldsymbol{p}')\rangle_\Xi + 2\langle \phi_{\mathrm{EMG}}, \mathcal{G}(\boldsymbol{p}') - \mathcal{G}(\boldsymbol{p})\rangle_\Xi \right| \\
\overset{\mathrm{TI}}{\leq} \;& \frac{1}{2}\left(|\langle \mathcal{G}(\boldsymbol{p}), \mathcal{G}(\boldsymbol{p}) - \mathcal{G}(\boldsymbol{p}')\rangle_\Xi| + |\langle \mathcal{G}(\boldsymbol{p}) - \mathcal{G}(\boldsymbol{p}'), \mathcal{G}(\boldsymbol{p}')\rangle_\Xi| \right) \\
& + |\langle \phi_{\mathrm{EMG}}, \mathcal{G}(\boldsymbol{p}') - \mathcal{G}(\boldsymbol{p})\rangle_\Xi| \\
\overset{\mathrm{HI}}{\leq} \;& \frac{1}{2}\left(\|\mathcal{G}(\boldsymbol{p})\|_\Xi \|\mathcal{G}(\boldsymbol{p}) - \mathcal{G}(\boldsymbol{p}')\|_\Xi + \|\mathcal{G}(\boldsymbol{p}) - \mathcal{G}(\boldsymbol{p}')\|_\Xi \|\mathcal{G}(\boldsymbol{p}')\|_\Xi \right) \\
& + \|\phi_{\mathrm{EMG}}\|_\Xi \|\mathcal{G}(\boldsymbol{p}') - \mathcal{G}(\boldsymbol{p})\|_\Xi \\
\underset{4.1.6}{\overset{\mathrm{Corrolary}}{\leq}} \;& c\|\Xi\|_\infty \|\mathcal{G}(\boldsymbol{p}') - \mathcal{G}(\boldsymbol{p})\|_{\mathbb{R}^{N_\mathrm{M}}} \\
\leq \;& c c_{\mathrm{L},\boldsymbol{p}} \|\boldsymbol{p} - \boldsymbol{p}'\|_\infty .
\end{aligned}$$

Note that the last estimate follows from Corollary 4.2.4 for $\boldsymbol{p} = \boldsymbol{\sigma}$ and from Corollary 4.2.5 for $\boldsymbol{p} = \boldsymbol{T}$.

b) Let $\phi_{\mathrm{EMG}}, \phi'_{\mathrm{EMG}} \in \mathbb{R}^{N_\mathrm{M}}$. Again, the Lipschitz continuity is clear for $\phi_{\mathrm{EMG}} = \phi'_{\mathrm{EMG}}$. For $\phi_{\mathrm{EMG}} \neq \phi'_{\mathrm{EMG}}$ we rewrite the norms in the definition of the potential Φ as scalar products and obtain

$$\begin{aligned}
|\Phi(\boldsymbol{p}, \phi_{\mathrm{EMG}}) - \Phi(\boldsymbol{p}, \phi'_{\mathrm{EMG}})| = \;& \frac{1}{2}\left| \|\phi_{\mathrm{EMG}} - \mathcal{G}(\boldsymbol{p})\|_\Xi^2 - \|\phi'_{\mathrm{EMG}} - \mathcal{G}(\boldsymbol{p})\|_\Xi^2 \right| \\
= \;& \frac{1}{2}\left| \langle \phi_{\mathrm{EMG}}, \phi_{\mathrm{EMG}}\rangle_\Xi + \langle \mathcal{G}(\boldsymbol{p}), \mathcal{G}(\boldsymbol{p})\rangle_\Xi \right. \\
& - \langle \phi'_{\mathrm{EMG}}, \phi'_{\mathrm{EMG}}\rangle_\Xi - \langle \mathcal{G}(\boldsymbol{p}), \mathcal{G}(\boldsymbol{p})\rangle_\Xi| \\
& \left. - 2\langle \phi_{\mathrm{EMG}}, \mathcal{G}(\boldsymbol{p})\rangle_\Xi + 2\langle \phi'_{\mathrm{EMG}}, \mathcal{G}(\boldsymbol{p})\rangle_\Xi \right| \\
= \;& |\langle (\phi'_{\mathrm{EMG}} - \phi_{\mathrm{EMG}}), \mathcal{G}(\boldsymbol{p})\rangle_\Xi| \\
\overset{\mathrm{HI}}{\leq} \;& \|\phi'_{\mathrm{EMG}} - \phi_{\mathrm{EMG}}\|_\Xi \|\mathcal{G}\| \\
\underset{4.1.6}{\overset{\mathrm{Corrolary}}{\leq}} \;& c_\mathrm{b} c_\mathrm{V} \|\phi_{\mathrm{EMG}} - \phi'_{\mathrm{EMG}}\|_\Xi \\
\leq \;& c_\mathrm{b} c_\mathrm{V} \|\Xi\|_\infty \|\phi_{\mathrm{EMG}} - \phi'_{\mathrm{EMG}}\|_{\mathbb{R}^{N_\mathrm{M}}} \qquad (4.22)
\end{aligned}$$

3. The existence of the posterior distribution $\boldsymbol{\rho}_{\phi_{\mathrm{EMG}}}$ of $\boldsymbol{p}$ given ϕ_{EMG} now directly follows from Theorem 2.4.1. □

Extending the Lipschitz continuity of the probabilistic forward EMG problem, we

now aim at proving the Lipschitz continuity of the solution of the Bayesian inverse EMG problem, i.e., of the posterior distribution $\boldsymbol{\rho}_{\phi_{\mathrm{EMG}}}$. For this purpose, we choose the Hellinger metric

$$d_{\mathrm{Hell}}(\mu, \mu') = \left(\frac{1}{2} \int \left(\sqrt{\frac{\mathrm{d}\mu}{\mathrm{d}\nu}} - \sqrt{\frac{\mathrm{d}\mu'}{\mathrm{d}\nu}} \right)^2 \mathrm{d}\nu \right)^{\frac{1}{2}},$$

as in [17, Chapter 4] and [50], that we defined in Section 2.2, see Definition 2.2.2.

Using the Hellinger metric, the posterior $\boldsymbol{\rho}_{\phi_{\mathrm{EMG}}}$ is Lipschitz continuous with respect to the measurements ϕ_{EMG} if there exists a constant $c_{\mathrm{L},\boldsymbol{\rho}_{\phi_{\mathrm{EMG}}}} > 0$ such that

$$d_{\mathrm{Hell}}(\boldsymbol{\rho}_{\phi_{\mathrm{EMG}}}, \boldsymbol{\rho}'_{\phi_{\mathrm{EMG}}}) \leq c_{\mathrm{L},\boldsymbol{\rho}_{\phi_{\mathrm{EMG}}}} \|\phi_{\mathrm{EMG}} - \phi'_{\mathrm{EMG}}\|_{\Xi}$$

for $\phi_{\mathrm{EMG}}, \phi'_{\mathrm{EMG}} \in \mathbb{R}^{N_{\mathrm{M}}}$ and $\boldsymbol{\rho}_{\phi_{\mathrm{EMG}}}, \boldsymbol{\rho}'_{\phi_{\mathrm{EMG}}}$ the posterior distributions of $\boldsymbol{p}$ given ϕ_{EMG} and ϕ'_{EMG}.

We use the prior $\boldsymbol{\rho}_0$ as reference measure in the definition of the Hellinger metric and achieve

$$\begin{aligned} 2d_{\mathrm{Hell}}(\boldsymbol{\rho}_{\phi_{\mathrm{EMG}}}, \boldsymbol{\rho}'_{\phi_{\mathrm{EMG}}})^2 &= \int \left(\sqrt{\frac{\mathrm{d}\boldsymbol{\rho}_{\phi_{\mathrm{EMG}}}}{\mathrm{d}\boldsymbol{\rho}_0}} - \sqrt{\frac{\mathrm{d}\boldsymbol{\rho}'_{\phi_{\mathrm{EMG}}}}{\mathrm{d}\boldsymbol{\rho}_0}} \right)^2 \mathrm{d}\boldsymbol{\rho}_0 \\ &= \int \left(\sqrt{\frac{1}{Z} \exp\left(-\Phi(\boldsymbol{p}, \phi_{\mathrm{EMG}})\right)} - \sqrt{\frac{1}{Z'} \exp\left(-\Phi(\boldsymbol{p}, \phi'_{\mathrm{EMG}})\right)} \right)^2 \mathrm{d}\boldsymbol{\rho}_0. \end{aligned}$$

Before further investigating the Hellinger metric of $\boldsymbol{\rho}_{\phi_{\mathrm{EMG}}}$ and $\boldsymbol{\rho}'_{\phi_{\mathrm{EMG}}}$, we reformulate the product

$$\begin{aligned} \frac{1}{Z} \exp\left(-\Phi(\boldsymbol{p}, \phi_{\mathrm{EMG}})\right) &= \frac{1}{Z} \exp\Big(-\frac{1}{2} \|\phi_{\mathrm{EMG}} - \mathcal{G}(\boldsymbol{p})\|_{\Xi}^2 + \frac{1}{2} \|\phi_{\mathrm{EMG}}\|_{\Xi}^2 \Big) \\ &= \frac{1}{Z \exp\left(-\frac{1}{2} \|\phi_{\mathrm{EMG}}\|_{\Xi}^2\right)} \exp\Big(-\frac{1}{2} \|\phi_{\mathrm{EMG}} - \mathcal{G}(\boldsymbol{p})\|_{\Xi}^2 \Big). \end{aligned} \tag{4.23}$$

Using the definition of the scaling factor Z, we see that

$$\begin{aligned} Z \exp\big(-\frac{1}{2}\|\phi_{\mathrm{EMG}}\|_{\Xi}^2\big) &= \int_{\boldsymbol{\mathcal{J}_p}} \exp\big(-\frac{1}{2}\|\phi_{\mathrm{EMG}} - \mathcal{G}(\boldsymbol{p})\|_{\Xi}^2 \\ &\quad + \frac{1}{2}\|\phi_{\mathrm{EMG}}\|_{\Xi}^2 - \frac{1}{2}\|\phi_{\mathrm{EMG}}\|_{\Xi}^2\big)\boldsymbol{\rho}_0(\mathrm{d}\boldsymbol{p}) \\ &= \int_{\boldsymbol{\mathcal{J}_p}} \exp\big(-\frac{1}{2}\|\phi_{\mathrm{EMG}} - \mathcal{G}(\boldsymbol{p})\|_{\Xi}^2\big)\boldsymbol{\rho}_0(\mathrm{d}\boldsymbol{p}). \end{aligned}$$

Inserting the definitions

$$\tilde{\Phi}(\boldsymbol{p}, \phi_{\mathrm{EMG}}) \coloneqq \frac{1}{2}\|\phi_{\mathrm{EMG}} - \mathcal{G}(\boldsymbol{p})\|_{\Xi}^2, \tag{4.24}$$

$$\tilde{Z} \coloneqq \int_{\boldsymbol{\mathcal{J}_p}} \exp\big(-\tilde{\Phi}(\boldsymbol{p}, \phi_{\mathrm{EMG}})\big)\boldsymbol{\rho}_0(\mathrm{d}\boldsymbol{p}) \tag{4.25}$$

into Equation (4.23) yields

$$\frac{1}{Z}\exp\left(-\Phi(\boldsymbol{p}, \phi_{\mathrm{EMG}})\right) = \frac{1}{\tilde{Z}}\exp\big(-\tilde{\Phi}(\boldsymbol{p}, \phi_{\mathrm{EMG}})\big).$$

We thus reason that the Lipschitz continuity of the posterior distribution $\boldsymbol{\rho}_{\phi_{\mathrm{EMG}}}$ with respect to ϕ_{EMG} follows from the Lipschitz continuity of $\tilde{Z}$ and $\tilde{\Phi}$.

Lemma 4.3.3. *Let Assumption 4.2.1 hold. Then the potential $\tilde{\Phi}$ as defined in Equation* (4.24) *is locally Lipschitz continuous with respect to ϕ_{EMG}, i.e., there exists a constant $c_{L,\tilde{\Phi}}$ such that*

$$|\tilde{\Phi}(\phi_{EMG}) - \tilde{\Phi}(\phi'_{EMG})| \leq c_{L,\tilde{\Phi}}\|\phi_{EMG} - \phi'_{EMG}\|_{\Xi}$$

holds for all $\phi_{EMG}, \phi'_{EMG} \in \mathbb{R}^{N_M}$ with $\max\{\|\phi_{EMG}\|_{\Xi}, \|\phi'_{EMG}\|_{\Xi}\} < \infty$.

Before proving the above lemma, we highlight that $\max\{\|\phi_{\mathrm{EMG}}\|_{\Xi}, \|\phi'_{\mathrm{EMG}}\|_{\Xi}\} < \infty$ is always fulfilled for physically meaningful EMG measurements ϕ_{EMG} and ϕ'_{EMG}. From a theoretical perspective, however, $\phi_{\mathrm{EMG}}, \phi'_{\mathrm{EMG}}$ are so far arbitrary elements of $\mathbb{R}^{N_{\mathrm{M}}}$ and thus bounding their norm becomes necessary.

Proof. Let $\phi_{\mathrm{EMG}} \neq \phi'_{\mathrm{EMG}} \in \mathbb{R}^{N_{\mathrm{M}}}$. Using the definition of $\tilde{\Phi}$ we calculate

$$\begin{aligned} |\tilde{\Phi}(\phi_{\mathrm{EMG}}) - \tilde{\Phi}(\phi'_{\mathrm{EMG}})| &= \frac{1}{2}|\|\phi_{\mathrm{EMG}} - \mathcal{G}(\boldsymbol{p})\|_{\Xi}^2 - \|\phi'_{\mathrm{EMG}} - \mathcal{G}(\boldsymbol{p})\|_{\Xi}^2| \\ &= \frac{1}{2}|\|\phi_{\mathrm{EMG}}\|_{\Xi}^2 - \|\phi'_{\mathrm{EMG}}\|_{\Xi}^2 - 2\langle\phi_{\mathrm{EMG}} - \phi'_{\mathrm{EMG}}, \mathcal{G}(\boldsymbol{p})\rangle| \end{aligned}$$

$$
\begin{aligned}
&\overset{\text{TI}}{\underset{\text{HI}}{\leq}} \frac{1}{2}|\|\phi_{\text{EMG}}\|_\Xi^2 - \|\phi'_{\text{EMG}}\|_\Xi^2| + \|\phi_{\text{EMG}} - \phi'_{\text{EMG}}\|_\Xi \|\mathcal{G}\| \\
&= |\langle \phi_{\text{EMG}} - \phi'_{\text{EMG}}, \phi_{\text{EMG}} \rangle + \langle \phi'_{\text{EMG}}, \phi_{\text{EMG}} - \phi'_{\text{EMG}} \rangle| \\
&\quad + \|\phi_{\text{EMG}} - \phi'_{\text{EMG}}\|_\Xi \|\mathcal{G}\| \\
&\leq \max\{\|\phi_{\text{EMG}}\|_\Xi, \|\phi'_{\text{EMG}}\|_\Xi\} \|\phi_{\text{EMG}} - \phi'_{\text{EMG}}\|_\Xi \\
&+ \|\phi_{\text{EMG}} - \phi'_{\text{EMG}}\|_\Xi \|\mathcal{G}\| \\
&\overset{\text{Corrolary}}{\underset{4.1.6}{\leq}} (\max\{\|\phi_{\text{EMG}}\|_\Xi, \|\phi'_{\text{EMG}}\|_\Xi\} + c_{\text{b}}) \|\phi_{\text{EMG}} - \phi'_{\text{EMG}}\|_\Xi
\end{aligned}
$$

and we deduce that $\tilde{\Phi}$ is Lipschitz continuous for all measurement data $\phi_{\text{EMG}}, \phi'_{\text{EMG}} \in \mathbb{R}^{N_{\text{M}}}$ with $\max\{\|\phi_{\text{EMG}}\|_\Xi, \|\phi'_{\text{EMG}}\|_\Xi\} < \infty$. □

The Lipschitz continuity of the potential $\tilde{\Phi}$ with respect to ϕ_{EMG} allows to furthermore prove the Lipschitz continuity of the scaling factor $\tilde{Z} = \tilde{Z}(\phi_{\text{EMG}})$.

Lemma 4.3.4. *Let Assumption 4.2.1 hold. Then the scaling factor $\tilde{Z}(\phi_{EMG})$ as defined in Equation* (4.25) *is Lipschitz continuous with respect to ϕ_{EMG}, i.e., there exists a constant $c_{L,\tilde{Z}}$ such that*

$$
|\tilde{Z}(\phi_{EMG}) - \tilde{Z}(\phi'_{EMG})| \leq c_{L,\tilde{Z}} \|\phi_{EMG} - \phi'_{EMG}\|_\Xi \tag{4.26}
$$

for all $\phi_{EMG}, \phi'_{EMG} \in \mathbb{R}^{N_M}$.

Proof. For $\phi_{\text{EMG}} \neq \phi'_{\text{EMG}} \in \mathbb{R}^{N_{\text{M}}}$ we estimate

$$
\begin{aligned}
|\tilde{Z}(\phi_{\text{EMG}}) - \tilde{Z}(\phi'_{\text{EMG}})| \leq & \int_{\boldsymbol{\mathcal{J}_p}} \Big| \exp\big(-\frac{1}{2}\|\phi_{\text{EMG}} - \mathcal{G}(\boldsymbol{p})\|_\Xi^2\big) \\
& - \exp\big(-\frac{1}{2}\|\phi'_{\text{EMG}} - \mathcal{G}(\boldsymbol{p})\|_\Xi^2\big) \Big| \, \mathrm{d}\boldsymbol{\rho}_0(\boldsymbol{p}) \\
= 2 & \int_{\boldsymbol{\mathcal{J}_p}} \Big| \exp\big(-\frac{1}{2}\|\phi_{\text{EMG}} - \mathcal{G}(\boldsymbol{p})\|_\Xi^2\big) \\
& - \exp\big(-\frac{1}{2}\|\phi'_{\text{EMG}} - \mathcal{G}(\boldsymbol{p})\|_\Xi^2\big) \Big| \, \mathrm{d}\boldsymbol{\rho}_0(\boldsymbol{p}) \\
\leq & \sqrt{2}\, |\|\phi_{\text{EMG}} - \mathcal{G}(\boldsymbol{p})\|_\Xi - \|\phi'_{\text{EMG}} - \mathcal{G}(\boldsymbol{p})\|_\Xi| \\
\overset{\text{TI}}{\leq} & \sqrt{2} \|\phi_{\text{EMG}} - \phi'_{\text{EMG}}\|_\Xi.
\end{aligned}
$$

Note that we used the Lipschitz continuity of $\exp(-x)$ for $x \in [0, \infty]$ with Lipschitz constant $c_{\text{L,exp}} = 1$. □

Theorem 4.3.5. *Let Assumption 4.2.1 hold and $\boldsymbol{\rho}_{\phi_{EMG}}$ denote the solution of the Bayesian inverse EMG problem for EMG measurement data ϕ_{EMG} that is given by Theorem 4.3.2. Then $\boldsymbol{\rho}_{\phi_{EMG}}$ is locally Lipschitz continuous with respect to the measured data ϕ_{EMG}, i.e., there exists a positive constant $c_{L,\boldsymbol{\rho}_{\phi_{EMG}}} > 0$ such that*

$$d_{Hell}(\boldsymbol{\rho}_{\phi_{EMG}}, \boldsymbol{\rho}'_{\phi_{EMG}}) \leq c_{L,\boldsymbol{\rho}_{\phi_{EMG}}} \|\phi_{EMG} - \phi'_{EMG}\|_{\Xi} \tag{4.27}$$

holds for all $\phi_{EMG}, \phi'_{EMG} \in \mathbb{R}^{N_M}$ with $\max\{\|\phi_{EMG}\|_{\Xi}, \|\phi'_{EMG}\|_{\Xi}\} < \infty$.

Proof. Let $\phi_{\mathrm{EMG}}, \phi'_{\mathrm{EMG}} \in \mathbb{R}^{N_{\mathrm{M}}}$. The Lipschitz continuity is obvious for $\phi_{\mathrm{EMG}} = \phi'_{\mathrm{EMG}}$. For $\phi_{\mathrm{EMG}} \neq \phi'_{\mathrm{EMG}}$ let $\boldsymbol{\rho}_{\phi_{\mathrm{EMG}}}, \boldsymbol{\rho}'_{\phi_{\mathrm{EMG}}}$ denote the corresponding solutions of the Bayesian inverse EMG problem. We use the scaling factor $\tilde{Z}$ and the potential $\tilde{\Phi}$ as defined in Equations (4.25) and (4.24). For further simplification of the notations, we define $\tilde{\Phi} \coloneqq \tilde{\Phi}(\boldsymbol{p}, \phi_{\mathrm{EMG}}), \tilde{\Phi}' \coloneqq \tilde{\Phi}(\boldsymbol{p}, \phi'_{\mathrm{EMG}})$ and $\tilde{Z} \coloneqq \tilde{Z}(\phi_{\mathrm{EMG}}), \tilde{Z}' \coloneqq \tilde{Z}(\phi'_{\mathrm{EMG}})$.

From the above considerations on the Hellinger metric of $\boldsymbol{\rho}_{\phi_{\mathrm{EMG}}}$ and $\boldsymbol{\rho}'_{\phi_{\mathrm{EMG}}}$ we thus have

$$\begin{aligned}
2d_{\mathrm{Hell}}(\boldsymbol{\rho}_{\phi_{\mathrm{EMG}}}, \boldsymbol{\rho}'_{\phi_{\mathrm{EMG}}})^2 &= \int_{\boldsymbol{\mathcal{J}}_{\boldsymbol{p}}} \left(\sqrt{\frac{1}{\tilde{Z}} \exp\Big(-\tilde{\Phi}\Big)} - \sqrt{\frac{1}{\tilde{Z}'} \exp\Big(-\tilde{\Phi}'\Big)} \right)^2 \mathrm{d}\boldsymbol{\rho}_0(\boldsymbol{p}) \\
&= \int_{\boldsymbol{\mathcal{J}}_{\boldsymbol{p}}} \left(\frac{1}{\sqrt{\tilde{Z}}} \left(\exp\Big(-\frac{1}{2}\tilde{\Phi}\Big) - \exp\Big(-\frac{1}{2}\tilde{\Phi}'\Big) \right) \right. \\
&\quad \left. + \left(\frac{1}{\sqrt{\tilde{Z}}} - \frac{1}{\sqrt{\tilde{Z}'}} \right) \exp\Big(-\frac{1}{2}\tilde{\Phi}'\Big) \right)^2 \mathrm{d}\boldsymbol{\rho}_0(\boldsymbol{p}) \\
&= \int_{\boldsymbol{\mathcal{J}}_{\boldsymbol{p}}} \frac{1}{\tilde{Z}} \left(\exp\Big(-\frac{1}{2}\tilde{\Phi}\Big) - \exp\Big(-\frac{1}{2}\tilde{\Phi}'\Big) \right)^2 \mathrm{d}\boldsymbol{\rho}_0(\boldsymbol{p}) \\
&\quad + \int_{\boldsymbol{\mathcal{J}}_{\boldsymbol{p}}} \left(\frac{1}{\sqrt{\tilde{Z}}} - \frac{1}{\sqrt{\tilde{Z}'}} \right)^2 \exp\Big(-\tilde{\Phi}'\Big) \mathrm{d}\boldsymbol{\rho}_0(\boldsymbol{p}) \\
&\quad + 2 \int_{\boldsymbol{\mathcal{J}}_{\boldsymbol{p}}} \frac{1}{\sqrt{\tilde{Z}}} \left(\exp\Big(-\frac{1}{2}\tilde{\Phi}\Big) - \exp\Big(-\frac{1}{2}\tilde{\Phi}'\Big) \right) \\
&\quad \cdot \Big(\frac{1}{\tilde{Z}} - \frac{1}{\tilde{Z}'} \Big) \exp\Big(-\frac{1}{2}\tilde{\Phi}'\Big) \mathrm{d}\boldsymbol{\rho}_0(\boldsymbol{p}).
\end{aligned}$$

Using Young's inequality (YI) to solve the last integral, we achieve

$$\begin{aligned}
2d_{\mathrm{Hell}}(\boldsymbol{\rho}_{\phi_{\mathrm{EMG}}}, \boldsymbol{\rho}'_{\phi_{\mathrm{EMG}}})^2 &\overset{\mathrm{YI}}{\leq} 2\int_{\boldsymbol{\mathcal{J}_p}} \frac{1}{\tilde{Z}} \left(\exp\Big(-\frac{1}{2}\tilde{\Phi}\Big) - \exp\Big(-\frac{1}{2}\tilde{\Phi}'\Big)\right)^2 \mathrm{d}\boldsymbol{\rho}_0(\boldsymbol{p}) \\
&\quad + 2\int_{\boldsymbol{\mathcal{J}_p}} \left(\frac{1}{\sqrt{\tilde{Z}}} - \frac{1}{\sqrt{\tilde{Z}'}}\right)^2 \exp\Big(-\tilde{\Phi}'\Big)\mathrm{d}\boldsymbol{\rho}_0(\boldsymbol{p}) \\
&= 2\int_{\boldsymbol{\mathcal{J}_p}} \frac{1}{\tilde{Z}} \left|\exp\Big(-\frac{1}{2}\tilde{\Phi}\Big) - \exp\Big(-\frac{1}{2}\tilde{\Phi}'\Big)\right|^2 \mathrm{d}\boldsymbol{\rho}_0(\boldsymbol{p}) \\
&\quad + 2\int_{\boldsymbol{\mathcal{J}_p}} \left|\frac{1}{\sqrt{\tilde{Z}}} - \frac{1}{\sqrt{\tilde{Z}'}}\right|^2 \exp\Big(-\tilde{\Phi}'\Big)\mathrm{d}\boldsymbol{\rho}_0(\boldsymbol{p}).
\end{aligned}$$

We apply the Lipschitz continuity properties that we proved in the previous corollaries. Additionally, we use that the square root function is Lipschitz continuous on $(0, \infty]$ with Lipschitz constant $c_{\mathrm{L,sqrt}}$ and that the reciprocal of the exponential function is Lipschitz continuous on $[0, \infty]$ with constant $c_{\mathrm{L,e}} = 1$:

$$\begin{aligned}
2d_{\mathrm{Hell}}(\boldsymbol{\rho}_{\phi_{\mathrm{EMG}}}, \boldsymbol{\rho}'_{\phi_{\mathrm{EMG}}})^2 \leq\ & 2\int_{\boldsymbol{\mathcal{J}_p}} \frac{1}{\tilde{Z}} \left|\tilde{\Phi} - \tilde{\Phi}'\right|^2 + c_{\mathrm{L,sqrt}}^2 \left|\tilde{Z} - \tilde{Z}'\right|^2 \exp\Big(-\tilde{\Phi}'\Big)\mathrm{d}\boldsymbol{\rho}_0(\boldsymbol{p}) \\
&\underset{4.3.3,4.3.4}{\overset{\text{Lemmas}}{\leq}} 2\int_{\boldsymbol{\mathcal{J}_p}} \frac{1}{\tilde{Z}} c_{\mathrm{L},\tilde{\Phi}}^2 \|\phi - \phi'\|_\Xi^2 + c_{\mathrm{L,sqrt}}^2 c_{\mathrm{L},\tilde{Z}}^2 \|\phi - \phi'\|_\Xi^2 \exp\Big(-\tilde{\Phi}'\Big)\mathrm{d}\boldsymbol{\rho}_0(\boldsymbol{p}) \\
=\ & 2\big(c_{\mathrm{L},\tilde{\Phi}}^2 \frac{1}{\tilde{Z}} + c_{\mathrm{L,sqrt}}^2 c_{\mathrm{L},\tilde{Z}}^2 \tilde{Z}'\big)\|\phi - \phi'\|_\Xi^2
\end{aligned}$$

Finally, it remains to show that $0 < \tilde{Z} < \infty$. Analogously to the positivity of Z in the proof of Theorem 4.3.2, the strict positivity of $\tilde{Z}$ follows from the boundedness of the forward operator $\mathcal{G}$, see Corollary 4.1.6. We deduce that $\frac{1}{\tilde{Z}} \leq c_{\tilde{Z}} < \infty$ for some constant $c_{\tilde{Z}} > 0$. Moreover, we have

$$\tilde{Z} = \int_{\boldsymbol{\mathcal{J}_p}} \exp\Big(-\frac{1}{2}\|\phi_{\mathrm{EMG}} - \mathcal{G}(\boldsymbol{p})\|^2\Big)\mathrm{d}\boldsymbol{\rho}_0(\boldsymbol{p}) \leq \int_{\boldsymbol{\mathcal{J}_p}} 1\mathrm{d}\boldsymbol{\rho}_0(\boldsymbol{p}) = \boldsymbol{\rho}_0(\boldsymbol{\mathcal{J}_p}) = 1 < \infty$$

The assertion then follows with Lipschitz constant $c_{\mathrm{L},\boldsymbol{\rho}_{\phi_{\mathrm{EMG}}}}^2 \coloneqq c_{\mathrm{L},\tilde{\Phi}} c_{\tilde{Z}} + c_{\mathrm{L,sqrt}}^2 c_{\mathrm{L},\tilde{Z}}^2$. □

We emphasize that estimate (4.27) also describes the behavior of the posterior with respect to the discretization of the underlying equations and variables as we will show in the following section.

4.4. Error Bounds

Building on the Lipschitz continuity results of the last sections, we quantify the influence of discretizing the underlying probabilistic forward EMG problem, as in Definition 4.2.2, on the solution of the Bayesian inverse EMG problem, i.e., the posterior distribution $\boldsymbol{\rho}_{\phi_{\mathrm{EMG}}}$. We perform the discretization in three steps: the discretization of the weak formulation of the probabilistic forward EMG problem $a_{\boldsymbol{\sigma}}(\phi, v) = \ell_{\boldsymbol{\sigma}}(v)$, as defined in (4.2), the discretization of the random conductivity $\boldsymbol{\sigma}(x, \omega)$, and the discretization of the evaluation operator (2.25).

We discretize the weak formulation (4.2)

$$\int_{D_{\mathrm{M}}} \big((\sigma_{\mathrm{i}} + \sigma_{\mathrm{e}})\nabla\phi_{\mathrm{e}}\big) \cdot \nabla v_{\mathrm{e}} + \int_{D_{\mathrm{B}}} (\sigma_0 \nabla\phi_0) \cdot \nabla v_0 = -\int_{D_{\mathrm{M}}} (\sigma_{\mathrm{i}} \nabla V_{\mathrm{m}}) \cdot \nabla v_{\mathrm{e}}$$

using the finite element method (FEM). Therefore, the domain $D = D_{\mathrm{M}} \cup D_{\mathrm{B}}$ is discretized by a triangulation $D^{\mathrm{h}} = D_{\mathrm{M}}^{\mathrm{h}} \cup D_{\mathrm{B}}^{\mathrm{h}}$ with mesh width h_x. Second, the ansatz and test space V is discretized. We choose the same discrete space $V^{\mathrm{h}} \subset V$ to approximate the ansatz and test spaces, making use of the coercivity of the bilinear form $a_{\boldsymbol{\sigma}}(\cdot, \cdot)$ to ease notation. Note that in general different ansatz and test spaces can be used.

Let now $v_1, \ldots, v_{N_{\mathrm{h}}}$ with $N_{\mathrm{h}} \in \mathbb{N}$ be a basis of V^{h} and

$$\phi \approx \phi^{\mathrm{h}} \coloneqq \sum_{k=1}^{N_{\mathrm{h}}} (\tau_{\mathrm{e},k} \mathbb{1}_{D_{\mathrm{M}}} + \tau_{0,k} \mathbb{1}_{D_{\mathrm{B}}}) v_k \in V^{\mathrm{h}} \subset V$$

be the basis representation of the FE solution with the characteristic functions $\mathbb{1}_{D_{\mathrm{M}}}$ and $\mathbb{1}_{D_{\mathrm{B}}}$ of the muscle and body region. The FE discrete forward EMG problem then reads as follows: Find $\phi^{\mathrm{h}} \in V^{\mathrm{h}}$ such that

$$\begin{aligned}\sum_{k=1}^{N_{\mathrm{h}}} \Big(\int_{D_{\mathrm{M}}^{\mathrm{h}}} \big((\sigma_{\mathrm{i}} + \sigma_{\mathrm{e}})\nabla v_{\mathrm{e},k}\big) \cdot \nabla v_{\mathrm{e},l} \Big) \tau_{\mathrm{e},k} + \sum_{k=1}^{N_{\mathrm{h}}} \Big(\int_{D_{\mathrm{B}}^{\mathrm{h}}} (\sigma_0 \nabla v_{0,k}) \cdot \nabla v_{0,l} \Big) \tau_{0,k} \\ = -\int_{D_{\mathrm{M}}^{\mathrm{h}}} (\sigma_{\mathrm{i}} \nabla V_{\mathrm{m}}) \cdot \nabla v_{\mathrm{e},l} \qquad (4.28)\end{aligned}$$

holds for all test functions v_l with $l = 1, \ldots, N_{\mathrm{h}}$. Within the FEM, the integrals are approximated using quadrature rules. We forebear from using additional notations to indicate the use of quadrature rules.

As briefly discussed in Section 3.1, there is no need to use a time discretization scheme when the Rosenfalck model is used to describe the muscle fiber APs. When using the

Hodgkin-Huxley model or any other ODE-based model for the electrophysiology of the muscle fibers, time stepping schemes with some time step size h_t are used. We denote the time- and space-discrete solution by ϕ^{h}.

Next, we discretize the random conductivities

$$\sigma_j(x,\omega) = m_j(x) + \sum_{k=1}^{\infty} \gamma_{j,k} T_{j,k}(\omega)\varphi_k(x),$$

for $j \in \{\mathrm{i},\mathrm{e},0\}$. We do so by truncating the series expansions after the first $N_{\mathrm{trunc}} \in \mathbb{N}$ terms and thus achieve the approximations

$$\sigma_j(x,\omega) \approx \sigma_j^{N_{\mathrm{trunc}}}(x,\omega) \coloneqq m_j(x) + \sum_{k=1}^{N_{\mathrm{trunc}}} \gamma_{j,k} T_{j,k}(\omega)\varphi_k(x) \tag{4.29}$$

of the series expansions (4.15) for $j \in \{\mathrm{i},\mathrm{e},0\}$. We denote the collection of the N_{trunc}^3 random coefficients $(\{T_{\mathrm{i},k}\}_{k=1}^{N_{\mathrm{trunc}}}, \{T_{\mathrm{e},k}\}_{k=1}^{N_{\mathrm{trunc}}}, \{T_{0,k}\}_{k=1}^{N_{\mathrm{trunc}}})$ by $\boldsymbol{T}^{N_{\mathrm{trunc}}}$.

Plugging the truncated series expansions into Equation (4.28), the discrete solution $\phi^{\mathrm{h},N_{\mathrm{trunc}}} \coloneqq \sum_{k=1}^{N_{\mathrm{h}}} (\tau_{\mathrm{e},k}^{N_{\mathrm{trunc}}} \mathbb{1}_{D_{\mathrm{M}}} + \tau_{0,k}^{N_{\mathrm{trunc}}} \mathbb{1}_{D_{\mathrm{B}}}) v_k \in V^{\mathrm{h}} \subset V$ must fulfill

$$\begin{aligned}
&\sum_{j=1}^{N_{\mathrm{h}}} \Big(\int_{D^{\mathrm{h}}} \big((m_{\mathrm{i}}(x) + m_{\mathrm{e}}(x) + \sum_{k=1}^{N_{\mathrm{trunc}}} (\gamma_{\mathrm{i},k} T_{\mathrm{i},k}(\omega) + \gamma_{\mathrm{e},k} T_{\mathrm{e},k}(\omega))\, \varphi_k(x)) \nabla v_{\mathrm{e},j} \big) \cdot \nabla v_{\mathrm{e},l} \Big) \tau_{\mathrm{e},j}^{N_{\mathrm{trunc}}} \\
&\quad + \sum_{j=1}^{N_{\mathrm{h}}} \left(\int_{D_{\mathrm{B}}^{\mathrm{h}}} \left(\left(m_0(x) + \sum_{k=1}^{N_{\mathrm{trunc}}} \gamma_{0,k} T_{0,k}(\omega) \varphi_k(x) \right) \nabla v_{0,j} \right) \cdot \nabla v_{0,l} \right) \tau_{0,j}^{N_{\mathrm{trunc}}} \\
&= - \int_{D_{\mathrm{M}}^{\mathrm{h}}} \left((m_{\mathrm{i}}(x) + \sum_{k=1}^{N_{\mathrm{trunc}}} \gamma_{\mathrm{i},k} T_{\mathrm{i},k}(\omega) \varphi_k(x)) \nabla V_{\mathrm{m}} \right) \cdot \nabla v_{\mathrm{e},l}
\end{aligned} \tag{4.30}$$

for all $l = 1, \ldots, N_{\mathrm{h}}$.

In case the conductivities are constant, the Bayesian inverse problem simplifies to searching for the posterior distribution of the conductivities themselves. A description of that case has previously been published in [88]. As the three random conductivities then are space-independent random variables, the above discretization of $\boldsymbol{\sigma}$ becomes obsolete in that case.

Finally, we insert the discrete solution $\phi^{\mathrm{h},N_{\mathrm{trunc}}}$ into the evaluation operator (2.25) and achieve

$$\phi_{\mathrm{x}}^{\mathrm{h},N_{\mathrm{trunc}}} = \frac{1}{\pi r_{\mathrm{el}}^2} \Big(\int_{B_{r_{\mathrm{el}}}(x_{\mathrm{m},j}) \cap \partial D^{\mathrm{h}}} \phi^{\mathrm{h},N_{\mathrm{trunc}}}(x) \mathrm{d}x \Big)_{j=1}^{N_{\mathrm{M}}} \in \mathbb{R}^{N_{\mathrm{M}}}.$$

As in the FEM, we use quadrature rules to approximate the boundary integrals in the above equation and denote the discrete computed EMG data by $\phi_{\mathbb{x}}^{\mathrm{h},N_{\mathrm{trunc}},\mathrm{Q}} \in \mathbb{R}^{N_{\mathrm{M}}}$. This is the solution of the fully discrete probabilistic forward EMG problem.

The discretization of the solution of the Bayesian inverse EMG problem, i.e., the discretization of the posterior distribution $\boldsymbol{\rho}_{\phi_{\mathrm{EMG}}}$ of $\boldsymbol{p}$ given measurement data ϕ_{EMG}, is discussed in Chapter 5.

We compare the solution $\phi_{\mathbb{x}}^{\mathrm{h},N_{\mathrm{trunc}},\mathrm{Q}}$ of the fully discrete probabilistic forward EMG problem to the exact solution $\phi^* \in V$ that satisfies $\phi_{\mathbb{x}}^* = \phi_{\mathrm{EMG}}$. Therefore, we denote the error of applying a quadrature rule to numerically evaluate the evaluation operator (2.25) by E_{Q}, the error resulting from truncating the series expansion (4.15) by E_{trunc}, and the time and space discretization error including the FE quadrature error by E_{h}. Using the triangle inequality, we obtain

$$\begin{aligned}
\left\|\phi^*(\mathbb{x}) - \phi^{\mathrm{h},N_{\mathrm{trunc}},\mathrm{Q}}(\mathbb{x})\right\|_{\Xi} &\leq \left\|\phi^*(\mathbb{x}) - \phi^{\mathrm{h},N_{\mathrm{trunc}}}(\mathbb{x})\right\|_{\Xi} + E_{\mathrm{Q}} \\
&\leq c\left\|\phi^*(\mathbb{x}) - \phi^{\mathrm{h},N_{\mathrm{trunc}}}(\mathbb{x})\right\|_{V} + E_{\mathrm{Q}} \\
&\leq c\Big(\underbrace{\left\|\phi^* - \phi^{\mathrm{h}}\right\|_{V}}_{=:E_{\mathrm{h}}} + \underbrace{\left\|\phi^{\mathrm{h}} - \phi^{\mathrm{h},N_{\mathrm{trunc}}}\right\|_{V}}_{=:E_{\mathrm{trunc}}}\Big) + E_{\mathrm{Q}} \\
&\leq c(E_{\mathrm{h}} + E_{\mathrm{trunc}} + E_{\mathrm{Q}}).
\end{aligned}$$

We emphasize that E_{h} includes both the FEM and time discretization error E_{FEM} and E_{t}, and we achieve

$$\left\|\phi^*(\mathbb{x}) - \phi^{\mathrm{h},N_{\mathrm{trunc}},\mathrm{Q}}(\mathbb{x})\right\|_{\Xi} \leq c(E_{\mathrm{FEM}} + E_{\mathrm{t}} + E_{\mathrm{trunc}} + E_{\mathrm{Q}}). \tag{4.31}$$

It follows from the above calculation that the overall discretization error is dominated by the maximum error in quadrature E_{Q}, FE discretization E_{FEM}, time discretization E_{t}, and truncation of the series expansions E_{trunc}. Recall that even if we did not indicate the use of FE discretization quadrature rules explicitly, E_{FEM} also includes this quadrature error.

The Lipschitz continuity of the electrical potential ϕ with respect to the global conductivity $\boldsymbol{\sigma}$

$$\|\phi(\boldsymbol{\sigma}) - \phi(\boldsymbol{\sigma}')\|_{V} \leq c_{\mathrm{L},\boldsymbol{\sigma}}\|\boldsymbol{\sigma} - \boldsymbol{\sigma}'\|_{\infty},$$

given by Lemma 4.2.3, yields a first estimate for the truncation error:

$$\begin{aligned}\left\|\phi^* - \phi^N_{\text{trunc}}\right\|_V &\overset{\text{Lemma 4.2.3}}{\leq} c_{\text{L},\boldsymbol{\sigma}'}\left\|\boldsymbol{\sigma}^* - \boldsymbol{\sigma}^{N_{\text{trunc}}}\right\|_\infty \\ &\leq c_{\text{L},\boldsymbol{\sigma}'} \max_{j\in\{\text{i,e,0}\}} \sum_{k=N_{\text{trunc}}+1}^{\infty} |\gamma_{j,k}||T_{j,k}|\|\varphi_k\| \\ &\leq c_{\text{L},\boldsymbol{\sigma}'} \max_{j\in\{\text{i,e,0}\}} \sum_{k=N_{\text{trunc}}+1}^{\infty} |\gamma_{j,k}|\end{aligned}$$

By Assumption 4.2.1 the ℓ_1-norm of the coefficients γ_j is bounded and thus the truncation error is bounded too. Moreover, we introduce the following assumptions to further quantify the error estimate:

Assumption 4.4.1.

1. *For $j \in \{i, e, 0\}$ we assume that $|\gamma_{j,k}| > |\gamma_{j,k+1}|$ for all $k = 1, \ldots, \infty$ and that there exists constants $c_j > 0$ and $o_{trunc} > 0$ such that $\sum_{k=N_{trunc}+1}^{\infty} |\gamma_{j,k}| \leq c_j N_{trunc}^{-o_{trunc}}$.*
2. *Assume that there exist constants $c_{FEM} > 0$ and $o_{FEM} > 0$ such that $E_{FEM} \leq c_{FEM} h_x^{o_{FEM}}$.*
3. *Assume that there exist constants $c_t > 0$ and $o_t > 0$ such that $E_t \leq c_t h_t^{o_t}$.*
4. *Assume that there exist constants $c_Q > 0$ and $o_Q > 0$ such that $E_Q \leq c_Q h_x^{o_Q}$.*

Note that the above assumption on the truncation error E_{trunc} implies that describing $\boldsymbol{\sigma}$ through the series expansions and searching for the posterior distribution of the random coefficients $\boldsymbol{T}$ is more efficient then inferring the global conductivity itself, whenever the conductivity is space-dependent. This is due to the assumption that the random coefficients $\boldsymbol{T}$ decay with rate o_{trunc} such that we can assume that a moderate number of coefficients is sufficient to describe the conductivities. On the other hand, discretizing the space-dependent conductivities using, e.g., finite differences or FEs, and inferring the corresponding coefficients leads to a huge number of parameters, thus rendering this approach infeasible.

Applying Assumptions 4.4.1 to Estimate (4.31) we achieve the error estimate

$$\left\|\phi^*_{\mathbb{X}} - \phi^{\text{h},N_{\text{trunc}},\text{Q}}_{\mathbb{X}}\right\|_\Xi \leq c\big(h_x^{o_{\text{FEM}}} + h_t^{o_t} + N_{\text{trunc}}^{-o_{\text{trunc}}} + h_x^{o_{\text{Q}}}\big), \tag{4.32}$$

where h_x is the maximal spatial grid size of the underlying FE grid.

Recall that following Theorem 4.3.5

$$d_{\mathrm{Hell}}(\boldsymbol{\rho}_{\phi_{\mathrm{EMG}}}, \boldsymbol{\rho}'_{\phi_{\mathrm{EMG}}}) \leq c_{\mathrm{L},\boldsymbol{\rho}_0} \|\phi - \phi'\|_{\Xi}$$

holds for all $\phi, \phi' \in \mathbb{R}^{N_{\mathrm{M}}}$ with $\max\{\|\phi_{\mathrm{EMG}}\|_{\Xi}, \|\phi'_{\mathrm{EMG}}\|_{\Xi}\} < \infty$. Thus, for $\phi = \phi^*$, $\phi' = \phi^{\mathrm{h},N_{\mathrm{trunc}},\mathrm{Q}}$, $\boldsymbol{\rho}_{\phi_{\mathrm{EMG}}} = \boldsymbol{\rho}^*_{\phi_{\mathrm{EMG}}}$, and $\boldsymbol{\rho}'_{\phi_{\mathrm{EMG}}} = \boldsymbol{\rho}^{\mathrm{h}}_{\phi_{\mathrm{EMG}}}$ denoting the posterior distribution of $\boldsymbol{\sigma}^{N_{\mathrm{trunc}}}$ or $\boldsymbol{T}^{N_{\mathrm{trunc}}}$ given $\phi^{\mathrm{h},N_{\mathrm{trunc}},\mathrm{Q}}$ we have the following corollary.

Corollary 4.4.2. *Let Assumptions 4.2.1 and 4.4.1 hold. Then there exists a constant $c > 0$ such that the Hellinger metric of the true posterior $\boldsymbol{\rho}^*_{\phi_{EMG}}$ and the posterior $\boldsymbol{\rho}^h_{\phi_{EMG}}$ of the computed EMG data using the above discretizations of the underlying probabilistic forward EMG problem fulfills*

$$d_{Hell}(\boldsymbol{\rho}^*_{\phi_{EMG}}, \boldsymbol{\rho}^h_{\phi_{EMG}}) \leq c\big(h_x^{o_{FEM}} + h_t^{o_t} + N_{trunc}^{-o_{trunc}} + h_x^{o_Q}\big)$$

if $\max\{\|\phi_{EMG}\|_{\Xi}, \big\|\phi_{\mathbb{X}}^{h,N_{trunc},Q}\big\|_{\Xi}\} < \infty$.

5. Sampling Algorithms for Solving the Bayesian Inverse EMG Problem

As stated in Definition 4.3.1 the Bayesian inverse EMG problem aims at finding the posterior measure $\boldsymbol{\rho}_{\phi_{\mathrm{EMG}}}$ of the global conductivity $\boldsymbol{\sigma}$ or the coefficients $\boldsymbol{T}$ for given surface EMG measurements $\phi_{\mathrm{EMG}} \in \mathbb{R}^{N_{\mathrm{M}}}$. For sampling from this posterior distribution, we introduced the prototype Metropolis-Hastings algorithm 2.3.1 in Section 2.4.2.

In Section 5.1 we adapt this general Metropolis-Hastings algorithm to the inverse setting used in the numerical experiments in Chapter 6. That means we assume that the conductivities are constant throughout their respective domains. This particularly implies that the muscle fibers are parallel to each other. The parameter of interest in that case is the global conductivity $\boldsymbol{\sigma}$ itself. Additionally, we assume that σ_0 and σ_{e} are known, what leaves the intracellular conductivity σ_{i} as unknown parameter. Recalling the construction of arbitrary intracellular conductivities in Section 3.2.2, we establish the conductivity magnitudes and the rotation angles as the parameters of interest. The above settings and assumptions lead to the definition of our *standard Metropolis-Hastings algorithm* (SA). We validate and quantify the performance of the SA in several parameter studies in Section 5.2 and notice that solving the forward EMG problem, as discussed in Chapter 3, for evaluating the acceptance strategy makes up a high percentage of the runtime. Furthermore, solving the forward EMG problem is time-consuming and thus impractical when a high number of proposals needs to be drawn until the SA converges.

For accelerating the forward EMG problem solves we combine the low-rank tensor representation of the parameter-dependent forward EMG problem derived in Section 3.2.4 with the SA in Section 5.3. Doing so enables us to precompute the solution of the forward EMG problem on a discrete parameter grid, store the solutions in a data-sparse format, and evaluate this tensor solution in each step of the SA. Our parameter studies in Sections 5.3.1 and 5.3.2 show that evaluating the precomputed tensor solution in each step of the Metropolis-Hastings algorithm is much faster than solving the forward EMG problem and, nevertheless, accurate.

5.1. Standard Metropolis-Hastings Algorithm

Recall that the Metropolis-Hastings algorithm is an acceptance-rejection algorithm that draws a proposal from a proposal distribution and accepts it as a sample from the posterior with a particular probability. If the proposal is rejected, the old sample is kept and a new proposal is drawn.

In Theorem 2.4.2 we stated that the Metropolis-Hastings algorithm produces a posterior-reversible Markov chain when choosing the proposal distribution to be the prior and the acceptance probability

$$a(\boldsymbol{p}, \boldsymbol{p}') = \min\{1, \exp(\Phi(\boldsymbol{p}) - \Phi(\boldsymbol{p}'))\}.$$

In the EMG setting $\boldsymbol{p} = \boldsymbol{\sigma}$ or $\boldsymbol{p} = \boldsymbol{T}$ and $\Phi(\boldsymbol{p})$ is the potential as defined in Equation (4.21). To get an intuition for the acceptance strategy a, we rewrite it inserting the definition of the potential $\Phi(\boldsymbol{p})$:

$$\begin{aligned} a(\boldsymbol{p}, \boldsymbol{p}') &= \min\left\{1, \exp\left(\Phi(\boldsymbol{p}) - \Phi(\boldsymbol{p}')\right)\right\} \\ &= \min\left\{1, \exp\left(\frac{1}{2}\|\phi_{\mathrm{EMG}} - \mathcal{G}(\boldsymbol{p})\|_{\Xi}^2 - \frac{1}{2}\|\phi_{\mathrm{EMG}} - \mathcal{G}(\boldsymbol{p}')\|_{\Xi}^2\right)\right\} \\ &= \min\left\{1, \frac{\exp\left(\frac{1}{2}\|\phi_{\mathrm{EMG}} - \mathcal{G}(\boldsymbol{p})\|_{\Xi}^2\right)}{\exp\left(\frac{1}{2}\|\phi_{\mathrm{EMG}} - \mathcal{G}(\boldsymbol{p}')\|_{\Xi}^2\right)}\right\} \\ &\begin{cases} > 1 & \text{if } \|\phi_{\mathrm{EMG}} - \mathcal{G}(\boldsymbol{p}')\|_{\Xi}^2 < \|\phi_{\mathrm{EMG}} - \mathcal{G}(\boldsymbol{p})\|_{\Xi}^2, \\ = 1 & \text{otherwise} \end{cases} \end{aligned} \tag{5.1}$$

Consequently, a new proposal is always accepted if it produces less error than the actual sample and is rejected otherwise with probability $1 - a$, i.e., the old sample is kept with probability $1 - a$. For a formal derivation of this Metropolis-Hastings algorithm and the acceptance strategy, we again refer to [17, Chapter 5] and the literature cited therein.

Recall that after discretization of the forward EMG problem for an arbitrary space-dependent global conductivity, the aim is to infer the N_{trunc}^3 space-independent coefficients of the truncated series expansions (4.29), i.e., to sample from their posterior distribution. In the discrete case, we thus have the N_{trunc}^3 coefficients $\boldsymbol{T}^{N_{\mathrm{trunc}}}$ as parameters, i.e., $\boldsymbol{p} = \boldsymbol{T}^{N_{\mathrm{trunc}}}$. Following Assumptions 4.4.1, the coefficients $\boldsymbol{T}$ decay fast, such that a moderate number N_{trunc}^3 of random coefficients leads to a good approximation of the global conductivity $\boldsymbol{\sigma}$. In this way, the number of parameters to be inferred from the given measurement data ϕ_{EMG} is limited.

Nevertheless, when the global conductivity can be assumed to be constant, there is no need to make use of the series expansions. Inferring the entries of the (then constant) conductivity matrices $\sigma_\mathrm{i}, \sigma_\mathrm{e}, \sigma_0 \in \mathbb{R}^{3\times 3}$ means inferring $3 \cdot 6 = 18$ parameters. This is more efficient than modeling the constant matrices through series expansions and inferring the resulting coefficients. Recall that the conductivity matrices $\sigma_\mathrm{i}, \sigma_\mathrm{e}, \sigma_0$ are symmetric and thus fully determined by 6 instead of 9 entries each.

In the following, we fix σ_0 and σ_e and adapt the general Metropolis-Hastings algorithm from Section 2.4.2 to sample from the posterior distribution of a constant conductivity matrix $\sigma_\mathrm{i} \in \mathbb{R}^{3\times 3}$ given measurement data $\phi_\mathrm{EMG} \in \mathbb{R}^{N_\mathrm{M}}$.

We construct arbitrary symmetric and positive definite conductivity matrices $\sigma_\mathrm{i} \in \mathbb{R}^{3\times 3}$ by rotating a given positive definite diagonal matrix σ_i^* by angles $\alpha = (\alpha_1, \alpha_2, \alpha_3)$ around the corresponding coordinate axes e_1, e_2 and e_3 as defined in Section 3.2.2:

$$\sigma_\mathrm{i}(\alpha) = R_1(\alpha_1)R_2(\alpha_2)R_3(\alpha_3)\sigma_\mathrm{i}^* R_3^\top(\alpha_3)R_2^\top(\alpha_2)R_1^\top(\alpha_1)$$

Here, R_k are the rotation matrices defined in Equation (3.2) and we call $\sigma_{\mathrm{i},jj}$ for $j = 1, 2, 3$ the *conductivity magnitudes*. Thus, we fully describe a constant intracellular conductivity matrix by six parameters: three conductivity magnitudes plus three rotation angles. We set $\boldsymbol{p} \coloneqq (\sigma_{\mathrm{i},11}, \sigma_{\mathrm{i},22}, \sigma_{\mathrm{i},33}, \alpha_1, \alpha_2, \alpha_3)$ and define the parameter space of the diagonal matrix entry describing the conductivity in longitudinal direction, i.e., in muscle fiber direction, $\mathcal{J}_\mathrm{l} \coloneqq [6, 10]$, the parameter space of the diagonal matrix entries describing the conductivity in transversal muscle fiber direction $\mathcal{J}_\mathrm{t} \coloneqq (0, 4]$, and the parameter space of the angles α_j for $j = 1, 2, 3$ as $\mathcal{J}_\alpha \coloneqq [0, \pi]$.

Note that we defined the parameter spaces for the conductivity magnitudes to contain the original values of the former KerMor implementation that we chose to serve as reference values in Section 3.3. For the rotation angles we use the fact that only the muscle fiber direction influences the forward EMG problem while the orientation of the muscle fiber direction has no impact, i.e., loosely speaking "$\mathcal{G}(d_\mathrm{F}) = \mathcal{G}(-d_\mathrm{F})$". Thus, choosing $\mathcal{J}_\alpha = [0, \pi]$ allows for arbitrary muscle fiber directions.

The parameter space $\boldsymbol{\mathcal{J}}$ of $\boldsymbol{p}$ is then defined as the product of these spaces. Note that the global parameter space depends on the physical interpretation of the conductivity magnitudes $\sigma_{\mathrm{d},11}, \sigma_{\mathrm{d},22}$, and $\sigma_{\mathrm{d},33}$. Exemplarily, if $\sigma_{\mathrm{d},11}$ is the longitudinal conductivity magnitude, we have $\boldsymbol{\mathcal{J}} = \mathcal{J}_\mathrm{l} \times \mathcal{J}_\mathrm{t} \times \mathcal{J}_\mathrm{t} \times \mathcal{J}_\alpha \times \mathcal{J}_\alpha \times \mathcal{J}_\alpha$.

Applying the above definitions, the goal of the Bayesian inverse EMG problem is to determine the conditional probability distribution $\boldsymbol{\rho}_{\phi_\mathrm{EMG}}$ of $\boldsymbol{p} \in \boldsymbol{\mathcal{J}}$ given ϕ_EMG. We

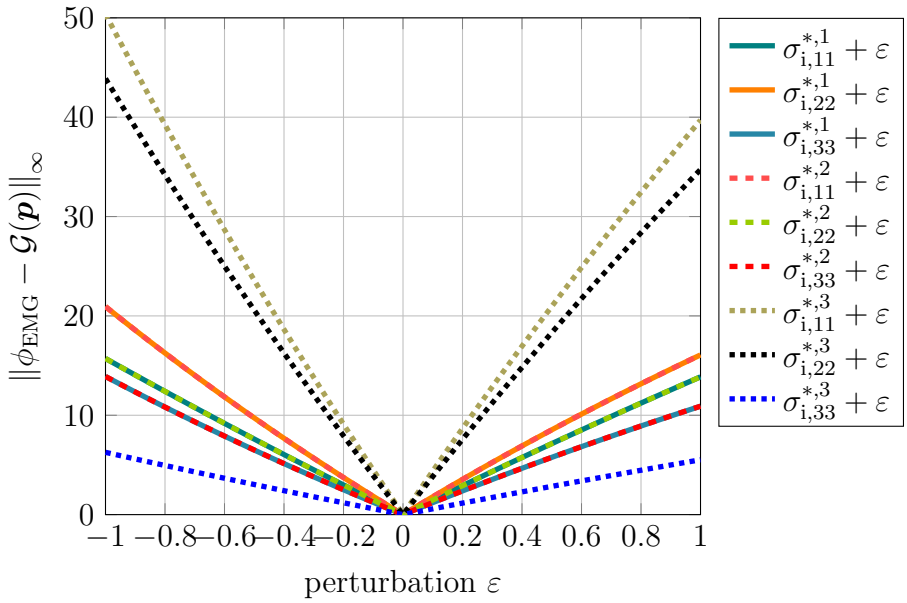

Figure 5.1.: Influence of changes in conductivity magnitudes $\sigma_{\text{i}}^{*,j}$ with $\alpha = (0, 0, 0)$ on the potential Φ

extend the KerMor forward EMG model, described in Chapter 3, by the Metropolis-Hastings algorithm to draw samples from this probability distribution. Our implementation provides the possibility to sample from the distribution of $\boldsymbol{p}$, as defined above, given measurement data ϕ_{EMG} or to fix either the magnitudes or the rotation angles. We denote the constructed Markov chain by $\mathfrak{p}$.

In the above discussion of the acceptance strategy we saw that the acceptance strategy of the Metropolis-Hastings algorithm is determined by the potential Φ, more precisely by the norm of the error between measured and computed surface EMG data $\|\phi_{\text{EMG}} - \mathcal{G}(\boldsymbol{p})\|_\Xi$.

For analyzing the acceptance strategy of the SA, our standard settings of the forward problem as described in Section 3.3 serve as reference configurations. We use the reference values of the intracellular conductivity $\sigma_{\text{i}}^{*,j}$ defined in Section 3.3 with $d_{\text{F}}^{*,j} = e_j$ for $j = 1, 2, 3$, and compute arbitrary intracellular conductivity matrices by rotating $\sigma_{\text{i}}^{*,j}$ as described above.

We show the influence of the six parameters $\boldsymbol{p} = (\sigma_{\text{i},11}, \sigma_{\text{i},22}, \sigma_{\text{i},33}, \alpha_1, \alpha_2, \alpha_3)$ on the error $\|\phi_{\text{EMG}} - \mathcal{G}(\boldsymbol{p})\|_\infty$ in the infinity norm in Figures 5.1 and 5.2. Note that the quantitative behavior of the error curves is independent of the choice of the norm due to the norm equivalence in $\mathbb{R}^{N_{\text{M}}}$.

We obtain from Figure 5.1 that changing the conductivity magnitudes influences the

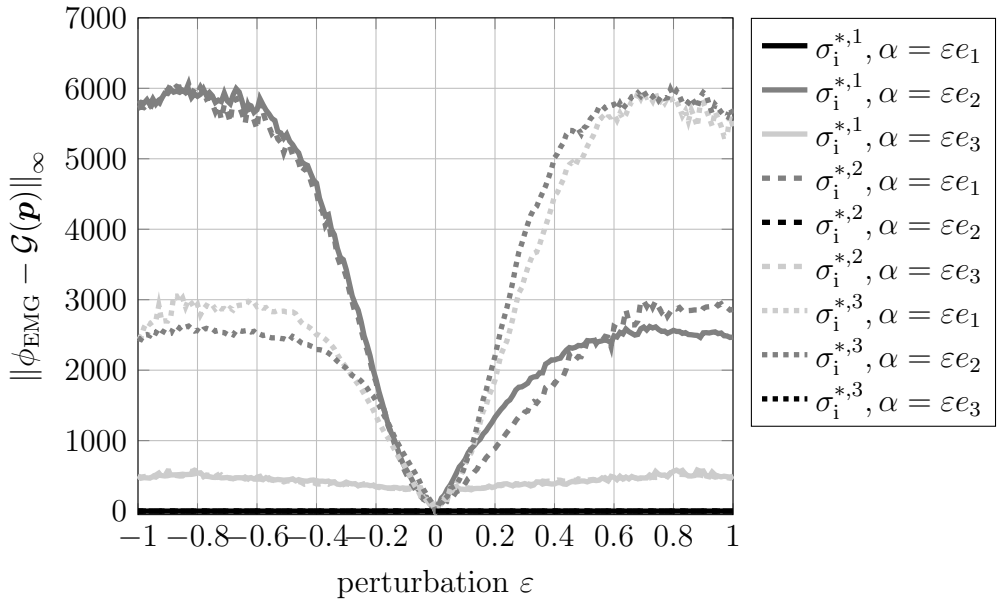

Figure 5.2.: Influence of changes in the rotation angles of $\sigma_{\mathrm{i}}(\alpha) = R_1(\alpha_1)R_2(\alpha_2)R_3(\alpha_3)\sigma_{\mathrm{i}}^{*,j}R_3^\top(\alpha_3)R_2^\top(\alpha_2)R_1^\top(\alpha_1)$ on the potential Φ

error norm linearly when keeping the rotation angles constant, here $\alpha = (0, 0, 0)$. Following our discussion in Section 3.2.4, we expected this linear behavior from the rank analysis in Figure 3.10. Further, we see that the influence of each conductivity magnitude is different. This behavior is explained by the underlying physical system. Knowing that $\sigma_{\mathrm{i},jj}^{*,j}$, $j = 1, 2, 3$, is the longitudinal intracellular conductivity, it is easy to understand that $\sigma_{\mathrm{i},jj}^{*,j}$ has the highest impact on the error norm for $j = 1, 2$.

Furthermore, for $j = 1, 2$ the influence of $\sigma_{\mathrm{i},33}^{*,j}$, i.e., the conductivity magnitude that describes the propagation of the electrical signals perpendicular to the measuring surface, is significantly higher than the influence of the conductivity magnitude describing the propagation of the electrical signals parallel to the measuring surface but perpendicular to the muscle fiber direction. This is due to the asymmetry of the geometry, i.e., the muscle cuboid, that has length 3 cm in e_1-and e_2-direction but only has length 1 cm in e_3-direction.

For the third reference conductivity, we observe that even though the muscle fiber direction is e_3, $\sigma_{\mathrm{i},33}^{*,3}$ has low impact on the potential while $\sigma_{\mathrm{i},33}^{*,1}$ and $\sigma_{\mathrm{i},33}^{*,2}$ have a similar impact. We reason the low impact of the longitudinal conductivity with the geometry used. Remember that we set `geo=[3,3,1]`, i.e., the muscle fibers are 1 cm long when $d_{\mathrm{F}} = \mathrm{e}_3$ and are 3 cm long when $d_{\mathrm{F}} = e_1$ or $d_{\mathrm{F}} = e_2$. Thus, the muscle fiber APs only travel a short distance when $d_{\mathrm{F}} = e_3$ compared to the other cases and altering

the longitudinal conductivity, which can be interpreted as the propagation speed of the APs through the muscle, has lower impact than altering the perpendicular conductivity magnitudes.

For changes in the rotation angels and fixed conductivity magnitudes $\sigma_{\mathrm{i}}^{*,j}$ as before, we see a strongly nonlinear behavior of the error norm $\|\phi_{\mathrm{EMG}} - \mathcal{G}(\boldsymbol{p})\|_{\infty}$ in Figure 5.2. Recapitulating the influence of the rotation angle and thus of the muscle fiber direction especially on the right-hand side of the forward EMG problem shows that the nonlinearity of the right-hand side is directly transferred to the error norm. See Section 2.6 for the theoretical and Section 3.2 for the discretization and implementation aspects of arbitrary muscle fiber directions and their influence on the right-hand side.

First, we see from the black lines in Figure 5.2 that rotations around the e_j-axis have no impact on the error norm $\|\phi_{\mathrm{EMG}} - \mathcal{G}(\boldsymbol{p})\|_{\infty}$ if the muscle fiber direction is e_j, for $j = 1, 2, 3$, for obvious reasons. As before, we split the discussion of our observations into the case $\sigma_{\mathrm{i}}^{*,j}$ for $j = 1, 2$ and the case $j = 3$. For the first two reference conductivities we again see a similar behavior when comparing the curves of $\alpha = \varepsilon e_2$ for $\sigma_{\mathrm{i}}^{*,1}$ and $\alpha = \varepsilon e_1$ for $\sigma_{\mathrm{i}}^{*,2}$, i.e., the gray straight and dashed lines, and the curves of $\alpha = \varepsilon e_3$ for $\sigma_{\mathrm{i}}^{*,1}$ and $\sigma_{\mathrm{i}}^{*,2}$, i.e., the light gray straight and dashed lines. The described behavior is, as before, explained by the symmetry of the forward EMG problem and the geometry for the reference values $\sigma_{\mathrm{i}}^{*,1}$ and $\sigma_{\mathrm{i}}^{*,2}$.

For $\sigma_{\mathrm{i}}^{*,3}$, we see a different behavior that is, however, similar for the rotations around the e_1- and e_2-axis, i.e., the dotted light gray and gray lines. The similarity of these two curves reflects the symmetry of the forward EMG problem under rotation of the muscle fiber direction $d_{\mathrm{F}} = e_3$ around the e_1- or e_2-axis.

Summarizing the influence of the parameters $\boldsymbol{p}$ on the error norm and thus on the acceptance strategy, we find a linear behavior for the conductivity magnitudes and a strongly nonlinear behavior for the rotation angles. We deduce that inferring the conductivity magnitudes is expected to be easier than inferring the rotation angles.

Using a local proposal distribution might improve the convergence of the Metropolis-Hastings algorithm significantly, especially when inferring the rotation angles. We thus introduce a sampling radius r_{s} and draw a new proposal $\boldsymbol{p}'$ uniformly from an interval of width $2r_{\mathrm{s}}$ around the latest accepted sample $\mathfrak{p}_j$ intersected with the parameter space $\boldsymbol{\mathcal{J}}$, i.e., $\boldsymbol{p}' \sim U([\mathfrak{p}_j - r_{\mathrm{s}}, \mathfrak{p}_j + r_{\mathrm{s}}] \cap \boldsymbol{\mathcal{J}})$. The initial proposal is drawn in the same manner with the reference value taking the place of the last accepted sample. We highlight, that our implementation of the Metropolis-Hastings algorithm allows choosing different sampling radii for the conductivity magnitudes and the rotation angles to account for

the significantly different influence of the magnitudes and angles on the potential Φ. Merging the above results into the general Metropolis-Hastings algorithm 2.3.1 finally leads to the SA as defined in Algorithm 5.1.1.

Algorithm 5.1.1 Standard Metropolis-Hastings algorithm (SA)

Input: Starting point $\mathfrak{p}_1$ for the Markov chain, sampling radius r_s, length of Markov chain N_s
Output: A Markov chain $\mathfrak{p}$

1: **for** $j = 1 \dots N_\mathrm{s} - 1$ **do**
2: propose $\boldsymbol{p}' \sim U([\mathfrak{p}_j - r_\mathrm{s}, \mathfrak{p}_j + r_\mathrm{s}] \cap \boldsymbol{\mathcal{J}})$ independent of $\mathfrak{p}_j$
draw $c \sim U([0,1])$
3: **if** $c \leq a(\mathfrak{p}_j, \boldsymbol{p}') = \min\left\{1, \exp\left(\Phi(\mathfrak{p}_j) - \Phi(\boldsymbol{p}')\right)\right\}$ **then**
4: set $\mathfrak{p}_{j+1} = \boldsymbol{p}'$
5: **else**
6: set $\mathfrak{p}_{j+1} = \mathfrak{p}_j$
7: **end if**
8: **end for**

Note that each accepted sample enters the Markov chain and that we forebear from the practice of discarding samples as so-called *burn-in*. Instead, we use the knowledge of the reference solution to obtain only valid proposals. We refer to [34, Section 11.4] for a detailed discussion of the usage of burn-in samples.

5.2. Validation of the Standard Metropolis-Hastings Algorithm

Within this section, our aims are to validate our implementation of the SA, quantify the convergence of the SA, and fix the sampling radius r_s for the conductivity magnitudes and the rotation angles. Moreover, we aim at determining how large the noise level ξ can grow before the SA diverges. Note that we compute artificial surface EMG measurements by adding Gaussian noise to the noise-free computed surface EMG data described in Chapter 3.

For validating the SA we proceed in several steps. First, we run the SA for inferring the conductivity magnitudes for a fixed number of proposals and varying sampling radius r_s and noise level ξ in Section 5.2.1. Second, we choose a Gaussian distribution for proposing new samples to the Markov chain and compare the behavior of the SA with Gaussian proposal distribution to the behavior of the SA with uniform proposal

distribution in Section 5.2.2. Third, we examine the influence of the number of parameters to be inferred on the behavior of the SA in Section 5.2.3. Finally, we examine the inferrability of the rotation angles in Section 5.2.4. As we have indicated above, we expect that the rotation angles are harder to infer than the conductivity magnitudes due to their nonlinear influence on the potential Φ and thus on the acceptance probability.

For evaluating our experiments, we denote the number of accepted proposals by N_a and the total number of proposals by N_s, and present the acceptance rate

$$\kappa_\mathrm{a} \coloneqq \frac{N_\mathrm{a}}{N_\mathrm{s}},$$

the mean absolute deviation

$$\mathrm{MAD}(\mathfrak{p}) \coloneqq \frac{1}{N_\mathrm{s}} \sum_{j=1}^{N_\mathrm{s}} |\mathfrak{p}_j - \bar{\mathfrak{p}}|,$$

and the variance

$$\mathrm{var}(\mathfrak{p}) \coloneqq \frac{1}{N_\mathrm{s} - 1} \sum_{j=1}^{N_\mathrm{s}} (\mathfrak{p}_j - \bar{\mathfrak{p}})^2$$

of the constructed Markov chain $\mathfrak{p}$, where $\bar{\mathfrak{p}}$ denotes the mean of the Markov chain $\mathfrak{p}$, compare Section 2.2.

5.2.1. Conductivity Magnitudes

As before, we use the standard settings from Section 3.3 as reference configurations and fix the rotation angles at $\alpha^* = (0, 0, 0)$. We run Algorithm 5.1.1 for sampling the conductivity magnitudes, i.e., $\boldsymbol{p} = (\sigma_{\mathrm{i},11}, \sigma_{\mathrm{i},22}, \sigma_{\mathrm{i},33}) \in \mathbb{R}^3$, for $r_\mathrm{s} \in \{0.3, 0.5, 0.7, 0.9\}$, $\xi \in \{0.05, 0.1, 0.2, 0.4\}$, and $N_\mathrm{s} = 1000$. The behavior of the sampled chains and the corresponding histogram plots are shown exemplarily in Figure 5.3.

Comparing the behavior of the chains in Figure 5.3c to the behavior of the chains in Figures 5.3a and 5.3e indicates that choosing a larger sampling radius r_s or higher noise level ξ leads to larger jumps in the chains. In the respective histogram plots, see Figure 5.3d, these jumps are represented by a larger variation, i.e., wider histograms with less significant peaks. Note that the blue histogram, which corresponds to the longitudinal conductivity magnitude, is higher and narrower than the red and green histograms that correspond to the transversal conductivity magnitudes. This behavior

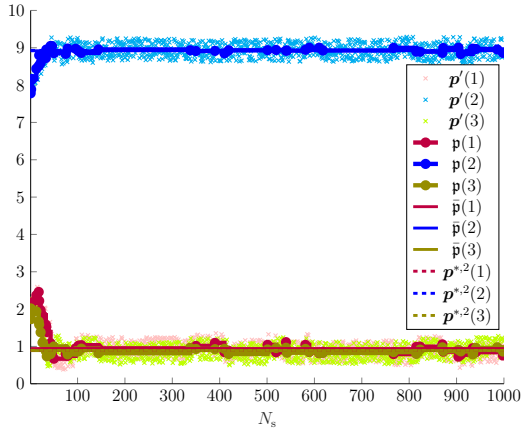

(a) Plot of sampled chains for $\boldsymbol{p}^{*,2}$, $r_s = 0.3$, $\xi = 0.1$

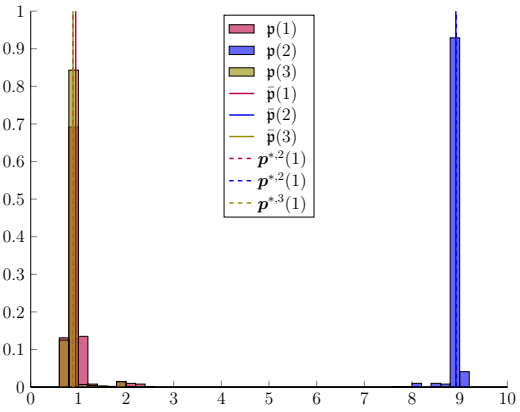

(b) Histogram plots for $\boldsymbol{p}^{*,2}$, $r_s = 0.3$, $\xi = 0.1$

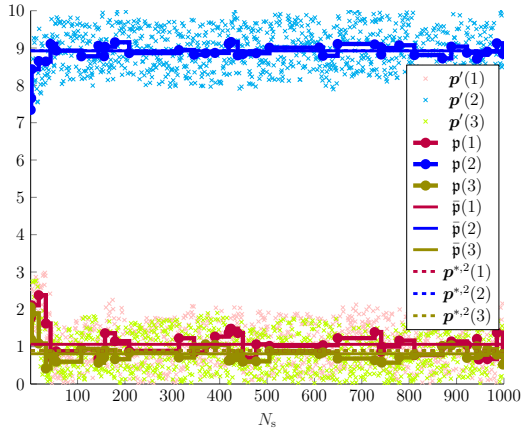

(c) Plot of sampled chains for $\boldsymbol{p}^{*,2}$, $r_s = 0.9$, $\xi = 0.4$

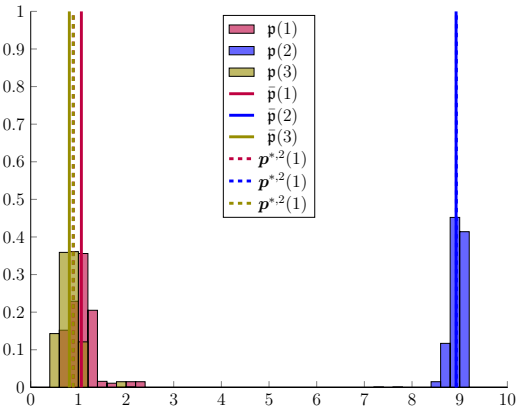

(d) Histogram plots for $\boldsymbol{p}^{*,2}$, $r_s = 0.9$, $\xi = 0.4$

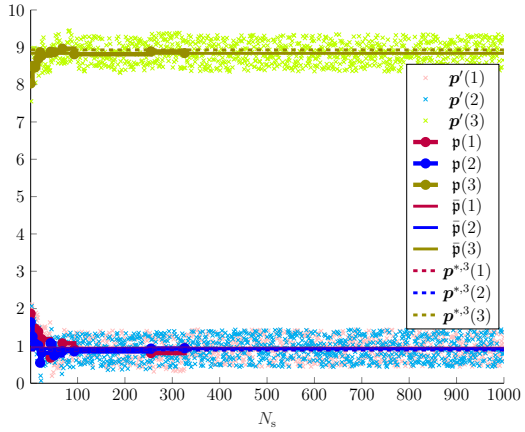

(e) Plot of sampled chains for $\boldsymbol{p}^{*,3}$, $r_s = 0.5$, $\xi = 0.05$

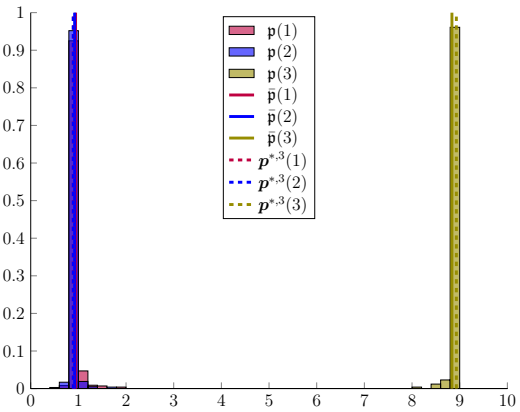

(f) Histogram plots for $\boldsymbol{p}^{*,3}$, $r_s = 0.5$, $\xi = 0.05$

Figure 5.3.: Plots of sampled chains of the conductivity magnitudes and corresponding histograms of the chains for different reference conductivities $\boldsymbol{p}^{*,j}$, sampling radius r_s, and noise level ξ in the standard settings from Section 3.3

Table 5.1.: Statistics of the standard algorithm for inferring the conductivity magnitudes with 1000 drawn samples for varying noise level ξ and sampling radius r_s in the standard settings from Section 3.3 and $\boldsymbol{p}^{*,1}$

r_s	ξ	κ_a	$\lvert\bar{\mathfrak{p}} - \boldsymbol{p}^{*,1}\rvert$ (%)			MAD($\mathfrak{p}$) (%)			var($\mathfrak{p}$) (%)		
0.30	0.05	3.00	0.13	7.64	0.02	3.88	8.02	5.81	0.87	3.14	2.09
0.30	0.10	4.70	0.19	2.83	1.32	4.77	11.95	6.79	1.11	4.04	2.97
0.30	0.20	14.10	1.50	1.76	0.74	6.35	13.05	9.90	1.14	4.89	2.75
0.30	0.40	32.70	3.78	12.80	4.76	9.28	23.46	16.13	1.66	9.79	4.91
0.50	0.05	1.70	2.08	1.31	4.10	2.34	9.04	4.58	0.71	2.66	2.89
0.50	0.10	2.40	0.13	1.31	2.98	4.65	12.24	7.46	0.88	3.44	3.20
0.50	0.20	5.60	0.69	11.60	6.55	6.72	14.63	10.46	1.10	4.30	3.85
0.50	0.40	14.50	0.73	9.47	5.71	10.12	23.42	16.71	1.84	8.50	5.76
0.70	0.05	1.40	1.04	3.81	1.72	6.28	14.42	6.18	1.11	4.96	3.98
0.70	0.10	1.60	1.71	4.94	1.76	6.70	15.75	7.30	1.15	5.42	4.25
0.70	0.20	2.90	2.78	1.58	3.04	4.65	13.50	10.19	0.79	4.47	4.30
0.70	0.40	7.70	1.89	12.83	3.16	8.63	22.52	15.80	1.51	8.89	5.54
0.90	0.05	1.30	0.21	5.92	0.15	7.01	6.00	7.54	1.27	2.71	4.87
0.90	0.10	1.70	2.21	2.32	3.23	5.66	13.50	15.24	1.33	5.20	6.27
0.90	0.20	1.50	2.86	16.70	4.21	5.01	15.22	7.84	1.19	7.04	4.91
0.90	0.40	4.80	1.03	13.38	1.66	8.75	19.39	13.64	1.79	7.92	6.25

results from the high influence of the longitudinal conductivity on the forward EMG problem compared to the low influence of the longitudinal conductivities, see Figure 5.1.

In Figure 5.3e, the Markov chain seems to be stuck at the values accepted in step 326. This behavior leads to a low acceptance rate, $\kappa_\mathrm{a} = 1.2$ in this case, as shown in Table 5.3. On the other hand, the value of the chain at step 326 is a point of high probability as it fulfills $|\mathfrak{p}_{326} - \boldsymbol{p}^{*,3}| = |(0.93916, 0.93818, 8.8451) - (0.893, 0.893, 8.930)| = (0.04616, 0.04518, 0.0849)$ and we thus expect the chain to put high weight on this value. Eventually, the chain will move to another point and continue exploring the parameter space. The described phenomenon of sampled Markov chains "getting stuck" at high probability points is further described in [101, Section 2.3.3]. The corresponding histogram plot, see Figure 5.3f, indicates that this behavior results in a very narrow histogram, where nearly all the mass lies in one histogram bin.

In Tables 5.1 to 5.3, we present the acceptance rate κ_a, the distance of the mean of the sampled chain to the reference parameters, i.e., $|\bar{\mathfrak{p}} - \boldsymbol{p}^{*,j}|$ and the MAD and variance of the constructed Markov chains for $r_\mathrm{s} \in \{0.3, 0.5, 0.7, 0.9\}$, $\xi \in \{0.05, 0.1, 0.2, 0.4\}$, and 1000 proposed samples as described before.

Analyzing the influence of the sampling radius r_s and the noise level ξ, we see that

Table 5.2.: Statistics of the standard algorithm for inferring the conductivity magnitudes with 1000 drawn samples for varying noise level ξ and sampling radius r_s in the standard settings from Section 3.3 and $\boldsymbol{p}^{*,2}$

r_s	ξ	κ_a	$\lvert\bar{\mathfrak{p}} - \boldsymbol{p}^{*,2}\rvert$ (%)			MAD($\mathfrak{p}$) (%)			var($\mathfrak{p}$) (%)		
0.30	0.05	2.30	7.26	1.54	1.08	8.35	3.66	6.33	4.85	1.07	2.50
0.30	0.10	4.50	5.07	1.03	0.54	11.78	4.96	8.34	5.58	1.21	2.71
0.30	0.20	14.50	8.15	0.55	2.76	15.14	5.88	11.18	6.35	1.35	3.44
0.30	0.40	34.20	10.63	0.85	6.98	20.98	9.84	16.56	8.67	2.03	5.39
0.50	0.05	1.50	9.74	1.76	0.91	7.55	2.59	5.28	4.19	0.96	2.25
0.50	0.10	2.10	8.16	1.72	1.97	9.38	3.73	8.23	4.55	1.00	2.59
0.50	0.20	4.70	9.84	0.02	3.80	15.41	6.40	11.02	6.35	1.21	3.08
0.50	0.40	14.70	13.86	0.23	5.84	20.03	8.04	15.43	8.12	1.63	4.83
0.70	0.05	1.60	11.45	3.67	1.11	13.56	5.21	6.95	6.85	1.21	2.58
0.70	0.10	1.60	5.31	0.92	3.80	15.06	5.24	8.39	7.03	1.14	2.81
0.70	0.20	2.90	3.96	1.23	6.65	19.49	8.79	12.21	8.28	1.72	3.61
0.70	0.40	7.40	15.27	0.40	7.60	21.01	9.52	15.35	9.79	1.98	4.76
0.90	0.05	1.10	10.57	6.03	5.63	11.73	4.27	7.33	5.95	1.26	2.30
0.90	0.10	1.20	12.81	4.87	3.67	2.93	4.65	8.95	6.04	1.27	2.45
0.90	0.20	1.90	10.53	2.07	4.42	23.54	7.35	9.74	9.96	1.51	2.79
0.90	0.40	4.00	16.99	0.58	8.28	20.27	11.80	14.18	8.60	2.36	4.19

increasing the noise level leads to higher acceptance rates as we allow higher uncertainties within the EMG data. On the other hand, increasing the sampling radius decreases the acceptance rate as the probability of drawing a valid proposal decreases with increasing the width of the proposal interval. Comparing the acceptance rates for the reference parameters $\boldsymbol{p}^{*,1}$, $\boldsymbol{p}^{*,2}$, and $\boldsymbol{p}^{*,3}$, we see that the acceptance rates behave similar for the first two reference parameters, see Tables 5.1, 5.2, while the acceptance rates are significantly lower for the third reference parameter, see Table 5.3. Note that we already expected the similarity of the chains for $\boldsymbol{p}^{*,1}$ and $\boldsymbol{p}^{*,2}$ from the analysis of the influence of the conductivity magnitudes on the potential, see Figure 5.1.

Aiming at a high acceptance rate thus implies choosing a small sampling radius and allowing for high noise levels, where the highest acceptance rates are reached for $r_\mathrm{s} = 0.3$ and $\xi = 0.4$. We emphasize that a high acceptance rate tells nothing about the quality of the accepted samples.

To quantify the quality of the sampled chains, we also discuss the distance of the mean of the chain to the reference parameters, the MAD, and the variance of the constructed Markov chains as shown in Tables 5.1 to 5.3. For the MAD and variance we again see the similarity of the sampled chains for $\boldsymbol{p}^{*,1}$ and $\boldsymbol{p}^{*,2}$ when exchanging the roles of

Table 5.3.: Statistics of the standard algorithm for inferring the conductivity magnitudes with 1000 drawn samples for varying noise level ξ and sampling radius r_s in the standard settings from Section 3.3 and $\boldsymbol{p}^{*,3}$

r_s	ξ	κ_a	$\lvert\bar{\mathfrak{p}} - \boldsymbol{p}^{*,3}\rvert$ (%)			MAD($\mathfrak{p}$) (%)			var($\mathfrak{p}$) (%)		
0.30	0.05	1.70	4.29	0.28	1.99	4.75	3.22	4.57	1.44	0.79	1.33
0.30	0.10	2.50	3.38	0.94	2.40	5.67	5.22	5.53	1.63	0.90	1.45
0.30	0.20	6.70	1.04	0.47	0.84	7.54	6.18	9.90	1.86	1.05	2.19
0.30	0.40	21.10	1.01	4.82	4.17	11.49	10.30	13.81	2.72	1.96	3.48
0.50	0.05	1.20	4.79	2.87	9.29	3.92	3.77	2.67	1.09	0.52	0.51
0.50	0.10	1.40	6.39	1.29	0.18	4.63	3.81	5.67	0.98	0.59	0.94
0.50	0.20	2.10	2.69	3.13	0.50	6.19	4.98	7.04	1.27	0.67	1.14
0.50	0.40	6.70	0.69	4.28	3.80	10.27	9.95	15.97	2.07	1.61	3.52
0.70	0.05	0.60	0.17	7.89	10.51	6.21	5.33	4.53	0.86	0.46	0.65
0.70	0.10	0.70	0.54	8.13	10.25	5.67	5.29	4.95	0.82	0.46	0.70
0.70	0.20	0.80	0.09	5.10	9.46	6.40	6.79	5.66	0.86	0.63	0.75
0.70	0.40	3.60	0.73	3.71	7.00	9.60	9.21	14.68	1.47	1.43	3.00
0.90	0.05	0.70	7.22	4.59	9.19	10.46	8.00	6.44	1.84	1.32	0.93
0.90	0.10	0.70	7.22	4.59	9.19	10.46	8.00	6.44	1.84	1.32	0.93
0.90	0.20	0.70	7.22	4.59	9.19	10.46	8.00	6.44	1.84	1.32	0.93
0.90	0.40	1.90	2.68	11.96	5.00	6.52	12.50	12.67	0.94	2.10	2.30

MAD($\mathfrak{p}(1)$) and MAD($\mathfrak{p}(2)$), and var($\mathfrak{p}(1)$) and var($\mathfrak{p}(2)$). The third reference parameter again shows a different behavior as expected from the discussion of Figure 5.1.

For minimizing the MAD and variance of the sampled chains, Tables 5.1 to 5.3 suggest choosing a small sampling radius together with a moderate noise level. Together with the aim of maximizing the acceptance rate, we deduce a preferred combination of $r_\mathrm{s} = 0.3$ and $\xi = 0.1$. Note that choosing the sampling radius to be 0.3 means that the proposal distribution samples from 15 % of the admissible intervals of width 4.

5.2.2. Gaussian Proposal Distribution

We redo the above parameter study and choose a Gaussian proposal distribution with the latest accepted sample as mean and the sampling radius r_s taking the place of the covariance. As the normal distribution is globally defined, we introduce the bounds of the parameter spaces by discarding the proposal whenever the proposed sample lies outside the admissible parameter space or the acceptance strategy suggests discarding the proposed sample. We run the Gaussian SA for $r_\mathrm{s} \in \{0.1, 0.3\}$ and $\xi \in \{0.05, 0.1, 0.2\}$. The acceptance rates κ_a, the distance of the mean of the sampled chains to the reference

Table 5.4.: Statistics of the standard algorithm for inferring the conductivity magnitudes with 1000 drawn samples for varying noise level ξ, sampling radius r_s, and Gaussian proposal distribution in the standard settings from Section 3.3

$\boldsymbol{p}^{*,j}$	r_s	ξ	κ_a	$\lvert\bar{\mathfrak{p}} - \boldsymbol{p}^{*,j}\rvert$ (%)			MAD($\mathfrak{p}$) (%)			var($\mathfrak{p}$) (%)		
1	0.1	0.05	8.90	3.36	5.03	5.37	6.38	13.08	9.14	1.73	5.75	3.84
1	0.1	0.1	19.80	3.44	4.25	2.94	7.14	15.48	9.24	1.88	6.83	4.00
1	0.1	0.2	37.20	4.11	1.59	0.83	8.43	20.19	13.69	2.04	8.87	5.26
1	0.3	0.05	1.70	0.46	7.82	0.13	4.53	7.21	7.43	0.97	4.04	3.64
1	0.3	0.1	2.80	0.53	0.10	1.21	4.43	10.99	6.51	0.87	4.65	3.04
1	0.3	0.2	7.40	1.69	4.27	1.54	7.54	17.61	10.76	1.26	6.83	3.73
2	0.1	0.05	7.60	5.26	1.67	2.05	8.88	3.81	5.81	4.28	0.94	2.44
2	0.1	0.1	20.30	6.63	2.54	1.75	11.00	4.73	7.90	4.54	1.00	2.70
2	0.1	0.2	39.00	6.89	0.63	1.68	14.55	7.02	10.36	5.52	1.33	3.32
2	0.3	0.05	1.40	6.41	2.52	1.94	8.31	3.52	5.44	4.08	0.79	1.71
2	0.3	0.1	2.40	11.52	1.70	1.19	8.69	5.91	7.74	3.88	0.92	1.86
2	0.3	0.2	6.80	10.11	0.14	1.99	18.07	7.32	10.07	6.89	1.19	2.33
3	0.1	0.05	4.90	2.47	2.57	3.06	6.73	4.24	7.75	3.04	1.28	2.42
3	0.1	0.1	10.60	2.35	1.74	2.62	7.01	5.13	8.41	3.08	1.36	2.57
3	0.1	0.2	26.60	2.69	0.25	1.78	8.81	7.47	10.83	3.26	1.72	3.03
3	0.3	0.05	1.30	3.44	1.16	3.16	3.83	2.79	4.06	1.03	0.72	0.68
3	0.3	0.1	1.70	3.35	1.75	4.93	3.85	3.62	4.93	1.06	0.74	0.80
3	0.3	0.2	3.10	1.58	0.30	1.33	6.47	7.15	7.81	1.32	1.14	1.15

parameters, i.e., $|\bar{\mathfrak{p}} - \boldsymbol{p}^{*,j}|$, and the MAD and variance of the constructed Markov chains are shown in Table 5.4.

As for the uniform proposal distribution, we see that increasing the sampling radius reduces the acceptance rate while increasing the noise level increases the acceptance rate. Again, we see a similarity of the acceptance rates for the first two reference parameters $\boldsymbol{p}^{*,1}$ and $\boldsymbol{p}^{*,2}$ and significantly lower acceptance rates for the third reference parameter $\boldsymbol{p}^{*,3}$. Further comparing the acceptance rates to the uniform case in Tables 5.1 to 5.3 shows that the acceptance rates for $r_\mathrm{s} = 0.1$ with the Gaussian proposal distribution are similar to the uniform case with $r_\mathrm{s} = 0.3$.

The MAD and variance of the sampled chains presented in Table 5.4 show that the symmetry of the chains for the first two parameters is less present than in the uniform case. For all reference parameters, we again achieve lowest MAD and variance for low sampling radius and noise level.

Summarizing the above observations, we deduce that the chains behave similar for

Table 5.5.: Acceptance rate for 1000 drawn samples, noise level $\xi = 0.1$, sampling radius $r_\mathrm{s} = 0.3$, and varying number of unknown parameters

unknown parameter(s)	$\boldsymbol{p}(1)$	$\boldsymbol{p}(1), \boldsymbol{p}(2)$	$\boldsymbol{p}(1), \boldsymbol{p}(2), \boldsymbol{p}(3)$
$\boldsymbol{p}^{*,1}$	18.70	11.10	4.70
$\boldsymbol{p}^{*,2}$	43.20	11.90	4.50
$\boldsymbol{p}^{*,3}$	19.90	3.70	2.50

uniform and Gaussian proposal distributions. In the following, we continue with uniform proposal distributions since the realization of the parameter bounds is more intuitive and since it represents our lack of knowledge about the unknown parameters $\boldsymbol{p}$.

5.2.3. Number of Parameters

For a uniform proposal distribution we fix the noise level $\xi = 0.1$ and the sampling radius $r_\mathrm{s} = 0.3$. We then run the SA for inferring $\boldsymbol{p}(1)$, $\boldsymbol{p}(1)$ and $\boldsymbol{p}(2)$, or $\boldsymbol{p}(1), \boldsymbol{p}(2)$ and $\boldsymbol{p}(3)$ for all three reference conductivities. Our aim is to investigate the influence of the number d of unknown parameters on the acceptance rate that we present in Table 5.5.

Again, we observe the symmetry of the forward EMG problem for the first two reference values from the similar acceptance rates when sampling the first two and all three magnitudes. Moreover, for $\boldsymbol{p}^{*,1}$ and $\boldsymbol{p}^{*,2}$ we clearly see the influence of the longitudinal conductivity magnitude, which reduces the acceptance rate drastically. For the first reference parameter this behavior shows in the low acceptance rate when inferring only the first (longitudinal) conductivity. For the second reference parameter the influence of the longitudinal conductivity shows in the significant reduction of the acceptance rate from 43.2 % to 11.9 %. In comparison, the influence of adding a transversal conductivity to the unknown parameters is low.

The difference in the behavior of the SA that we saw so far for the third reference parameter is obviously also present in this experiment. We see the high impact of $\boldsymbol{p}(1)$ and $\boldsymbol{p}(2)$ in the reduction of the acceptance rate from 19.9 % to 3.7 %, while additionally inferring $\boldsymbol{p}(3)$ leads to a reduction of less than 50 % of the acceptance rate down to 2.5 %. We again refer to Figure 5.1 for an illustration of the influence of the parameters on the forward EMG problem.

We conclude that increasing the number d of parameters in general leads to a reduction of the acceptance rate and that the magnitude of this reduction depends on the influence that the new parameter has on the forward model.

5.2.4. Rotation Angles

We rerun the parameter study shown in Tables 5.1 to 5.3 for validating the SA for inferring the rotation angles while fixing the conductivity magnitudes. Therefore, we choose the reference conductivity magnitudes $\sigma_{\mathrm{i}}^{*,j}$ for $j = 1, 2, 3$ as defined in Section 3.3, and the reference rotation angles $\alpha^{*,1} = (0, 0, \frac{\pi}{3})$, $\alpha^{*,2} = (0, \frac{\pi}{3}, 0)$, and $\alpha^{*,3} = (\frac{\pi}{3}, 0, 0)$. We vary the sampling radius $r_{\mathrm{s}} \in \{0.1, 0.3, 0.5\}$ and the noise level $\xi \in \{0.01, 0.05, 0.1, 0.2\}$, keep the conductivity magnitudes fixed, and infer the rotation angles, i.e., $\boldsymbol{p} = (\alpha_1, \alpha_2, \alpha_3)$.

Before presenting and discussing the results of the described parameter study, we define the chain of sampled muscle fiber directions $\mathfrak{d}$ as the Markov chain resulting from calculating the muscle fiber direction from the sampled rotation angles and we define the reference muscle fiber directions $d_{\mathrm{F}}^{*,j}$ as the muscle fiber direction calculated from the reference rotation angles $\alpha^{*,j}$ for $j = 1, 2, 3$. Remember that our overall goal is to detect the structure of the muscle tissue, not the rotation angles, compare our motivation in Section 1.1. For further explaining our interest in the chain of muscle fiber directions we plot the sampled chains of the rotation angles for $\sigma_{\mathrm{i}}^{*,2}$, $\alpha^{*,2}$, $r_{\mathrm{s}} = 0.5$, and $\xi = 0.01$ (Figure 5.4a) next to the corresponding chains of the sampled muscle fiber directions (Figure 5.4b) and the respective muscle fiber directions (Figure 5.4c) in Figure 5.4.

Comparing the chain of the sampled angles in Figure 5.4a to the chain of the sampled muscle fiber directions in Figure 5.4b we see that, e.g., the chain of the second rotation angle (plotted in blue) is far from the desired value represented by the blue dashed line. On the other hand, the chains of the entries of the muscle fiber directions clearly seem to converge to the desired reference direction. Figure 5.4c illustrates this convergence and also shows that the last accepted direction, which is plotted in black and nearly shadowed by the red reference direction, is close to the reference direction. This direction thus represents a point of high probability and hence explains the phenomenon of getting stuck that we already discussed in Section 5.2.1. We deduce that similar muscle fiber directions can be generated by largely differing rotation angles.

For calculating the mean, MAD, and variance of the sampled chains of the muscle fiber directions, we turn the accepted muscle fiber directions to be oriented in positive direction. We present the acceptance rates κ_{a} and statistics of the Markov chain $\mathfrak{d}$ produced by the SA for inferring the rotation angles for varying sampling radius and noise level in Table 5.6 for the reference rotation angle $\alpha^{*,1}$.

We observe that the noise level has nearly no influence on the behavior of the sampled chains. The only exception is the configuration $\sigma_{\mathrm{i}}^{*,1}$, $\alpha^{*,1}$, $r_{\mathrm{s}} = 0.3$, and $\xi = 0.2$, where the acceptance rate is slightly higher and, as a result, the chain varies more. For the reference

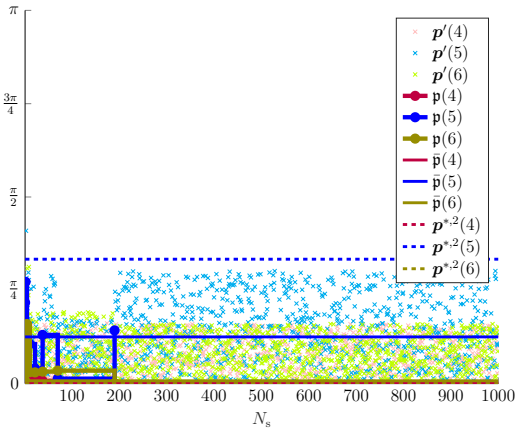

(a) Plot of sampled chains of rotation angles

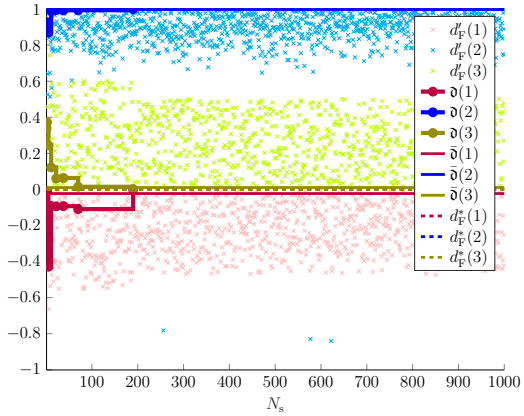

(b) Plot of sampled chains of muscle fiber directions

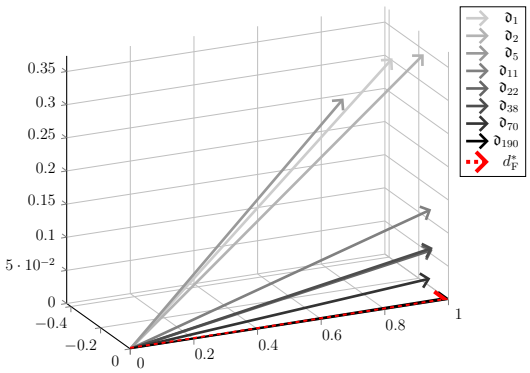

(c) Plot of accepted muscle fiber directions

Figure 5.4.: Plots of sampled chains and accepted directions for the SA for inferring the rotation angles for $\sigma_i^{*,2}$, $\alpha^{*,2}$, $r_s = 0.5$, and $\xi = 0.01$ in Section 5.2.4

Table 5.6.: Statistics of the standard algorithm for inferring the rotation angles with 1000 drawn samples for varying noise level ξ and sampling radius r_s in the standard settings from Section 3.3 and $\alpha^{*,1}$

$\sigma_\mathrm{i}^{*,j}$	r_s	ξ	κ_a	$\lvert\bar{\mathfrak{d}} - d_\mathrm{F}^*\rvert$ (%)			MAD($\mathfrak{d}$) (%)			var($\mathfrak{d}$) (%)		
1.00	0.10	0.01	0.40	0.27	0.16	0.84	0.41	0.23	0.27	0.00	0.00	0.00
1.00	0.10	0.05	0.40	0.27	0.16	0.84	0.41	0.23	0.27	0.00	0.00	0.00
1.00	0.10	0.10	0.40	0.27	0.16	0.84	0.41	0.23	0.27	0.00	0.00	0.00
1.00	0.10	0.20	0.40	0.27	0.16	0.84	0.41	0.23	0.27	0.00	0.00	0.00
1.00	0.30	0.01	1.00	0.42	0.29	0.77	1.12	0.64	1.30	0.04	0.01	0.02
1.00	0.30	0.05	1.00	0.42	0.29	0.77	1.12	0.64	1.30	0.04	0.01	0.02
1.00	0.30	0.10	1.00	0.42	0.29	0.77	1.12	0.64	1.30	0.04	0.01	0.02
1.00	0.30	0.20	1.20	0.53	0.25	0.99	1.61	0.89	0.51	0.05	0.01	0.01
1.00	0.50	0.01	0.70	0.07	0.14	1.01	1.24	0.62	1.55	0.11	0.02	0.04
1.00	0.50	0.05	0.70	0.07	0.14	1.01	1.24	0.62	1.55	0.11	0.02	0.04
1.00	0.50	0.10	0.70	0.07	0.14	1.01	1.24	0.62	1.55	0.11	0.02	0.04
1.00	0.50	0.20	0.70	0.07	0.14	1.01	1.24	0.62	1.55	0.11	0.02	0.04
2.00	0.10	0.01	0.50	0.31	0.57	0.98	0.20	0.34	0.12	0.00	0.01	0.00
2.00	0.10	0.05	0.50	0.31	0.57	0.98	0.20	0.34	0.12	0.00	0.01	0.00
2.00	0.10	0.10	0.50	0.31	0.57	0.98	0.20	0.34	0.12	0.00	0.01	0.00
2.00	0.10	0.20	0.50	0.31	0.57	0.98	0.20	0.34	0.12	0.00	0.01	0.00
2.00	0.30	0.01	0.80	1.74	3.44	2.64	0.92	2.02	0.85	0.03	0.17	0.01
2.00	0.30	0.05	0.80	1.74	3.44	2.64	0.92	2.02	0.85	0.03	0.17	0.01
2.00	0.30	0.10	0.80	1.74	3.44	2.64	0.92	2.02	0.85	0.03	0.17	0.01
2.00	0.30	0.20	0.80	1.74	3.44	2.64	0.92	2.02	0.85	0.03	0.17	0.01
2.00	0.50	0.01	0.70	4.44	5.53	3.05	2.30	5.57	0.59	0.20	1.34	0.02
2.00	0.50	0.05	0.70	4.44	5.53	3.05	2.30	5.57	0.59	0.20	1.34	0.02
2.00	0.50	0.10	0.70	4.44	5.53	3.05	2.30	5.57	0.59	0.20	1.34	0.02
2.00	0.50	0.20	0.70	4.44	5.53	3.05	2.30	5.57	0.59	0.20	1.34	0.02
3.00	0.10	0.01	0.60	0.30	0.28	0.00	0.24	0.12	0.00	0.00	0.00	0.00
3.00	0.10	0.05	0.60	0.30	0.28	0.00	0.24	0.12	0.00	0.00	0.00	0.00
3.00	0.10	0.10	0.60	0.30	0.28	0.00	0.24	0.12	0.00	0.00	0.00	0.00
3.00	0.10	0.20	0.60	0.30	0.28	0.00	0.24	0.12	0.00	0.00	0.00	0.00
3.00	0.30	0.01	0.40	0.91	0.73	0.01	0.72	0.17	0.01	0.01	0.00	0.00
3.00	0.30	0.05	0.40	0.91	0.73	0.01	0.72	0.17	0.01	0.01	0.00	0.00
3.00	0.30	0.10	0.40	0.91	0.73	0.01	0.72	0.17	0.01	0.01	0.00	0.00
3.00	0.30	0.20	0.40	0.91	0.73	0.01	0.72	0.17	0.01	0.01	0.00	0.00
3.00	0.50	0.01	0.30	2.86	1.18	0.06	0.51	0.28	0.04	0.01	0.01	0.00
3.00	0.50	0.05	0.30	2.86	1.18	0.06	0.51	0.28	0.04	0.01	0.01	0.00
3.00	0.50	0.10	0.30	2.86	1.18	0.06	0.51	0.28	0.04	0.01	0.01	0.00
3.00	0.50	0.20	0.30	2.86	1.18	0.06	0.51	0.28	0.04	0.01	0.01	0.00

Table 5.7.: Statistics of the standard algorithm for inferring the rotation angles with 1000 drawn samples for varying noise level ξ and sampling radius r_s in the standard settings from Section 3.3 and $\alpha^{*,2}$

$\sigma_\mathrm{i}^{*,j}$	r_s	κ_a	$\lvert\bar{\mathfrak{d}} - d_\mathrm{F}^*\rvert$ (%)			MAD($\mathfrak{d}$) (%)			var($\mathfrak{d}$) (%)		
1.00	0.10	0.60	4.66	0.56	2.91	1.59	0.81	1.10	0.05	0.01	0.02
1.00	0.30	0.50	4.40	1.56	3.11	4.68	2.25	3.60	0.36	0.10	0.21
1.00	0.50	1.10	5.18	12.98	29.78	33.08	25.00	30.30	18.82	11.67	15.49
2.00	0.10	0.80	0.61	0.01	1.10	0.34	0.02	0.62	0.00	0.00	0.01
2.00	0.30	0.70	1.00	0.07	1.06	1.48	0.11	1.50	0.04	0.00	0.08
2.00	0.50	0.80	2.27	0.22	1.07	3.41	0.36	1.40	0.26	0.01	0.12
3.00	0.10	1.00	0.10	2.42	0.24	0.04	0.39	0.06	0.00	0.01	0.00
3.00	0.30	0.90	3.27	17.69	0.82	4.09	17.04	0.60	0.17	3.06	0.01
3.00	0.50	0.50	0.29	3.04	0.10	0.68	2.94	0.12	0.03	0.46	0.01

angles $\alpha^{*,2}$ and $\alpha^{*,3}$, the Markov chains are completely independent of the examined noise levels and we thus present the statistics for $\alpha^{*,2}$ and $\alpha^{*,3}$ without mentioning the noise level in Tables 5.7 and 5.8.

From Tables 5.6 to 5.8 we immediately see that the acceptance rates are significantly lower compared to the acceptance rates of inferring the conductivity magnitudes in Tables 5.1 to 5.3. Recall that we expected such a behavior from the discussion of Figure 5.2 in the beginning of Section 5.1.

In contrast to the case of inferring the conductivity magnitudes, see Section 5.2.1, there is no obvious dependency of the acceptance rate on the sampling radius. The MAD and variance, however, have a tendency to be lowest for the smallest sampling radius, i.e., for $r_\mathrm{s} = 0.1$.

Since we have seen that the noise level has no influence on the sampled Markov chain of rotation angles, we set $\xi = 0.1$ as in the case of sampling the conductivity magnitudes. Furthermore, we specify the sampling radius for the rotation angles to be $r_\mathrm{s} = 0.1$, i.e., smaller than in the case of sampling the conductivity magnitudes, and thus account for the highly nonlinear dependence of the forward EMG problem on the rotation angles.

Moreover, the low acceptance rates indicate that a high number of samples needs to be drawn to explore the complete parameter space. Recall that drawing new samples includes evaluating the acceptance strategy to decide whether the proposed sample should become part of the Markov chain.

Motivated by the need of evaluating the acceptance strategy, which includes solving

Table 5.8.: Statistics of the standard algorithm for inferring the rotation angles with 1000 drawn samples for varying noise level ξ and sampling radius r_s in the standard settings from Section 3.3 and $\alpha^{*,3}$

$\sigma_\mathrm{i}^{*,j}$	r_s	κ_a	$\lvert\bar{\mathfrak{d}} - d_\mathrm{F}^*\rvert$ (%)			MAD($\mathfrak{d}$) (%)			var($\mathfrak{d}$) (%)		
1.00	0.10	0.90	0.02	1.24	0.17	0.03	0.98	0.55	0.00	0.03	0.00
1.00	0.30	1.00	0.20	3.51	0.18	0.26	4.08	1.29	0.00	0.24	0.03
1.00	0.50	1.60	4.70	45.26	3.16	40.19	42.95	4.26	17.22	19.34	0.24
2.00	0.10	0.90	0.56	0.48	0.27	0.22	0.39	0.23	0.00	0.00	0.00
2.00	0.30	0.50	0.84	0.34	0.18	0.37	0.74	0.43	0.00	0.01	0.00
2.00	0.50	0.50	2.83	6.22	3.21	0.51	1.24	0.69	0.01	0.07	0.02
3.00	0.10	0.90	3.35	0.09	0.24	3.70	0.13	0.40	0.27	0.00	0.00
3.00	0.30	0.80	7.03	0.15	0.55	4.32	0.24	0.55	0.30	0.00	0.01
3.00	0.50	0.70	5.94	0.95	1.13	4.08	1.99	1.36	0.77	1.06	0.58

the forward EMG problem, for a large number of samples, we look at the computation time. Running the SA for 100 000 proposals takes approximately 7.14 h. More significantly, evaluating the acceptance strategy makes up 97.47 % of the computing time. Obviously, we need a way to accelerate the evaluation of the acceptance strategy to achieve a competitive algorithm.

5.3. Tensorized Metropolis-Hastings Algorithm

In Section 3.2.4 we derived a low-rank tensor representation of the parameter-dependent forward EMG problem and mentioned that using this tensor representation could accelerate the sampling process of the SA. The reason for this consideration is that once the tensor solution $\boldsymbol{\phi}$ is computed for all parameters $\boldsymbol{p}^\mathrm{h}$ on a discrete parameter grid $\boldsymbol{\mathcal{J}}^\mathrm{h}$, the evaluation of the tensor solution, and thus the forward EMG problem, for a specific parameter $\boldsymbol{p}^\mathrm{h} \in \boldsymbol{\mathcal{J}}^\mathrm{h}$ is cheap, compare Section 2.5. Combining the low-rank tensor representation and the SA, we proceed as follows.

We discretize the parameter space $\boldsymbol{\mathcal{J}}$ with grid size $h_{\boldsymbol{p}}$ and precompute the solution of the parameter-dependent forward EMG problem for all $\boldsymbol{p}^\mathrm{h} \in \boldsymbol{\mathcal{J}}^\mathrm{h}$ using our standard settings from Section 3.3. Recall, that storing the parameter-dependent solution for all parameters $\boldsymbol{p}^\mathrm{h} \in \boldsymbol{\mathcal{J}}^\mathrm{h}$ is infeasible unless using low-rank tensor formats, such as the hierarchical Tucker format.

Having precomputed the parameter-dependent tensor solution $\boldsymbol{\phi}$ for all parameters

$\boldsymbol{p}^{\mathrm{h}} \in \boldsymbol{\mathcal{J}}^{\mathrm{h}}$ enables us to evaluate the precomputed tensor solution with arithmetic cost in $\mathcal{O}(dr^3)$, where d is the number of parameters and r the representation rank of the tensor, see Section 2.5. Thus, we accelerate the evaluation of the acceptance strategy by evaluating the tensor solution $\boldsymbol{\phi}$ for a proposed parameter $\boldsymbol{p}^{\mathrm{h}} \in \boldsymbol{\mathcal{J}}^{\mathrm{h}}$ instead of solving the forward EMG problem. Note that, due to the discretization of the parameter space, we restrict the proposal distribution to $\boldsymbol{\mathcal{J}}^{\mathrm{h}}$ intersected with an interval of radius r_{s} around the last accepted sample. Inserting the above changes into the SA yields the algorithm that we call the *tensorized algorithm (TA)* presented in Algorithm 5.3.1. This is joint work with Tim A. Werthmann and has similarly been published previously in [88].

Algorithm 5.3.1 Tensorized Metropolis-Hastings algorithm (TA)

Input: Starting point $\mathfrak{p}_1$ for the Markov chain, sampling radius r_{s}, parameter grid size $h_{\boldsymbol{p}}$, length of Markov chain N_{s}
Output: A Markov chain $\mathfrak{p}$

Precompute $\mathcal{G}(\boldsymbol{p}^{\mathrm{h}})$ for all $\boldsymbol{p}^{\mathrm{h}} \in \boldsymbol{\mathcal{J}}^{\mathrm{h}}$ using tensor formats and Algorithm 2.5.1
for $j = 1 \dots N_{\mathrm{s}} - 1$ **do**
  propose $\boldsymbol{p}' \sim U([\mathfrak{p}_j - r_{\mathrm{s}}, \mathfrak{p}_j + r_{\mathrm{s}}] \cap \boldsymbol{\mathcal{J}}^{\mathrm{h}})$ independent of $\mathfrak{p}_j$
  draw $c \sim U([0,1])$
  if $c \leq a(\mathfrak{p}_j, \boldsymbol{p}') = a(\mathcal{G}(\mathfrak{p}_j), \mathcal{G}(\boldsymbol{p}'))$ **then**
    set $\mathfrak{p}_{j+1} = \boldsymbol{p}'$
  else
    set $\mathfrak{p}_{j+1} = \mathfrak{p}_j$
  end if
end for

We emphasize that we exactly represent the operator and the right-hand side of the forward EMG problem for all discrete parameter combinations within the hierarchical Tucker format. Additionally, we compute the tensor solution using Algorithm 2.5.1 with specified truncation accuracy, resulting in an error-controlled approximation of the solution tensor. Moreover, the fast decay of the singular values in Figure 3.10 justifies the use of low-rank tensor formats to represent the tensor solution. Summarizing, we thus expect that the Markov chains constructed by the SA and TA behave similarly despite the additional discretization of the parameter space.

5.3.1. Validation of the Tensorized Metropolis-Hastings Algorithm

We validate the TA against the SA within the standard setting from Section 3.3 with noise level $\xi = 0.1$ and sampling radius $r_{\mathrm{s}} = 0.3$. We draw the initial proposal uniformly from the interval with radius r_{s} around the midpoint of the parameter grid.

Table 5.9.: Comparison of the tensorized algorithm (upper half) and the standard algorithm (lower half) with 1000 drawn samples, Gaussian noise with $\xi = 0.1$ and sampling radius $r_\mathrm{s} = 0.3$ in the standard settings of Section 3.3

$\boldsymbol{p}^{*,j}$	κ_a	$\lvert\bar{\mathfrak{p}} - \boldsymbol{p}^{*,j}\rvert$ (%)			MAD($\mathfrak{p}$) (%)			var($\mathfrak{p}$) (%)		
1	5.70	1.67	4.54	1.30	5.69	11.06	7.40	1.16	3.61	3.05
2	4.40	4.33	1.53	0.30	11.67	4.82	8.65	5.62	1.17	2.73
3	2.20	4.62	0.58	3.41	4.43	5.22	4.85	1.46	0.90	1.31
1	4.70	0.19	2.83	1.32	4.77	11.95	6.79	1.11	4.04	2.97
2	4.50	5.07	1.03	0.54	11.78	4.96	8.34	5.58	1.21	2.71
3	2.50	3.38	0.94	2.40	5.67	5.22	5.53	1.63	0.90	1.45

As in Section 3.2.4 we compute the tensor solution on a conductivity grid with grid size $h_{\boldsymbol{p}} = 0.001$ and $A^{\mathrm{h},(0)}$ using the conductivity at the midpoint of the corresponding grid. Note that by using $h_{\boldsymbol{p}} = 0.001$ we introduce an additional error in the third decimal place.

We run both algorithms proposing 1000 samples. We present the acceptance rate κ_a, the distance of the mean of the sampled chains to the reference parameters, and the MAD and variance of the sampled chains in Table 5.9. We observe that both methods have similar acceptance rates and that the chains produced using the TA also show the symmetric behavior for the reference conductivity magnitudes $\boldsymbol{p}^{*,1}$ and $\boldsymbol{p}^{*,2}$. We further notice that the MAD and variance of the SA and TA agree at least in the order of magnitude and we expect these values to approach further when drawing more samples. We draw this conclusion from the fact that we potentially choose different initial proposals for the Markov chain in the SA and the TA.

For validation of this claim we rerun the above experiment but this time draw 5000 samples. We present the results in Table 5.10. We observe, that the acceptance rates, the distance of the mean of the sampled chains to the reference parameters, the MAD, and the variance of the chains sampled using the TA are closer to the values generated using the SA for 5000 samples than for 1000 samples. Moreover, most differences are in the third or fourth decimal place. Recall that we choose the parameter grid size to be $h_{\boldsymbol{p}} = 0.001$ such that we cannot expect the TA to have higher accuracy.

We conclude that the sampling process of both algorithms is similar and that our tensor approach is therefore a promising ansatz for accelerating the SA.

Table 5.10.: Comparison of the tensorized algorithm (upper half) and the standard algorithm (lower half) with 5000 drawn samples, Gaussian noise with $\xi = 0.1$, sampling radius $r_\mathrm{s} = 0.3$, and truncation accuracy 1×10^{-6} in the setting of Section 3.3

$\boldsymbol{p}^{*,j}$	κ_a	$\lvert\bar{\mathfrak{p}} - \boldsymbol{p}^{*,j}\rvert$ (%)			MAD($\mathfrak{p}$) (%)			var($\mathfrak{p}$) (%)		
1	3.18	0.06	0.59	0.34	3.57	7.04	4.70	0.34	1.20	0.79
2	4.60	0.44	0.86	2.03	7.91	3.46	5.02	1.75	0.35	0.75
3	0.90	1.25	1.24	2.82	3.79	3.08	3.93	0.43	0.26	0.45
1	2.84	0.70	3.01	0.09	3.19	6.98	4.91	0.27	1.18	0.67
2	4.78	0.55	0.67	0.41	10.26	3.82	5.42	2.17	0.38	0.81
3	1.00	1.18	0.37	2.47	3.51	2.68	3.25	0.41	0.23	0.40

5.3.2. Speedup Tests

As indicated at the end of Section 5.2, the cost of drawing one sample from the posterior distribution approximately equals the solution time T_s of the discretized forward EMG problem for the SA and thus approximately equals the evaluation time T_e of the precomputed tensor solution for the TA. Therefore, the runtime of the SA is $T_{\mathrm{tot,SA}} = N_\mathrm{s} T_\mathrm{s}$, while the runtime of the tensorized algorithm equals the sum of the precomputation time T_p and the evaluation times, i.e., $T_{\mathrm{tot,TA}} = T_\mathrm{p} + N_\mathrm{s} T_\mathrm{e}$. We notice that asymptotically the speedup $\frac{N_\mathrm{s} T_\mathrm{s}}{T_\mathrm{p} + N_\mathrm{s} T_\mathrm{e}}$ is limited by the quotient $\frac{T_\mathrm{s}}{T_\mathrm{e}}$ for $N_\mathrm{s} \to \infty$.

We run two experiments to quantify the (absolute) speedup $\frac{\text{runtime SA}}{\text{runtime TA}}$ of the TA compared to the SA using the standard settings from Section 3.3. In the first test, we vary the number of samples while keeping all other parameters fixed. We thus run both algorithms in the standard setting from Section 3.3 for 125 samples and double the number of samples until reaching 128 000 samples. We present the speedup of the TA compared to the SA in Figure 5.5a. Moreover, we plot the limit $\frac{\bar{T}_\mathrm{s}}{T_\mathrm{e}} = 156.80$ of the speedup for the average solution and evaluation time in red. We observe that the speedup curve grows steadily and flattens as the number of samples increases. For the last plotted data point we see a slight decrease in the speedup curve towards the computed average limit $\frac{\bar{T}_\mathrm{s}}{T_\mathrm{e}}$. This decrease in the speedup is caused by slight fluctuations in the average sampling and tensor evaluation times throughout the test runs. Even if the speedup slowly decreases for the last shown data point, the acceleration by using the tensor representation makes a difference of running the SA for multiple hours (10.07 h for 128 000 samples) or the TA for several minutes (8.89 min for 128 000 samples).

Second, we run both algorithms in the standard settings for spatial grid sizes $h_x =$

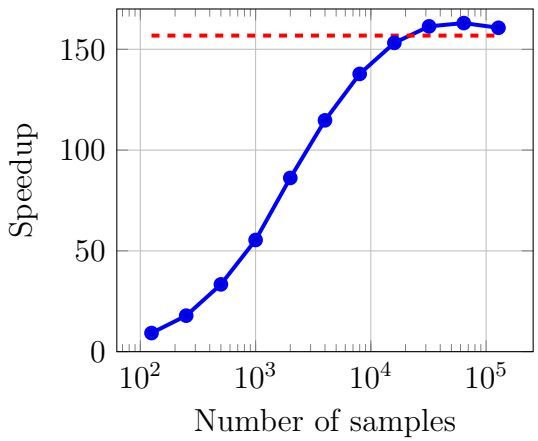

(a) Fixed grid size and varying number of samples

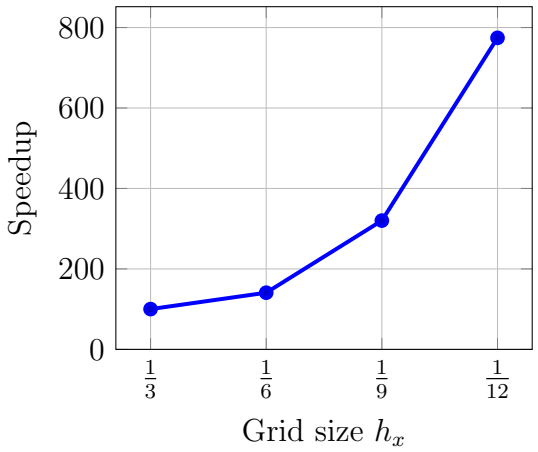

(b) 100 000 samples and varying grid size h_x

Figure 5.5.: Speedup of the tensorized algorithm compared to the standard algorithm in the setting of Section 3.3

$\frac{1}{3}, \frac{1}{6}, \frac{1}{9}, \frac{1}{12}$. Furthermore, we reduce the number of samples to 100 and extrapolate the measured sampling times to 100 000 samples to reduce the overall computation time. For the interpolation we use the above formulas $T_{\text{tot,SA}} = N_\text{s} T_\text{s}$ for the SA and $T_{\text{tot,TA}} = T_\text{p} + N_\text{s} T_\text{e}$ for the TA inserting the average sampling and evaluation times. Figure 5.5b shows the speedup resulting from this extrapolation.

As expected, we observe that the speedup in Figure 5.5b grows steadily and is unbounded in contrast to the speedup for fixed grid size and increasing number of samples in Figure 5.5a. For $h_x = \frac{1}{12}$ we observe a speedup of 774.37 which corresponds to an estimated runtime of 2.78 h for the TA compared to an estimated runtime of 2150.90 h($\approx$ 89.62 d) for the SA. These numbers explain our need for extrapolation of the above numbers.

We conclude that using the TA enables us to solve problems in reasonable time that are infeasible to solve using the SA. More precisely, inferring the conductivity magnitudes for geometries with a high spatial resolution becomes feasible using the tensor approach.

5.3.3. Limitations of the Tensorized Algorithm

When deriving the tensor representation of the right-hand side of the forward EMG problem in Section 3.2.4, we already discussed that our approach only holds for known muscle fiber directions, i.e., known rotation angles. We saw that the dependence of the right-hand side on the rotation angles is highly nonlinear and, to our knowledge, there

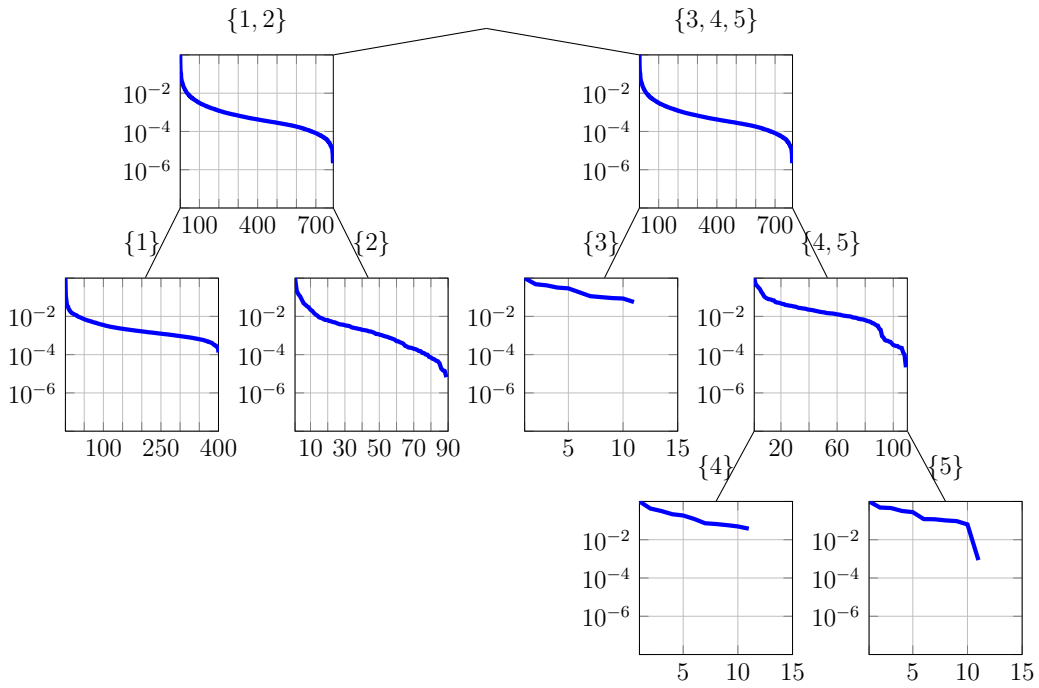

Figure 5.6.: Relative singular values of the corresponding matricization of the tensor solution of the forward EMG problem described in Section 3.2.4 for varying rotation angles

exists no algorithm to exactly represent this behavior using low-rank tensor formats.

Furthermore, the tensor solution of the rotation angle-dependent forward EMG problem has full rank as shown in Figure 5.6. For generating the singular value plot in Figure 5.6 we solve the parameter-dependent forward EMG problem with the rotation angles being the free parameters, i.e., $\boldsymbol{p} = \alpha \in [0, \pi] \times [0, \pi] \times [0, \pi]$, on a parameter grid with grid size $h_{\boldsymbol{p}} = 0.1\pi$. For plotting the singular values of the resulting solution tensor, which then is of size $400 \times 101 \times 11 \times 11 \times 11$, we use the `plot_sv` function of the `htucker` toolbox [61], compare Section 3.2.4. We read from Figure 5.6 that the solution tensor has full rank, i.e., rank 11, in the parameter dimensions $3, 4$ and 5. Moreover, the matricizations combining the parameters, i.e., the matricizations indexed by $\{4, 5\}$ and $\{3, 4, 5\}$, also have full rank. Further, the rank of the matricizations of the solution tensor with respect to the spatial and time dimension, i.e., dimensions 1 and 2, is 400 and 89 and thus full compared to the dimension of the solution tensor.

Consequently, the geometry must be known for applying the TA. Therefore, the TA is not suitable for the development of a radiation free imaging technique and different techniques are needed to accelerate the sampling process in the SA, see the outlook

in Chapter 7. We emphasize that the TA, nevertheless, enables us to infer material parameters, here the conductivity magnitudes, that are not directly measurable in living patients. The knowledge of patient specific parameters is crucial, e.g., in personalized treatment.

5.4. Standard Settings for Sampling

Summarizing the parameter studies of the last two sections, we define the following standard settings for the sampling algorithms in addition to the settings in Section 3.3. We allow additive Gaussian measurement errors with noise level $\xi = 0.1$ and set the sampling radius for the conductivity magnitudes to $r_{\mathrm{s}} = 0.3$. For inferring the rotation angles, we choose the sampling radius to be $r_{\mathrm{s}} = 0.1$. We use the parameter space of the diagonal matrix entry describing the conductivity in longitudinal direction $\mathcal{J}_{\mathrm{l}} \coloneqq [6, 10]$, the parameter space of the diagonal matrix entries describing the conductivities in the transversal muscle fiber directions $\mathcal{J}_{\mathrm{t}} \coloneqq (0, 4]$, and the parameter space of the rotation angles $\mathcal{J}_{\alpha} \coloneqq [0, \pi]$.

6. Use Cases

Throughout this chapter we apply the SA and TA derived and validated in Chapter 5 to several use cases that are related to clinical applications. Therefore, we modify the muscle cuboid setting described in Section 3.3.

In Section 6.1, we apply the TA for quantifying the influence of a layer of surrounding tissue on the inferability of the conductivity magnitudes. Here, we assume that the muscle fiber directions or rotation angles are known by an imaging technique such as CT scans.

We generalize the scenario from Section 6.1 to inferring the structure of electrically active tissue in Section 6.2. Here, we examine the suitability of the SA for inferring the muscle fiber direction and conductivity magnitudes simultaneously. Moreover, we quantify the influence of a layer of surrounding tissue on the inferability of the muscle fiber direction and conductivity magnitudes.

In Section 6.3, we investigate the inversion of the two muscle scenario introduced in Section 3.2.3. This scenario introduces additional model parameters, namely the thickness of the two muscles and the conductivity magnitudes and rotation angle of the second muscle. Estimating these parameters, we start with inferring only the thickness of the muscles in Section 6.3.1 and increase the number of parameters until inferring all nine model parameters in Section 6.3.5.

6.1. Use Case 1: Inferring the Magnitude of the Electrical Conductivity

Within this section we investigate the parameter identification problem of inferring the conductivity magnitudes from surface EMG measurements. More precisely, we look at the muscle cuboid described in Section 5.4 and add a layer of surrounding tissue D_{B} of thickness θ on top, i.e., in e_3-direction, of the muscle tissue cuboid as depicted in Figure 2.4. We then place the measuring electrodes at the skin surface, i.e., the top boundary of the layer of surrounding tissue. The muscle cuboid can be interpreted as the

idealized geometry of the muscle part lying under a rectangular (here square) electrode grid. Our interest now is to infer the conductivity magnitudes and to investigate the influence of the thickness θ of the surrounding tissue.

Transferring the above assumptions to a clinical setup, imagine that the structure of a body region of interest is known through an imaging technique like a CT or MRI scan, see Chapter 1. The muscle fiber directions of the underlying muscle tissue as well as the boundaries between different types of tissue can be extracted from the results of those imaging techniques. The electrical conductivity of the regarded tissue is, however, still unknown and we apply the TA introduced in Section 5.3 for inferring the conductivity values of the muscle tissue.

We thus fix the rotation angles at $\alpha^* = (0, 0, 0)$ such that the conductivity magnitudes remain as the free parameters, i.e., $\boldsymbol{p} = (\sigma_{\mathrm{i},11}, \sigma_{\mathrm{i},22}, \sigma_{\mathrm{i},33})$. Furthermore, we chose $\boldsymbol{p}^{*,1} = (8.93, 0.893, 0.893)$ as reference values for the conductivity magnitudes and otherwise use the standard settings defined in Sections 3.3 and 5.4. For investigating the influence of the thickness θ of the layer of surrounding tissue on the quality of the estimated parameters, we vary $\theta \in \{0, \frac{1}{6}, \frac{1}{3}, \frac{1}{2}, \frac{2}{3}, \frac{5}{6}, 1\}$. We remark that the thickness of the surrounding tissue must be a multiple of the spatial grid size h_x in the original KerMor implementation of the geometry and we thus set $h_x = \frac{1}{6}$. Note further that $\theta = 0\,\mathrm{cm}$ corresponds to the setting of Section 5.2.1.

We present the acceptance rates and statistical data of the sampled chains for varying thickness θ of the layer of surrounding tissue in Table 6.1. The values for $\theta = 0\,\mathrm{cm}$, i.e., the case of no surrounding tissue, serve as reference values.

Table 6.1.: Statistics of the chains of the conductivity magnitudes for different thicknesses of the surrounding tissue layer θ with reference conductivity $\boldsymbol{p}^{*,1}$

θ	κ_{a}	$\lvert\bar{\mathfrak{p}} - \boldsymbol{p}^{*,1}\rvert$ (%)			MAD($\mathfrak{p}$) (%)			var($\mathfrak{p}$) (%)		
0	3.18	0.06	0.59	0.34	3.57	7.04	4.70	0.34	1.20	0.79
1/6	4.90	1.78	13.35	2.21	4.12	20.16	5.53	0.76	9.22	2.41
1/3	6.00	0.12	6.88	2.53	4.27	21.20	5.42	0.84	9.82	2.41
1/2	7.90	1.84	5.18	0.27	5.02	24.03	5.79	1.07	11.75	2.11
2/3	10.60	0.63	8.76	0.25	6.68	26.50	6.39	1.23	12.53	2.18
5/6	14.40	2.03	2.39	0.80	9.42	30.20	5.85	1.93	12.72	1.44
1	19.80	4.06	3.74	1.01	12.52	24.52	6.42	3.02	9.08	1.48

From Table 6.1 we observe that the acceptance rate κ_{a} grows steadily with increasing thickness θ of the surrounding tissue. For the MAD and variance of the sampled chain we observe a similar behavior and deduce that adding surrounding tissue on top of the

muscle cuboid introduces uncertainty to the algorithm. This additional uncertainty is caused by the smoothing effect of the Laplace equation that is solved in the additional surrounding tissue layer, see Section 2.6.4.

Examples of the sampled chains and corresponding histogram plots for $\theta = \frac{1}{6}\,\text{cm}$, $\theta = \frac{1}{2}\,\text{cm}$, and $\theta = \frac{5}{6}\,\text{cm}$ are shown in Figure 6.1. Figures 6.1a, 6.1c, and 6.1e show that the sampled chains of the conductivity magnitudes vary more with growing thickness of the layer of surrounding tissue. This behavior results in the growing MAD and variance that we observed from Table 6.1. Figures 6.1b, 6.1d, and 6.1f show the respective histogram plots, where the increasing uncertainty of the TA shows in a widening and shrinking of the histograms, especially in the red histograms that correspond to the longitudinal conductivity magnitude.

We deduce that the conductivity magnitudes of the muscle can be inferred, but, as expected, uncertainty grows with increasing thickness of the layer of surrounding tissue. Since the drawn samples of the posterior probability distribution of the conductivity magnitudes include knowledge of these uncertainties, the algorithm has high potential to not only estimate the conductivity magnitudes but also quantify the uncertainties included in these estimates. Hence, the TA is a powerful tool for inferring the conductivity magnitudes of the biological tissue.

6.2. Use Case 2: Inferring the Structure of Electrically Active Tissue

For further approaching our overall goal of contributing to a new radiation-free and non-invasive imaging technique as described in Section 1.1 we also need to infer the structure of the body part of interest. In a first step, we thus extend the scenario described in Section 6.1 by also inferring the muscle fiber directions represented by the rotation angles such that the free parameter also includes the rotation angles, i.e., $\boldsymbol{p} \in \mathbb{R}^6$.

Note that we need to use the SA in the described scenario as the muscle fiber direction is no longer fixed, compare our discussion in Section 5.3.3. Apart from changing the sampling algorithm to be the SA, we stay in the setting described in Section 6.1 with $\boldsymbol{p}^{*,1} = (8.93, 0.893, 0.893, 0, 0, 0)$. As discussed in Section 5.2.4, we use the muscle fiber directions computed from the sampled rotation angles to quantify the quality of the sampled rotation angles.

We present the statistics of the sampled chains of the conductivity magnitudes in Table 6.2 and the statistics of the sampled chains of the muscle fiber directions in

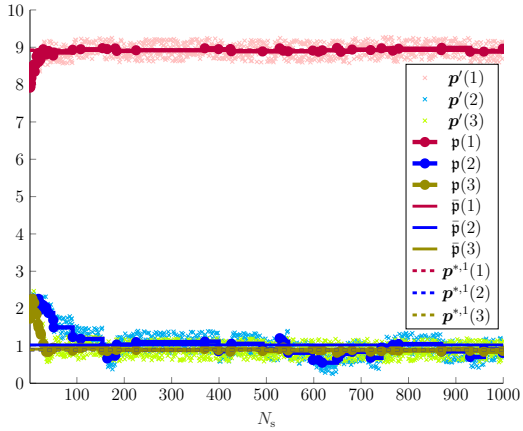

(a) Plot of sampled chains for $\theta = \frac{1}{6}$ cm

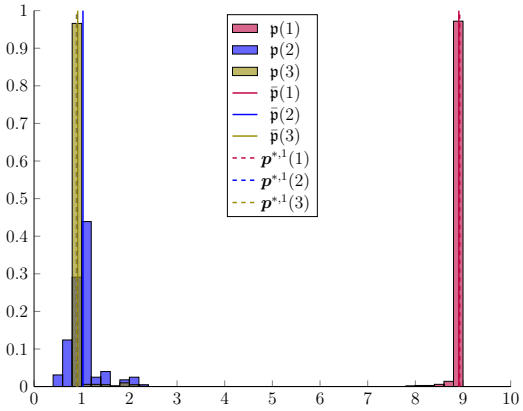

(b) Histogram plots for $\theta = \frac{1}{6}$ cm

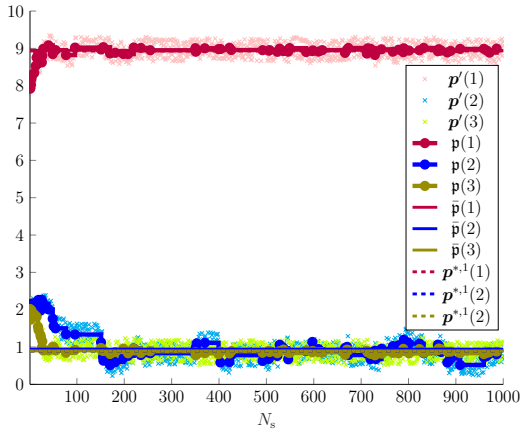

(c) Plot of sampled chains for $\theta = \frac{1}{2}$ cm

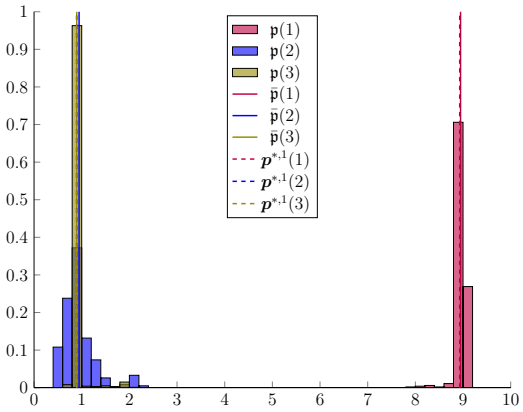

(d) Histogram plots for $\theta = \frac{1}{2}$ cm

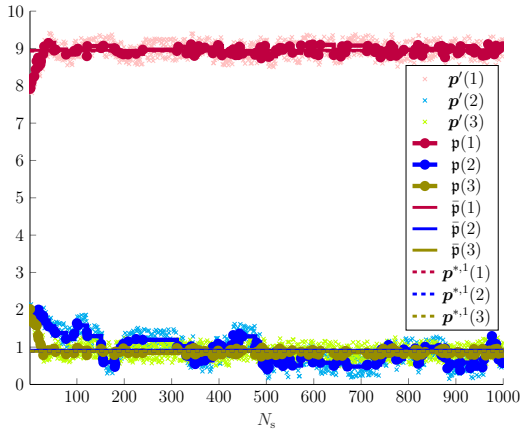

(e) Plot of sampled chains for $\theta = \frac{5}{6}$ cm

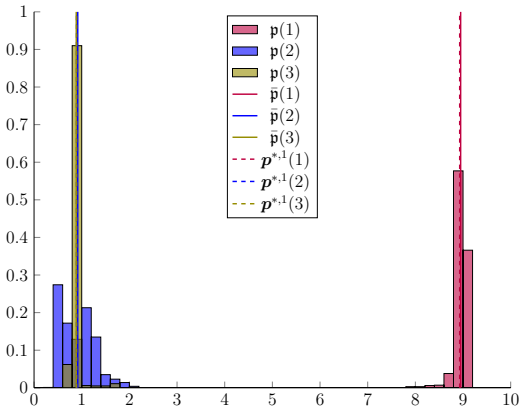

(f) Histogram plots for $\theta = \frac{5}{6}$ cm

Figure 6.1.: Plots of sampled chains of the conductivity magnitudes and corresponding histograms for different thicknesses of the surrounding tissue layer θ with reference conductivity $\boldsymbol{p}^{*,1}$

Table 6.2.: Statistics of the chains of the conductivity magnitudes for different thicknesses of the surrounding tissue layer θ with reference parameter $\boldsymbol{p}^{*,1}$

θ	κ_a	$\lvert\bar{\mathfrak{p}}(1:3)-\boldsymbol{p}^*(1:3)\rvert$ (%)			MAD($\mathfrak{p}(1:3)$) (%)			var($\mathfrak{p}(1:3)$) (%)		
0	0.90	183.75	172.23	177.24	5.96	8.52	10.85	1.04	1.75	2.38
1/6	1.50	190.15	139.37	184.58	7.48	15.40	12.57	1.09	6.46	1.78
1/3	1.10	202.35	75.27	195.76	11.48	11.00	8.03	2.76	1.53	1.01
1/2	1.30	242.70	120.20	121.00	7.29	7.94	7.91	2.77	1.09	1.57
2/3	1.60	257.19	146.00	112.74	17.27	12.76	13.04	6.94	2.44	3.36
5/6	1.00	206.50	65.35	178.04	8.40	1.63	9.48	1.94	0.27	1.72
1	1.00	206.50	65.35	178.04	8.40	1.63	9.48	1.94	0.27	1.72

Table 6.3.: Statistics of the sampled chains of the muscle fiber directions for different thicknesses of the surrounding tissue layer θ for reference parameter $\boldsymbol{p}^{*,1}$

θ	κ_a	$\lvert\bar{\mathfrak{d}}-d_\mathrm{F}^*\rvert$ (%)			MAD($\mathfrak{d}$) (%)			var($\mathfrak{d}$) (%)		
0	0.90	0.32	3.35	0.17	0.54	4.45	0.47	0.01	0.49	0.02
1/6	1.50	0.42	6.31	0.43	0.51	3.46	0.76	0.02	0.40	0.01
1/3	1.10	0.73	8.06	1.06	0.85	5.91	0.74	0.04	0.74	0.01
1/2	1.30	0.33	4.45	0.60	0.45	3.72	0.82	0.02	0.43	0.02
2/3	1.60	0.44	5.93	0.37	0.59	3.37	0.85	0.03	0.48	0.02
5/6	1.00	0.85	7.74	1.79	1.09	7.97	0.44	0.05	1.00	0.01
1	1.00	0.85	7.74	1.79	1.09	7.97	0.44	0.05	1.00	0.01

Table 6.3.

Again, the values for $\theta = 0\,\mathrm{cm}$ play the role of reference values. Comparing the statistics of the conductivity magnitudes for $\theta = 0\,\mathrm{cm}$ from Table 6.2 to the corresponding values from Table 5.1 we see that the acceptance rate κ_a is significantly lower when inferring all six parameters instead of inferring the conductivity magnitudes only. Moreover, we observe that the MAD and variance are comparable in both tables while the absolute distance between the mean of the sampled conductivity magnitudes and the reference solution is tremendously higher when inferring all six parameters. We later come back to the latter phenomenon.

Comparing the statistics of the muscle fiber directions for $\theta = 0\,\mathrm{cm}$ from Table 6.3 to the corresponding values from Tables 5.6 to 5.8 we see that the acceptance rates κ_a are in the same range. Further, we observe that the MAD and variance are a bit higher in Table 6.3 than in Tables 5.6 to 5.8 while the absolute distance between the mean of the sampled muscle fiber directions and the reference solution is comparable in both settings.

The plots of the sampled chains of the conductivity magnitudes and muscle fiber directions together with the respective histogram plots for $\theta = 0\,\text{cm}$ are shown in Figure 6.2. Comparing the acceptance rates κ_a for $\theta = 0\,\text{cm}$ with the values for $\theta > 0$ from Tables 6.2 and 6.3 we see no clear tendency of the acceptance rate to increase or decrease with increasing thickness θ of the layer of surrounding tissue. We already saw a similar behavior in Tables 5.6 to 5.8 in Section 5.2.4 during the validation of the SA for inferring only the rotation angles when increasing the sampling radius.

Looking at the statistical data in Table 6.3, we observe that the muscle fiber direction is inferred with low absolute distance of the mean $\bar{\mathfrak{d}}$ to the true muscle fiber direction d_F^* and with low MAD and variance. Contrarily, the statistical values of the conductivity magnitudes in Table 6.2 are significantly higher independent of the thickness of the surrounding tissue including the case $\theta = 0\,\text{cm}$.

Moreover, we see from Table 6.3 that the MAD and variance of the chains of the muscle fiber directions tend to increase with increasing thickness θ of the on top layer of surrounding tissue similar to use case 1 in Section 6.1. We suppose that, when sampling the conductivity magnitudes and the rotation angles, the muscle fiber direction takes the "leading" role of the conductivity magnitudes when only sampling the conductivity magnitudes.

For justification of this idea, recall our discussion on the influence of the rotation angles and conductivity magnitudes on the forward EMG model in Section 5.1. There, we observed from Figures 5.1 and 5.2 that the rotation angles have a significantly higher influence on the solution of the forward EMG problem than the conductivity magnitudes. This explains why the acceptance strategy seems to pay more attention to inferring meaningful muscle fiber directions than to the conductivity magnitudes.

For illustrating this behavior, we look at the plot of the sampled chains and histogram plots for $\theta = \frac{1}{6}\,\text{cm}$, $\theta = \frac{1}{2}\,\text{cm}$, and $\theta = \frac{5}{6}\,\text{cm}$ in Figures 6.3 and 6.4.

From the histogram plots we observe that the histograms are similarly narrow with high peaks for both conductivity magnitudes and rotation angles. Looking at the corresponding plots of the sampled chains we see that the chains "get stuck", which explains the narrow and high peaks in the histogram plots. The similarity of the histogram plots for the conductivity magnitudes and the muscle fiber directions is a result of the simultaneous sampling of the conductivity magnitudes and the rotation angles.

Summarizing, we deduce that the conductivity magnitudes are barely inferable when sampling the conductivity magnitudes and the rotation angles simultaneously, compared to inferring only the magnitudes for fixed muscle fiber directions. Moreover, the addi-

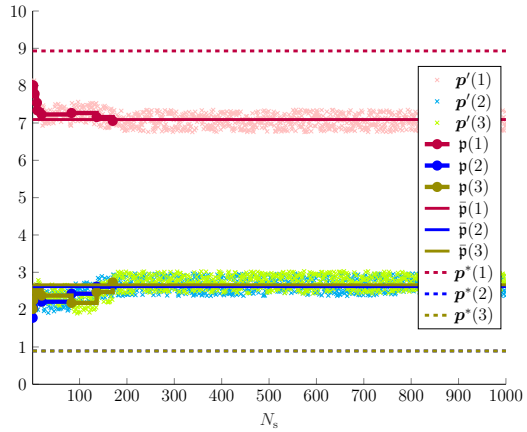

(a) Plot of sampled chains of conductivity magnitudes

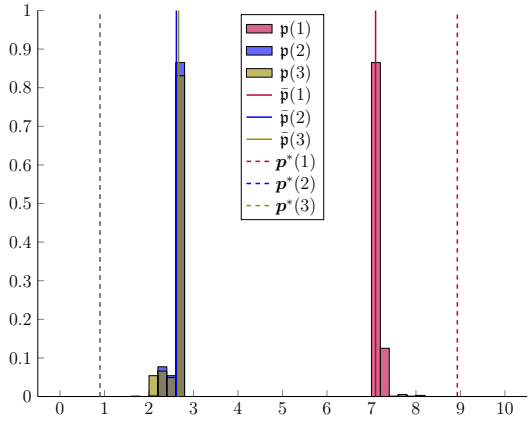

(b) Histogram plots of conductivity magnitudes

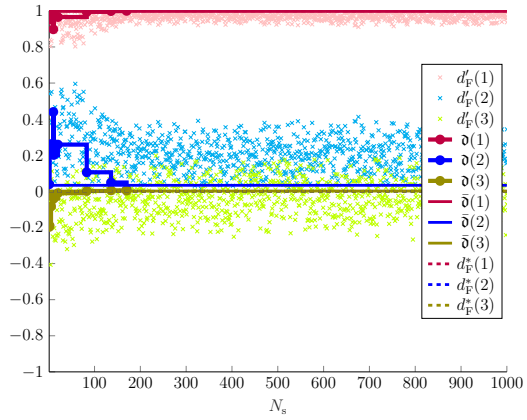

(c) Plot of sampled chains of muscle fiber directions

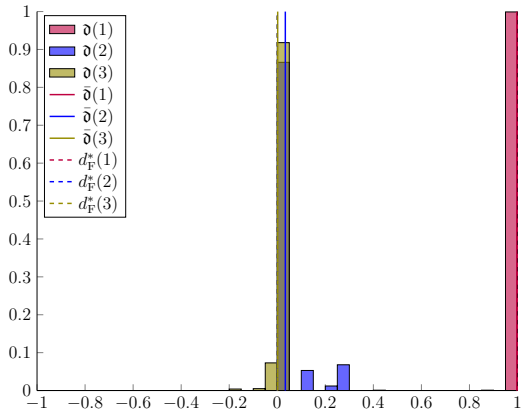

(d) Histogram plots of sampled directions

Figure 6.2.: Plots of sampled chains of the conductivity magnitudes and rotation angles and corresponding histograms without surrounding tissue for reference parameter $\boldsymbol{p}^{*,1}$

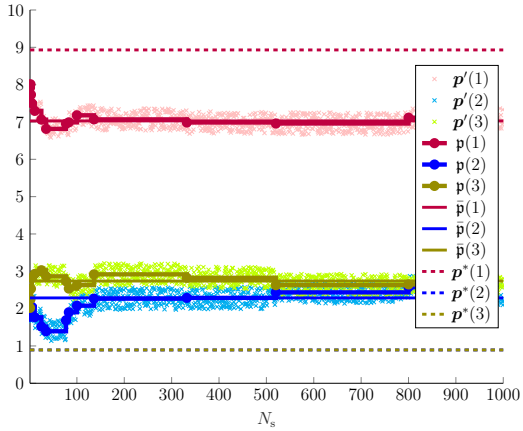

(a) Plot of sampled chains for $\theta = \frac{1}{6}$ cm

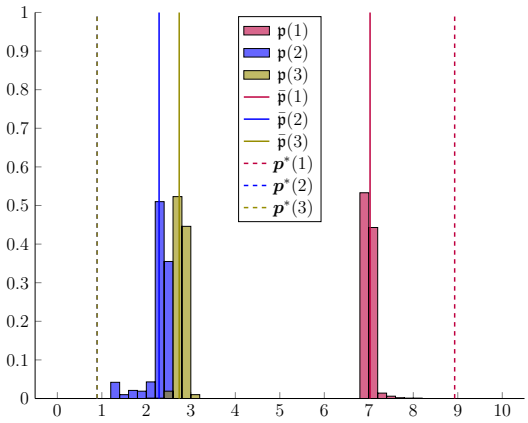

(b) Histogram plots for $\theta = \frac{1}{6}$ cm

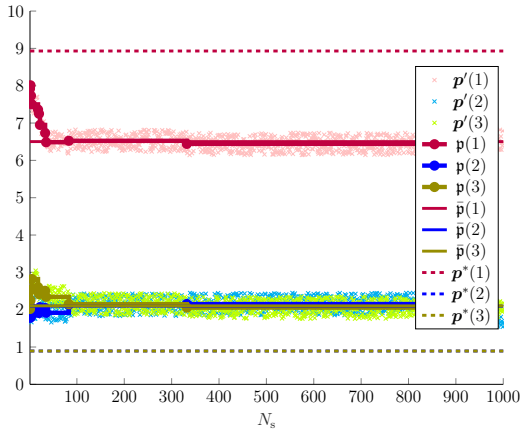

(c) Plot of sampled chains for $\theta = \frac{1}{2}$ cm

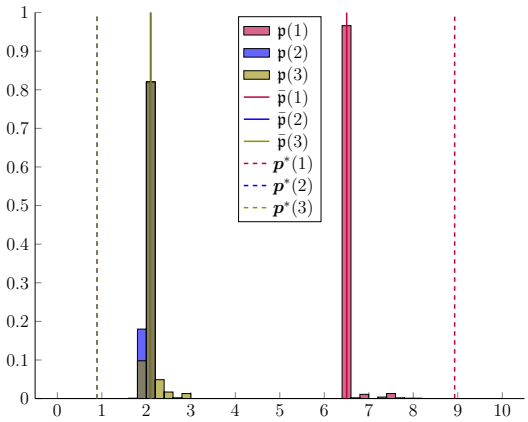

(d) Histogram plots for $\theta = \frac{1}{2}$ cm

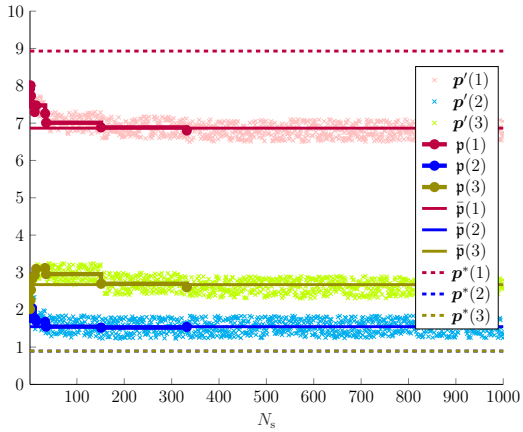

(e) Plot of sampled chains for $\theta = \frac{5}{6}$ cm

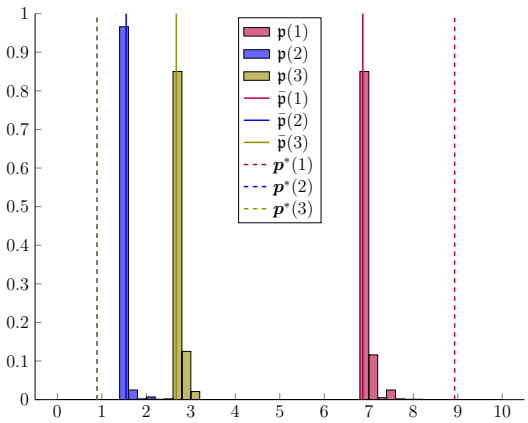

(f) Histogram plots for $\theta = \frac{5}{6}$ cm

Figure 6.3.: Plots of sampled chains of the conductivity magnitudes and corresponding histograms for different thickness of the surrounding tissue layer θ with reference conductivity $\boldsymbol{p}^{*,1}$

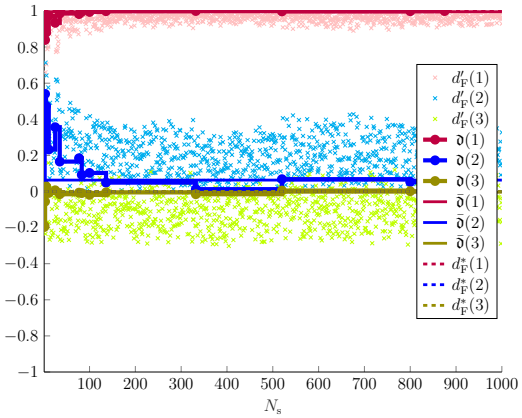

(a) Plot of sampled chains for $\theta = \frac{1}{6}$ cm

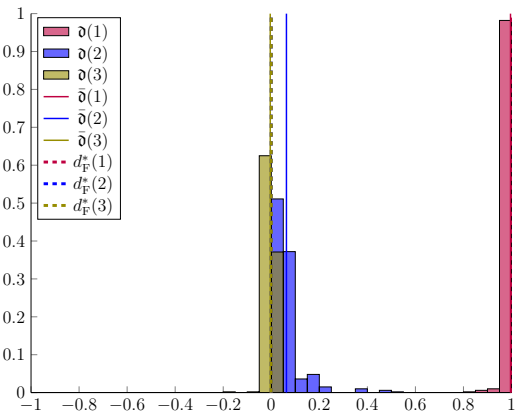

(b) Histogram plots for $\theta = \frac{1}{6}$ cm

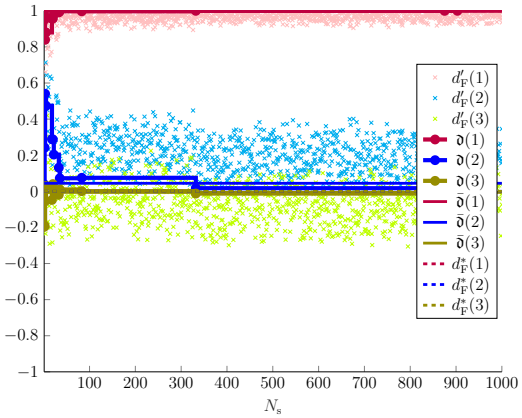

(c) Plot of sampled chains for $\theta = \frac{1}{2}$ cm

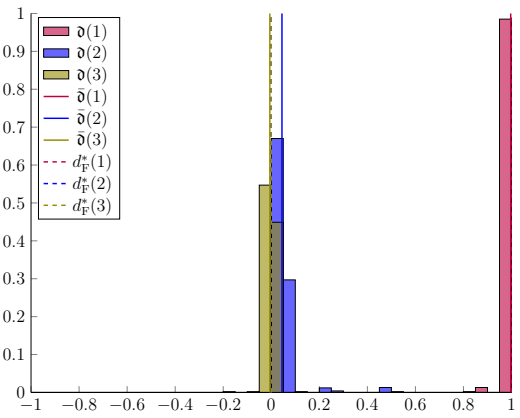

(d) Histogram plots for $\theta = \frac{1}{2}$ cm

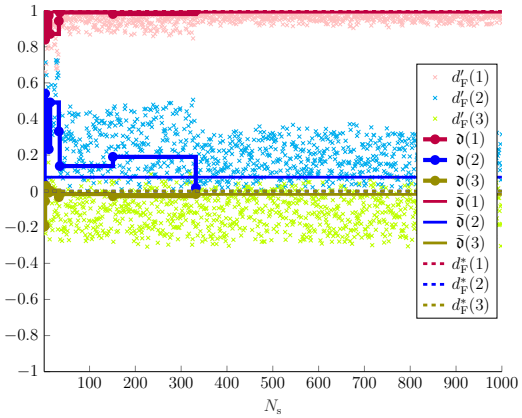

(e) Plot of sampled chains for $\theta = \frac{5}{6}$ cm

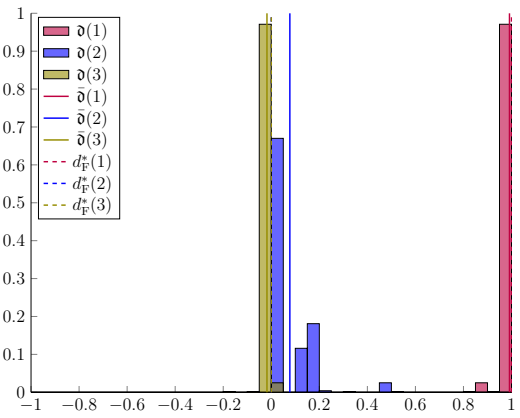

(f) Histogram plots for $\theta = \frac{5}{6}$ cm

Figure 6.4.: Plots of sampled chains of the rotation angles and corresponding histograms for different thickness of the surrounding tissue layer θ with reference parameter $\boldsymbol{p}^{*,1}$

tional layer of surrounding tissue, again, leads to growing uncertainties, i.e., growing MAD and variance, in the sampled chains. Following our discussion at the end of Section 6.1, the SA has the potential to not only infer the muscle fiber direction from surface EMG measurements but additionally quantify the uncertainties within these estimates.

6.3. Use Case 3: Inferring the Structure of a Muscle Composite

Further approaching a clinical scenario, we now investigate the setting of two muscles lying on top of each other that we introduced in Section 3.2.3. In clinical applications it is common that one muscle shadows the other, for example when examining agonists and antagonists. For building a reliable medical imaging method, it is crucial to tell such overlapping muscles apart.

In the following parameter studies, we use the standard settings established in Sections 3.3 and 5.4 with $h_x = \frac{1}{6}$. We further set the conductivity magnitudes in both muscles to be equal, namely $\sigma^*_{\mathrm{i},1} = \sigma^*_{\mathrm{i},2} = \mathrm{diag}(8.91, 0.891, 0.891)$, where index 1 indicates that the property belongs to the upper muscle and index 2 indicates that the property belongs to the lower muscle, as depicted in Figure 3.7.

Note that, by choosing the same conductivity magnitudes for both muscles, we assume that the corresponding muscle fibers show the same conductive behavior. The change of the intracellular conductivity that indicates the border between the two muscles is thus only introduced by the rotation angles of the corresponding muscle fibers.

The rotation angle of the upper muscle is fixed at $\alpha^*_1 = 0$, i.e., the muscle fibers of the upper muscle are aligned with the e_1-axis, while the rotation angle of the lower muscle α^*_2 is left variable, see the settings below.

Recall, that the two-muscle scenario is determined by 9 parameters, namely the $3+3 = 6$ conductivity magnitudes $\sigma_{\mathrm{i},1}$ and $\sigma_{\mathrm{i},2}$, the $1+1 = 2$ rotation angles α_1 and α_2, and the height of the lower muscle θ_{b}. We additionally examine the influence of the thickness of a layer of surrounding tissue θ.

Our investigations are structured as follows: In Section 6.3.1, we aim at inferring the thickness of the lower muscle, while assuming all other parameters to be known. Afterwards, we aim at inferring the conductivity magnitudes of the lower muscle in Section 6.3.2, while, again, assuming all other parameters to be known. Extending the latter scenario, we add the rotation angle of the lower muscle α_2 to the unknown parameters in Section 6.3.3 and the thickness of the lower muscle in Section 6.3.4. Further

adding the conductivity magnitudes and the rotation angle of the upper muscle to the unknown parameters in Section 6.3.5 leads to inferring all nine parameters describing the two-muscle scenario.

In each setting, we vary the rotation angle of the lower muscle $\alpha_2 \in \{0, \frac{\pi}{4}, \frac{\pi}{2}, \frac{3\pi}{4}\}$, the thickness of the lower muscle $\theta_\mathrm{b} \in \{0.1, 0, 3, 0.5, 0.7, 0.9\}$, and the thickness of the layer of surrounding tissue $\theta \in \{0, \frac{1}{6}, \frac{1}{3}, \frac{1}{2}, \frac{2}{3}, \frac{5}{6}, 1\}$. Due to the high amount of data generated by these parameter studies, we exemplarily present the results for $\alpha_2^* = \frac{\pi}{2}$, i.e., when the muscle fibers of the upper and lower muscle are perpendicular to each other, in the respective sections and show the results for the rotation angles $\alpha_2 \in \{0, \frac{\pi}{4}, \frac{3\pi}{4}\}$ in the Appendices A–E.

We emphasize that choosing the rotation angle of the lower muscle $\alpha_2 = 0$ plays a special role in the described setting, since the muscle fibers of both muscles are then aligned in the same direction and additionally possess the same conductivity magnitudes. The resulting intracellular conductivity $\sigma_\mathrm{i} = \sigma_{\mathrm{i},1}\mathbb{1}_{D_{\mathrm{M},1}} + \sigma_{\mathrm{i},2}\mathbb{1}_{D_{\mathrm{M},2}}$ is thus continuous, while it shows discontinuities at the border between the two muscles whenever $\alpha_2 \in (0, \pi)$.

6.3.1. 1 Parameter Case

The only parameter that we wish to infer in this section is the thickness of the lower muscle, i.e., we set $\boldsymbol{p} = \theta_\mathrm{b}$. We choose the sampling radius for θ_b to be 0.1, similar to the sampling radius for the rotation angles.

The acceptance rate κ_a, the absolute distance of the mean of the sampled chains to the reference value $|\bar{\mathfrak{p}} - \boldsymbol{p}^*|$, and the MAD and variance of the sampled chains are presented in Table 6.4 for $\alpha_2 = \frac{\pi}{2}$ and in Appendix A for $\alpha_2 \in \{0, \frac{\pi}{4}, \frac{3\pi}{4}\}$ for varying reference thicknesses of the lower muscle $\boldsymbol{p}^*$ and thicknesses θ of the surrounding tissue.

For all four rotation angles $\alpha_2 \in \{0, \frac{\pi}{4}, \frac{\pi}{2}, \frac{3\pi}{4}\}$ we observe that the statistical values increase rapidly with increasing thickness of the lower muscle $\boldsymbol{p}^*$ and there is no clearly visible influence of the thickness θ of the layer of surrounding tissue. Further, the acceptance rate increases drastically with increasing thickness of the lower muscle until it reaches $\kappa_\mathrm{a} = 100\,\%$ for $\boldsymbol{p}^* = 0.9$. In other words, the sampling algorithm accepts each proposed sample, what also explains the high statistical values. We deduce that the thickness of the lower muscle θ_b is weakly inferable in this setting. Another possible reason for the low ability of the algorithm to infer θ_b is the finite difference discretization. As discussed before, the two-muscle scenario introduces a discontinuity into the intracellular conductivity $\sigma_\mathrm{i} = \sigma_{\mathrm{i},1}\mathbb{1}_{D_{\mathrm{M},1}} + \sigma_{\mathrm{i},2}\mathbb{1}_{D_{\mathrm{M},2}}$. Since the applied finite differences of second order require C^4-continuity to guarantee convergence, we cannot generally ex-

pect low discretization errors. In the following sections we will, however, see that some parameters are still inferable.

Table 6.4.: Statistics of $\boldsymbol{p}$ using the standard algorithm for the 1 parameter case with 1000 drawn samples for varying height of the lower muscle $\boldsymbol{p}^*$ and thickness of the surrounding tissue layer θ in the settings from Section 6.3.1 with $\alpha_2 = \frac{\pi}{2}$

$\boldsymbol{p}^* = 0.1$							
θ	0	$\frac{1}{6}$	$\frac{1}{3}$	$\frac{1}{2}$	$\frac{2}{3}$	$\frac{5}{6}$	1
κ_a	10.00	10.90	10.90	10.00	10.00	10.70	8.40
$\lvert\bar{\mathfrak{p}} - \boldsymbol{p}^*\rvert$ (%)	11.22	11.09	11.09	11.22	11.22	11.11	0.58
MAD($\mathfrak{p}$) (%)	0.58	0.66	0.66	0.58	0.58	0.64	0.27
var($\mathfrak{p}$) (%)	0.01	0.01	0.01	0.01	0.01	0.01	0.00
$\boldsymbol{p}^* = 0.3$							
θ	0	$\frac{1}{6}$	$\frac{1}{3}$	$\frac{1}{2}$	$\frac{2}{3}$	$\frac{5}{6}$	1
κ_a	9.00	9.00	9.10	9.50	8.10	51.00	85.60
$\lvert\bar{\mathfrak{p}} - \boldsymbol{p}^*\rvert$ (%)	10.49	10.49	10.66	10.57	1.99	3.26	8.41
MAD($\mathfrak{p}$) (%)	0.48	0.48	0.47	0.48	0.42	5.69	4.80
var($\mathfrak{p}$) (%)	0.01	0.01	0.01	0.01	0.00	0.43	0.32
$\boldsymbol{p}^* = 0.5$							
θ	0	$\frac{1}{6}$	$\frac{1}{3}$	$\frac{1}{2}$	$\frac{2}{3}$	$\frac{5}{6}$	1
κ_a	92.70	92.70	92.70	92.70	92.70	92.70	92.70
$\lvert\bar{\mathfrak{p}} - \boldsymbol{p}^*\rvert$ (%)	17.46	17.46	17.46	17.46	17.46	17.46	17.46
MAD($\mathfrak{p}$) (%)	9.57	9.57	9.57	9.57	9.57	9.57	9.57
var($\mathfrak{p}$) (%)	1.24	1.24	1.24	1.24	1.24	1.24	1.24
$\boldsymbol{p}^* = 0.7$							
θ	0	$\frac{1}{6}$	$\frac{1}{3}$	$\frac{1}{2}$	$\frac{2}{3}$	$\frac{5}{6}$	1
κ_a	94.50	94.50	94.50	94.50	94.50	94.50	94.50
$\lvert\bar{\mathfrak{p}} - \boldsymbol{p}^*\rvert$ (%)	27.58	27.58	27.58	27.58	27.58	27.58	27.58
MAD($\mathfrak{p}$) (%)	13.88	13.88	13.88	13.88	13.88	13.88	13.88
var($\mathfrak{p}$) (%)	2.72	2.72	2.72	2.72	2.72	2.72	2.72
$\boldsymbol{p}^* = 0.9$							
θ	0	$\frac{1}{6}$	$\frac{1}{3}$	$\frac{1}{2}$	$\frac{2}{3}$	$\frac{5}{6}$	1
κ_a	100.00	100.00	100.00	100.00	100.00	100.00	100.00
$\lvert\bar{\mathfrak{p}} - \boldsymbol{p}^*\rvert$ (%)	37.83	37.83	37.83	37.83	37.83	37.83	37.83
MAD($\mathfrak{p}$) (%)	18.43	18.43	18.43	18.43	18.43	18.43	18.43
var($\mathfrak{p}$) (%)	4.69	4.69	4.69	4.69	4.69	4.69	4.69

6.3.2. 3 Parameter Case

The three parameters that we wish to infer in this section are the three conductivity magnitudes of the lower muscle, i.e., we set $\boldsymbol{p} = ((\sigma_{\mathrm{i},2})_{11}, (\sigma_{\mathrm{i},2})_{22}, (\sigma_{\mathrm{i},2})_{33})$.

The acceptance rate κ_{a}, the absolute distance of the mean of the sampled chains to the reference value $|\bar{\mathfrak{p}} - \boldsymbol{p}^*|$, and the MAD and variance of the sampled chains are presented in Table 6.5 for $\alpha_2 = \frac{\pi}{2}$ and in Appendix B for $\alpha_2 \in \{0, \frac{\pi}{4}, \frac{3\pi}{4}\}$ for varying thicknesses of the lower muscle θ_{b} and thicknesses of the surrounding tissue θ.

While there is, again, no clearly visible dependency of the statistical values on θ, the statistical values tend to decrease with increasing thickness of the lower muscle θ_{b}.

The only exception is the case $\alpha_2 = 0$, presented in Table B.1. Here, we see that the statistical values of the conductivity magnitudes are clearly smaller, indicating good inferability of the conductivity magnitudes, see our discussion on the choice $\alpha_2 = 0$ in the introduction to Section 6.3. Moreover, we see no clear dependency of the statistical values on θ or θ_{b}. Recalling our short discussion on the finite difference discretization in Section 6.3.1, we blame the lack of inferability of the conductivity magnitudes for $\alpha_2 \neq 0$ on the discretization error arising from the use of finite differences to discretize the discontinuous intracellular conductivity.

Table 6.5.: Statistics of $\boldsymbol{p}$ using the standard algorithm for the 3 parameter case with 1000 drawn samples for varying height of the lower muscle θ_b and thickness of the surrounding tissue layer θ in the settings from Section 6.3.2 with $\alpha_2 = \frac{\pi}{2}$

θ_b	θ	κ_a	$\lvert\bar{\mathfrak{p}} - \boldsymbol{p}^*\rvert$ (%)			MAD($\mathfrak{p}$) (%)			var($\mathfrak{p}$) (%)		
0.10	0	2.50	107.47	300.98	18.73	5.79	16.97	1.99	1.03	14.99	0.52
0.10	$\frac{1}{6}$	2.20	67.88	302.98	20.84	4.90	14.37	4.44	0.40	12.56	0.91
0.10	$\frac{1}{3}$	2.40	83.81	302.10	17.07	4.09	15.73	4.08	0.23	13.97	0.79
0.10	$\frac{1}{2}$	2.60	112.84	301.84	16.31	6.57	15.87	4.00	0.93	14.03	0.73
0.10	$\frac{2}{3}$	2.30	123.74	301.66	11.40	6.79	16.21	4.06	1.06	14.36	0.81
0.10	$\frac{5}{6}$	2.40	92.58	299.77	7.45	6.21	19.49	3.82	0.72	18.29	0.82
0.10	1	2.60	152.68	299.16	4.14	10.90	20.19	2.61	4.78	18.79	0.79
0.30	0	2.10	117.24	300.05	8.26	5.39	18.60	2.28	0.79	16.46	0.70
0.30	$\frac{1}{6}$	2.10	150.53	301.50	21.98	7.12	16.12	2.08	2.02	14.61	0.58
0.30	$\frac{1}{3}$	2.70	118.77	300.19	14.89	7.32	18.87	3.91	1.93	17.71	0.71
0.30	$\frac{1}{2}$	2.50	207.54	299.48	8.72	15.84	19.66	2.25	10.02	18.39	0.74
0.30	$\frac{2}{3}$	2.70	150.46	297.34	5.19	13.07	21.88	3.04	4.50	20.26	0.81
0.30	$\frac{5}{6}$	2.80	153.19	294.75	2.00	15.52	25.85	3.07	5.13	23.47	0.87
0.30	1	2.80	82.82	285.53	2.19	17.71	35.18	2.56	4.48	27.98	0.84
0.50	0	3.10	58.97	293.42	7.53	15.17	26.07	2.51	3.86	22.27	0.72
0.50	$\frac{1}{6}$	2.50	142.05	299.77	10.88	9.00	19.40	2.17	3.59	18.34	0.66
0.50	$\frac{1}{3}$	2.30	192.96	299.17	7.89	14.06	20.27	2.24	7.94	19.41	0.71
0.50	$\frac{1}{2}$	2.70	150.46	297.34	5.19	13.07	21.88	3.04	4.50	20.26	0.81
0.50	$\frac{2}{3}$	3.00	137.90	297.23	3.92	12.49	21.86	3.18	3.80	20.25	0.83
0.50	$\frac{5}{6}$	2.70	177.09	295.70	3.32	16.18	24.03	3.08	7.65	21.13	0.82
0.50	1	2.40	140.12	289.38	2.96	12.28	34.31	2.25	3.82	28.40	0.81
0.70	0	3.00	59.45	274.12	4.84	35.18	44.89	2.20	16.24	35.43	0.77
0.70	$\frac{1}{6}$	2.80	107.17	294.67	7.05	7.52	25.45	2.62	1.71	22.26	0.73
0.70	$\frac{1}{3}$	2.50	122.11	296.28	6.01	8.25	23.69	2.38	1.90	21.43	0.75
0.70	$\frac{1}{2}$	2.60	121.06	294.44	4.70	7.33	25.36	2.63	1.96	22.18	0.78
0.70	$\frac{2}{3}$	2.40	123.25	288.43	3.90	6.79	35.23	2.33	1.84	29.90	0.79
0.70	$\frac{5}{6}$	2.20	135.60	286.55	3.32	11.51	38.78	2.23	3.18	32.09	0.80
0.70	1	3.30	28.99	263.35	2.12	23.36	57.45	2.49	7.03	54.43	0.84
0.90	0	3.00	34.14	187.17	2.69	32.82	44.30	2.36	13.27	29.88	0.81
0.90	$\frac{1}{6}$	2.40	84.58	275.20	4.96	10.83	38.28	2.16	2.36	30.12	0.76
0.90	$\frac{1}{3}$	2.20	131.54	276.24	4.42	12.88	39.63	2.18	3.40	31.13	0.77
0.90	$\frac{1}{2}$	3.30	11.34	251.74	3.64	23.53	51.33	2.30	7.27	45.20	0.81
0.90	$\frac{2}{3}$	3.00	11.52	248.11	3.07	38.31	48.75	2.33	17.14	42.49	0.82
0.90	$\frac{5}{6}$	3.30	91.16	245.08	2.67	26.71	71.35	2.37	8.86	69.98	0.82
0.90	1	3.20	8.62	225.86	1.95	38.22	79.05	2.47	18.47	76.59	0.83

6.3.3. 4 Parameter Case

Within this section, we add the rotation angle α_2 of the lower muscle to the parameters of interest defined in the last section, i.e., we set $\boldsymbol{p} = ((\sigma_{\mathrm{i},2})_{11}, (\sigma_{\mathrm{i},2})_{22}, (\sigma_{\mathrm{i},2})_{33}, \alpha_2)$.

The acceptance rate κ_{a}, the absolute distance of the mean of the sampled chains to the reference value $|\bar{\mathfrak{p}} - \boldsymbol{p}^*|$, and the MAD and variance of the sampled chains are presented in Table 6.6 for the conductivity magnitudes $\boldsymbol{p}(1:3)$ and in Table 6.7 for the rotation angle $\boldsymbol{p}(4)$ for $\boldsymbol{p}^*(4) = \frac{\pi}{2}$ and varying thicknesses of the lower muscle θ_{b} and thicknesses of the surrounding tissue θ. The statistical values for $\boldsymbol{p}^*(4) \in \{0, \frac{\pi}{4}, \frac{3\pi}{4}\}$ are shown in Appendix C, more precisely in Tables C.1 to C.3 for $\boldsymbol{p}(1:3)$ and in Tables C.4 to C.6 for $\boldsymbol{p}(4)$. Note that we present the acceptance rate only in the tables for $\boldsymbol{p}(4)$ since the acceptance rates are the same for all entries of the parameter.

Comparing the results in Tables 6.6 and C.1 to C.3 to the numbers in Tables 6.5 and B.1 to B.3, we clearly see the influence of additionally inferring the rotation angles of the lower muscle. Most significantly, the case $\alpha_2 = 0$ seems to lose its special role. Recall, however, that even in the one-muscle case, inferring the conductivity magnitudes and the rotation angles simultaneously, led to an increase in the statistical values for the conductivity magnitudes, see Section 6.2. More precisely, we lost the inferability of the conductivity magnitudes when also inferring the rotation angles.

Looking at Tables 6.7 and C.4 to C.6, we observe that the statistical values decrease with increasing thickness of the lower muscle θ_{b}. In other words, the thicker the lower muscle, the better the inferability of the rotation angle of the muscle fibers of this muscle.

Table 6.6.: Statistics of $\boldsymbol{p}(1:3)$ using the standard algorithm for the 4 parameter case with 1000 drawn samples for varying height of the lower muscle θ_b and thickness of the surrounding tissue layer θ in the settings from Section 6.3.3 with $\boldsymbol{p}^*(4) = \frac{\pi}{2}$

θ_b	θ	$\lvert\bar{\mathfrak{p}}(1:3) - \boldsymbol{p}^*(1:3)\rvert$ (%)			MAD($\mathfrak{p}(1:3)$) (%)			var($\mathfrak{p}(1:3)$) (%)		
0.10	0	27.70	40.05	1.94	30.27	58.81	5.14	13.63	67.84	1.33
0.10	$\frac{1}{6}$	22.12	142.92	1.59	29.31	55.44	3.98	21.02	44.81	1.00
0.10	$\frac{1}{3}$	28.29	155.36	1.42	27.57	49.78	3.70	19.10	39.65	0.96
0.10	$\frac{1}{2}$	27.46	161.85	1.19	24.39	44.56	3.29	13.26	32.01	0.95
0.10	$\frac{2}{3}$	39.57	169.51	1.15	28.02	43.65	3.11	18.11	31.24	0.93
0.10	$\frac{5}{6}$	85.81	231.43	1.11	46.16	68.35	3.94	24.61	53.60	0.97
0.10	1	115.33	236.59	1.16	57.42	65.55	3.61	45.54	50.89	0.95
0.30	0	47.24	76.63	1.35	33.46	45.55	4.19	21.49	47.32	1.01
0.30	$\frac{1}{6}$	73.76	258.61	0.51	70.14	30.86	4.04	70.62	16.62	1.00
0.30	$\frac{1}{3}$	138.44	249.48	0.53	68.46	44.69	3.33	57.66	27.50	0.95
0.30	$\frac{1}{2}$	188.00	294.74	1.21	50.25	20.90	3.82	28.29	18.22	0.93
0.30	$\frac{2}{3}$	158.31	296.37	1.79	19.25	21.73	3.58	6.79	20.04	0.91
0.30	$\frac{5}{6}$	93.54	294.62	0.67	9.19	25.83	3.07	1.34	23.43	0.91
0.30	1	77.82	285.13	1.60	9.55	35.03	2.68	1.48	27.79	0.85
0.50	0	36.09	104.86	5.87	38.52	19.34	2.47	22.51	8.47	0.79
0.50	$\frac{1}{6}$	28.91	107.35	4.99	31.01	20.57	2.46	14.31	7.55	0.82
0.50	$\frac{1}{3}$	12.74	126.15	4.42	18.96	13.36	2.58	8.47	3.25	0.82
0.50	$\frac{1}{2}$	34.26	278.95	3.39	26.58	24.28	2.84	10.60	18.61	0.83
0.50	$\frac{2}{3}$	63.31	263.48	2.72	40.59	30.71	2.74	19.76	20.14	0.84
0.50	$\frac{5}{6}$	88.17	284.73	1.15	27.92	25.33	3.23	11.55	19.82	0.88
0.50	1	34.83	277.74	2.27	26.04	36.51	2.73	9.97	29.25	0.84
0.70	0	121.72	218.81	6.45	11.10	29.43	2.42	2.50	16.24	0.76
0.70	$\frac{1}{6}$	72.80	226.48	6.21	15.36	22.34	2.19	3.59	12.99	0.75
0.70	$\frac{1}{3}$	115.61	262.35	5.00	18.64	21.02	2.36	5.07	15.86	0.79
0.70	$\frac{1}{2}$	107.41	278.10	4.06	16.72	23.57	2.49	3.67	19.48	0.80
0.70	$\frac{2}{3}$	100.15	273.99	2.65	18.10	33.32	2.67	4.89	26.77	0.83
0.70	$\frac{5}{6}$	64.46	265.39	2.45	13.12	37.74	2.41	3.23	27.36	0.83
0.70	1	107.01	248.42	1.99	21.30	46.03	2.57	6.41	30.32	0.84
0.90	0	85.27	127.06	5.17	8.41	11.30	2.17	1.12	2.73	0.76
0.90	$\frac{1}{6}$	57.34	178.23	5.10	9.97	16.52	2.18	2.63	6.07	0.76
0.90	$\frac{1}{3}$	65.99	101.58	3.68	6.66	9.26	2.30	1.72	2.31	0.80
0.90	$\frac{1}{2}$	70.88	121.51	3.00	8.34	9.49	2.33	1.88	3.40	0.81
0.90	$\frac{2}{3}$	201.32	169.57	3.06	36.98	39.32	2.33	19.21	23.33	0.81
0.90	$\frac{5}{6}$	166.01	203.31	2.86	25.85	54.86	2.35	9.56	41.64	0.80
0.90	1	173.27	189.67	1.95	32.30	52.03	2.47	14.01	35.52	0.83

Table 6.7.: Statistics of $\boldsymbol{p}(4)$ using the standard algorithm for the 4 parameter case with 1000 drawn samples for varying height of the lower muscle θ_b and thickness of the surrounding tissue layer θ in the settings from Section 6.3.3 with $\boldsymbol{p}^*(4) = \frac{\pi}{2}$

$\theta_\mathrm{b} = 0.1$							
θ	0	$\frac{1}{6}$	$\frac{1}{3}$	$\frac{1}{2}$	$\frac{2}{3}$	$\frac{5}{6}$	1
κ_a	5.60	5.20	5.10	4.60	5.00	6.60	6.70
$\lvert\bar{\mathfrak{p}}(4) - \boldsymbol{p}^*(4)\rvert$ (%)	145.40	145.96	145.87	145.00	144.60	107.99	102.17
MAD($\mathfrak{p}(4)$) (%)	17.73	17.74	16.86	17.16	17.06	54.31	55.37
var($\mathfrak{p}(4)$) (%)	10.72	10.55	10.09	10.20	10.14	33.66	33.87
$\theta_\mathrm{b} = 0.3$							
θ	0	$\frac{1}{6}$	$\frac{1}{3}$	$\frac{1}{2}$	$\frac{2}{3}$	$\frac{5}{6}$	1
κ_a	6.20	6.10	6.30	4.00	3.10	2.70	3.00
$\lvert\bar{\mathfrak{p}}(4) - \boldsymbol{p}^*(4)\rvert$ (%)	145.65	136.61	119.42	59.62	22.17	21.71	15.63
MAD($\mathfrak{p}(4)$) (%)	17.32	27.49	39.08	16.62	16.71	9.72	3.94
var($\mathfrak{p}(4)$) (%)	10.27	13.96	19.19	4.17	3.29	1.26	0.24
$\theta_\mathrm{b} = 0.5$							
θ	0	$\frac{1}{6}$	$\frac{1}{3}$	$\frac{1}{2}$	$\frac{2}{3}$	$\frac{5}{6}$	1
κ_a	5.00	4.30	4.00	5.40	5.20	5.20	4.50
$\lvert\bar{\mathfrak{p}}(4) - \boldsymbol{p}^*(4)\rvert$ (%)	140.26	135.27	131.54	123.05	97.60	85.57	42.71
MAD($\mathfrak{p}(4)$) (%)	19.66	20.20	21.12	35.75	49.83	51.80	32.04
var($\mathfrak{p}(4)$) (%)	10.74	10.55	11.41	20.69	29.20	31.85	13.92
$\theta_\mathrm{b} = 0.7$							
θ	0	$\frac{1}{6}$	$\frac{1}{3}$	$\frac{1}{2}$	$\frac{2}{3}$	$\frac{5}{6}$	1
κ_a	5.00	3.70	4.70	4.80	4.80	4.50	4.50
$\lvert\bar{\mathfrak{p}}(4) - \boldsymbol{p}^*(4)\rvert$ (%)	114.62	104.28	103.49	84.12	50.54	49.46	65.51
MAD($\mathfrak{p}(4)$) (%)	33.07	25.57	35.52	41.45	39.47	37.76	39.96
var($\mathfrak{p}(4)$) (%)	17.68	11.84	18.24	20.92	20.43	17.88	20.44
$\theta_\mathrm{b} = 0.9$							
θ	0	$\frac{1}{6}$	$\frac{1}{3}$	$\frac{1}{2}$	$\frac{2}{3}$	$\frac{5}{6}$	1
κ_a	2.10	2.40	2.40	2.50	2.70	2.80	2.80
$\lvert\bar{\mathfrak{p}}(4) - \boldsymbol{p}^*(4)\rvert$ (%)	55.55	48.24	61.57	59.45	54.13	35.75	44.37
MAD($\mathfrak{p}(4)$) (%)	10.45	8.95	5.29	7.96	11.01	10.36	14.18
var($\mathfrak{p}(4)$) (%)	2.47	1.74	1.35	1.68	1.91	1.52	2.57

6.3.4. 5 Parameter Case

Within this section, we add the thickness of the lower muscle θ_b to the parameters of interest defined in the last section, i.e., we set $\boldsymbol{p} = ((\sigma_{\mathrm{i},2})_{11}, (\sigma_{\mathrm{i},2})_{22}, (\sigma_{\mathrm{i},2})_{33}, \alpha_2, \theta_\mathrm{b})$.

The acceptance rate κ_a, the absolute distance of the mean of the sampled chains to the reference value $|\bar{\mathfrak{p}} - \boldsymbol{p}^*|$, and the MAD and variance of the sampled chains are presented in Table 6.8 for the conductivity magnitudes $\boldsymbol{p}(1:3)$, in Table 6.9 for the rotation angle $\boldsymbol{p}(4)$, and in Table 6.10 for the thickness of the lower muscle $\boldsymbol{p}(5)$ for $\boldsymbol{p}^*(4) = \frac{\pi}{2}$ and varying reference thicknesses of the lower muscle $\boldsymbol{p}^*(5)$ and thicknesses of the surrounding tissue θ. The statistical values for $\boldsymbol{p}^*(4) \in \{0, \frac{\pi}{4}, \frac{3\pi}{4}\}$ are shown in Appendix D, more precisely in Tables D.1 to D.3 for $\boldsymbol{p}(1:3)$, in Tables D.4 to D.6 for $\boldsymbol{p}(4)$, and in Tables D.7 to D.9 for $\boldsymbol{p}(5)$.

Again, we see that the conductivity magnitudes $\boldsymbol{p}(1:3)$ are not inferable, but the statistical values show a slight tendency to decrease with increasing thickness of the lower muscle $\boldsymbol{p}^*(5)$. This indicates that the conductivity magnitudes of the lower muscle are better inferable with growing thickness of the lower muscle.

The statistical values for $\boldsymbol{p}(4)$ show a similar behavior but are in general smaller than the values for $\boldsymbol{p}(1:3)$. This behavior is in accordance with our previous findings on the influence of the rotation angles and conductivity magnitudes, see Sections 5.1 and 6.2.

Further, the thickness of the lower muscle $\boldsymbol{p}(5)$ shows the lowest statistical values compared to the first four parameters. In contrast to the rotation angle, $\boldsymbol{p}(5)$ seems to be less inferable with increasing $\boldsymbol{p}^*(5)$, showing in the growing statistical values.

All in all, $\boldsymbol{p}(5)$ shows the smallest statistical values and we deduce that the thickness of the lower muscle has higher influence on the forward model than the material parameters $\boldsymbol{p}(1:4)$ of the lower muscle. Recalling the high acceptance rates when only inferring the thickness of the lower muscle, as done in Section 6.3.1, we clearly see that additionally inferring the material parameters $\boldsymbol{p}(1:4)$ reduces the acceptance rates.

Table 6.8.: Statistics of $\boldsymbol{p}(1:3)$ using the standard algorithm for the 5 parameter case with 1000 drawn samples for varying height of the lower muscle $\boldsymbol{p}^*(5)$ and thickness of the surrounding tissue layer θ in the settings from Section 6.3.4 with $\boldsymbol{p}^*(4) = \frac{\pi}{2}$

$\boldsymbol{p}^*(5)$	θ	$\lvert\bar{\mathfrak{p}}(1:3) - \boldsymbol{p}^*(1:3)\rvert$ (%)			MAD($\mathfrak{p}(1:3)$) (%)			var($\mathfrak{p}(1:3)$) (%)		
0.10	0	202.18	301.29	20.02	6.14	14.40	3.97	2.45	12.08	1.17
0.10	$\frac{1}{6}$	166.26	300.37	18.70	3.13	16.07	3.96	0.81	12.43	1.18
0.10	$\frac{1}{3}$	161.13	294.75	14.77	8.21	19.59	7.12	2.10	13.18	1.73
0.10	$\frac{1}{2}$	156.59	296.71	9.00	15.29	18.67	5.78	3.60	13.16	1.76
0.10	$\frac{2}{3}$	153.90	213.66	3.42	41.66	46.24	7.29	21.95	27.38	1.82
0.10	$\frac{5}{6}$	207.42	298.64	0.19	11.17	18.34	6.31	4.53	13.56	1.77
0.10	1	160.78	292.99	8.13	15.38	19.34	6.84	3.24	14.25	1.99
0.30	0	103.80	257.64	6.80	10.60	34.61	11.76	2.12	17.03	3.86
0.30	$\frac{1}{6}$	194.87	287.04	8.08	32.12	24.24	4.89	12.92	16.83	1.33
0.30	$\frac{1}{3}$	69.75	293.78	10.61	13.72	26.29	5.21	2.81	20.03	1.22
0.30	$\frac{1}{2}$	95.33	296.11	1.28	8.29	18.04	6.27	1.27	14.71	1.41
0.30	$\frac{2}{3}$	87.35	280.86	17.14	1.89	15.68	2.15	0.32	12.20	0.87
0.30	$\frac{5}{6}$	97.73	281.47	3.72	18.71	34.08	2.93	4.66	28.51	1.11
0.30	1	140.19	203.93	0.87	11.32	22.37	3.71	2.27	12.98	1.22
0.50	0	78.23	216.55	35.67	5.55	8.34	7.12	1.09	4.48	2.24
0.50	$\frac{1}{6}$	31.78	270.24	56.36	25.66	29.38	6.35	8.21	18.40	1.39
0.50	$\frac{1}{3}$	85.54	295.99	54.43	14.08	19.49	7.36	3.55	15.21	1.50
0.50	$\frac{1}{2}$	57.51	288.82	52.51	11.70	26.72	4.61	2.38	20.86	1.23
0.50	$\frac{2}{3}$	105.71	285.25	54.03	4.72	35.65	3.69	0.70	28.86	1.14
0.50	$\frac{5}{6}$	119.42	199.69	55.89	8.60	24.72	4.58	1.04	10.31	1.16
0.50	1	93.00	128.70	54.67	12.86	16.77	3.63	1.86	4.02	1.09
0.70	0	44.00	214.90	5.54	13.66	22.19	8.70	5.66	9.31	2.61
0.70	$\frac{1}{6}$	135.05	138.38	34.01	5.49	23.89	4.33	0.71	7.87	0.55
0.70	$\frac{1}{3}$	136.04	131.48	69.02	2.98	28.71	1.89	0.21	9.70	0.11
0.70	$\frac{1}{2}$	100.89	120.11	113.87	0.65	2.13	0.95	0.03	0.19	0.07
0.70	$\frac{2}{3}$	124.38	168.46	163.21	5.44	16.65	6.21	0.81	5.55	1.44
0.70	$\frac{5}{6}$	158.16	207.42	4.31	7.34	31.96	2.82	1.33	20.40	1.24
0.70	1	103.89	212.13	3.70	18.14	37.74	3.43	5.06	18.07	1.63
0.90	0	55.98	140.38	0.94	5.22	6.32	2.53	1.27	1.78	1.00
0.90	$\frac{1}{6}$	55.98	140.38	0.94	5.22	6.32	2.53	1.27	1.78	1.00
0.90	$\frac{1}{3}$	55.98	140.38	0.94	5.22	6.32	2.53	1.27	1.78	1.00
0.90	$\frac{1}{2}$	21.92	158.35	1.20	15.53	12.13	2.89	6.09	4.20	1.07
0.90	$\frac{2}{3}$	72.01	158.40	0.38	10.16	42.33	2.91	1.44	20.89	1.04
0.90	$\frac{5}{6}$	78.77	126.09	1.08	6.25	23.24	2.67	0.82	6.73	1.01
0.90	1	86.30	102.60	1.24	5.97	5.05	2.66	1.11	0.55	1.00

Table 6.9.: Statistics of $\boldsymbol{p}(4)$ using the standard algorithm for the 5 parameter case with 1000 drawn samples for varying height of the lower muscle $\boldsymbol{p}^*(5)$ and thickness of the surrounding tissue layer θ in the settings from Section 6.3.4 with $\boldsymbol{p}^*(4) = \frac{\pi}{2}$

$\boldsymbol{p}^*(5) = 0.1$							
θ	0	$\frac{1}{6}$	$\frac{1}{3}$	$\frac{1}{2}$	$\frac{2}{3}$	$\frac{5}{6}$	1
κ_a	2.00	2.20	4.60	3.90	5.20	2.50	1.90
$\lvert\bar{\mathfrak{p}}(4) - \boldsymbol{p}^*(4)\rvert$ (%)	6.57	12.43	41.92	35.68	120.94	30.82	44.99
MAD($\mathfrak{p}(4)$) (%)	0.87	2.54	24.25	13.85	35.80	4.08	6.76
var($\mathfrak{p}(4)$) (%)	0.05	0.23	10.80	4.12	19.23	0.56	1.09
$\boldsymbol{p}^*(5) = 0.3$							
θ	0	$\frac{1}{6}$	$\frac{1}{3}$	$\frac{1}{2}$	$\frac{2}{3}$	$\frac{5}{6}$	1
κ_a	3.80	4.60	2.50	2.50	1.60	2.60	2.10
$\lvert\bar{\mathfrak{p}}(4) - \boldsymbol{p}^*(4)\rvert$ (%)	106.53	92.68	24.68	28.26	8.71	10.89	10.22
MAD($\mathfrak{p}(4)$) (%)	35.05	37.44	5.80	7.73	0.93	4.14	4.86
var($\mathfrak{p}(4)$) (%)	16.05	17.60	0.79	1.01	0.07	0.31	0.32
$\boldsymbol{p}^*(5) = 0.5$							
θ	0	$\frac{1}{6}$	$\frac{1}{3}$	$\frac{1}{2}$	$\frac{2}{3}$	$\frac{5}{6}$	1
κ_a	2.50	3.30	2.20	2.60	1.80	1.70	1.20
$\lvert\bar{\mathfrak{p}}(4) - \boldsymbol{p}^*(4)\rvert$ (%)	73.30	83.59	18.46	28.58	10.23	27.43	0.79
MAD($\mathfrak{p}(4)$) (%)	9.86	34.67	8.34	4.44	2.47	11.14	5.90
var($\mathfrak{p}(4)$) (%)	3.24	15.13	1.08	0.79	0.22	1.94	0.45
$\boldsymbol{p}^*(5) = 0.7$							
θ	0	$\frac{1}{6}$	$\frac{1}{3}$	$\frac{1}{2}$	$\frac{2}{3}$	$\frac{5}{6}$	1
κ_a	3.00	1.30	0.70	0.60	1.40	2.30	1.70
$\lvert\bar{\mathfrak{p}}(4) - \boldsymbol{p}^*(4)\rvert$ (%)	80.57	12.83	12.12	0.19	3.56	30.20	23.09
MAD($\mathfrak{p}(4)$) (%)	25.09	2.97	3.90	0.15	1.63	3.87	7.40
var($\mathfrak{p}(4)$) (%)	8.94	0.11	0.16	0.00	0.05	0.51	1.02
$\boldsymbol{p}^*(5) = 0.9$							
θ	0	$\frac{1}{6}$	$\frac{1}{3}$	$\frac{1}{2}$	$\frac{2}{3}$	$\frac{5}{6}$	1
κ_a	1.50	1.50	1.50	1.70	2.10	1.90	1.60
$\lvert\bar{\mathfrak{p}}(4) - \boldsymbol{p}^*(4)\rvert$ (%)	18.74	18.74	18.74	14.32	4.32	1.67	0.59
MAD($\mathfrak{p}(4)$) (%)	0.88	0.88	0.88	2.22	9.24	7.34	5.01
var($\mathfrak{p}(4)$) (%)	0.05	0.05	0.05	0.15	0.99	0.72	0.40

Table 6.10.: Statistics of $\boldsymbol{p}(5)$ using the standard algorithm for the 5 parameter case with 1000 drawn samples for varying height of the lower muscle $\boldsymbol{p}^*(5)$ and thickness of the surrounding tissue layer θ in the settings from Section 6.3.4 with $\boldsymbol{p}^*(4) = \frac{\pi}{2}$

$\boldsymbol{p}^*(5) = 0.1$							
θ	0	$\frac{1}{6}$	$\frac{1}{3}$	$\frac{1}{2}$	$\frac{2}{3}$	$\frac{5}{6}$	1
κ_a	2.00	2.20	4.60	3.90	5.20	2.50	1.90
$\lvert\bar{\mathfrak{p}}(5) - \boldsymbol{p}^*(5)\rvert$ (%)	11.99	9.84	8.42	9.83	5.70	11.97	7.22
MAD($\mathfrak{p}(5)$) (%)	0.66	0.54	1.97	1.15	2.53	2.58	3.23
var($\mathfrak{p}(5)$) (%)	0.03	0.02	0.07	0.04	0.09	0.11	0.13
$\boldsymbol{p}^*(5) = 0.3$							
θ	0	$\frac{1}{6}$	$\frac{1}{3}$	$\frac{1}{2}$	$\frac{2}{3}$	$\frac{5}{6}$	1
κ_a	3.80	4.60	2.50	2.50	1.60	2.60	2.10
$\lvert\bar{\mathfrak{p}}(5) - \boldsymbol{p}^*(5)\rvert$ (%)	10.95	6.47	3.28	14.99	8.94	0.36	2.37
MAD($\mathfrak{p}(5)$) (%)	4.66	6.57	4.13	6.74	1.09	3.25	4.58
var($\mathfrak{p}(5)$) (%)	0.34	0.58	0.26	0.69	0.08	0.21	0.27
$\boldsymbol{p}^*(5) = 0.5$							
θ	0	$\frac{1}{6}$	$\frac{1}{3}$	$\frac{1}{2}$	$\frac{2}{3}$	$\frac{5}{6}$	1
κ_a	2.50	3.30	2.20	2.60	1.80	1.70	1.20
$\lvert\bar{\mathfrak{p}}(5) - \boldsymbol{p}^*(5)\rvert$ (%)	33.41	16.82	34.34	12.92	28.86	19.49	14.48
MAD($\mathfrak{p}(5)$) (%)	3.36	5.60	5.92	5.29	4.99	2.53	3.27
var($\mathfrak{p}(5)$) (%)	0.34	0.37	0.53	0.44	0.38	0.10	0.14
$\boldsymbol{p}^*(5) = 0.7$							
θ	0	$\frac{1}{6}$	$\frac{1}{3}$	$\frac{1}{2}$	$\frac{2}{3}$	$\frac{5}{6}$	1
κ_a	3.00	1.30	0.70	0.60	1.40	2.30	1.70
$\lvert\bar{\mathfrak{p}}(5) - \boldsymbol{p}^*(5)\rvert$ (%)	19.95	18.69	15.12	13.17	19.28	0.13	4.81
MAD($\mathfrak{p}(5)$) (%)	7.36	1.20	3.38	1.36	0.99	2.51	3.11
var($\mathfrak{p}(5)$) (%)	0.94	0.06	0.15	0.08	0.09	0.12	0.19
$\boldsymbol{p}^*(5) = 0.9$							
θ	0	$\frac{1}{6}$	$\frac{1}{3}$	$\frac{1}{2}$	$\frac{2}{3}$	$\frac{5}{6}$	1
κ_a	1.50	1.50	1.50	1.70	2.10	1.90	1.60
$\lvert\bar{\mathfrak{p}}(5) - \boldsymbol{p}^*(5)\rvert$ (%)	13.18	13.18	13.18	12.37	7.71	4.51	7.69
MAD($\mathfrak{p}(5)$) (%)	0.34	0.34	0.34	0.39	3.00	1.27	3.72
var($\mathfrak{p}(5)$) (%)	0.02	0.02	0.02	0.02	0.12	0.05	0.17

6.3.5. 9 Parameter Case

For this final parameter study, we also add the material parameters of the upper muscle to the parameters of interest, i.e., we set

$$\boldsymbol{p} = ((\sigma_{\mathrm{i},2})_{11}, (\sigma_{\mathrm{i},2})_{22}, (\sigma_{\mathrm{i},2})_{33}, \alpha_2, (\sigma_{\mathrm{i},1})_{11}, (\sigma_{\mathrm{i},1})_{22}, (\sigma_{\mathrm{i},1})_{33}, \alpha_1, \theta_{\mathrm{b}}).$$

Note that we put the material parameters, i.e., the conductivity magnitudes and rotation angles of both muscles, in front of the thickness of the lower muscle.

The acceptance rate κ_{a}, the absolute distance of the mean of the sampled chains to the reference value $|\bar{\mathfrak{p}} - \boldsymbol{p}^*|$, and the MAD and variance of the sampled chains are presented in Table 6.11 for the conductivity magnitudes of the lower muscle $\boldsymbol{p}(1:3)$, in Table 6.12 for the rotation angle of the lower muscle $\boldsymbol{p}(4)$, in Table 6.13 for the conductivity magnitudes of the upper muscle $\boldsymbol{p}(5:7)$, in Table 6.14 for the rotation angle of the upper muscle $\boldsymbol{p}(8)$, and in Table 6.15 for the thickness of the lower muscle $\boldsymbol{p}(9)$ for $\boldsymbol{p}^*(4) = \frac{\pi}{2}$ and varying reference thicknesses of the lower muscle $\boldsymbol{p}^*(9)$ and thicknesses of the surrounding tissue θ. The statistical values for $\boldsymbol{p}^*(4) \in \{0, \frac{\pi}{4}, \frac{3\pi}{4}\}$ are shown in Appendix E, more precisely in Tables E.1 to E.3 for $\boldsymbol{p}(1:3)$, in Tables E.4 to E.6 for $\boldsymbol{p}(4)$, in Tables E.7 to E.9 for $\boldsymbol{p}(5:7)$, in Tables E.10 to E.12 for $\boldsymbol{p}(8)$, and in Tables E.13 to E.15 for $\boldsymbol{p}(9)$.

Again, the high statistical values for the conductivity magnitudes of the lower muscle $\boldsymbol{p}(1:3)$ indicate that these parameters are not inferable within the given setting. The rotation angle of the lower muscle $\boldsymbol{p}(4)$ seems to be better inferable than $\boldsymbol{p}(1:3)$ but still shows high statistical values that do not show any clear dependency on θ or $\boldsymbol{p}^*(9)$. As in Section 6.3.2, we see that $\boldsymbol{p}(4)^* = 0$ plays a special role due to the lack of discontinuities in the resulting intracellular conductivity. Precisely, the statistical values of $\boldsymbol{p}(4)$ are clearly smaller for $\boldsymbol{p}^*(4) = 0$, see Table E.4, than for the other reference values $\boldsymbol{p}^*(4)$.

For the upper muscle, we see that the conductivity magnitudes $\boldsymbol{p}(5:7)$ are not inferable in the given setting, similar to $\boldsymbol{p}(1:3)$. Moreover, we observe that the statistical values increase with increasing thickness of the lower muscle, i.e., the thinner the upper muscle gets the worse the statistical values.

In accordance with our previous discussions on the influence of the rotation angles, we observe small statistical values for the rotation angle of the upper muscle $\boldsymbol{p}(8)$. Similar to the corresponding conductivity magnitudes, the statistical values of $\boldsymbol{p}(8)$ increase with decreasing influence of the upper muscle, i.e., with increasing thickness of the lower muscle.

The statistical values of the thickness of the lower muscle $\boldsymbol{p}(9)$ show a comparable behavior but are slightly worse.

6.3.6. Summary

From the parameter studies conducted in Sections 6.3.1 to 6.3.5, we deduce that the angles dominate the magnitudes (as observed before in the one-muscle case) and that the parameters of the upper muscle have a higher influence on the resulting EMG signals than the parameters of the lower muscle. These observations are in accordance with our observation that the rotation angle of the upper muscle seems to have the highest influence on the resulting EMG signals and is thus best inferable. Moreover, the thickness of the lower muscle seems to have similar influence as the rotation angles.

Furthermore, we see that the used finite difference discretization yields well-explainable results, especially for the 9 parameter case, even if the resulting intracellular conductivity $\sigma_{\mathrm{i}} = \sigma_{\mathrm{i},1}\mathbb{1}_{D_{\mathrm{M},1}} + \sigma_{\mathrm{i},2}\mathbb{1}_{D_{\mathrm{M},2}}$ is discontinuous. For further investigations we, nevertheless, suggest to use better suited discretizations that can resolve these discontinuities.

Table 6.11.: Statistics of $\boldsymbol{p}(1:3)$ using the standard algorithm for the 9 parameter case with 1000 drawn samples for varying height of the lower muscle $\boldsymbol{p}^*(9)$ and thickness of the surrounding tissue layer θ in the settings from Section 6.3.5 with $\boldsymbol{p}^*(4) = \frac{\pi}{2}$

$\boldsymbol{p}^*(9)$	θ	$\lvert\bar{\mathfrak{p}}(1:3) - \boldsymbol{p}^*(1:3)\rvert$ (%)			MAD($\mathfrak{p}(1:3)$) (%)			var($\mathfrak{p}(1:3)$) (%)		
0.10	0	133.27	182.72	12.59	29.20	36.24	24.64	11.13	20.20	8.44
0.10	$\frac{1}{6}$	160.50	238.48	11.71	26.65	51.54	15.95	9.61	39.48	4.56
0.10	$\frac{1}{3}$	38.19	196.28	0.72	54.69	66.89	12.08	38.26	58.94	3.54
0.10	$\frac{1}{2}$	131.48	134.16	2.62	26.35	28.21	10.93	11.57	13.02	3.25
0.10	$\frac{2}{3}$	129.18	241.46	3.86	44.11	51.91	9.89	25.67	49.69	3.07
0.10	$\frac{5}{6}$	96.39	244.94	12.56	19.44	78.02	11.23	5.45	84.86	3.31
0.10	1	149.70	172.45	4.81	26.82	61.02	6.86	10.04	47.70	2.34
0.30	0	83.15	229.87	6.13	17.00	87.28	14.83	3.74	91.03	4.30
0.30	$\frac{1}{6}$	126.82	201.95	8.91	21.23	58.57	11.15	7.84	43.68	3.46
0.30	$\frac{1}{3}$	169.69	149.85	17.35	35.45	18.95	7.79	19.88	8.32	3.28
0.30	$\frac{1}{2}$	87.66	186.45	10.48	10.33	44.59	7.34	2.09	50.66	2.58
0.30	$\frac{2}{3}$	104.16	172.91	5.59	9.47	47.33	6.21	2.83	32.76	2.43
0.30	$\frac{5}{6}$	101.15	124.45	2.74	5.64	38.26	7.58	0.91	23.66	2.65
0.30	1	145.93	76.68	2.51	10.09	14.14	5.15	1.77	3.50	2.47
0.50	0	220.22	147.74	7.81	29.56	31.74	11.17	16.26	17.21	2.35
0.50	$\frac{1}{6}$	113.34	166.21	101.90	7.69	12.15	6.95	0.84	2.35	0.75
0.50	$\frac{1}{3}$	129.51	38.88	160.09	8.36	3.55	6.03	1.34	0.46	0.81
0.50	$\frac{1}{2}$	172.35	85.16	255.37	7.19	10.23	7.54	1.95	2.16	3.18
0.50	$\frac{2}{3}$	104.39	142.10	61.20	19.85	37.79	2.50	5.06	20.46	0.49
0.50	$\frac{5}{6}$	137.95	133.66	56.58	5.55	31.39	2.93	0.72	15.26	0.53
0.50	1	136.83	68.22	55.43	9.06	15.29	3.00	1.49	3.44	0.60
0.70	0	203.11	173.78	23.29	27.37	40.22	8.13	13.15	26.34	1.36
0.70	$\frac{1}{6}$	115.94	98.95	45.36	6.59	2.94	1.11	0.77	0.29	0.28
0.70	$\frac{1}{3}$	104.83	157.51	69.37	6.74	3.18	0.92	0.75	0.82	0.10
0.70	$\frac{1}{2}$	111.97	142.92	107.91	11.05	10.88	5.37	1.34	1.37	0.32
0.70	$\frac{2}{3}$	71.06	23.39	163.91	13.50	5.87	3.01	2.37	0.69	0.22
0.70	$\frac{5}{6}$	49.45	0.18	238.78	12.74	14.07	8.78	2.57	3.15	2.36
0.70	1	127.78	96.88	301.70	1.90	5.68	10.90	0.42	1.42	7.53
0.90	0	102.42	154.78	22.50	2.56	5.03	3.36	0.26	1.40	1.07
0.90	$\frac{1}{6}$	113.81	143.25	0.96	15.50	8.92	6.04	3.29	2.12	1.55
0.90	$\frac{1}{3}$	135.55	150.91	2.85	6.76	19.77	5.77	1.85	6.92	1.43
0.90	$\frac{1}{2}$	177.23	149.67	6.21	15.20	14.36	7.29	4.53	5.04	1.55
0.90	$\frac{2}{3}$	160.62	62.11	25.49	8.45	8.34	2.12	1.87	1.38	0.57
0.90	$\frac{5}{6}$	135.73	70.34	20.56	1.30	1.46	2.11	0.35	0.18	0.64
0.90	1	135.73	70.34	20.56	1.30	1.46	2.11	0.35	0.18	0.64

Table 6.12.: Statistics of $\boldsymbol{p}(4)$ using the standard algorithm for the 9 parameter case with 1000 drawn samples for varying height of the lower muscle $\boldsymbol{p}^*(9)$ and thickness of the surrounding tissue layer θ in the settings from Section 6.3.5 with $\boldsymbol{p}^*(4) = \frac{\pi}{2}$

$\boldsymbol{p}^*(9) = 0.1$							
θ	0	$\frac{1}{6}$	$\frac{1}{3}$	$\frac{1}{2}$	$\frac{2}{3}$	$\frac{5}{6}$	1
κ_a	4.10	4.10	3.90	4.60	4.80	2.70	3.40
$\lvert\bar{\mathfrak{p}}(4) - \boldsymbol{p}^*(4)\rvert$ (%)	92.75	97.06	108.54	112.44	58.44	63.84	39.63
MAD($\mathfrak{p}(4)$) (%)	42.28	42.16	32.15	36.46	28.72	20.06	16.49
var($\mathfrak{p}(4)$) (%)	24.25	23.71	16.08	18.11	11.74	5.60	3.70
$\boldsymbol{p}^*(9) = 0.3$							
θ	0	$\frac{1}{6}$	$\frac{1}{3}$	$\frac{1}{2}$	$\frac{2}{3}$	$\frac{5}{6}$	1
κ_a	2.50	1.90	2.30	2.50	2.60	2.20	1.60
$\lvert\bar{\mathfrak{p}}(4) - \boldsymbol{p}^*(4)\rvert$ (%)	68.62	51.31	34.43	2.47	0.11	16.59	14.49
MAD($\mathfrak{p}(4)$) (%)	28.64	11.17	7.30	3.53	2.61	5.78	2.48
var($\mathfrak{p}(4)$) (%)	10.86	2.28	1.24	0.23	0.10	0.54	0.18
$\boldsymbol{p}^*(9) = 0.5$							
θ	0	$\frac{1}{6}$	$\frac{1}{3}$	$\frac{1}{2}$	$\frac{2}{3}$	$\frac{5}{6}$	1
κ_a	2.90	0.80	1.30	1.60	2.40	1.90	1.70
$\lvert\bar{\mathfrak{p}}(4) - \boldsymbol{p}^*(4)\rvert$ (%)	33.23	10.56	4.42	10.64	32.08	1.98	16.04
MAD($\mathfrak{p}(4)$) (%)	7.02	2.70	1.40	2.41	9.54	2.86	4.39
var($\mathfrak{p}(4)$) (%)	1.13	0.10	0.03	0.15	1.50	0.12	0.29
$\boldsymbol{p}^*(9) = 0.7$							
θ	0	$\frac{1}{6}$	$\frac{1}{3}$	$\frac{1}{2}$	$\frac{2}{3}$	$\frac{5}{6}$	1
κ_a	2.70	1.10	1.00	0.60	0.70	1.80	1.90
$\lvert\bar{\mathfrak{p}}(4) - \boldsymbol{p}^*(4)\rvert$ (%)	17.17	0.33	3.50	8.25	10.21	14.45	3.16
MAD($\mathfrak{p}(4)$) (%)	4.55	0.80	0.86	1.70	3.70	7.81	3.31
var($\mathfrak{p}(4)$) (%)	0.54	0.02	0.02	0.10	0.14	0.80	0.15
$\boldsymbol{p}^*(9) = 0.9$							
θ	0	$\frac{1}{6}$	$\frac{1}{3}$	$\frac{1}{2}$	$\frac{2}{3}$	$\frac{5}{6}$	1
κ_a	1.80	2.50	2.80	2.30	1.80	1.40	1.40
$\lvert\bar{\mathfrak{p}}(4) - \boldsymbol{p}^*(4)\rvert$ (%)	2.96	54.56	60.99	44.98	32.56	32.32	32.32
MAD($\mathfrak{p}(4)$) (%)	0.89	11.59	10.74	7.68	2.51	1.39	1.39
var($\mathfrak{p}(4)$) (%)	0.06	2.29	2.38	1.15	0.21	0.15	0.15

Table 6.13.: Statistics of $\boldsymbol{p}(5:7)$ using the standard algorithm for the 9 parameter case with 1000 drawn samples for varying height of the lower muscle $\boldsymbol{p}^*(9)$ and thickness of the surrounding tissue layer θ in the settings from Section 6.3.5 with $\boldsymbol{p}^*(4) = \frac{\pi}{2}$

$\boldsymbol{p}^*(9)$	θ	$\lvert\bar{\mathfrak{p}}(5:7) - \boldsymbol{p}^*(5:7)\rvert$ (%)			MAD($\mathfrak{p}(5:7)$) (%)			var($\mathfrak{p}(5:7)$) (%)		
0.10	0	119.42	60.87	138.65	24.66	18.09	25.47	9.12	5.26	8.98
0.10	$\frac{1}{6}$	199.18	12.42	195.81	38.77	29.13	70.78	19.56	16.15	62.66
0.10	$\frac{1}{3}$	110.81	31.17	62.21	35.43	24.21	17.99	15.50	9.53	6.29
0.10	$\frac{1}{2}$	83.16	1.41	190.46	27.92	51.68	75.92	10.41	35.40	72.55
0.10	$\frac{2}{3}$	103.55	129.12	63.90	41.61	18.60	27.03	24.39	4.96	10.67
0.10	$\frac{5}{6}$	165.85	62.15	54.04	13.22	22.90	41.72	5.77	7.04	21.09
0.10	1	150.09	31.00	104.30	44.13	34.52	33.55	22.76	20.45	14.01
0.30	0	140.08	129.02	215.27	6.50	21.59	77.78	1.03	7.66	75.09
0.30	$\frac{1}{6}$	113.29	108.76	201.96	3.88	7.46	43.56	0.56	1.85	27.69
0.30	$\frac{1}{3}$	118.29	164.23	82.49	11.46	13.28	6.76	3.71	2.69	1.26
0.30	$\frac{1}{2}$	166.51	180.99	112.07	18.19	17.75	13.09	5.10	4.23	3.32
0.30	$\frac{2}{3}$	165.94	224.86	99.83	14.09	18.16	18.31	3.91	6.11	5.05
0.30	$\frac{5}{6}$	241.86	155.85	65.57	17.48	11.40	6.73	8.62	2.21	1.27
0.30	1	190.55	134.04	27.03	15.63	10.99	4.76	5.12	3.37	1.01
0.50	0	116.08	118.95	126.93	11.42	8.18	13.62	3.39	1.10	2.92
0.50	$\frac{1}{6}$	81.36	140.90	111.05	7.93	15.57	13.63	1.04	2.96	2.53
0.50	$\frac{1}{3}$	26.61	102.74	52.28	17.14	18.85	10.00	5.44	5.37	1.82
0.50	$\frac{1}{2}$	116.28	264.62	62.81	2.43	13.36	8.73	0.41	5.81	1.29
0.50	$\frac{2}{3}$	164.01	154.92	83.42	29.08	8.47	6.85	13.82	2.29	0.73
0.50	$\frac{5}{6}$	146.54	123.73	90.11	17.82	9.65	3.66	7.42	3.56	0.58
0.50	1	69.49	157.95	113.99	7.36	10.35	11.32	0.94	1.99	2.53
0.70	0	103.69	82.50	64.08	13.53	20.00	27.73	2.38	6.24	10.47
0.70	$\frac{1}{6}$	149.16	95.35	80.28	1.70	6.25	7.54	0.37	0.70	0.96
0.70	$\frac{1}{3}$	123.99	98.71	67.19	1.57	6.35	7.52	0.13	0.69	1.00
0.70	$\frac{1}{2}$	125.61	105.30	100.49	12.95	7.51	5.91	1.70	0.58	0.48
0.70	$\frac{2}{3}$	136.35	146.78	131.58	12.38	9.03	19.27	1.59	1.48	4.49
0.70	$\frac{5}{6}$	149.47	144.93	93.38	13.40	9.02	14.05	2.42	1.44	3.33
0.70	1	134.44	260.56	80.81	13.65	8.16	5.84	2.40	4.21	0.69
0.90	0	62.54	194.21	145.46	8.12	7.59	10.69	2.16	2.33	3.97
0.90	$\frac{1}{6}$	92.15	183.14	117.07	23.10	9.19	14.50	6.90	3.09	5.26
0.90	$\frac{1}{3}$	119.71	11.71	128.71	18.19	38.34	17.97	5.43	29.42	6.81
0.90	$\frac{1}{2}$	87.80	61.32	195.27	9.69	21.46	35.32	2.21	9.28	24.41
0.90	$\frac{2}{3}$	8.47	166.90	136.97	17.06	5.01	16.89	7.14	1.56	5.76
0.90	$\frac{5}{6}$	78.69	152.95	102.99	1.43	1.76	4.13	0.25	0.47	0.97
0.90	1	78.69	152.95	102.99	1.43	1.76	4.13	0.25	0.47	0.97

Table 6.14.: Statistics of $\boldsymbol{p}(8)$ using the standard algorithm for the 9 parameter case with 1000 drawn samples for varying height of the lower muscle $\boldsymbol{p}^*(9)$ and thickness of the surrounding tissue layer θ in the settings from Section 6.3.5 with $\boldsymbol{p}^*(4) = \frac{\pi}{2}$

$\boldsymbol{p}^*(9) = 0.1$							
θ	0	$\frac{1}{6}$	$\frac{1}{3}$	$\frac{1}{2}$	$\frac{2}{3}$	$\frac{5}{6}$	1
κ_a	4.10	4.10	3.90	4.60	4.80	2.70	3.40
$\lvert\bar{\mathfrak{p}}(8) - \boldsymbol{p}^*(8)\rvert$ (%)	1.02	1.94	1.69	1.55	2.34	1.29	1.92
MAD($\mathfrak{p}(8)$) (%)	0.82	0.58	0.77	0.93	1.87	1.39	1.40
var($\mathfrak{p}(8)$) (%)	0.01	0.01	0.02	0.02	0.12	0.04	0.05
$\boldsymbol{p}^*(9) = 0.3$							
θ	0	$\frac{1}{6}$	$\frac{1}{3}$	$\frac{1}{2}$	$\frac{2}{3}$	$\frac{5}{6}$	1
κ_a	2.50	1.90	2.30	2.50	2.60	2.20	1.60
$\lvert\bar{\mathfrak{p}}(8) - \boldsymbol{p}^*(8)\rvert$ (%)	2.22	2.91	2.34	1.33	3.08	3.77	4.40
MAD($\mathfrak{p}(8)$) (%)	1.04	0.43	1.54	1.61	1.28	1.60	3.58
var($\mathfrak{p}(8)$) (%)	0.02	0.02	0.06	0.07	0.08	0.09	0.32
$\boldsymbol{p}^*(9) = 0.5$							
θ	0	$\frac{1}{6}$	$\frac{1}{3}$	$\frac{1}{2}$	$\frac{2}{3}$	$\frac{5}{6}$	1
κ_a	2.90	0.80	1.30	1.60	2.40	1.90	1.70
$\lvert\bar{\mathfrak{p}}(8) - \boldsymbol{p}^*(8)\rvert$ (%)	1.33	1.47	8.07	34.16	2.49	3.49	3.74
MAD($\mathfrak{p}(8)$) (%)	1.59	0.62	3.22	2.56	1.88	1.62	3.13
var($\mathfrak{p}(8)$) (%)	0.10	0.01	0.19	0.17	0.13	0.11	0.18
$\boldsymbol{p}^*(9) = 0.7$							
θ	0	$\frac{1}{6}$	$\frac{1}{3}$	$\frac{1}{2}$	$\frac{2}{3}$	$\frac{5}{6}$	1
κ_a	2.70	1.10	1.00	0.60	0.70	1.80	1.90
$\lvert\bar{\mathfrak{p}}(8) - \boldsymbol{p}^*(8)\rvert$ (%)	1.10	1.75	1.81	6.08	16.52	21.08	25.12
MAD($\mathfrak{p}(8)$) (%)	1.17	1.44	1.52	1.65	4.03	5.18	1.43
var($\mathfrak{p}(8)$) (%)	0.08	0.04	0.04	0.03	0.19	0.41	0.06
$\boldsymbol{p}^*(9) = 0.9$							
θ	0	$\frac{1}{6}$	$\frac{1}{3}$	$\frac{1}{2}$	$\frac{2}{3}$	$\frac{5}{6}$	1
κ_a	1.80	2.50	2.80	2.30	1.80	1.40	1.40
$\lvert\bar{\mathfrak{p}}(8) - \boldsymbol{p}^*(8)\rvert$ (%)	2.84	3.06	7.86	10.47	16.71	36.39	36.39
MAD($\mathfrak{p}(8)$) (%)	1.44	2.29	6.54	5.37	4.37	1.16	1.16
var($\mathfrak{p}(8)$) (%)	0.10	0.18	0.76	0.61	0.39	0.12	0.12

Table 6.15.: Statistics of $\boldsymbol{p}(9)$ using the standard algorithm for the 9 parameter case with 1000 drawn samples for varying height of the lower muscle $\boldsymbol{p}^*(9)$ and thickness of the surrounding tissue layer θ in the settings from Section 6.3.5 with $\boldsymbol{p}^*(4) = \frac{\pi}{2}$

$\boldsymbol{p}^*(9) = 0.1$							
θ	0	$\frac{1}{6}$	$\frac{1}{3}$	$\frac{1}{2}$	$\frac{2}{3}$	$\frac{5}{6}$	1
κ_a	4.10	4.10	3.90	4.60	4.80	2.70	3.40
$\lvert\bar{\mathfrak{p}}(9) - \boldsymbol{p}^*(9)\rvert$ (%)	6.43	7.26	7.18	5.88	7.31	6.73	5.51
MAD($\mathfrak{p}(9)$) (%)	3.21	2.86	4.07	2.87	4.52	1.32	3.08
var($\mathfrak{p}(9)$) (%)	0.13	0.11	0.20	0.12	0.24	0.03	0.13
$\boldsymbol{p}^*(9) = 0.3$							
θ	0	$\frac{1}{6}$	$\frac{1}{3}$	$\frac{1}{2}$	$\frac{2}{3}$	$\frac{5}{6}$	1
κ_a	2.50	1.90	2.30	2.50	2.60	2.20	1.60
$\lvert\bar{\mathfrak{p}}(9) - \boldsymbol{p}^*(9)\rvert$ (%)	7.50	10.70	10.34	3.65	13.73	13.26	13.26
MAD($\mathfrak{p}(9)$) (%)	9.34	10.80	7.64	4.16	6.69	6.66	6.65
var($\mathfrak{p}(9)$) (%)	1.10	1.38	0.83	0.25	0.64	0.65	0.59
$\boldsymbol{p}^*(9) = 0.5$							
θ	0	$\frac{1}{6}$	$\frac{1}{3}$	$\frac{1}{2}$	$\frac{2}{3}$	$\frac{5}{6}$	1
κ_a	2.90	0.80	1.30	1.60	2.40	1.90	1.70
$\lvert\bar{\mathfrak{p}}(9) - \boldsymbol{p}^*(9)\rvert$ (%)	1.35	20.54	23.36	21.42	33.11	29.87	29.90
MAD($\mathfrak{p}(9)$) (%)	6.21	1.97	1.48	1.28	8.44	7.81	7.79
var($\mathfrak{p}(9)$) (%)	0.63	0.10	0.09	0.09	1.04	0.83	0.84
$\boldsymbol{p}^*(9) = 0.7$							
θ	0	$\frac{1}{6}$	$\frac{1}{3}$	$\frac{1}{2}$	$\frac{2}{3}$	$\frac{5}{6}$	1
κ_a	2.70	1.10	1.00	0.60	0.70	1.80	1.90
$\lvert\bar{\mathfrak{p}}(9) - \boldsymbol{p}^*(9)\rvert$ (%)	24.71	18.03	18.11	19.12	19.30	19.38	19.32
MAD($\mathfrak{p}(9)$) (%)	9.10	1.61	1.52	0.52	0.26	0.46	0.46
var($\mathfrak{p}(9)$) (%)	1.27	0.06	0.05	0.01	0.01	0.03	0.02
$\boldsymbol{p}^*(9) = 0.9$							
θ	0	$\frac{1}{6}$	$\frac{1}{3}$	$\frac{1}{2}$	$\frac{2}{3}$	$\frac{5}{6}$	1
κ_a	1.80	2.50	2.80	2.30	1.80	1.40	1.40
$\lvert\bar{\mathfrak{p}}(9) - \boldsymbol{p}^*(9)\rvert$ (%)	29.04	11.87	24.06	18.75	35.88	42.95	42.95
MAD($\mathfrak{p}(9)$) (%)	1.72	3.64	4.65	3.30	2.31	1.97	1.97
var($\mathfrak{p}(9)$) (%)	0.13	0.31	0.35	0.29	0.19	0.25	0.25

7. Summary, Conclusion and Outlook

Within this thesis, we contributed crucial steps towards an imaging method based on surface EMG measurements. More precisely, we discussed how to gain structural information from the electrical conductivity of the respective tissue.

Furthermore, we applied a Bayesian approach to the inverse EMG problem of inferring the electrical conductivity from surface EMG measurements and proved the well-posedness of the resulting Bayesian inverse EMG problem. Running a function space Metropolis-Hastings algorithm, we sampled from the posterior distribution of the electrical conductivity given surface EMG measurements. We observed low acceptance rates, especially when inferring the muscle fiber direction, and high runtimes that arise from solving the forward EMG problem in each step of the Metropolis-Hastings algorithm. We achieved tremendous speedups using an exact low-rank tensor representation of the forward EMG model when inferring only the conductivity magnitudes.

Finally, we applied the Metropolis-Hastings algorithm for inferring the electrical conductivity of a composite of two muscles and a layer of surrounding tissue. Future work resulting from the limitations discovered during this thesis is discussed below.

Sampling

Our observations in Chapters 5 and 6 clearly indicate that more elaborate techniques for accelerating the sampling process and evaluating the forward EMG model are needed to achieve a competitive imaging method that can be applied in real clinical scenarios.

From the experiments in Section 6.2 we saw that the structure of muscle tissue, i.e., the rotation angles, gets inferred with high accuracy even if the conductivity magnitudes show huge errors. We thus suggest, to run the SA for inferring the rotation angles with an initial guess on the conductivity magnitudes that is backed up by experiments or the literature and afterwards run the much faster TA for inferring the conductivity magnitudes for the previously inferred rotation angles.

Sampling the rotation angles may further be accelerated by generalizing the low-rank representation of the right-hand side of the forward EMG model to arbitrary muscle fiber

directions. This may possibly only lead to a surrogate of the right-hand side when using a cross approximation of which the approximation accuracy can, however, be prescribed under certain assumptions [42]. This generalization could enable the computation of realistic problems in medical applications and lead to a non-invasive and radiation-free imaging method.

Another promising approach for speeding up the expensive evaluations of the forward EMG model that is supported by mathematical theory was introduced in [12]. Here, the authors proved that although using local approximations of the forward model in MCMC methods, the sampling methods still sample from the exact posterior distribution asymptotically. Adopting this approach to the Bayesian inverse EMG problem therefore offers an alternative to using a global low-rank tensor representation surrogate.

Further algorithms that use surrogates or highly sophisticated sampling strategies were already introduced in Section 1.3. When applying these techniques in the future, care must be taken in order not to lose the mathematically guaranteed convergence of the Metropolis-Hastings algorithm.

Modeling and Theory

Combining the developed sampling algorithms with the model of force generation introduced in [48, Chapter 7] will result in a non-invasive and radiation-free imaging technique that infers medical images from voluntary muscle contractions and the resulting surface EMG signals.

For guaranteeing the well-posedness of the resulting inverse imaging problem, the well-posedness theory has to be extended to the Shorten model of the chemo-electrical behavior of muscle fibers [97]. The difficulty here is that the right-hand side of the model equations depends nonlinearly on the electrical conductivities so that properties like the boundedness of the forward EMG problem become more difficult to show.

Integration of continuum mechanics, i.e., of non-isometric muscle contractions, is computationally even more demanding, see the discussion in [48, Section 7.3.2], and thus infeasible unless accelerating the sampling process significantly. For this task surrogate models resulting from model order reduction, Gaussian process regression, or machine learning are likely to play an important role.

A. Appendix - 1 Parameter Case in Use Case 3

Table A.1.: Statistics of $\boldsymbol{p}$ using the standard algorithm for the 1 parameter case with 1000 drawn samples for varying height of the lower muscle $\boldsymbol{p}^*$ and thickness of the surrounding tissue layer θ in the settings from Section 6.3.1 with $\alpha_2 = 0$

$\boldsymbol{p}^* = 0.1$							
θ	0	$\frac{1}{6}$	$\frac{1}{3}$	$\frac{1}{2}$	$\frac{2}{3}$	$\frac{5}{6}$	1
κ_a	8.40	8.40	8.40	8.40	8.40	8.40	8.40
$\lvert\bar{\mathfrak{p}} - \boldsymbol{p}^*\rvert$ (%)	0.58	0.58	0.58	0.58	0.58	0.58	0.58
MAD($\mathfrak{p}$) (%)	0.27	0.27	0.27	0.27	0.27	0.27	0.27
var($\mathfrak{p}$) (%)	0.00	0.00	0.00	0.00	0.00	0.00	0.00
$\boldsymbol{p}^* = 0.3$							
θ	0	$\frac{1}{6}$	$\frac{1}{3}$	$\frac{1}{2}$	$\frac{2}{3}$	$\frac{5}{6}$	1
κ_a	85.60	85.60	85.60	85.60	85.60	85.60	85.60
$\lvert\bar{\mathfrak{p}} - \boldsymbol{p}^*\rvert$ (%)	8.41	8.41	8.41	8.41	8.41	8.41	8.41
MAD($\mathfrak{p}$) (%)	0.48	0.48	0.47	0.48	0.42	5.69	4.80
var($\mathfrak{p}$) (%)	4.80	4.80	4.80	4.80	4.80	4.80	4.80
$\boldsymbol{p}^* = 0.5$							
θ	0	$\frac{1}{6}$	$\frac{1}{3}$	$\frac{1}{2}$	$\frac{2}{3}$	$\frac{5}{6}$	1
κ_a	92.70	92.70	92.70	92.70	92.70	92.70	92.70
$\lvert\bar{\mathfrak{p}} - \boldsymbol{p}^*\rvert$ (%)	17.46	17.46	17.46	17.46	17.46	17.46	17.46
MAD($\mathfrak{p}$) (%)	9.57	9.57	9.57	9.57	9.57	9.57	9.57
var($\mathfrak{p}$) (%)	1.24	1.24	1.24	1.24	1.24	1.24	1.24
$\boldsymbol{p}^* = 0.7$							
θ	0	$\frac{1}{6}$	$\frac{1}{3}$	$\frac{1}{2}$	$\frac{2}{3}$	$\frac{5}{6}$	1
κ_a	94.50	94.50	94.50	94.50	94.50	94.50	94.50
$\lvert\bar{\mathfrak{p}} - \boldsymbol{p}^*\rvert$ (%)	27.58	27.58	27.58	27.58	27.58	27.58	27.58
MAD($\mathfrak{p}$) (%)	13.88	13.88	13.88	13.88	13.88	13.88	13.88
var($\mathfrak{p}$) (%)	2.72	2.72	2.72	2.72	2.72	2.72	2.72
$\boldsymbol{p}^* = 0.9$							
θ	0	$\frac{1}{6}$	$\frac{1}{3}$	$\frac{1}{2}$	$\frac{2}{3}$	$\frac{5}{6}$	1
κ_a	100.00	100.00	100.00	100.00	100.00	100.00	100.00
$\lvert\bar{\mathfrak{p}} - \boldsymbol{p}^*\rvert$ (%)	37.83	37.83	37.83	37.83	37.83	37.83	37.83
MAD($\mathfrak{p}$) (%)	18.43	18.43	18.43	18.43	18.43	18.43	18.43
var($\mathfrak{p}$) (%)	4.69	4.69	4.69	4.69	4.69	4.69	4.69

Table A.2.: Statistics of $\boldsymbol{p}$ using the standard algorithm for the 1 parameter case with 1000 drawn samples for varying height of the lower muscle $\boldsymbol{p}^*$ and thickness of the surrounding tissue layer θ in the settings from Section 6.3.1 with $\alpha_2 = \frac{\pi}{4}$

$\boldsymbol{p}^* = 0.1$							
θ	0	$\frac{1}{6}$	$\frac{1}{3}$	$\frac{1}{2}$	$\frac{2}{3}$	$\frac{5}{6}$	1
κ_a	8.40	8.40	8.40	8.40	8.40	8.40	8.40
$\lvert\bar{\mathfrak{p}} - \boldsymbol{p}^*\rvert$ (%)	0.58	0.58	0.58	0.58	0.58	0.58	0.58
MAD($\mathfrak{p}$) (%)	0.27	0.27	0.27	0.27	0.27	0.27	0.27
var($\mathfrak{p}$) (%)	0.00	0.00	0.00	0.00	0.00	0.00	0.00
$\boldsymbol{p}^* = 0.3$							
θ	0	$\frac{1}{6}$	$\frac{1}{3}$	$\frac{1}{2}$	$\frac{2}{3}$	$\frac{5}{6}$	1
κ_a	8.60	9.40	9.70	9.70	85.60	85.60	85.60
$\lvert\bar{\mathfrak{p}} - \boldsymbol{p}^*\rvert$ (%)	7.11	3.66	3.56	3.56	8.41	8.41	8.41
MAD($\mathfrak{p}$) (%)	0.47	0.47	0.53	0.53	4.80	4.80	4.80
var($\mathfrak{p}$) (%)	0.01	0.01	0.01	0.01	0.32	0.32	0.32
$\boldsymbol{p}^* = 0.5$							
θ	0	$\frac{1}{6}$	$\frac{1}{3}$	$\frac{1}{2}$	$\frac{2}{3}$	$\frac{5}{6}$	1
κ_a	6.90	6.90	6.90	6.90	6.90	6.70	6.70
$\lvert\bar{\mathfrak{p}} - \boldsymbol{p}^*\rvert$ (%)	5.24	5.24	5.24	5.24	4.00	3.94	3.94
MAD($\mathfrak{p}$) (%)	0.41	0.41	0.41	0.41	0.33	0.37	0.37
var($\mathfrak{p}$) (%)	0.01	0.01	0.01	0.01	0.01	0.01	0.01
$\boldsymbol{p}^* = 0.7$							
θ	0	$\frac{1}{6}$	$\frac{1}{3}$	$\frac{1}{2}$	$\frac{2}{3}$	$\frac{5}{6}$	1
κ_a	3.90	3.90	3.90	3.90	4.10	3.90	3.90
$\lvert\bar{\mathfrak{p}} - \boldsymbol{p}^*\rvert$ (%)	3.40	3.40	3.40	3.40	2.76	1.35	1.35
MAD($\mathfrak{p}$) (%)	0.29	0.29	0.29	0.29	0.25	0.16	0.16
var($\mathfrak{p}$) (%)	0.00	0.00	0.00	0.00	0.00	0.00	0.00
$\boldsymbol{p}^* = 0.9$							
θ	0	$\frac{1}{6}$	$\frac{1}{3}$	$\frac{1}{2}$	$\frac{2}{3}$	$\frac{5}{6}$	1
κ_a	100.00	100.00	100.00	100.00	100.00	100.00	100.00
$\lvert\bar{\mathfrak{p}} - \boldsymbol{p}^*\rvert$ (%)	37.83	37.83	37.83	37.83	37.83	37.83	37.83
MAD($\mathfrak{p}$) (%)	18.43	18.43	18.43	18.43	18.43	18.43	18.43
var($\mathfrak{p}$) (%)	4.69	4.69	4.69	4.69	4.69	4.69	4.69

Table A.3.: Statistics of $\boldsymbol{p}$ using the standard algorithm for the 1 parameter case with 1000 drawn samples for varying height of the lower muscle $\boldsymbol{p}^*$ and thickness of the surrounding tissue layer θ in the settings from Section 6.3.1 with $\alpha_2 = \frac{3\pi}{4}$

				$\boldsymbol{p}^* = 0.1$			
θ	0	$\frac{1}{6}$	$\frac{1}{3}$	$\frac{1}{2}$	$\frac{2}{3}$	$\frac{5}{6}$	1
κ_a	10.00	10.00	10.00	10.00	10.00	10.00	10.00
$\lvert\bar{\mathfrak{p}} - \boldsymbol{p}^*\rvert$ (%)	11.22	11.22	11.22	11.22	11.22	11.22	11.22
MAD($\mathfrak{p}$) (%)	0.58	0.58	0.58	0.58	0.58	0.58	0.58
var($\mathfrak{p}$) (%)	0.01	0.01	0.01	0.01	0.01	0.01	0.01
				$\boldsymbol{p}^* = 0.3$			
θ	0	$\frac{1}{6}$	$\frac{1}{3}$	$\frac{1}{2}$	$\frac{2}{3}$	$\frac{5}{6}$	1
κ_a	9.10	9.80	9.70	85.60	85.60	85.60	85.60
$\lvert\bar{\mathfrak{p}} - \boldsymbol{p}^*\rvert$ (%)	7.15	7.09	3.56	8.41	8.41	8.41	8.41
MAD($\mathfrak{p}$) (%)	0.47	0.54	0.53	4.80	4.80	4.80	4.80
var($\mathfrak{p}$) (%)	0.01	0.01	0.01	0.32	0.32	0.32	0.32
				$\boldsymbol{p}^* = 0.5$			
θ	0	$\frac{1}{6}$	$\frac{1}{3}$	$\frac{1}{2}$	$\frac{2}{3}$	$\frac{5}{6}$	1
κ_a	6.90	6.90	6.90	6.90	6.90	6.90	6.90
$\lvert\bar{\mathfrak{p}} - \boldsymbol{p}^*\rvert$ (%)	5.24	5.24	5.24	5.24	5.24	5.24	5.24
MAD($\mathfrak{p}$) (%)	0.41	0.41	0.41	0.41	0.41	0.41	0.41
var($\mathfrak{p}$) (%)	0.01	0.01	0.01	0.01	0.01	0.01	0.01
				$\boldsymbol{p}^* = 0.7$			
θ	0	$\frac{1}{6}$	$\frac{1}{3}$	$\frac{1}{2}$	$\frac{2}{3}$	$\frac{5}{6}$	1
κ_a	3.90	3.90	3.90	3.90	3.90	3.90	5.20
$\lvert\bar{\mathfrak{p}} - \boldsymbol{p}^*\rvert$ (%)	3.40	3.40	3.40	3.40	3.40	3.40	2.86
MAD($\mathfrak{p}$) (%)	0.29	0.29	0.29	0.29	0.29	0.29	0.32
var($\mathfrak{p}$) (%)	0.00	0.00	0.00	0.00	0.00	0.00	0.00
				$\boldsymbol{p}^* = 0.9$			
θ	0	$\frac{1}{6}$	$\frac{1}{3}$	$\frac{1}{2}$	$\frac{2}{3}$	$\frac{5}{6}$	1
κ_a	100.00	100.00	100.00	100.00	100.00	100.00	100.00
$\lvert\bar{\mathfrak{p}} - \boldsymbol{p}^*\rvert$ (%)	37.83	37.83	37.83	37.83	37.83	37.83	37.83
MAD($\mathfrak{p}$) (%)	18.43	18.43	18.43	18.43	18.43	18.43	18.43
var($\mathfrak{p}$) (%)	4.69	4.69	4.69	4.69	4.69	4.69	4.69

B. Appendix - 3 Parameter Case in Use Case 3

Table B.1.: Statistics of $\boldsymbol{p}$ using the standard algorithm for the 3 parameter case with 1000 drawn samples for varying height of the lower muscle θ_b and thickness of the surrounding tissue layer θ in the settings from Section 6.3.2 with $\alpha_2 = 0$

θ_b	θ	κ_a	$\lvert\bar{\mathfrak{p}} - \boldsymbol{p}^*\rvert$ (%)			MAD($\mathfrak{p}$) (%)			var($\mathfrak{p}$) (%)		
0.10	0	2.50	11.75	4.60	1.24	19.07	9.67	2.54	7.06	2.77	0.86
0.10	$\frac{1}{6}$	2.10	1.64	8.04	1.28	11.13	15.97	2.46	3.02	4.05	0.84
0.10	$\frac{1}{3}$	2.00	0.56	7.67	1.01	11.40	23.60	2.49	3.20	7.86	0.85
0.10	$\frac{1}{2}$	2.50	0.17	1.71	1.05	11.26	22.61	2.48	3.18	7.69	0.85
0.10	$\frac{2}{3}$	2.70	0.93	13.02	1.25	12.98	17.10	2.47	3.59	4.77	0.84
0.10	$\frac{5}{6}$	3.60	3.91	12.24	1.60	17.38	20.03	2.44	5.54	5.84	0.83
0.10	1	4.40	4.84	20.37	1.41	24.77	33.68	2.32	9.87	15.15	0.83
0.30	0	2.00	6.58	9.52	0.90	8.00	10.07	2.49	2.25	2.82	0.85
0.30	$\frac{1}{6}$	2.30	14.44	55.75	0.85	14.67	14.30	2.36	3.82	3.39	0.84
0.30	$\frac{1}{3}$	2.10	14.50	61.18	1.22	15.25	7.47	2.33	4.13	1.42	0.83
0.30	$\frac{1}{2}$	2.30	10.87	40.98	1.20	22.25	23.08	2.33	6.92	6.98	0.83
0.30	$\frac{2}{3}$	2.00	13.98	43.54	1.13	18.95	21.21	2.33	5.16	5.79	0.83
0.30	$\frac{5}{6}$	1.80	25.54	57.14	1.12	12.46	18.49	2.33	2.61	4.06	0.83
0.30	1	1.80	25.54	57.14	1.12	12.46	18.49	2.33	2.61	4.06	0.83
0.50	0	1.70	0.03	1.25	1.22	11.01	17.75	2.47	3.06	4.97	0.84
0.50	$\frac{1}{6}$	1.80	10.85	16.15	1.21	6.86	18.59	2.47	2.06	4.63	0.84
0.50	$\frac{1}{3}$	10.15	17.45	1.24	7.77	20.86	2.47	2.32	5.47	0.84	
0.50	$\frac{1}{2}$	2.30	1.00	1.92	1.18	12.70	29.04	2.47	3.60	10.56	0.84
0.50	$\frac{2}{3}$	2.30	4.54	8.18	1.27	14.69	23.87	2.47	4.59	8.27	0.84
0.50	$\frac{5}{6}$	2.30	13.11	8.47	1.19	19.78	23.95	2.47	6.52	7.59	0.84
0.50	1	2.60	22.45	0.87	1.24	26.87	31.85	2.47	10.56	12.74	0.84
0.70	0	1.90	5.30	8.63	1.18	17.26	14.85	2.47	4.27	3.82	0.84
0.70	$\frac{1}{6}$	1.60	9.24	27.58	1.20	8.67	14.98	2.47	2.20	3.05	0.84
0.70	$\frac{1}{3}$	1.90	9.16	5.35	1.22	9.09	30.47	2.47	2.31	11.29	0.84
0.70	$\frac{1}{2}$	1.90	9.16	5.35	1.22	9.09	30.47	2.47	2.31	11.29	0.84
0.70	$\frac{2}{3}$	2.00	3.79	13.89	1.17	14.27	21.42	2.47	4.11	5.90	0.84
0.70	$\frac{5}{6}$	2.00	3.79	13.89	1.17	14.27	21.42	2.47	4.11	5.90	0.84
0.70	1	2.20	12.63	7.30	1.12	19.42	24.84	2.48	6.36	8.00	0.84
0.90	0	1.80	10.85	16.15	1.21	6.86	18.59	2.47	2.06	4.63	0.84
0.90	$\frac{1}{6}$	1.90	9.16	5.35	1.22	9.09	30.47	2.47	2.31	11.29	0.84
0.90	$\frac{1}{3}$	1.90	9.16	5.35	1.22	9.09	30.47	2.47	2.31	11.29	0.84
0.90	$\frac{1}{2}$	1.90	9.16	5.35	1.22	9.09	30.47	2.47	2.31	11.29	0.84
0.90	$\frac{2}{3}$	1.90	9.16	5.35	1.22	9.09	30.47	2.47	2.31	11.29	0.84
0.90	$\frac{5}{6}$	1.90	9.16	5.35	1.22	9.09	30.47	2.47	2.31	11.29	0.84
0.90	1	1.90	9.16	5.35	1.22	9.09	30.47	2.47	2.31	11.29	0.84

Table B.2.: Statistics of $\boldsymbol{p}$ using the standard algorithm for the 3 parameter case with 1000 drawn samples for varying height of the lower muscle θ_b and thickness of the surrounding tissue layer θ in the settings from Section 6.3.2 with $\alpha_2 = \frac{\pi}{4}$

θ_b	θ	κ_a	$\lvert\bar{\mathfrak{p}} - \boldsymbol{p}^*\rvert$ (%)			MAD($\mathfrak{p}$) (%)			var($\mathfrak{p}$) (%)		
0.10	0	1.80	87.59	158.57	14.03	3.87	5.64	2.31	0.26	1.70	0.61
0.10	$\frac{1}{6}$	2.90	2.76	301.53	7.85	27.85	15.64	5.17	14.58	14.03	0.97
0.10	$\frac{1}{3}$	3.10	48.97	301.10	7.01	26.02	16.14	5.52	11.33	14.26	1.00
0.10	$\frac{1}{2}$	3.10	86.94	299.14	5.48	16.95	19.90	4.98	7.58	18.71	1.07
0.10	$\frac{2}{3}$	2.40	148.22	300.15	2.76	8.44	18.67	2.53	3.12	17.62	0.86
0.10	$\frac{5}{6}$	2.80	178.47	299.78	0.73	17.98	19.16	2.68	8.38	18.07	0.89
0.10	1	2.40	246.57	298.91	0.17	18.46	20.73	2.59	14.47	19.69	0.88
0.30	0	1.40	77.77	154.16	1.06	2.79	5.22	2.38	0.25	1.39	0.85
0.30	$\frac{1}{6}$	3.60	102.84	298.39	0.07	30.08	18.80	6.53	14.44	16.47	1.29
0.30	$\frac{1}{3}$	3.20	131.94	296.59	1.25	34.19	22.65	4.90	19.15	20.59	1.05
0.30	$\frac{1}{2}$	2.50	144.95	295.27	0.91	13.05	26.66	3.79	4.39	24.59	0.92
0.30	$\frac{2}{3}$	2.70	164.51	279.51	0.76	22.53	43.88	2.64	11.19	35.37	0.87
0.30	$\frac{5}{6}$	2.80	202.29	278.11	0.69	32.43	43.40	2.48	20.41	34.76	0.86
0.30	1	2.30	187.11	251.21	1.17	55.75	60.42	2.51	37.89	47.57	0.85
0.50	0	2.10	12.37	86.91	4.71	22.97	5.72	2.17	9.64	1.00	0.76
0.50	$\frac{1}{6}$	3.40	39.22	293.59	5.06	74.37	24.58	2.59	66.62	20.95	0.79
0.50	$\frac{1}{3}$	3.70	23.44	293.37	3.67	67.69	24.62	2.83	54.76	20.95	0.82
0.50	$\frac{1}{2}$	3.30	31.47	292.56	3.00	58.82	26.32	2.86	41.97	23.20	0.83
0.50	$\frac{2}{3}$	2.90	39.55	289.75	1.72	41.01	30.61	3.41	22.15	26.43	0.88
0.50	$\frac{5}{6}$	2.50	116.34	289.02	1.57	11.33	34.18	2.58	2.16	28.26	0.84
0.50	1	2.60	81.61	283.12	0.83	13.27	38.88	2.66	2.82	31.48	0.86
0.70	0	2.20	39.07	58.64	2.84	22.76	6.07	2.35	10.14	0.80	0.80
0.70	$\frac{1}{6}$	3.80	7.61	288.45	3.38	52.06	29.41	2.66	33.33	25.86	0.81
0.70	$\frac{1}{3}$	3.40	0.49	287.19	2.97	60.74	33.46	2.46	43.73	27.52	0.83
0.70	$\frac{1}{2}$	3.10	40.13	283.23	2.37	44.94	37.62	2.79	24.49	30.67	0.85
0.70	$\frac{2}{3}$	2.60	52.90	282.90	1.84	24.98	38.80	2.67	8.36	31.36	0.85
0.70	$\frac{5}{6}$	2.90	43.22	279.38	1.57	32.62	40.42	2.46	13.37	31.91	0.84
0.70	1	2.50	119.39	259.85	1.70	20.49	58.32	2.46	5.68	47.23	0.83
0.90	0	2.10	32.71	66.48	1.26	29.22	9.83	2.47	12.51	1.45	0.84
0.90	$\frac{1}{6}$	3.00	11.59	196.61	3.13	40.38	50.98	2.32	19.82	35.17	0.81
0.90	$\frac{1}{3}$	3.00	16.68	205.59	2.77	40.53	57.13	2.35	20.90	44.47	0.81
0.90	$\frac{1}{2}$	2.20	40.81	221.26	2.25	29.46	38.18	2.28	11.34	22.31	0.81
0.90	$\frac{2}{3}$	2.40	67.04	234.36	2.26	11.63	51.49	2.28	2.65	37.50	0.81
0.90	$\frac{5}{6}$	2.60	69.23	223.60	1.87	27.61	43.97	2.30	11.27	30.80	0.82
0.90	1	2.30	49.80	197.93	1.29	24.01	44.90	2.32	7.97	26.97	0.83

Table B.3.: Statistics of $\boldsymbol{p}$ using the standard algorithm for the 3 parameter case with 1000 drawn samples for varying height of the lower muscle θ_b and thickness of the surrounding tissue layer θ in the settings from Section 6.3.2 with $\alpha_2 = \frac{3\pi}{4}$

θ_b	θ	κ_a	$\lvert\bar{\mathfrak{p}} - \boldsymbol{p}^*\rvert$ (%)			MAD($\mathfrak{p}$) (%)			var($\mathfrak{p}$) (%)		
0.10	0	2.40	122.89	301.73	25.01	13.43	16.09	3.93	2.90	14.64	0.64
0.10	$\frac{1}{6}$	3.00	2.39	301.08	14.22	38.12	16.15	4.49	20.92	14.26	0.79
0.10	$\frac{1}{3}$	2.90	44.73	301.28	11.35	32.43	15.85	4.20	13.03	13.95	0.80
0.10	$\frac{1}{2}$	2.90	110.11	300.09	11.17	12.11	18.64	4.81	3.90	17.60	0.90
0.10	$\frac{2}{3}$	2.20	163.59	299.91	8.46	9.77	19.01	2.35	4.34	17.83	0.77
0.10	$\frac{5}{6}$	2.80	204.30	299.19	6.69	14.86	20.12	2.75	9.44	18.47	0.79
0.10	1	2.90	233.40	299.35	6.97	33.01	19.64	3.18	20.86	18.37	0.82
0.30	0	2.60	189.55	301.36	18.26	13.91	16.29	2.10	7.40	14.41	0.55
0.30	$\frac{1}{6}$	3.40	120.70	300.05	2.74	31.24	17.96	6.34	13.63	15.91	1.18
0.30	$\frac{1}{3}$	3.10	146.37	296.89	2.00	31.81	22.60	5.47	17.64	20.63	1.05
0.30	$\frac{1}{2}$	3.50	172.13	292.54	1.11	25.74	28.49	3.03	10.82	24.78	0.88
0.30	$\frac{2}{3}$	2.50	195.28	291.72	1.76	24.38	30.95	3.63	13.57	26.53	0.89
0.30	$\frac{5}{6}$	3.00	227.14	277.91	1.84	43.62	43.26	3.03	33.73	34.50	0.85
0.30	1	2.80	223.92	274.85	0.90	54.11	43.24	2.52	41.09	33.95	0.85
0.50	0	3.00	90.10	294.93	10.35	16.39	23.82	2.57	4.25	21.96	0.68
0.50	$\frac{1}{6}$	3.30	3.71	293.45	5.17	47.49	24.55	2.88	28.37	20.92	0.79
0.50	$\frac{1}{3}$	3.50	23.54	294.00	4.67	35.82	4.67	2.62	16.83	21.08	0.80
0.50	$\frac{1}{2}$	3.40	49.66	293.54	3.94	42.74	25.33	2.70	22.62	21.19	0.82
0.50	$\frac{2}{3}$	2.90	118.72	293.06	3.50	16.80	26.45	2.54	3.91	23.34	0.81
0.50	$\frac{5}{6}$	2.20	135.60	286.55	3.32	11.51	38.78	2.23	3.18	32.09	0.80
0.50	1	2.80	171.95	283.58	2.12	48.32	37.75	2.51	26.23	30.78	0.83
0.70	0	2.80	105.05	293.10	6.91	14.61	26.04	2.36	3.02	22.40	0.73
0.70	$\frac{1}{6}$	2.90	42.20	288.78	4.24	16.54	32.85	2.30	5.22	28.96	0.79
0.70	$\frac{1}{3}$	2.70	45.42	285.90	3.25	28.34	36.70	2.28	10.08	30.72	0.81
0.70	$\frac{1}{2}$	2.30	131.58	286.24	3.49	12.14	38.67	2.23	3.04	31.95	0.80
0.70	$\frac{2}{3}$	3.20	66.51	267.78	2.63	11.48	52.67	2.42	2.75	48.54	0.83
0.70	$\frac{5}{6}$	3.30	54.01	263.14	2.65	12.26	57.31	2.36	2.68	54.37	0.83
0.70	1	3.40	79.02	262.06	2.54	12.43	58.32	2.38	2.87	54.75	0.83
0.90	0	2.10	135.56	273.83	4.26	11.00	38.70	2.19	3.34	29.72	0.77
0.90	$\frac{1}{6}$	2.90	51.80	246.42	3.28	25.90	54.35	2.31	8.83	48.69	0.80
0.90	$\frac{1}{3}$	2.80	55.83	238.97	3.12	22.94	49.68	2.33	6.93	41.45	0.80
0.90	$\frac{1}{2}$	2.70	63.56	206.16	2.95	9.91	56.86	2.34	2.26	44.10	0.80
0.90	$\frac{2}{3}$	2.70	44.60	192.99	2.30	10.99	56.41	2.40	3.20	41.18	0.82
0.90	$\frac{5}{6}$	2.30	69.15	186.07	2.09	12.84	48.83	2.40	2.45	34.88	0.82
0.90	1	2.80	55.32	187.37	1.77	12.18	49.64	2.43	2.18	35.74	0.83

C. Appendix - 4 Parameter Case in Use Case 3

Table C.1.: Statistics of $\boldsymbol{p}(1:3)$ using the standard algorithm for the 4 parameter case with 1000 drawn samples for varying height of the lower muscle θ_b and thickness of the surrounding tissue layer θ in the settings from Section 6.3.3 with $\boldsymbol{p}^*(4) = 0$

θ_b	θ	$\lvert\bar{\mathfrak{p}}(1:3) - \boldsymbol{p}^*(1:3)\rvert$ (%)			MAD($\mathfrak{p}(1:3)$) (%)			var($\mathfrak{p}(1:3)$) (%)		
0.10	0	29.70	8.81	2.04	12.51	15.33	2.50	4.19	4.93	0.83
0.10	$\frac{1}{6}$	23.29	56.10	0.70	16.45	10.96	2.62	6.53	2.77	0.87
0.10	$\frac{1}{3}$	23.29	56.10	0.70	16.45	10.96	2.62	6.53	2.77	0.87
0.10	$\frac{1}{2}$	31.23	38.25	1.19	14.83	8.96	2.74	5.55	1.58	0.86
0.10	$\frac{2}{3}$	31.96	21.11	1.25	21.45	10.35	2.58	9.81	2.60	0.85
0.10	$\frac{5}{6}$	42.73	50.56	1.40	21.27	4.83	2.58	10.22	0.76	0.84
0.10	1	55.97	45.17	0.95	20.28	5.16	2.62	8.33	0.92	0.85
0.30	0	41.27	22.33	0.67	12.56	9.59	2.91	3.60	2.19	0.87
0.30	$\frac{1}{6}$	60.24	111.92	1.50	13.80	5.14	2.86	4.65	0.71	0.91
0.30	$\frac{1}{3}$	64.50	82.61	0.98	10.80	15.78	2.42	2.88	3.02	0.84
0.30	$\frac{1}{2}$	69.98	73.19	0.94	8.84	7.61	2.37	1.58	1.26	0.84
0.30	$\frac{2}{3}$	69.98	73.19	0.94	8.84	7.61	2.37	1.58	1.26	0.84
0.30	$\frac{5}{6}$	85.21	68.98	0.57	8.48	9.19	2.44	1.05	1.60	0.85
0.30	1	91.64	80.89	1.66	4.32	5.46	2.31	0.48	0.67	0.82
0.50	0	41.56	19.91	1.57	31.03	15.14	2.52	13.25	4.31	0.84
0.50	$\frac{1}{6}$	48.12	69.61	0.94	24.47	8.01	2.59	9.77	1.11	0.85
0.50	$\frac{1}{3}$	54.64	80.01	0.86	17.58	9.16	2.60	7.08	1.07	0.85
0.50	$\frac{1}{2}$	71.99	53.61	0.93	19.78	15.10	2.50	6.04	3.81	0.85
0.50	$\frac{2}{3}$	82.13	29.42	0.79	14.08	11.43	2.50	3.50	2.08	0.85
0.50	$\frac{5}{6}$	89.27	3.57	1.71	12.50	19.94	2.43	2.50	7.70	0.83
0.50	1	103.96	43.68	0.92	11.93	8.79	2.49	1.70	1.11	0.85
0.70	0	74.75	27.92	1.26	15.82	11.64	2.47	4.76	2.21	0.84
0.70	$\frac{1}{6}$	72.19	48.49	1.20	19.74	8.55	2.49	5.85	1.19	0.85
0.70	$\frac{1}{3}$	74.53	55.94	1.36	16.92	11.79	2.46	4.55	1.88	0.84
0.70	$\frac{1}{2}$	70.50	43.67	1.26	25.93	15.04	2.47	9.75	2.80	0.84
0.70	$\frac{2}{3}$	103.96	43.68	0.92	11.93	8.79	2.49	1.70	1.11	0.85
0.70	$\frac{5}{6}$	109.86	28.25	1.52	9.57	15.03	2.45	1.15	3.51	0.83
0.70	1	92.74	32.92	1.26	12.39	9.74	2.47	2.37	1.96	0.84
0.90	0	74.75	27.92	1.26	15.82	11.64	2.47	4.76	2.21	0.84
0.90	$\frac{1}{6}$	74.75	27.92	1.26	15.82	11.64	2.47	4.76	2.21	0.84
0.90	$\frac{1}{3}$	70.50	43.67	1.26	25.93	15.04	2.47	9.75	2.80	0.84
0.90	$\frac{1}{2}$	103.96	43.68	0.92	11.93	8.79	2.49	1.70	1.11	0.85
0.90	$\frac{2}{3}$	109.86	28.25	1.52	9.57	15.03	2.45	1.15	3.51	0.83
0.90	$\frac{5}{6}$	92.74	32.92	1.26	12.39	9.74	2.47	2.37	1.96	0.84
0.90	1	92.74	32.92	1.26	12.39	9.74	2.47	2.37	1.96	0.84

Table C.2.: Statistics of $\boldsymbol{p}(1:3)$ using the standard algorithm for the 4 parameter case with 1000 drawn samples for varying height of the lower muscle θ_b and thickness of the surrounding tissue layer θ in the settings from Section 6.3.3 with $\boldsymbol{p}^*(4) = \frac{\pi}{4}$

θ_b	θ	$\lvert\bar{\mathfrak{p}}(1:3) - \boldsymbol{p}^*(1:3)\rvert$ (%)			MAD($\mathfrak{p}(1:3)$) (%)			var($\mathfrak{p}(1:3)$) (%)		
0.10	0	22.75	2.57	1.12	21.81	21.07	2.92	11.41	10.18	0.89
0.10	$\frac{1}{6}$	9.65	94.00	0.38	24.40	18.58	3.18	12.09	4.94	0.90
0.10	$\frac{1}{3}$	7.07	96.94	0.90	25.32	17.15	2.82	14.00	4.26	0.87
0.10	$\frac{1}{2}$	30.98	87.01	0.94	23.48	9.02	2.63	10.32	2.21	0.86
0.10	$\frac{2}{3}$	52.25	82.01	1.03	24.23	9.12	2.62	11.74	1.97	0.87
0.10	$\frac{5}{6}$	58.13	17.83	1.27	31.39	16.02	2.97	14.87	6.02	0.87
0.10	1	52.07	8.29	1.60	12.27	15.76	2.51	3.59	4.81	0.84
0.30	0	78.15	47.97	1.22	20.13	27.89	3.63	5.84	8.91	0.91
0.30	$\frac{1}{6}$	77.10	256.67	0.87	39.57	34.77	3.62	25.40	27.24	0.94
0.30	$\frac{1}{3}$	77.52	170.58	2.16	14.19	17.40	2.43	3.56	4.88	0.84
0.30	$\frac{1}{2}$	28.54	120.24	1.12	12.73	24.33	2.55	5.02	8.57	0.85
0.30	$\frac{2}{3}$	57.82	93.96	1.47	9.93	11.90	2.64	2.36	2.74	0.84
0.30	$\frac{5}{6}$	58.95	177.75	1.00	8.54	11.78	2.51	2.13	4.68	0.84
0.30	1	122.55	81.38	1.73	14.91	6.78	2.31	3.23	0.97	0.82
0.50	0	31.98	26.06	3.43	53.35	32.97	2.46	38.93	13.15	0.80
0.50	$\frac{1}{6}$	34.64	84.16	2.84	41.91	11.83	2.67	30.36	2.17	0.82
0.50	$\frac{1}{3}$	8.74	133.81	2.00	31.48	22.96	2.65	18.69	8.19	0.85
0.50	$\frac{1}{2}$	31.25	95.20	1.16	33.12	19.39	2.67	15.68	4.74	0.86
0.50	$\frac{2}{3}$	78.00	19.65	0.80	22.76	14.93	2.57	6.41	3.95	0.85
0.50	$\frac{5}{6}$	53.49	133.99	1.41	15.90	11.50	2.38	3.64	2.45	0.84
0.50	1	25.96	167.21	0.99	18.77	12.88	2.43	7.77	3.88	0.84
0.70	0	80.15	26.39	4.52	11.87	24.55	2.22	1.99	7.25	0.77
0.70	$\frac{1}{6}$	80.27	26.90	3.93	14.17	8.78	2.27	2.88	2.21	0.79
0.70	$\frac{1}{3}$	59.34	99.47	3.16	15.80	9.20	2.32	5.02	1.61	0.81
0.70	$\frac{1}{2}$	22.92	134.52	3.24	17.40	9.54	2.23	8.32	2.16	0.80
0.70	$\frac{2}{3}$	42.31	113.25	2.61	16.71	15.34	2.26	4.88	4.30	0.81
0.70	$\frac{5}{6}$	69.41	91.11	2.38	14.82	7.54	2.27	3.12	1.31	0.81
0.70	1	77.26	128.16	1.42	16.31	9.44	2.39	3.20	1.51	0.83
0.90	0	145.16	43.28	3.34	10.89	16.97	2.31	2.20	3.45	0.80
0.90	$\frac{1}{6}$	118.72	36.46	3.22	3.91	23.35	2.32	0.36	6.30	0.79
0.90	$\frac{1}{3}$	116.49	52.09	3.15	2.78	11.74	2.32	0.25	1.72	0.80
0.90	$\frac{1}{2}$	109.58	69.01	2.97	3.35	1.41	2.34	0.25	0.19	0.80
0.90	$\frac{2}{3}$	119.65	77.29	2.29	6.08	12.56	2.28	0.63	1.90	0.81
0.90	$\frac{5}{6}$	114.75	58.86	2.06	9.12	26.74	2.29	1.16	8.24	0.81
0.90	1	130.01	66.96	1.40	14.07	19.74	2.32	2.60	5.04	0.83

Table C.3.: Statistics of $\boldsymbol{p}(1:3)$ using the standard algorithm for the 4 parameter case with 1000 drawn samples for varying height of the lower muscle θ_b and thickness of the surrounding tissue layer θ in the settings from Section 6.3.3 with $\boldsymbol{p}^*(4) = \frac{3\pi}{4}$

θ_b	θ	$\lvert\bar{\mathfrak{p}}(1:3) - \boldsymbol{p}^*(1:3)\rvert$ (%)			MAD($\mathfrak{p}(1:3)$) (%)			var($\mathfrak{p}(1:3)$) (%)		
0.10	0 31.11	19.84	2.68	16.14	13.55	3.15	6.44	3.71	0.96	
0.10	$\frac{1}{6}$	27.78	79.64	1.54	16.65	17.65	3.49	7.58	4.74	1.01
0.10	$\frac{1}{3}$	25.17	89.26	2.14	28.18	32.12	3.31	14.30	13.32	0.96
0.10	$\frac{1}{2}$	42.09	99.75	1.53	39.48	33.75	3.57	24.75	15.19	0.97
0.10	$\frac{2}{3}$	37.84	108.42	1.72	38.14	25.02	2.88	24.22	10.08	0.87
0.10	$\frac{5}{6}$	62.59	103.28	0.75	27.20	21.55	2.90	10.23	7.87	0.89
0.10	1	105.64	143.57	1.79	32.39	32.72	3.33	17.49	14.20	0.91
0.30	0	88.10	100.73	1.71	40.40	43.93	3.68	21.62	27.83	0.96
0.30	$\frac{1}{6}$	52.83	222.75	2.24	38.20	27.57	3.01	22.24	14.10	0.90
0.30	$\frac{1}{3}$	77.60	227.78	1.92	60.99	33.69	3.19	56.42	19.93	0.90
0.30	$\frac{1}{2}$	121.62	264.07	1.58	32.48	29.67	2.61	14.34	18.03	0.85
0.30	$\frac{2}{3}$	127.39	258.32	1.62	17.22	26.60	2.62	4.59	18.21	0.85
0.30	$\frac{5}{6}$	147.36	170.04	1.23	25.14	29.10	2.57	9.14	12.85	0.85
0.30	1	179.99	266.52	1.34	36.99	46.18	2.40	19.01	34.85	0.84
0.50	0	14.37	85.82	4.58	58.86	19.98	2.36	52.28	5.80	0.81
0.50	$\frac{1}{6}$	2.93	140.35	3.55	53.87	17.94	2.66	42.45	4.65	0.81
0.50	$\frac{1}{3}$	5.19	170.92	3.20	38.19	29.02	2.59	27.03	10.48	0.82
0.50	$\frac{1}{2}$	48.34	203.12	2.34	55.89	25.26	2.74	42.54	10.76	0.84
0.50	$\frac{2}{3}$	43.29	236.92	2.01	23.21	20.36	2.67	12.13	11.70	0.83
0.50	$\frac{5}{6}$	29.83	175.57	1.44	12.18	13.21	2.50	4.07	4.66	0.84
0.50	1	67.53	165.33	1.62	10.79	16.00	2.46	1.66	6.16	0.83
0.70	0	99.04	153.28	4.48	16.44	52.18	2.30	3.64	34.08	0.78
0.70	$\frac{1}{6}$	59.35	179.16	4.08	14.21	32.25	2.32	4.10	15.02	0.79
0.70	$\frac{1}{3}$	47.64	154.42	3.67	11.74	18.92	2.30	2.56	5.18	0.79
0.70	$\frac{1}{2}$	0.13	147.21	3.00	21.20	14.21	2.35	10.62	3.53	0.80
0.70	$\frac{2}{3}$	30.82	116.18	2.82	23.55	17.28	2.32	8.52	4.15	0.80
0.70	$\frac{5}{6}$	34.52	168.99	2.39	32.60	17.97	2.32	18.72	5.19	0.81
0.70	1	110.87	140.44	1.46	14.83	25.50	2.77	3.35	10.79	0.85
0.90	0	104.96	144.16	3.17	10.50	19.99	2.25	1.93	6.29	0.79
0.90	$\frac{1}{6}$	138.20	175.28	3.21	11.07	12.99	2.23	2.28	4.72	0.79
0.90	$\frac{1}{3}$	104.26	94.46	2.96	8.74	10.25	2.34	1.44	1.66	0.80
0.90	$\frac{1}{2}$	128.73	128.82	2.46	3.84	15.07	2.44	0.67	4.77	0.83
0.90	$\frac{2}{3}$	92.60	139.41	2.34	9.29	13.19	2.38	1.49	4.84	0.82
0.90	$\frac{5}{6}$	117.39	91.55	2.25	7.27	15.00	2.41	0.94	3.33	0.82
0.90	1	121.38	103.72	1.97	10.08	17.56	2.47	1.31	3.68	0.83

Table C.4.: Statistics of $\boldsymbol{p}(4)$ using the standard algorithm for the 4 parameter case with 1000 drawn samples for varying height of the lower muscle θ_b and thickness of the surrounding tissue layer θ in the settings from Section 6.3.3 with $\boldsymbol{p}^*(4) = 0$

$\theta_\mathrm{b} = 0.1$							
θ	0	$\frac{1}{6}$	$\frac{1}{3}$	$\frac{1}{2}$	$\frac{2}{3}$	$\frac{5}{6}$	1
κ_a	1.80	2.00	2.00	1.80	2.70	2.10	2.20
$\lvert\bar{\mathfrak{p}}(4) - \boldsymbol{p}^*(4)\rvert$ (%)	0.97	1.65	1.65	1.14	1.57	1.83	1.77
MAD($\mathfrak{p}(4)$) (%)	0.55	1.12	1.12	0.60	0.83	1.26	1.18
var($\mathfrak{p}(4)$) (%)	0.02	0.03	0.03	0.02	0.03	0.04	0.04
$\theta_\mathrm{b} = 0.3$							
θ	0	$\frac{1}{6}$	$\frac{1}{3}$	$\frac{1}{2}$	$\frac{2}{3}$	$\frac{5}{6}$	1
κ_a	1.70	1.80	1.50	1.30	1.30	1.50	1.30
$\lvert\bar{\mathfrak{p}}(4) - \boldsymbol{p}^*(4)\rvert$ (%)	0.95	1.03	1.05	0.96	0.96	1.05	0.99
MAD($\mathfrak{p}(4)$) (%)	0.45	0.53	0.69	0.52	0.52	0.56	0.54
var($\mathfrak{p}(4)$) (%)	0.02	0.02	0.03	0.02	0.02	0.02	0.02
$\theta_\mathrm{b} = 0.5$							
θ	0	$\frac{1}{6}$	$\frac{1}{3}$	$\frac{1}{2}$	$\frac{2}{3}$	$\frac{5}{6}$	1
κ_a	2.50	2.30	2.30	1.90	1.70	1.70	1.60
$\lvert\bar{\mathfrak{p}}(4) - \boldsymbol{p}^*(4)\rvert$ (%)	2.81	5.00	4.28	3.44	2.98	2.02	3.49
MAD($\mathfrak{p}(4)$) (%)	1.34	1.67	2.19	1.30	1.26	1.48	0.97
var($\mathfrak{p}(4)$) (%)	0.04	0.05	0.06	0.04	0.04	0.05	0.03
$\theta_\mathrm{b} = 0.7$							
θ	0	$\frac{1}{6}$	$\frac{1}{3}$	$\frac{1}{2}$	$\frac{2}{3}$	$\frac{5}{6}$	1
κ_a	1.80	2.00	2.10	2.10	1.60	1.70	1.50
$\lvert\bar{\mathfrak{p}}(4) - \boldsymbol{p}^*(4)\rvert$ (%)	4.68	3.09	3.40	6.00	3.49	4.98	2.37
MAD($\mathfrak{p}(4)$) (%)	1.67	1.47	1.54	1.53	0.97	1.52	1.45
var($\mathfrak{p}(4)$) (%)	0.05	0.06	0.06	0.04	0.03	0.05	0.05
$\theta_\mathrm{b} = 0.9$							
θ	0	$\frac{1}{6}$	$\frac{1}{3}$	$\frac{1}{2}$	$\frac{2}{3}$	$\frac{5}{6}$	1
κ_a	1.80	1.80	2.10	1.60	1.70	1.50	1.50
$\lvert\bar{\mathfrak{p}}(4) - \boldsymbol{p}^*(4)\rvert$ (%)	4.68	4.68	6.00	3.49	4.98	2.37	2.37
MAD($\mathfrak{p}(4)$) (%)	1.67	1.67	1.53	0.97	1.52	1.45	1.45
var($\mathfrak{p}(4)$) (%)	0.05	0.05	0.04	0.03	0.05	0.05	0.05

Table C.5.: Statistics of $\boldsymbol{p}(4)$ using the standard algorithm for the 4 parameter case with 1000 drawn samples for varying height of the lower muscle θ_b and thickness of the surrounding tissue layer θ in the settings from Section 6.3.3 with $\boldsymbol{p}^*(4) = \frac{\pi}{4}$

$\theta_\mathrm{b} = 0.1$							
θ	0	$\frac{1}{6}$	$\frac{1}{3}$	$\frac{1}{2}$	$\frac{2}{3}$	$\frac{5}{6}$	1
κ_a	3.10	3.00	2.70	3.10	3.40	3.60	2.40
$\lvert\bar{\mathfrak{p}}(4) - \boldsymbol{p}^*(4)\rvert$ (%)	74.89	74.65	74.86	74.66	74.39	73.63	74.72
MAD($\mathfrak{p}(4)$) (%)	4.74	4.78	4.82	4.86	5.41	5.09	5.52
var($\mathfrak{p}(4)$) (%)	1.54	1.53	1.54	1.60	1.69	1.63	1.79
$\theta_\mathrm{b} = 0.3$							
θ	0	$\frac{1}{6}$	$\frac{1}{3}$	$\frac{1}{2}$	$\frac{2}{3}$	$\frac{5}{6}$	1
κ_a	2.40	3.20	2.80	2.30	2.20	2.20	1.90
$\lvert\bar{\mathfrak{p}}(4) - \boldsymbol{p}^*(4)\rvert$ (%)	68.15	60.78	62.98	65.23	65.42	59.72	58.69
MAD($\mathfrak{p}(4)$) (%)	3.98	6.58	6.59	5.42	6.00	10.52	13.98
var($\mathfrak{p}(4)$) (%)	1.23	1.71	1.63	1.49	1.57	2.62	3.34
$\theta_\mathrm{b} = 0.5$							
θ	0	$\frac{1}{6}$	$\frac{1}{3}$	$\frac{1}{2}$	$\frac{2}{3}$	$\frac{5}{6}$	1
κ_a	3.60	3.20	2.90	2.60	2.20	2.70	2.50
$\lvert\bar{\mathfrak{p}}(4) - \boldsymbol{p}^*(4)\rvert$ (%)	65.69	63.22	64.06	65.26	66.68	59.46	55.50
MAD($\mathfrak{p}(4)$) (%)	5.07	5.85	5.92	6.09	6.52	11.85	10.52
var($\mathfrak{p}(4)$) (%)	1.41	1.49	1.53	1.59	1.69	2.92	2.37
$\theta_\mathrm{b} = 0.7$							
θ	0	$\frac{1}{6}$	$\frac{1}{3}$	$\frac{1}{2}$	$\frac{2}{3}$	$\frac{5}{6}$	1
κ_a	2.40	2.40	2.40	2.20	2.60	2.30	2.30
$\lvert\bar{\mathfrak{p}}(4) - \boldsymbol{p}^*(4)\rvert$ (%)	62.18	61.73	56.53	52.56	53.62	55.52	52.98
MAD($\mathfrak{p}(4)$) (%)	5.59	5.34	6.81	9.27	9.59	11.93	11.18
var($\mathfrak{p}(4)$) (%)	1.41	1.35	1.41	1.97	2.12	2.73	2.42
$\theta_\mathrm{b} = 0.9$							
θ	0	$\frac{1}{6}$	$\frac{1}{3}$	$\frac{1}{2}$	$\frac{2}{3}$	$\frac{5}{6}$	1
κ_a	1.80	1.70	1.60	1.50	1.40	1.60	1.70
$\lvert\bar{\mathfrak{p}}(4) - \boldsymbol{p}^*(4)\rvert$ (%)	34.62	32.15	33.31	30.17	30.51	29.11	28.19
MAD($\mathfrak{p}(4)$) (%)	3.47	2.09	2.39	1.61	4.78	3.86	3.25
var($\mathfrak{p}(4)$) (%)	0.40	0.30	0.33	0.27	0.49	0.41	0.35

Table C.6.: Statistics of $\boldsymbol{p}(4)$ using the standard algorithm for the 4 parameter case with 1000 drawn samples for varying height of the lower muscle θ_b and thickness of the surrounding tissue layer θ in the settings from Section 6.3.3 with $\boldsymbol{p}^*(4) = \frac{3\pi}{4}$

$\theta_\mathrm{b} = 0.1$							
θ	0	$\frac{1}{6}$	$\frac{1}{3}$	$\frac{1}{2}$	$\frac{2}{3}$	$\frac{5}{6}$	1
κ_a	3.20	3.50	4.00	4.30	4.40	3.50	4.60
$\lvert\bar{\mathfrak{p}}(4) - \boldsymbol{p}^*(4)\rvert$ (%)	76.79	76.20	76.51	76.27	77.10	76.73	73.67
MAD($\mathfrak{p}(4)$) (%)	6.96	7.02	6.75	7.38	6.82	6.93	10.54
var($\mathfrak{p}(4)$) (%)	2.21	2.20	2.10	2.37	2.10	2.21	3.18
$\theta_\mathrm{b} = 0.3$							
θ	0	$\frac{1}{6}$	$\frac{1}{3}$	$\frac{1}{2}$	$\frac{2}{3}$	$\frac{5}{6}$	1
κ_a	4.60	3.90	4.10	3.30	3.60	3.30	3.10
$\lvert\bar{\mathfrak{p}}(4) - \boldsymbol{p}^*(4)\rvert$ (%)	65.69	59.22	58.21	53.57	48.08	48.09	4.70
MAD($\mathfrak{p}(4)$) (%)	6.19	7.82	10.49	15.48	21.12	23.38	6.02
var($\mathfrak{p}(4)$) (%)	1.80	2.22	2.90	4.76	6.74	7.45	0.50
$\theta_\mathrm{b} = 0.5$							
θ	0	$\frac{1}{6}$	$\frac{1}{3}$	$\frac{1}{2}$	$\frac{2}{3}$	$\frac{5}{6}$	1
κ_a	3.80	3.70	3.50	3.50	3.00	3.10	2.70
$\lvert\bar{\mathfrak{p}}(4) - \boldsymbol{p}^*(4)\rvert$ (%)	65.71	60.86	59.32	60.46	58.32	55.68	53.62
MAD($\mathfrak{p}(4)$) (%)	6.86	10.74	10.43	11.88	11.35	13.01	11.55
var($\mathfrak{p}(4)$) (%)	1.99	2.93	2.79	3.46	3.21	3.49	2.95
$\theta_\mathrm{b} = 0.7$							
θ	0	$\frac{1}{6}$	$\frac{1}{3}$	$\frac{1}{2}$	$\frac{2}{3}$	$\frac{5}{6}$	1
κ_a	3.80	3.10	2.90	2.70	2.90	2.90	4.00
$\lvert\bar{\mathfrak{p}}(4) - \boldsymbol{p}^*(4)\rvert$ (%)	60.31	52.50	50.45	49.64	51.01	43.79	30.26
MAD($\mathfrak{p}(4)$) (%)	12.38	11.50	11.11	9.83	11.89	13.48	27.84
var($\mathfrak{p}(4)$) (%)	3.66	2.87	2.72	2.40	3.04	3.31	10.20
$\theta_\mathrm{b} = 0.9$							
θ	0	$\frac{1}{6}$	$\frac{1}{3}$	$\frac{1}{2}$	$\frac{2}{3}$	$\frac{5}{6}$	1
κ_a	2.20	2.20	2.40	3.00	2.70	2.60	2.90
$\lvert\bar{\mathfrak{p}}(4) - \boldsymbol{p}^*(4)\rvert$ (%)	20.25	21.29	20.34	16.42	9.20	13.56	10.72
MAD($\mathfrak{p}(4)$) (%)	6.74	5.73	10.81	12.89	11.78	15.25	13.30
var($\mathfrak{p}(4)$) (%)	1.01	0.71	2.31	3.07	2.52	3.49	2.85

D. Appendix - 5 Parameter Case in Use Case 3

Table D.1.: Statistics of $\boldsymbol{p}(1:3)$ using the standard algorithm for the 5 parameter case with 1000 drawn samples for varying height of the lower muscle $\boldsymbol{p}^*(5)$ and thickness of the surrounding tissue layer θ in the settings from Section 6.3.4 with $\boldsymbol{p}^*(4) = 0$

$\boldsymbol{p}^*(5)$	θ	$\lvert\bar{\mathfrak{p}}(1:3) - \boldsymbol{p}^*(1:3)\rvert$ (%)			MAD($\mathfrak{p}(1:3)$) (%)			var($\mathfrak{p}(1:3)$) (%)		
0.10	0	157.66	84.36	6.06	7.95	8.38	7.55	0.89	1.27	2.01
0.10	$\frac{1}{6}$	55.77	174.24	3.83	28.43	9.94	4.41	13.84	2.47	1.44
0.10	$\frac{1}{3}$	67.96	167.41	3.16	21.05	13.71	3.51	8.04	2.77	1.41
0.10	$\frac{1}{2}$	88.53	220.25	3.53	17.69	30.49	6.34	5.89	14.41	1.59
0.10	$\frac{2}{3}$	131.03	122.63	5.82	11.95	10.13	4.54	3.06	1.35	1.38
0.10	$\frac{5}{6}$	163.14	106.02	5.24	8.20	11.71	5.11	1.25	1.54	1.42
0.10	1	175.96	147.45	1.97	13.63	8.24	6.94	2.71	1.41	1.68
0.30	0	124.33	70.69	3.51	5.56	19.05	5.06	0.80	6.05	2.88
0.30	$\frac{1}{6}$	81.57	191.96	2.44	12.83	17.13	3.98	1.90	5.78	1.30
0.30	$\frac{1}{3}$	104.40	129.39	1.05	19.51	19.18	3.12	4.21	6.37	1.19
0.30	$\frac{1}{2}$	140.22	133.71	1.58	12.04	6.03	3.27	2.31	0.95	1.25
0.30	$\frac{2}{3}$	160.75	96.09	1.08	11.00	11.22	2.75	2.04	1.45	1.16
0.30	$\frac{5}{6}$	164.85	104.83	1.71	8.80	3.24	2.73	2.06	0.57	1.14
0.30	1	166.23	103.62	1.81	6.84	1.93	2.73	1.79	0.27	1.13
0.50	0	130.01	41.51	50.18	11.40	38.12	3.47	2.52	23.03	1.21
0.50	$\frac{1}{6}$	99.56	96.50	54.48	0.77	0.64	2.82	0.06	0.06	1.06
0.50	$\frac{1}{3}$	95.32	94.43	54.60	7.50	3.59	2.81	0.96	0.30	1.06
0.50	$\frac{1}{2}$	91.76	85.99	54.85	7.78	8.02	2.80	0.72	0.76	1.05
0.50	$\frac{2}{3}$	91.76	85.99	54.85	7.78	8.02	2.80	0.72	0.76	1.05
0.50	$\frac{5}{6}$	92.02	87.90	57.60	2.21	5.15	2.69	0.24	0.46	0.99
0.50	1	92.02	87.90	57.60	2.21	5.15	2.69	0.24	0.46	0.99
0.70	0	87.15	153.84	2.15	14.03	11.17	3.88	2.61	1.80	1.68
0.70	$\frac{1}{6}$	181.35	63.10	7.63	9.56	17.32	12.15	2.33	3.66	2.63
0.70	$\frac{1}{3}$	143.23	76.39	59.84	3.69	2.11	1.75	0.51	0.14	0.17
0.70	$\frac{1}{2}$	107.14	110.12	106.94	2.34	3.51	3.24	0.15	0.20	0.19
0.70	$\frac{2}{3}$	124.38	168.46	163.21	5.44	16.65	6.21	0.81	5.55	1.44
0.70	$\frac{5}{6}$	141.86	94.00	2.25	1.96	2.44	2.96	0.51	0.35	1.28
0.70	1	101.65	164.56	2.20	22.59	20.87	3.39	5.98	5.67	1.66
0.90	0	132.88	101.60	2.34	2.46	2.73	2.52	0.90	0.39	1.11
0.90	$\frac{1}{6}$	147.66	94.70	1.37	2.94	2.49	2.48	1.27	0.38	1.09
0.90	$\frac{1}{3}$	140.19	72.86	2.09	2.55	1.64	2.32	0.90	0.23	0.98
0.90	$\frac{1}{2}$	147.77	7.43	0.09	8.70	7.95	2.62	1.67	2.22	1.04
0.90	$\frac{2}{3}$	96.77	97.49	1.00	9.06	9.10	4.55	1.04	0.98	1.14
0.90	$\frac{5}{6}$	96.77	97.49	1.00	9.06	9.10	4.55	1.04	0.98	1.14
0.90	1	72.32	95.40	0.78	3.08	1.89	2.40	0.32	0.14	1.00

Table D.2.: Statistics of $\boldsymbol{p}(1:3)$ using the standard algorithm for the 5 parameter case with 1000 drawn samples for varying height of the lower muscle $\boldsymbol{p}^*(5)$ and thickness of the surrounding tissue layer θ in the settings from Section 6.3.4 with $\boldsymbol{p}^*(4) = \frac{\pi}{2}$

$\boldsymbol{p}^*(5)$	θ	$\lvert\bar{\mathfrak{p}}(1:3) - \boldsymbol{p}^*(1:3)\rvert$ (%)			MAD($\mathfrak{p}(1:3)$) (%)			var($\mathfrak{p}(1:3)$) (%)		
0.10	0	110.30	65.50	2.62	27.41	23.76	4.29	12.02	6.78	1.62
0.10	$\frac{1}{6}$	114.92	105.52	1.67	30.72	22.00	7.88	14.44	7.27	1.95
0.10	$\frac{1}{3}$	128.76	142.29	0.49	24.92	18.86	7.66	9.37	5.51	1.86
0.10	$\frac{1}{2}$	120.51	251.70	2.40	24.36	24.01	6.16	10.24	15.82	1.67
0.10	$\frac{2}{3}$	140.34	239.51	2.52	17.39	30.21	5.94	4.01	18.88	1.64
0.10	$\frac{5}{6}$	180.66	259.74	0.94	21.40	22.84	4.60	6.65	14.78	1.62
0.10	1	153.98	232.37	0.94	10.82	20.37	4.85	2.08	10.27	1.60
0.30	0	63.25	109.61	3.70	27.04	23.56	6.00	8.89	9.70	2.95
0.30	$\frac{1}{6}$	146.90	230.96	8.50	5.56	17.76	3.98	1.16	9.83	1.50
0.30	$\frac{1}{3}$	136.48	193.77	3.09	23.43	25.58	5.19	7.73	9.70	1.29
0.30	$\frac{1}{2}$	168.77	204.67	3.17	12.61	11.55	3.81	3.19	5.76	1.16
0.30	$\frac{2}{3}$	189.34	155.32	3.59	25.42	19.35	5.33	8.92	4.96	1.29
0.30	$\frac{5}{6}$	189.78	173.90	1.39	28.69	37.70	3.61	12.38	16.61	1.20
0.30	1	222.81	165.24	1.77	26.57	32.00	3.86	11.91	13.04	1.19
0.50	0	149.56	51.53	53.39	6.23	19.65	3.50	1.91	6.03	1.17
0.50	$\frac{1}{6}$	158.98	99.20	52.73	15.58	7.60	4.34	4.67	1.10	1.24
0.50	$\frac{1}{3}$	134.13	171.31	55.03	14.17	16.25	3.28	3.39	4.75	1.09
0.50	$\frac{1}{2}$	116.94	170.62	52.62	14.53	16.38	4.14	2.69	4.83	1.19
0.50	$\frac{2}{3}$	75.54	164.18	55.11	4.81	15.02	3.17	0.57	4.18	1.06
0.50	$\frac{5}{6}$	106.20	162.78	55.51	13.13	19.63	3.01	2.26	5.63	1.06
0.50	1	82.18	104.28	56.77	8.09	3.09	3.43	0.86	0.28	1.03
0.70	0	83.76	205.79	1.96	12.75	12.13	3.66	2.65	3.60	1.70
0.70	$\frac{1}{6}$	50.44	173.54	0.15	11.55	18.77	3.44	2.19	6.40	1.09
0.70	$\frac{1}{3}$	144.07	282.20	60.35	37.90	32.13	2.71	18.52	23.97	0.22
0.70	$\frac{1}{2}$	130.92	259.48	104.22	20.37	37.79	1.77	5.44	20.71	0.11
0.70	$\frac{2}{3}$	206.69	89.67	161.82	15.21	2.39	4.31	4.70	0.25	1.19
0.70	$\frac{5}{6}$	190.06	124.62	3.05	5.88	10.22	2.87	1.27	1.31	1.24
0.70	1	101.06	196.07	3.82	5.61	14.55	3.33	0.73	3.46	1.62
0.90	0	163.50	58.05	1.18	13.68	6.73	2.70	3.10	1.33	1.03
0.90	$\frac{1}{6}$	89.86	58.77	1.87	13.58	4.50	3.57	2.49	0.73	1.12
0.90	$\frac{1}{3}$	111.11	33.45	0.46	8.78	10.98	2.88	1.34	2.17	1.03
0.90	$\frac{1}{2}$	96.28	128.66	0.18	5.22	7.09	2.99	0.82	1.70	1.05
0.90	$\frac{2}{3}$	100.79	86.40	0.01	4.37	6.22	2.91	0.49	0.86	1.05
0.90	$\frac{5}{6}$	76.35	95.35	0.38	6.90	1.88	2.42	0.54	0.14	1.01
0.90	1	76.35	95.35	0.38	6.90	1.88	2.42	0.54	0.14	1.01

Table D.3.: Statistics of $\boldsymbol{p}(1:3)$ using the standard algorithm for the 5 parameter case with 1000 drawn samples for varying height of the lower muscle $\boldsymbol{p}^*(5)$ and thickness of the surrounding tissue layer θ in the settings from Section 6.3.4 with $\boldsymbol{p}^*(4) = \frac{3\pi}{4}$

$\boldsymbol{p}^*(5)$	θ	$\lvert\bar{\mathfrak{p}}(1:3) - \boldsymbol{p}^*(1:3)\rvert$ (%)			MAD($\mathfrak{p}(1:3)$) (%)			var($\mathfrak{p}(1:3)$) (%)		
0.10	0	169.64	152.49	0.71	18.64	13.10	5.47	7.07	3.80	1.66
0.10	$\frac{1}{6}$	110.51	135.50	0.51	55.70	18.50	6.69	42.63	4.96	1.78
0.10	$\frac{1}{3}$	88.07	239.13	1.49	27.94	43.99	5.48	16.98	26.06	2.01
0.10	$\frac{1}{2}$	127.35	237.41	1.11	20.83	38.60	5.17	7.96	27.75	1.86
0.10	$\frac{2}{3}$	178.73	215.76	2.50	33.00	40.09	5.19	14.87	19.96	1.61
0.10	$\frac{5}{6}$	149.73	252.35	2.83	15.94	39.33	3.73	5.41	22.90	1.52
0.10	1	201.19	198.69	0.00	17.79	40.95	7.10	6.31	22.99	1.93
0.30	0	90.69	108.77	3.65	26.14	40.11	8.00	9.14	20.95	3.19
0.30	$\frac{1}{6}$	84.46	222.53	2.38	40.01	28.59	3.88	19.37	15.63	1.26
0.30	$\frac{1}{3}$	91.42	276.99	2.18	43.82	29.95	6.26	21.95	23.44	1.48
0.30	$\frac{1}{2}$	128.86	177.23	0.89	14.11	16.70	3.18	2.68	6.69	1.19
0.30	$\frac{2}{3}$	174.31	83.99	1.11	17.62	16.64	3.13	4.60	5.09	1.19
0.30	$\frac{5}{6}$	171.53	119.89	1.30	6.50	6.94	3.20	2.15	1.03	1.17
0.30	1	166.70	74.00	0.67	12.82	7.77	3.29	2.72	1.16	1.22
0.50	0	39.88	106.01	50.68	13.76	7.32	5.52	2.79	0.83	1.38
0.50	$\frac{1}{6}$	113.51	91.41	54.47	2.36	6.41	3.32	0.55	1.40	1.10
0.50	$\frac{1}{3}$	83.02	77.41	54.98	10.70	4.31	3.53	1.59	0.70	1.10
0.50	$\frac{1}{2}$	126.95	97.25	52.92	19.47	5.82	3.43	7.32	0.64	1.15
0.50	$\frac{2}{3}$	53.44	169.93	54.47	5.47	9.57	3.32	0.92	2.89	1.08
0.50	$\frac{5}{6}$	27.25	158.73	55.33	19.32	16.09	3.22	6.08	5.23	1.06
0.50	1	72.73	107.97	53.21	5.46	0.71	2.87	0.57	0.04	1.10
0.70	0	99.42	185.52	1.21	15.49	12.80	5.07	2.94	2.73	1.79
0.70	$\frac{1}{6}$	94.72	144.53	0.61	9.42	6.28	2.45	1.16	1.19	1.02
0.70	$\frac{1}{3}$	77.67	131.38	64.14	12.77	18.37	1.32	2.66	4.55	0.14
0.70	$\frac{1}{2}$	84.73	238.69	102.39	4.48	15.91	1.59	0.50	8.53	0.11
0.70	$\frac{2}{3}$	177.71	134.41	162.01	8.82	12.02	7.13	2.57	2.92	1.42
0.70	$\frac{5}{6}$	153.30	169.62	0.96	3.90	4.66	2.93	0.50	0.93	1.30
0.70	1	128.80	194.31	2.83	16.16	21.62	4.06	3.28	5.70	1.67
0.90	0	149.21	59.95	2.32	5.29	1.96	2.31	1.43	0.31	0.97
0.90	$\frac{1}{6}$	149.21	59.95	2.32	5.29	1.96	2.31	1.43	0.31	0.97
0.90	$\frac{1}{3}$	132.95	30.27	0.61	9.10	2.85	2.46	1.33	0.96	1.04
0.90	$\frac{1}{2}$	92.10	89.47	2.63	1.50	0.67	2.95	0.20	0.06	1.10
0.90	$\frac{2}{3}$	96.77	97.49	1.00	9.06	9.10	4.55	1.04	0.98	1.14
0.90	$\frac{5}{6}$	63.21	94.48	0.49	7.91	1.75	2.41	1.16	0.13	1.01
0.90	1	63.21	94.48	0.49	7.91	1.75	2.41	1.16	0.13	1.01

Table D.4.: Statistics of $\boldsymbol{p}(4)$ using the standard algorithm for the 5 parameter case with 1000 drawn samples for varying height of the lower muscle $\boldsymbol{p}^*(5)$ and thickness of the surrounding tissue layer θ in the settings from Section 6.3.4 with $\boldsymbol{p}^*(4) = 0$

$\boldsymbol{p}^*(5) = 0.1$							
θ	0	$\frac{1}{6}$	$\frac{1}{3}$	$\frac{1}{2}$	$\frac{2}{3}$	$\frac{5}{6}$	1
κ_a	1.40	1.60	1.50	1.50	1.30	1.20	1.20
$\lvert\bar{\mathfrak{p}}(4) - \boldsymbol{p}^*(4)\rvert$ (%)	4.56	6.91	5.59	11.74	6.83	6.27	8.61
MAD($\mathfrak{p}(4)$) (%)	1.15	2.78	4.28	2.94	4.23	4.12	4.23
var($\mathfrak{p}(4)$) (%)	0.03	0.10	0.19	0.14	0.22	0.19	0.22
$\boldsymbol{p}^*(5) = 0.3$							
θ	0	$\frac{1}{6}$	$\frac{1}{3}$	$\frac{1}{2}$	$\frac{2}{3}$	$\frac{5}{6}$	1
κ_a	1.90	1.70	1.80	1.50	1.50	1.50	1.40
$\lvert\bar{\mathfrak{p}}(4) - \boldsymbol{p}^*(4)\rvert$ (%)	2.07	2.75	3.79	7.17	5.55	7.31	7.30
MAD($\mathfrak{p}(4)$) (%)	2.34	1.37	2.44	1.31	2.92	1.48	1.48
var($\mathfrak{p}(4)$) (%)	0.10	0.08	0.13	0.06	0.16	0.07	0.07
$\boldsymbol{p}^*(5) = 0.5$							
θ	0	$\frac{1}{6}$	$\frac{1}{3}$	$\frac{1}{2}$	$\frac{2}{3}$	$\frac{5}{6}$	1
κ_a	1.80	0.70	0.80	0.90	0.90	0.90	0.90
$\lvert\bar{\mathfrak{p}}(4) - \boldsymbol{p}^*(4)\rvert$ (%)	3.37	11.40	10.16	11.52	11.52	17.29	17.29
MAD($\mathfrak{p}(4)$) (%)	2.08	0.19	2.12	0.51	0.51	2.00	2.00
var($\mathfrak{p}(4)$) (%)	0.10	0.01	0.09	0.01	0.01	0.07	0.07
$\boldsymbol{p}^*(5) = 0.7$							
θ	0	$\frac{1}{6}$	$\frac{1}{3}$	$\frac{1}{2}$	$\frac{2}{3}$	$\frac{5}{6}$	1
κ_a	1.50	1.80	1.00	0.80	1.40	1.50	1.70
$\lvert\bar{\mathfrak{p}}(4) - \boldsymbol{p}^*(4)\rvert$ (%)	2.70	8.09	4.18	4.58	14.03	3.30	4.94
MAD($\mathfrak{p}(4)$) (%)	1.92	4.68	1.53	1.45	1.84	0.67	2.35
var($\mathfrak{p}(4)$) (%)	0.05	0.27	0.07	0.04	0.06	0.04	0.09
$\boldsymbol{p}^*(5) = 0.9$							
θ	0	$\frac{1}{6}$	$\frac{1}{3}$	$\frac{1}{2}$	$\frac{2}{3}$	$\frac{5}{6}$	1
κ_a	1.50	1.60	1.50	1.70	1.30	1.30	1.20
$\lvert\bar{\mathfrak{p}}(4) - \boldsymbol{p}^*(4)\rvert$ (%)	23.26	20.10	7.02	24.75	18.58	18.58	17.44
MAD($\mathfrak{p}(4)$) (%)	1.02	1.01	1.55	2.37	0.49	0.49	1.13
var($\mathfrak{p}(4)$) (%)	0.07	0.07	0.12	0.12	0.04	0.04	0.06

Table D.5.: Statistics of $\boldsymbol{p}(4)$ using the standard algorithm for the 5 parameter case with 1000 drawn samples for varying height of the lower muscle $\boldsymbol{p}^*(5)$ and thickness of the surrounding tissue layer θ in the settings from Section 6.3.4 with $\boldsymbol{p}^*(4) = \frac{\pi}{4}$

$\boldsymbol{p}^*(5) = 0.1$							
θ	0	$\frac{1}{6}$	$\frac{1}{3}$	$\frac{1}{2}$	$\frac{2}{3}$	$\frac{5}{6}$	1
κ_a	3.00	2.90	2.80	3.00	2.90	3.10	2.50
$\lvert\bar{\mathfrak{p}}(4) - \boldsymbol{p}^*(4)\rvert$ (%)	66.01	69.57	66.64	55.96	57.56	55.65	48.08
MAD($\mathfrak{p}(4)$) (%)	8.74	7.58	8.19	14.67	14.87	18.30	21.06
var($\mathfrak{p}(4)$) (%)	2.38	2.24	2.24	4.11	4.33	5.37	6.18
$\boldsymbol{p}^*(5) = 0.3$							
θ	0	$\frac{1}{6}$	$\frac{1}{3}$	$\frac{1}{2}$	$\frac{2}{3}$	$\frac{5}{6}$	1
κ_a	2.70	2.10	3.20	2.30	2.50	2.60	2.10
$\lvert\bar{\mathfrak{p}}(4) - \boldsymbol{p}^*(4)\rvert$ (%)	63.23	27.76	56.79	37.77	35.85	24.91	5.84
MAD($\mathfrak{p}(4)$) (%)	8.37	5.17	13.20	12.32	15.41	17.89	4.39
var($\mathfrak{p}(4)$) (%)	2.17	0.77	3.75	2.17	3.47	3.93	0.25
$\boldsymbol{p}^*(5) = 0.5$							
θ	0	$\frac{1}{6}$	$\frac{1}{3}$	$\frac{1}{2}$	$\frac{2}{3}$	$\frac{5}{6}$	1
κ_a	3.00	2.50	1.90	1.70	1.60	1.50	1.00
$\lvert\bar{\mathfrak{p}}(4) - \boldsymbol{p}^*(4)\rvert$ (%)	69.30	54.19	42.77	29.58	19.31	10.72	3.15
MAD($\mathfrak{p}(4)$) (%)	10.41	11.34	11.11	7.41	4.90	5.99	5.69
var($\mathfrak{p}(4)$) (%)	3.39	2.75	2.36	1.21	0.56	0.51	0.39
$\boldsymbol{p}^*(5) = 0.7$							
θ	0	$\frac{1}{6}$	$\frac{1}{3}$	$\frac{1}{2}$	$\frac{2}{3}$	$\frac{5}{6}$	1
κ_a	1.80	1.90	3.10	2.00	1.60	1.40	1.40
$\lvert\bar{\mathfrak{p}}(4) - \boldsymbol{p}^*(4)\rvert$ (%)	32.72	30.75	41.19	40.63	41.30	18.27	23.90
MAD($\mathfrak{p}(4)$) (%)	5.72	16.03	15.29	5.27	5.90	4.77	3.29
var($\mathfrak{p}(4)$) (%)	0.84	3.59	2.90	0.89	0.93	0.38	0.25
$\boldsymbol{p}^*(5) = 0.9$							
θ	0	$\frac{1}{6}$	$\frac{1}{3}$	$\frac{1}{2}$	$\frac{2}{3}$	$\frac{5}{6}$	1
κ_a	2.00	2.00	2.20	2.10	2.00	1.30	1.30
$\lvert\bar{\mathfrak{p}}(4) - \boldsymbol{p}^*(4)\rvert$ (%)	15.02	0.42	20.17	11.02	3.29	8.91	8.91
MAD($\mathfrak{p}(4)$) (%)	9.32	9.50	12.37	8.84	5.04	1.16	1.16
var($\mathfrak{p}(4)$) (%)	1.18	1.24	1.99	1.11	0.37	0.06	0.06

Table D.6.: Statistics of $\boldsymbol{p}(4)$ using the standard algorithm for the 5 parameter case with 1000 drawn samples for varying height of the lower muscle $\boldsymbol{p}^*(5)$ and thickness of the surrounding tissue layer θ in the settings from Section 6.3.4 with $\boldsymbol{p}^*(4) = \frac{\pi}{2}$

$\boldsymbol{p}^*(5) = 0.1$							
θ	0	$\frac{1}{6}$	$\frac{1}{3}$	$\frac{1}{2}$	$\frac{2}{3}$	$\frac{5}{6}$	1
κ_a	2.80	3.30	3.30	2.70	3.00	2.60	2.60
$\lvert\bar{\mathfrak{p}}(4) - \boldsymbol{p}^*(4)\rvert$ (%)	75.72	75.06	72.84	72.53	74.39	71.19	48.22
MAD($\mathfrak{p}(4)$) (%)	9.97	11.12	18.29	18.64	21.74	20.37	24.71
var($\mathfrak{p}(4)$) (%)	2.31	2.71	5.61	5.68	7.11	5.94	7.65
$\boldsymbol{p}^*(5) = 0.3$							
θ	0	$\frac{1}{6}$	$\frac{1}{3}$	$\frac{1}{2}$	$\frac{2}{3}$	$\frac{5}{6}$	1
κ_a	3.10	3.70	3.50	2.90	2.60	2.10	1.70
$\lvert\bar{\mathfrak{p}}(4) - \boldsymbol{p}^*(4)\rvert$ (%)	63.10	57.30	49.17	49.44	49.78	36.86	37.50
MAD($\mathfrak{p}(4)$) (%)	6.74	9.18	15.91	17.31	18.08	13.32	12.42
var($\mathfrak{p}(4)$) (%)	1.48	1.83	3.97	4.35	4.81	2.38	2.09
$\boldsymbol{p}^*(5) = 0.5$							
θ	0	$\frac{1}{6}$	$\frac{1}{3}$	$\frac{1}{2}$	$\frac{2}{3}$	$\frac{5}{6}$	1
κ_a	1.70	1.50	1.50	1.90	1.10	1.10	0.80
$\lvert\bar{\mathfrak{p}}(4) - \boldsymbol{p}^*(4)\rvert$ (%)	57.71	53.54	52.29	44.42	29.77	20.20	19.48
MAD($\mathfrak{p}(4)$) (%)	13.25	5.65	6.18	10.22	3.53	4.69	2.48
var($\mathfrak{p}(4)$) (%)	2.52	0.94	0.97	1.84	0.34	0.28	0.14
$\boldsymbol{p}^*(5) = 0.7$							
θ	0	$\frac{1}{6}$	$\frac{1}{3}$	$\frac{1}{2}$	$\frac{2}{3}$	$\frac{5}{6}$	1
κ_a	2.00	1.50	2.30	1.70	2.00	1.10	1.40
$\lvert\bar{\mathfrak{p}}(4) - \boldsymbol{p}^*(4)\rvert$ (%)	26.82	33.28	75.60	42.13	46.85	5.75	18.33
MAD($\mathfrak{p}(4)$) (%)	10.69	7.08	10.64	5.71	6.78	1.00	2.45
var($\mathfrak{p}(4)$) (%)	2.11	0.76	2.42	0.90	1.32	0.05	0.12
$\boldsymbol{p}^*(5) = 0.9$							
θ	0	$\frac{1}{6}$	$\frac{1}{3}$	$\frac{1}{2}$	$\frac{2}{3}$	$\frac{5}{6}$	1
κ_a	1.60	1.60	1.60	1.30	1.30	1.40	1.40
$\lvert\bar{\mathfrak{p}}(4) - \boldsymbol{p}^*(4)\rvert$ (%)	11.69	11.69	16.66	15.81	10.27	17.27	17.27
MAD($\mathfrak{p}(4)$) (%)	2.03	2.03	5.77	0.60	0.49	1.49	1.49
var($\mathfrak{p}(4)$) (%)	0.12	0.12	0.44	0.03	0.03	0.08	0.08

Table D.7.: Statistics of $\boldsymbol{p}(5)$ using the standard algorithm for the 5 parameter case with 1000 drawn samples for varying height of the lower muscle $\boldsymbol{p}^*(5)$ and thickness of the surrounding tissue layer θ in the settings from Section 6.3.4 with $\boldsymbol{p}^*(4) = 0$

$\boldsymbol{p}^*(5) = 0.1$							
θ	0	$\frac{1}{6}$	$\frac{1}{3}$	$\frac{1}{2}$	$\frac{2}{3}$	$\frac{5}{6}$	1
κ_a	1.40	1.60	1.50	1.50	1.30	1.20	1.20
$\lvert\bar{\mathfrak{p}}(5) - \boldsymbol{p}^*(5)\rvert$ (%)	11.94	4.73	5.61	4.51	4.06	4.87	4.67
MAD($\mathfrak{p}(5)$) (%)	0.91	2.25	1.38	2.28	0.55	1.17	2.08
var($\mathfrak{p}(5)$) (%)	0.04	0.07	0.04	0.06	0.02	0.02	0.06
$\boldsymbol{p}^*(5) = 0.3$							
θ	0	$\frac{1}{6}$	$\frac{1}{3}$	$\frac{1}{2}$	$\frac{2}{3}$	$\frac{5}{6}$	1
κ_a	1.90	1.70	1.80	1.50	1.50	1.50	1.40
$\lvert\bar{\mathfrak{p}}(5) - \boldsymbol{p}^*(5)\rvert$ (%)	5.08	0.35	3.90	13.48	1.50	0.92	0.44
MAD($\mathfrak{p}(5)$) (%)	2.91	2.29	2.14	7.09	1.71	1.07	0.52
var($\mathfrak{p}(5)$) (%)	0.15	0.08	0.08	0.62	0.05	0.07	0.02
$\boldsymbol{p}^*(5) = 0.5$							
θ	0	$\frac{1}{6}$	$\frac{1}{3}$	$\frac{1}{2}$	$\frac{2}{3}$	$\frac{5}{6}$	1
κ_a	1.80	0.70	0.80	0.90	0.90	0.90	0.90
$\lvert\bar{\mathfrak{p}}(5) - \boldsymbol{p}^*(5)\rvert$ (%)	22.32	18.77	17.79	23.23	23.23	20.83	20.83
MAD($\mathfrak{p}(5)$) (%)	6.20	0.34	1.91	3.41	3.41	0.92	0.92
var($\mathfrak{p}(5)$) (%)	0.46	0.02	0.07	0.16	0.16	0.03	0.03
$\boldsymbol{p}^*(5) = 0.7$							
θ	0	$\frac{1}{6}$	$\frac{1}{3}$	$\frac{1}{2}$	$\frac{2}{3}$	$\frac{5}{6}$	1
κ_a	1.50	1.80	1.00	0.80	1.40	1.50	1.70
$\lvert\bar{\mathfrak{p}}(5) - \boldsymbol{p}^*(5)\rvert$ (%)	0.99	6.37	19.31	18.15	19.28	3.54	4.88
MAD($\mathfrak{p}(5)$) (%)	1.09	7.23	0.77	2.71	0.99	0.86	1.83
var($\mathfrak{p}(5)$) (%)	0.05	0.65	0.05	0.19	0.09	0.03	0.05
$\boldsymbol{p}^*(5) = 0.9$							
θ	0	$\frac{1}{6}$	$\frac{1}{3}$	$\frac{1}{2}$	$\frac{2}{3}$	$\frac{5}{6}$	1
κ_a	1.50	1.60	1.50	1.70	1.30	1.30	1.20
$\lvert\bar{\mathfrak{p}}(5) - \boldsymbol{p}^*(5)\rvert$ (%)	13.52	11.25	2.75	2.90	21.01	21.01	4.44
MAD($\mathfrak{p}(5)$) (%)	0.37	0.38	0.31	0.52	4.01	4.01	0.94
var($\mathfrak{p}(5)$) (%)	0.02	0.02	0.01	0.02	0.20	0.20	0.03

Table D.8.: Statistics of $\boldsymbol{p}(5)$ using the standard algorithm for the 5 parameter case with 1000 drawn samples for varying height of the lower muscle $\boldsymbol{p}^*(5)$ and thickness of the surrounding tissue layer θ in the settings from Section 6.3.4 with $\boldsymbol{p}^*(4) = \frac{\pi}{4}$

$\boldsymbol{p}^*(5) = 0.1$							
θ	0	$\frac{1}{6}$	$\frac{1}{3}$	$\frac{1}{2}$	$\frac{2}{3}$	$\frac{5}{6}$	1
κ_a	3.00	2.90	2.80	3.00	2.90	3.10	2.50
$\lvert\bar{\mathfrak{p}}(5) - \boldsymbol{p}^*(5)\rvert$ (%)	11.71	9.94	9.42	6.09	5.09	5.42	4.54
MAD($\mathfrak{p}(5)$) (%)	2.40	2.81	3.24	2.25	3.62	1.86	2.43
var($\mathfrak{p}(5)$) (%)	0.11	0.10	0.12	0.07	0.17	0.06	0.09
$\boldsymbol{p}^*(5) = 0.3$							
θ	0	$\frac{1}{6}$	$\frac{1}{3}$	$\frac{1}{2}$	$\frac{2}{3}$	$\frac{5}{6}$	1
κ_a	2.70	2.10	3.20	2.30	2.50	2.60	2.10
$\lvert\bar{\mathfrak{p}}(5) - \boldsymbol{p}^*(5)\rvert$ (%)	3.19	15.20	7.26	10.01	0.93	4.23	0.17
MAD($\mathfrak{p}(5)$) (%)	4.62	3.43	7.58	8.22	7.06	4.35	5.50
var($\mathfrak{p}(5)$) (%)	0.34	0.34	0.80	0.87	0.61	0.32	0.35
$\boldsymbol{p}^*(5) = 0.5$							
θ	0	$\frac{1}{6}$	$\frac{1}{3}$	$\frac{1}{2}$	$\frac{2}{3}$	$\frac{5}{6}$	1
κ_a	3.00	2.50	1.90	1.70	1.60	1.50	1.00
$\lvert\bar{\mathfrak{p}}(5) - \boldsymbol{p}^*(5)\rvert$ (%)	28.44	16.66	20.62	19.50	20.70	20.67	20.47
MAD($\mathfrak{p}(5)$) (%)	5.77	4.59	1.35	3.48	1.26	1.91	0.96
var($\mathfrak{p}(5)$) (%)	0.46	0.29	0.07	0.15	0.05	0.08	0.03
$\boldsymbol{p}^*(5) = 0.7$							
θ	0	$\frac{1}{6}$	$\frac{1}{3}$	$\frac{1}{2}$	$\frac{2}{3}$	$\frac{5}{6}$	1
κ_a	1.80	1.90	3.10	2.00	1.60	1.40	1.40
$\lvert\bar{\mathfrak{p}}(5) - \boldsymbol{p}^*(5)\rvert$ (%)	3.64	0.86	17.72	18.70	18.71	0.74	1.72
MAD($\mathfrak{p}(5)$) (%)	5.57	2.54	1.04	1.20	0.93	3.44	3.10
var($\mathfrak{p}(5)$) (%)	0.43	0.14	0.05	0.10	0.09	0.15	0.13
$\boldsymbol{p}^*(5) = 0.9$							
θ	0	$\frac{1}{6}$	$\frac{1}{3}$	$\frac{1}{2}$	$\frac{2}{3}$	$\frac{5}{6}$	1
κ_a	2.00	2.00	2.20	2.10	2.00	1.30	1.30
$\lvert\bar{\mathfrak{p}}(5) - \boldsymbol{p}^*(5)\rvert$ (%)	6.99	10.54	8.00	8.18	9.11	7.45	7.45
MAD($\mathfrak{p}(5)$) (%)	3.15	3.87	5.25	3.69	3.27	4.25	4.25
var($\mathfrak{p}(5)$) (%)	0.11	0.18	0.34	0.16	0.14	0.20	0.20

Table D.9.: Statistics of $\boldsymbol{p}(5)$ using the standard algorithm for the 5 parameter case with 1000 drawn samples for varying height of the lower muscle $\boldsymbol{p}^*(5)$ and thickness of the surrounding tissue layer θ in the settings from Section 6.3.4 with $\boldsymbol{p}^*(4) = \frac{3\pi}{4}$

$\boldsymbol{p}^*(5) = 0.1$							
θ	0	$\frac{1}{6}$	$\frac{1}{3}$	$\frac{1}{2}$	$\frac{2}{3}$	$\frac{5}{6}$	1
κ_a	2.80	3.30	3.30	2.70	3.00	2.60	2.60
$\lvert\bar{\mathfrak{p}}(5) - \boldsymbol{p}^*(5)\rvert$ (%)	11.82	5.43	5.40	4.34	4.72	1.95	4.80
MAD($\mathfrak{p}(5)$) (%)	3.22	2.87	1.87	2.06	2.48	2.26	3.18
var($\mathfrak{p}(5)$) (%)	0.17	0.10	0.07	0.08	0.09	0.07	0.14
$\boldsymbol{p}^*(5) = 0.3$							
θ	0	$\frac{1}{6}$	$\frac{1}{3}$	$\frac{1}{2}$	$\frac{2}{3}$	$\frac{5}{6}$	1
κ_a	3.10	3.70	3.50	2.90	2.60	2.10	1.70
$\lvert\bar{\mathfrak{p}}(5) - \boldsymbol{p}^*(5)\rvert$ (%)	4.90	7.65	3.19	7.97	4.50	10.14	7.44
MAD($\mathfrak{p}(5)$) (%)	5.83	3.82	4.56	7.45	4.66	7.47	7.57
var($\mathfrak{p}(5)$) (%)	0.39	0.25	0.37	0.75	0.34	0.69	0.79
$\boldsymbol{p}^*(5) = 0.5$							
θ	0	$\frac{1}{6}$	$\frac{1}{3}$	$\frac{1}{2}$	$\frac{2}{3}$	$\frac{5}{6}$	1
κ_a	1.70	1.50	1.50	1.90	1.10	1.10	0.80
$\lvert\bar{\mathfrak{p}}(5) - \boldsymbol{p}^*(5)\rvert$ (%)	31.31	18.72	19.62	15.21	14.32	15.67	27.41
MAD($\mathfrak{p}(5)$) (%)	2.79	0.55	0.96	3.48	3.49	2.68	1.21
var($\mathfrak{p}(5)$) (%)	0.19	0.03	0.04	0.14	0.19	0.16	0.09
$\boldsymbol{p}^*(5) = 0.7$							
θ	0	$\frac{1}{6}$	$\frac{1}{3}$	$\frac{1}{2}$	$\frac{2}{3}$	$\frac{5}{6}$	1
κ_a	2.00	1.50	2.30	1.70	2.00	1.10	1.40
$\lvert\bar{\mathfrak{p}}(5) - \boldsymbol{p}^*(5)\rvert$ (%)	5.37	17.83	18.00	19.07	19.25	1.84	7.40
MAD($\mathfrak{p}(5)$) (%)	4.82	3.90	1.16	1.15	1.12	3.84	7.20
var($\mathfrak{p}(5)$) (%)	0.30	0.30	0.06	0.10	0.10	0.23	0.62
$\boldsymbol{p}^*(5) = 0.9$							
θ	0	$\frac{1}{6}$	$\frac{1}{3}$	$\frac{1}{2}$	$\frac{2}{3}$	$\frac{5}{6}$	1
κ_a	1.60	1.60	1.60	1.30	1.30	1.40	1.40
$\lvert\bar{\mathfrak{p}}(5) - \boldsymbol{p}^*(5)\rvert$ (%)	7.68	7.68	11.13	20.84	21.01	8.89	8.89
MAD($\mathfrak{p}(5)$) (%)	1.21	1.21	3.32	1.10	4.01	0.81	0.81
var($\mathfrak{p}(5)$) (%)	0.05	0.05	0.14	0.06	0.20	0.04	0.04

E. Appendix - 9 Parameter Case in Use Case 3

Table E.1.: Statistics of $\boldsymbol{p}(1:3)$ using the standard algorithm for the 9 parameter case with 1000 drawn samples for varying height of the lower muscle $\boldsymbol{p}^*(9)$ and thickness of the surrounding tissue layer θ in the settings from Section 6.3.5 with $\boldsymbol{p}^*(4) = 0$

$\boldsymbol{p}^*(9)$	θ	$\lvert\bar{\mathfrak{p}}(1:3) - \boldsymbol{p}^*(1:3)\rvert$ (%)			MAD($\mathfrak{p}(1:3)$) (%)			var($\mathfrak{p}(1:3)$) (%)		
0.10	0	144.82	71.70	1.06	7.04	7.82	12.77	1.26	1.47	3.31
0.10	$\frac{1}{6}$	63.08	9.20	2.84	20.56	11.64	6.07	7.23	3.90	2.03
0.10	$\frac{1}{3}$	87.14	13.00	1.04	15.51	12.37	6.66	3.87	3.75	2.08
0.10	$\frac{1}{2}$	60.89	24.05	3.29	42.55	20.17	5.54	22.50	7.19	1.94
0.10	$\frac{2}{3}$	113.97	14.85	0.36	13.01	11.93	5.56	2.63	3.66	1.94
0.10	$\frac{5}{6}$	127.96	14.87	3.67	11.58	9.94	6.89	2.16	3.01	2.11
0.10	1	130.79	49.10	3.59	8.20	11.77	4.43	1.29	1.91	1.86
0.30	0	143.44	6.29	8.55	7.48	7.26	7.38	1.95	2.11	2.98
0.30	$\frac{1}{6}$	22.13	64.11	4.85	22.52	8.35	10.71	7.64	1.20	4.81
0.30	$\frac{1}{3}$	36.35	111.16	8.07	9.81	6.30	8.36	2.86	1.14	3.63
0.30	$\frac{1}{2}$	90.36	47.11	6.17	4.91	12.31	4.97	0.74	5.69	2.29
0.30	$\frac{2}{3}$	149.46	19.79	1.64	8.86	8.02	5.26	1.26	1.49	2.52
0.30	$\frac{5}{6}$	142.66	49.17	2.42	11.61	14.36	5.23	1.99	3.41	2.48
0.30	1	161.22	46.33	2.81	8.28	16.11	5.13	2.64	3.37	2.46
0.50	0	260.03	62.23	5.94	23.89	10.46	3.73	11.68	3.30	1.39
0.50	$\frac{1}{6}$	99.05	131.85	102.16	5.71	4.97	1.73	0.77	0.45	0.05
0.50	$\frac{1}{3}$	120.69	42.23	170.05	3.26	8.31	3.64	0.27	1.04	0.41
0.50	$\frac{1}{2}$	152.62	80.16	292.32	1.96	4.34	10.06	0.45	0.91	6.08
0.50	$\frac{2}{3}$	223.31	62.53	54.28	10.50	11.75	4.20	2.91	1.80	0.71
0.50	$\frac{5}{6}$	182.81	5.52	55.48	14.51	13.18	2.04	3.05	2.90	0.54
0.50	1	182.27	0.37	53.70	2.32	4.48	2.12	0.89	1.38	0.56
0.70	0	109.74	11.58	8.02	10.41	34.24	18.50	1.75	14.99	4.57
0.70	$\frac{1}{6}$	110.56	115.80	35.87	3.34	7.39	2.46	0.26	0.80	0.48
0.70	$\frac{1}{3}$	137.48	65.23	64.29	3.24	1.57	2.76	0.48	0.16	0.28
0.70	$\frac{1}{2}$	76.42	59.18	106.17	7.88	12.20	4.90	1.07	1.91	0.31
0.70	$\frac{2}{3}$	62.27	32.04	167.85	22.30	7.38	2.98	5.92	0.81	0.28
0.70	$\frac{5}{6}$	64.45	23.66	243.75	10.77	4.22	7.43	2.19	0.69	2.56
0.70	1	132.27	92.88	301.13	1.59	5.88	10.82	0.41	1.25	7.48
0.90	0	125.28	93.24	21.33	0.74	0.80	2.82	0.14	0.06	0.70
0.90	$\frac{1}{6}$	149.86	82.72	32.92	7.52	9.96	9.02	0.94	1.06	1.17
0.90	$\frac{1}{3}$	125.28	93.24	21.33	0.74	0.80	2.82	0.14	0.06	0.70
0.90	$\frac{1}{2}$	200.34	119.33	21.97	15.49	14.24	7.55	4.45	2.91	1.56
0.90	$\frac{2}{3}$	152.18	76.18	24.85	7.35	12.77	2.08	0.95	1.77	0.59
0.90	$\frac{5}{6}$	180.52	151.13	7.29	13.24	19.27	9.36	3.43	7.79	1.79
0.90	1	145.84	100.48	24.86	2.31	4.15	2.36	0.44	0.89	0.57

Table E.2.: Statistics of $\boldsymbol{p}(1:3)$ using the standard algorithm for the 9 parameter case with 1000 drawn samples for varying height of the lower muscle $\boldsymbol{p}^*(9)$ and thickness of the surrounding tissue layer θ in the settings from Section 6.3.5 with $\boldsymbol{p}^*(4) = \frac{\pi}{4}$

$\boldsymbol{p}^*(9)$	θ	$\lvert\bar{\mathfrak{p}}(1:3) - \boldsymbol{p}^*(1:3)\rvert$ (%)			MAD($\mathfrak{p}(1:3)$) (%)			var($\mathfrak{p}(1:3)$) (%)		
0.10	0	168.17	49.78	6.40	10.80	12.42	7.69	2.01	3.03	2.56
0.10	$\frac{1}{6}$	48.62	89.90	0.56	38.08	21.73	10.19	18.16	7.24	2.77
0.10	$\frac{1}{3}$	85.59	103.67	1.74	31.79	22.04	7.80	12.80	6.85	2.43
0.10	$\frac{1}{2}$	102.06	107.69	0.90	42.02	33.16	7.85	23.12	17.67	2.45
0.10	$\frac{2}{3}$	86.17	58.11	2.67	36.71	21.39	9.01	16.88	9.90	2.87
0.10	$\frac{5}{6}$	177.22	62.34	1.49	23.99	15.90	8.34	9.65	6.95	2.82
0.10	1	105.27	52.55	1.86	34.30	13.17	6.08	14.50	5.08	2.45
0.30	0	119.33	55.43	10.30	16.28	19.50	10.84	4.40	5.56	2.87
0.30	$\frac{1}{6}$	93.87	262.41	8.06	12.77	60.77	9.42	4.18	53.77	4.18
0.30	$\frac{1}{3}$	65.33	132.47	1.95	7.31	44.36	9.37	1.59	24.58	4.18
0.30	$\frac{1}{2}$	105.43	45.37	0.78	12.82	13.57	6.77	2.01	2.83	2.67
0.30	$\frac{2}{3}$	122.76	128.28	5.51	6.03	30.75	5.03	0.97	16.65	2.34
0.30	$\frac{5}{6}$	173.88	54.02	3.26	20.71	9.90	5.24	6.01	2.40	2.47
0.30	1	185.75	29.91	5.02	20.27	17.24	4.98	6.59	3.79	2.36
0.50	0	218.50	39.76	3.60	29.81	46.59	8.90	10.60	26.03	1.88
0.50	$\frac{1}{6}$	144.64	248.58	103.77	9.82	16.62	3.95	1.94	6.88	0.30
0.50	$\frac{1}{3}$	241.80	111.33	174.11	15.09	6.55	6.27	6.87	0.97	1.20
0.50	$\frac{1}{2}$	204.46	115.91	263.17	9.73	9.05	9.42	2.69	1.69	3.58
0.50	$\frac{2}{3}$	173.12	55.85	57.61	8.21	6.70	3.14	1.57	1.00	0.66
0.50	$\frac{5}{6}$	175.29	42.73	52.75	12.25	16.15	6.87	2.24	6.52	0.98
0.50	1	182.78	73.04	51.17	15.49	20.40	5.43	3.70	5.08	0.83
0.70	0	149.32	75.02	1.76	26.11	16.23	6.00	8.44	2.88	1.37
0.70	$\frac{1}{6}$	151.28	8.28	3.61	11.06	17.01	3.87	1.88	5.33	1.16
0.70	$\frac{1}{3}$	189.54	281.61	64.63	6.09	27.21	1.46	2.61	17.58	0.14
0.70	$\frac{1}{2}$	112.83	178.23	109.13	12.21	15.61	3.97	2.11	3.62	0.22
0.70	$\frac{2}{3}$	154.04	76.61	170.27	26.33	16.37	2.85	8.58	3.90	0.40
0.70	$\frac{5}{6}$	150.30	49.93	244.20	5.44	11.24	11.11	1.35	1.75	2.87
0.70	1	129.45	1.28	297.06	10.76	8.85	11.82	1.47	1.61	7.74
0.90	0	121.23	69.38	8.99	4.12	11.61	8.49	0.27	1.52	1.63
0.90	$\frac{1}{6}$	124.08	173.60	1.57	4.50	17.63	3.66	0.66	5.04	1.23
0.90	$\frac{1}{3}$	127.81	161.43	6.30	6.97	23.10	10.97	0.89	9.31	2.06
0.90	$\frac{1}{2}$	164.25	111.78	14.83	2.83	2.84	2.91	0.80	0.57	0.83
0.90	$\frac{2}{3}$	205.57	54.46	5.30	19.25	6.96	9.82	7.19	0.99	1.95
0.90	$\frac{5}{6}$	172.33	120.25	3.45	10.20	17.06	9.41	1.96	4.97	1.98
0.90	1	152.81	115.25	24.18	7.65	15.95	2.57	0.98	3.39	0.59

Table E.3.: Statistics of $\boldsymbol{p}(1:3)$ using the standard algorithm for the 9 parameter case with 1000 drawn samples for varying height of the lower muscle $\boldsymbol{p}^*(9)$ and thickness of the surrounding tissue layer θ in the settings from Section 6.3.5 with $\boldsymbol{p}^*(4) = \frac{3\pi}{4}$

$\boldsymbol{p}^*(9)$	θ	$\lvert\bar{\mathfrak{p}}(1:3) - \boldsymbol{p}^*(1:3)\rvert$ (%)			MAD($\mathfrak{p}(1:3)$) (%)			var($\mathfrak{p}(1:3)$) (%)		
0.10	0	156.76	107.27	16.69	12.76	10.93	13.66	4.96	2.18	3.58
0.10	$\frac{1}{6}$	154.75	162.95	6.22	18.31	41.78	14.42	5.84	24.55	3.61
0.10	$\frac{1}{3}$	57.76	86.61	1.78	67.51	17.96	12.36	51.12	4.79	3.37
0.10	$\frac{1}{2}$	76.70	117.97	5.68	40.88	25.57	7.89	19.88	11.41	2.23
0.10	$\frac{2}{3}$	96.59	136.93	9.05	48.19	49.03	8.83	27.80	35.77	2.38
0.10	$\frac{5}{6}$	128.69	55.95	7.82	14.02	18.41	7.83	2.65	5.74	2.23
0.10	1	194.20	104.15	7.02	18.61	26.39	10.65	4.84	8.01	2.63
0.30	0	161.79	36.27	3.48	33.58	16.67	12.90	12.84	3.49	3.98
0.30	$\frac{1}{6}$	115.03	86.64	8.82	15.48	18.68	7.87	4.21	4.39	3.71
0.30	$\frac{1}{3}$	116.64	122.29	7.20	14.32	12.52	8.11	3.87	3.06	3.83
0.30	$\frac{1}{2}$	67.19	126.06	4.28	15.35	24.43	8.27	4.27	8.21	3.89
0.30	$\frac{2}{3}$	152.72	61.15	2.39	16.33	15.95	5.53	5.61	3.45	2.55
0.30	$\frac{5}{6}$	208.26	55.95	1.24	26.90	14.64	5.28	11.20	2.63	2.53
0.30	1	194.86	81.36	1.69	20.40	21.35	5.78	8.63	8.00	2.55
0.50	0	151.19	47.54	15.55	13.13	26.62	14.46	3.55	11.84	3.74
0.50	$\frac{1}{6}$	202.66	270.79	104.20	24.62	27.15	4.01	10.01	15.42	0.42
0.50	$\frac{1}{3}$	155.42	45.95	191.95	1.55	1.08	2.37	0.33	0.18	0.69
0.50	$\frac{1}{2}$	151.98	146.55	257.07	10.63	31.64	9.08	1.56	17.52	3.30
0.50	$\frac{2}{3}$	127.11	27.35	61.87	10.35	13.75	6.24	1.44	2.29	0.78
0.50	$\frac{5}{6}$	84.44	27.59	58.13	14.59	10.11	2.98	4.05	2.36	0.54
0.50	1	45.91	83.64	57.45	23.71	12.94	7.29	8.92	1.89	0.93
0.70	0	114.44	53.47	31.96	9.02	11.69	2.65	1.66	6.48	0.59
0.70	$\frac{1}{6}$	124.48	74.44	33.82	8.29	10.56	7.02	1.66	1.55	1.54
0.70	$\frac{1}{3}$	257.63	262.58	62.91	20.11	23.08	3.89	8.94	13.58	0.32
0.70	$\frac{1}{2}$	118.10	105.17	106.13	11.42	24.72	4.32	1.91	9.40	0.25
0.70	$\frac{2}{3}$	127.49	184.90	163.85	26.07	17.76	3.92	9.07	11.08	0.41
0.70	$\frac{5}{6}$	101.30	61.86	236.30	18.13	9.76	6.71	4.02	1.33	2.65
0.70	1	145.72	77.81	301.47	2.18	5.79	10.53	0.60	1.03	7.50
0.90	0	123.77	68.98	0.72	0.95	2.10	3.79	0.22	0.24	1.27
0.90	$\frac{1}{6}$	97.09	80.85	2.25	1.69	0.67	3.87	0.25	0.06	1.23
0.90	$\frac{1}{3}$	104.59	84.73	12.16	12.97	22.34	11.59	1.90	5.29	2.41
0.90	$\frac{1}{2}$	165.49	68.13	13.78	2.87	1.78	2.78	0.90	0.22	0.83
0.90	$\frac{2}{3}$	147.41	101.42	23.47	6.67	4.27	5.79	0.82	0.95	0.87
0.90	$\frac{5}{6}$	173.03	129.37	24.52	9.19	12.11	2.37	2.08	3.59	0.58
0.90	1	178.35	98.49	5.40	9.20	13.69	8.49	2.02	3.17	1.67

Table E.4.: Statistics of $\boldsymbol{p}(4)$ using the standard algorithm for the 9 parameter case with 1000 drawn samples for varying height of the lower muscle $\boldsymbol{p}^*(9)$ and thickness of the surrounding tissue layer θ in the settings from Section 6.3.5 with $\boldsymbol{p}^*(4) = 0$

$\boldsymbol{p}^*(9) = 0.1$							
θ	0	$\frac{1}{6}$	$\frac{1}{3}$	$\frac{1}{2}$	$\frac{2}{3}$	$\frac{5}{6}$	1
κ_a	1.40	1.80	1.90	2.40	1.70	2.00	1.50
$\lvert\bar{\mathfrak{p}}(4) - \boldsymbol{p}^*(4)\rvert$ (%)	4.82	5.54	5.31	6.76	4.65	4.58	8.03
MAD($\mathfrak{p}(4)$) (%)	2.65	2.94	3.02	3.97	2.99	1.99	3.77
var($\mathfrak{p}(4)$) (%)	0.08	0.14	0.17	0.24	0.11	0.08	0.20
$\boldsymbol{p}^*(9) = 0.3$							
θ	0	$\frac{1}{6}$	$\frac{1}{3}$	$\frac{1}{2}$	$\frac{2}{3}$	$\frac{5}{6}$	1
κ_a	1.50	1.60	1.40	1.20	1.30	1.40	1.30
$\lvert\bar{\mathfrak{p}}(4) - \boldsymbol{p}^*(4)\rvert$ (%)	5.08	5.23	7.37	5.41	5.06	8.05	13.54
MAD($\mathfrak{p}(4)$) (%)	1.57	1.48	2.70	1.30	2.83	3.35	1.61
var($\mathfrak{p}(4)$) (%)	0.06	0.05	0.20	0.05	0.10	0.13	0.06
$\boldsymbol{p}^*(9) = 0.5$							
θ	0	$\frac{1}{6}$	$\frac{1}{3}$	$\frac{1}{2}$	$\frac{2}{3}$	$\frac{5}{6}$	1
κ_a	2.40	0.40	1.00	1.50	1.40	1.10	0.90
$\lvert\bar{\mathfrak{p}}(4) - \boldsymbol{p}^*(4)\rvert$ (%)	14.33	1.16	7.68	16.56	23.73	12.58	13.64
MAD($\mathfrak{p}(4)$) (%)	3.09	0.79	3.74	0.73	6.10	2.52	0.19
var($\mathfrak{p}(4)$) (%)	0.27	0.01	0.16	0.03	0.79	0.12	0.01
$\boldsymbol{p}^*(9) = 0.7$							
θ	0	$\frac{1}{6}$	$\frac{1}{3}$	$\frac{1}{2}$	$\frac{2}{3}$	$\frac{5}{6}$	1
κ_a	2.20	1.00	1.00	0.50	0.80	1.90	1.80
$\lvert\bar{\mathfrak{p}}(4) - \boldsymbol{p}^*(4)\rvert$ (%)	21.68	3.57	4.30	11.12	14.51	14.98	7.17
MAD($\mathfrak{p}(4)$) (%)	3.69	1.46	0.46	3.81	3.43	3.19	3.65
var($\mathfrak{p}(4)$) (%)	0.20	0.03	0.01	0.17	0.12	0.17	0.15
$\boldsymbol{p}^*(9) = 0.9$							
θ	0	$\frac{1}{6}$	$\frac{1}{3}$	$\frac{1}{2}$	$\frac{2}{3}$	$\frac{5}{6}$	1
κ_a	1.10	1.20	1.10	2.60	1.40	1.90	1.40
$\lvert\bar{\mathfrak{p}}(4) - \boldsymbol{p}^*(4)\rvert$ (%)	21.98	18.40	21.98	51.69	30.13	32.99	23.59
MAD($\mathfrak{p}(4)$) (%)	0.39	1.05	0.39	8.47	3.58	3.17	0.41
var($\mathfrak{p}(4)$) (%)	0.02	0.02	0.02	1.10	0.16	0.20	0.03

Table E.5.: Statistics of $\boldsymbol{p}(4)$ using the standard algorithm for the 9 parameter case with 1000 drawn samples for varying height of the lower muscle $\boldsymbol{p}^*(9)$ and thickness of the surrounding tissue layer θ in the settings from Section 6.3.5 with $\boldsymbol{p}^*(4) = \frac{\pi}{4}$

$\boldsymbol{p}^*(9) = 0.1$							
θ	0	$\frac{1}{6}$	$\frac{1}{3}$	$\frac{1}{2}$	$\frac{2}{3}$	$\frac{5}{6}$	1
κ_a	2.10	2.50	2.50	2.70	3.10	3.20	2.40
$\lvert\bar{\mathfrak{p}}(4) - \boldsymbol{p}^*(4)\rvert$ (%)	46.28	61.45	59.76	57.47	50.79	17.53	2.27
MAD($\mathfrak{p}(4)$) (%)	8.68	15.96	14.59	14.41	18.68	13.94	5.03
var($\mathfrak{p}(4)$) (%)	1.41	3.45	3.20	3.28	4.55	3.11	0.32
$\boldsymbol{p}^*(9) = 0.3$							
θ	0	$\frac{1}{6}$	$\frac{1}{3}$	$\frac{1}{2}$	$\frac{2}{3}$	$\frac{5}{6}$	1
κ_a	1.80	2.30	1.70	1.90	2.20	1.50	1.60
$\lvert\bar{\mathfrak{p}}(4) - \boldsymbol{p}^*(4)\rvert$ (%)	45.00	13.40	16.58	10.17	17.52	5.46	12.51
MAD($\mathfrak{p}(4)$) (%)	15.32	9.20	4.51	5.86	6.80	5.33	5.67
var($\mathfrak{p}(4)$) (%)	3.23	1.04	0.34	0.58	0.62	0.39	0.41
$\boldsymbol{p}^*(9) = 0.5$							
θ	0	$\frac{1}{6}$	$\frac{1}{3}$	$\frac{1}{2}$	$\frac{2}{3}$	$\frac{5}{6}$	1
κ_a	2.30	1.70	1.90	1.60	1.50	1.50	1.50
$\lvert\bar{\mathfrak{p}}(4) - \boldsymbol{p}^*(4)\rvert$ (%)	46.70	37.57	38.96	14.03	7.33	2.78	8.63
MAD($\mathfrak{p}(4)$) (%)	22.58	11.00	8.60	2.77	0.37	2.74	2.94
var($\mathfrak{p}(4)$) (%)	5.75	1.93	1.48	0.13	0.01	0.11	0.11
$\boldsymbol{p}^*(9) = 0.7$							
θ	0	$\frac{1}{6}$	$\frac{1}{3}$	$\frac{1}{2}$	$\frac{2}{3}$	$\frac{5}{6}$	1
κ_a	2.30	2.00	2.10	1.70	1.60	1.60	2.10
$\lvert\bar{\mathfrak{p}}(4) - \boldsymbol{p}^*(4)\rvert$ (%)	19.76	25.96	5.02	53.32	47.62	25.76	6.44
MAD($\mathfrak{p}(4)$) (%)	12.61	7.51	3.39	11.08	11.25	3.99	2.00
var($\mathfrak{p}(4)$) (%)	1.82	0.74	0.25	1.68	1.72	0.56	0.12
$\boldsymbol{p}^*(9) = 0.9$							
θ	0	$\frac{1}{6}$	$\frac{1}{3}$	$\frac{1}{2}$	$\frac{2}{3}$	$\frac{5}{6}$	1
κ_a	1.60	2.30	2.40	1.40	2.40	2.10	1.50
$\lvert\bar{\mathfrak{p}}(4) - \boldsymbol{p}^*(4)\rvert$ (%)	6.29	0.31	26.07	30.64	22.20	18.78	20.17
MAD($\mathfrak{p}(4)$) (%)	0.61	2.38	7.04	1.37	1.77	3.00	3.38
var($\mathfrak{p}(4)$) (%)	0.02	0.12	0.68	0.13	0.12	0.15	0.14

Table E.6.: Statistics of $\boldsymbol{p}(4)$ using the standard algorithm for the 9 parameter case with 1000 drawn samples for varying height of the lower muscle $\boldsymbol{p}^*(9)$ and thickness of the surrounding tissue layer θ in the settings from Section 6.3.5 with $\boldsymbol{p}^*(4) = \frac{3\pi}{4}$

$\boldsymbol{p}^*(9) = 0.1$							
θ	0	$\frac{1}{6}$	$\frac{1}{3}$	$\frac{1}{2}$	$\frac{2}{3}$	$\frac{5}{6}$	1
κ_a	2.80	3.60	3.00	3.10	3.40	2.90	2.70
$\lvert\bar{\mathfrak{p}}(4) - \boldsymbol{p}^*(4)\rvert$ (%)	33.23	37.95	47.64	41.23	23.65	25.21	17.89
MAD($\mathfrak{p}(4)$) (%)	18.38	24.60	21.19	23.11	30.86	28.11	7.58
var($\mathfrak{p}(4)$) (%)	4.38	7.90	5.03	6.11	11.09	8.71	0.78
$\boldsymbol{p}^*(9) = 0.3$							
θ	0	$\frac{1}{6}$	$\frac{1}{3}$	$\frac{1}{2}$	$\frac{2}{3}$	$\frac{5}{6}$	1
κ_a	2.30	2.20	1.80	1.90	2.50	1.80	1.60
$\lvert\bar{\mathfrak{p}}(4) - \boldsymbol{p}^*(4)\rvert$ (%)	35.92	60.74	59.15	43.05	52.88	40.76	23.13
MAD($\mathfrak{p}(4)$) (%)	12.30	9.70	9.22	12.76	13.93	12.50	4.76
var($\mathfrak{p}(4)$) (%)	2.33	2.26	2.13	2.34	3.29	2.48	0.52
$\boldsymbol{p}^*(9) = 0.5$							
θ	0	$\frac{1}{6}$	$\frac{1}{3}$	$\frac{1}{2}$	$\frac{2}{3}$	$\frac{5}{6}$	1
κ_a	3.10	1.80	0.50	1.80	1.50	1.70	2.00
$\lvert\bar{\mathfrak{p}}(4) - \boldsymbol{p}^*(4)\rvert$ (%)	45.92	18.86	13.99	19.22	0.57	42.10	37.64
MAD($\mathfrak{p}(4)$) (%)	12.02	5.67	0.28	5.85	3.14	5.34	5.38
var($\mathfrak{p}(4)$) (%)	2.47	0.59	0.01	0.44	0.13	0.61	0.55
$\boldsymbol{p}^*(9) = 0.7$							
θ	0	$\frac{1}{6}$	$\frac{1}{3}$	$\frac{1}{2}$	$\frac{2}{3}$	$\frac{5}{6}$	1
κ_a	2.80	2.30	2.80	1.50	2.20	2.10	1.70
$\lvert\bar{\mathfrak{p}}(4) - \boldsymbol{p}^*(4)\rvert$ (%)	29.90	27.72	0.26	63.93	22.44	39.88	16.00
MAD($\mathfrak{p}(4)$) (%)	8.90	6.67	8.17	10.22	5.58	10.76	4.46
var($\mathfrak{p}(4)$) (%)	1.00	0.93	1.19	1.78	0.61	1.85	0.29
$\boldsymbol{p}^*(9) = 0.9$							
θ	0	$\frac{1}{6}$	$\frac{1}{3}$	$\frac{1}{2}$	$\frac{2}{3}$	$\frac{5}{6}$	1
κ_a	1.60	1.50	1.70	1.50	1.40	1.70	1.50
$\lvert\bar{\mathfrak{p}}(4) - \boldsymbol{p}^*(4)\rvert$ (%)	20.12	6.75	5.47	29.29	16.55	10.39	21.87
MAD($\mathfrak{p}(4)$) (%)	0.82	0.40	1.21	1.24	0.74	2.01	1.36
var($\mathfrak{p}(4)$) (%)	0.05	0.02	0.06	0.11	0.03	0.09	0.06

Table E.7.: Statistics of $\boldsymbol{p}(5:7)$ using the standard algorithm for the 9 parameter case with 1000 drawn samples for varying height of the lower muscle $\boldsymbol{p}^*(9)$ and thickness of the surrounding tissue layer θ in the settings from Section 6.3.5 with $\boldsymbol{p}^*(4) = 0$

$\boldsymbol{p}^*(9)$	θ	$\lvert\bar{\mathfrak{p}}(5:7) - \boldsymbol{p}^*(5:7)\rvert$ (%)			MAD($\mathfrak{p}(5:7)$) (%)			var($\mathfrak{p}(5:7)$) (%)		
0.10	0	63.73	49.55	92.45	16.63	17.56	14.60	4.09	4.51	2.85
0.10	$\frac{1}{6}$	148.82	75.16	46.10	9.50	9.87	14.94	3.00	1.48	2.48
0.10	$\frac{1}{3}$	157.34	68.39	36.52	22.86	12.50	10.18	7.28	2.36	1.46
0.10	$\frac{1}{2}$	175.17	113.90	22.93	29.35	7.01	18.02	11.20	0.93	4.18
0.10	$\frac{2}{3}$	113.03	97.72	32.35	10.90	16.59	10.57	1.49	3.57	1.99
0.10	$\frac{5}{6}$	152.70	36.44	53.85	28.83	11.22	28.64	9.46	2.45	9.47
0.10	1	172.84	83.04	3.40	16.16	7.20	10.68	4.78	0.88	2.14
0.30	0	132.45	105.72	120.65	4.78	7.14	25.85	0.86	1.13	8.98
0.30	$\frac{1}{6}$	76.98	225.98	66.79	10.78	20.76	9.61	1.57	9.88	2.00
0.30	$\frac{1}{3}$	66.18	132.90	109.62	5.49	8.86	7.57	1.39	2.07	1.24
0.30	$\frac{1}{2}$	194.26	160.18	22.21	6.93	4.04	3.26	2.27	0.52	1.01
0.30	$\frac{2}{3}$	172.49	169.56	68.82	10.68	11.18	8.46	2.27	1.98	1.15
0.30	$\frac{5}{6}$	219.79	126.04	34.56	12.50	21.21	11.03	4.54	6.87	2.19
0.30	1	213.34	163.74	22.58	10.56	9.15	11.08	3.79	1.56	3.96
0.50	0	218.65	205.96	70.27	27.33	8.40	10.95	15.10	3.31	1.88
0.50	$\frac{1}{6}$	84.94	142.15	94.84	3.11	8.86	0.69	0.21	1.16	0.03
0.50	$\frac{1}{3}$	102.91	170.47	5.24	7.97	3.38	17.16	0.78	0.76	5.37
0.50	$\frac{1}{2}$	99.09	168.76	19.84	2.61	2.87	3.45	0.37	0.85	0.74
0.50	$\frac{2}{3}$	62.73	130.47	99.59	13.68	6.82	11.38	3.25	0.72	2.28
0.50	$\frac{5}{6}$	59.15	132.50	81.84	7.99	16.48	5.71	0.95	3.29	0.75
0.50	1	90.08	103.43	82.00	1.39	1.21	1.63	0.11	0.12	0.17
0.70	0	134.75	200.93	147.69	24.76	30.01	28.60	7.20	10.20	11.00
0.70	$\frac{1}{6}$	121.37	119.01	122.32	3.99	1.87	5.48	0.59	0.12	0.66
0.70	$\frac{1}{3}$	81.28	167.53	137.10	4.83	8.84	4.43	0.47	1.39	0.93
0.70	$\frac{1}{2}$	132.72	103.16	113.91	3.00	4.76	6.38	0.28	0.41	0.70
0.70	$\frac{2}{3}$	125.82	153.01	127.21	22.76	15.27	14.89	5.81	3.20	3.10
0.70	$\frac{5}{6}$	140.68	237.18	90.72	14.28	8.83	11.54	2.43	3.43	1.83
0.70	1	153.43	253.48	74.24	11.75	7.24	6.62	1.79	3.74	0.84
0.90	0	47.49	155.64	50.30	3.12	2.99	1.22	0.69	0.61	0.22
0.90	$\frac{1}{6}$	83.40	159.89	78.11	9.99	6.24	6.14	1.09	0.85	0.48
0.90	$\frac{1}{3}$	47.49	155.64	50.30	3.12	2.99	1.22	0.69	0.61	0.22
0.90	$\frac{1}{2}$	45.98	158.79	109.92	12.30	8.61	11.36	2.52	1.52	3.32
0.90	$\frac{2}{3}$	59.42	163.18	76.08	4.69	3.87	13.35	0.75	0.77	2.05
0.90	$\frac{5}{6}$	98.20	65.61	90.56	6.36	21.56	17.51	0.88	8.79	6.58
0.90	1	96.97	115.36	42.75	8.05	7.04	7.11	1.09	1.05	1.28

Table E.8.: Statistics of $\boldsymbol{p}(5:7)$ using the standard algorithm for the 9 parameter case with 1000 drawn samples for varying height of the lower muscle $\boldsymbol{p}^*(9)$ and thickness of the surrounding tissue layer θ in the settings from Section 6.3.5 with $\boldsymbol{p}^*(4) = \frac{\pi}{4}$

$\boldsymbol{p}^*(9)$	θ	$\lvert\bar{\mathfrak{p}}(5:7) - \boldsymbol{p}^*(5:7)\rvert$ (%)			MAD($\mathfrak{p}(5:7)$) (%)			var($\mathfrak{p}(5:7)$) (%)		
0.10	0	115.86	29.28	62.18	15.26	9.65	8.42	5.28	2.47	1.28
0.10	$\frac{1}{6}$	185.17	20.14	105.83	35.32	39.10	42.63	15.39	20.25	22.60
0.10	$\frac{1}{3}$	112.52	50.20	44.21	12.89	35.80	31.98	2.87	15.78	14.62
0.10	$\frac{1}{2}$	165.34	42.42	62.00	16.68	15.49	11.45	3.98	3.52	1.99
0.10	$\frac{2}{3}$	172.24	24.99	94.35	32.22	13.79	46.58	13.11	3.67	25.83
0.10	$\frac{5}{6}$	230.26	55.35	48.18	36.33	31.62	13.40	24.77	16.68	2.64
0.10	1	142.91	122.92	94.75	12.56	6.33	31.58	2.83	0.98	12.34
0.30	0	71.24	186.15	79.65	32.55	13.43	15.67	15.94	3.02	4.02
0.30	$\frac{1}{6}$	153.07	116.97	143.88	16.44	14.83	43.86	3.60	3.07	23.29
0.30	$\frac{1}{3}$	160.14	161.44	94.04	10.85	8.32	9.82	2.93	2.01	1.79
0.30	$\frac{1}{2}$	204.40	257.52	36.78	8.98	20.61	13.22	3.01	8.83	2.34
0.30	$\frac{2}{3}$	232.27	109.18	128.34	19.59	18.63	17.28	7.91	6.06	7.27
0.30	$\frac{5}{6}$	180.21	180.83	45.97	18.27	8.24	6.45	5.49	1.41	0.88
0.30	1	175.40	99.33	47.73	10.31	28.74	27.45	2.93	12.78	12.06
0.50	0	71.37	163.35	167.59	34.36	15.56	46.14	13.24	2.94	23.25
0.50	$\frac{1}{6}$	149.26	154.35	89.82	21.54	16.17	8.88	5.95	3.40	1.10
0.50	$\frac{1}{3}$	148.31	285.46	53.00	15.76	13.60	9.33	3.33	7.50	2.20
0.50	$\frac{1}{2}$	163.05	243.38	65.60	7.36	7.99	4.36	1.92	3.89	0.73
0.50	$\frac{2}{3}$	100.52	132.59	96.48	6.33	11.39	4.24	0.78	1.89	0.49
0.50	$\frac{5}{6}$	119.65	122.38	105.77	8.53	8.72	20.45	1.28	1.04	5.17
0.50	1	153.95	163.31	130.02	33.11	9.69	14.90	13.24	2.24	3.55
0.70	0	86.78	106.72	120.23	21.64	17.58	11.45	5.69	4.06	2.17
0.70	$\frac{1}{6}$	162.38	136.61	140.09	32.24	13.55	3.65	13.19	4.03	0.50
0.70	$\frac{1}{3}$	86.30	109.30	124.86	8.07	11.80	4.97	2.04	3.02	0.72
0.70	$\frac{1}{2}$	133.53	91.24	137.24	12.32	14.42	14.81	2.15	3.65	4.27
0.70	$\frac{2}{3}$	165.67	113.08	181.21	10.56	8.83	18.67	1.86	1.29	7.63
0.70	$\frac{5}{6}$	184.17	240.87	90.34	6.31	18.04	5.58	1.22	5.61	0.74
0.70	1	65.76	269.79	103.38	16.09	17.76	18.89	3.62	6.62	4.70
0.90	0	70.85	178.69	103.63	7.41	3.68	5.14	0.81	1.16	1.00
0.90	$\frac{1}{6}$	74.16	140.11	121.40	7.69	11.33	11.31	2.26	2.36	3.77
0.90	$\frac{1}{3}$	93.77	164.67	68.15	4.08	23.00	5.68	0.57	6.95	1.02
0.90	$\frac{1}{2}$	75.59	191.74	60.98	1.27	4.85	1.10	0.17	1.70	0.22
0.90	$\frac{2}{3}$	40.82	171.32	108.47	15.97	23.11	10.42	3.95	7.72	3.76
0.90	$\frac{5}{6}$	114.44	167.77	181.80	11.13	15.40	28.00	3.55	3.46	16.63
0.90	1	98.12	117.06	27.36	8.50	6.39	13.18	1.22	0.93	2.25

Table E.9.: Statistics of $\boldsymbol{p}(5:7)$ using the standard algorithm for the 9 parameter case with 1000 drawn samples for varying height of the lower muscle $\boldsymbol{p}^*(9)$ and thickness of the surrounding tissue layer θ in the settings from Section 6.3.5 with $\boldsymbol{p}^*(4) = \frac{3\pi}{4}$

$\boldsymbol{p}^*(9)$	θ	$\lvert\bar{\mathfrak{p}}(5:7) - \boldsymbol{p}^*(5:7)\rvert$ (%)			MAD($\mathfrak{p}(5:7)$) (%)			var($\mathfrak{p}(5:7)$) (%)		
0.10	0	235.36	103.69	137.24	34.50	13.13	53.37	16.97	2.86	35.93
0.10	$\frac{1}{6}$	200.46	7.77	129.83	36.24	47.76	70.36	18.00	28.58	60.19
0.10	$\frac{1}{3}$	174.35	116.81	12.59	55.48	23.57	17.63	33.90	7.75	4.01
0.10	$\frac{1}{2}$	118.57	133.41	132.71	40.69	19.45	55.81	20.95	5.54	45.87
0.10	$\frac{2}{3}$	134.01	29.74	116.03	31.83	22.31	48.92	14.03	6.67	33.53
0.10	$\frac{5}{6}$	149.12	47.26	27.90	45.58	17.51	13.40	23.26	4.18	2.83
0.10	1	125.98	34.85	15.60	14.73	36.34	12.14	3.54	18.01	2.74
0.30	0	213.48	212.42	128.05	28.86	13.10	23.68	12.63	3.90	9.07
0.30	$\frac{1}{6}$	196.45	208.43	202.96	37.58	24.51	39.48	19.62	8.75	23.01
0.30	$\frac{1}{3}$	127.91	171.34	130.10	13.70	12.48	16.13	2.55	2.81	3.89
0.30	$\frac{1}{2}$	17.04	111.80	111.43	38.30	18.13	12.06	20.86	4.01	2.69
0.30	$\frac{2}{3}$	257.75	107.00	153.64	28.87	21.16	36.89	14.69	8.65	21.47
0.30	$\frac{5}{6}$	206.51	85.67	92.88	7.38	28.72	21.46	3.28	14.46	8.87
0.30	1	209.06	130.27	79.71	16.67	12.87	17.28	5.76	4.25	5.61
0.50	0	173.21	199.08	145.98	22.98	33.84	37.23	8.80	13.80	16.75
0.50	$\frac{1}{6}$	116.26	79.14	133.92	9.49	24.70	9.35	1.82	10.90	1.39
0.50	$\frac{1}{3}$	112.95	157.06	77.36	1.06	1.23	1.49	0.13	0.19	0.32
0.50	$\frac{1}{2}$	115.47	186.85	26.71	11.00	11.63	9.24	2.14	2.13	1.75
0.50	$\frac{2}{3}$	26.59	115.11	83.43	15.20	4.79	15.51	3.08	0.49	2.79
0.50	$\frac{5}{6}$	201.91	139.09	44.89	19.44	13.25	3.73	7.88	2.40	0.58
0.50	1	81.22	207.57	74.59	11.27	36.99	6.75	1.41	16.34	0.95
0.70	0	87.40	267.53	147.65	22.89	29.05	11.31	7.60	13.46	3.18
0.70	$\frac{1}{6}$	180.71	165.95	130.58	31.42	18.44	8.25	18.55	4.97	1.69
0.70	$\frac{1}{3}$	81.58	37.75	194.67	7.74	29.02	11.37	1.59	16.05	3.84
0.70	$\frac{1}{2}$	96.88	96.79	91.64	6.17	12.32	7.81	0.72	2.49	0.96
0.70	$\frac{2}{3}$	173.42	196.81	135.28	15.99	43.13	16.65	3.64	22.91	3.80
0.70	$\frac{5}{6}$	173.98	213.54	154.57	20.12	11.40	13.60	4.87	2.52	2.88
0.70	1	157.67	228.85	61.21	12.12	5.90	7.11	2.06	2.23	0.98
0.90	0	68.74	161.87	118.66	1.44	2.39	5.12	0.32	0.72	1.44
0.90	$\frac{1}{6}$	30.93	195.04	80.96	4.81	4.72	1.55	1.48	1.82	0.24
0.90	$\frac{1}{3}$	136.02	171.33	61.98	9.15	8.76	9.10	1.64	2.01	0.99
0.90	$\frac{1}{2}$	86.77	145.14	93.71	1.22	1.41	3.76	0.17	0.38	0.85
0.90	$\frac{2}{3}$	85.03	130.55	17.35	11.53	4.08	5.10	1.53	0.43	1.35
0.90	$\frac{5}{6}$	104.43	94.97	49.65	9.48	12.59	7.81	1.58	3.11	1.46
0.90	1	73.97	173.84	68.82	5.73	6.76	4.05	0.73	1.31	0.52

Table E.10.: Statistics of $\boldsymbol{p}(8)$ using the standard algorithm for the 9 parameter case with 1000 drawn samples for varying height of the lower muscle $\boldsymbol{p}^*(9)$ and thickness of the surrounding tissue layer θ in the settings from Section 6.3.5 with $\boldsymbol{p}^*(4) = 0$

$\boldsymbol{p}^*(9) = 0.1$							
θ	0	$\frac{1}{6}$	$\frac{1}{3}$	$\frac{1}{2}$	$\frac{2}{3}$	$\frac{5}{6}$	1
κ_a	1.40	1.80	1.90	2.40	1.70	2.00	1.50
$\lvert\bar{\mathfrak{p}}(8) - \boldsymbol{p}^*(8)\rvert$ (%)	0.51	1.34	1.94	2.36	1.74	1.64	2.03
MAD($\mathfrak{p}(8)$) (%)	0.49	1.07	1.18	0.85	1.10	0.78	1.16
var($\mathfrak{p}(8)$) (%)	0.01	0.02	0.02	0.02	0.03	0.02	0.02
$\boldsymbol{p}^*(9) = 0.3$							
θ	0	$\frac{1}{6}$	$\frac{1}{3}$	$\frac{1}{2}$	$\frac{2}{3}$	$\frac{5}{6}$	1
κ_a	1.50	1.60	1.40	1.20	1.30	1.40	1.30
$\lvert\bar{\mathfrak{p}}(8) - \boldsymbol{p}^*(8)\rvert$ (%)	0.71	2.06	4.87	6.03	4.96	5.80	7.43
MAD($\mathfrak{p}(8)$) (%)	0.62	1.40	1.11	1.27	1.88	3.86	4.45
var($\mathfrak{p}(8)$) (%)	0.02	0.05	0.04	0.06	0.10	0.34	0.34
$\boldsymbol{p}^*(9) = 0.5$							
θ	0	$\frac{1}{6}$	$\frac{1}{3}$	$\frac{1}{2}$	$\frac{2}{3}$	$\frac{5}{6}$	1
κ_a	2.40	0.40	1.00	1.50	1.40	1.10	0.90
$\lvert\bar{\mathfrak{p}}(8) - \boldsymbol{p}^*(8)\rvert$ (%)	2.22	5.03	9.61	8.86	4.42	13.51	22.90
MAD($\mathfrak{p}(8)$) (%)	1.89	1.07	4.62	0.39	4.80	2.32	0.81
var($\mathfrak{p}(8)$) (%)	0.18	0.02	0.23	0.02	0.45	0.08	0.04
$\boldsymbol{p}^*(9) = 0.7$							
θ	0	$\frac{1}{6}$	$\frac{1}{3}$	$\frac{1}{2}$	$\frac{2}{3}$	$\frac{5}{6}$	1
κ_a	2.20	1.00	1.00	0.50	0.80	1.90	1.80
$\lvert\bar{\mathfrak{p}}(8) - \boldsymbol{p}^*(8)\rvert$ (%)	2.00	0.70	1.88	6.46	14.45	34.74	30.64
MAD($\mathfrak{p}(8)$) (%)	1.35	0.82	1.82	2.47	2.74	3.39	0.65
var($\mathfrak{p}(8)$) (%)	0.08	0.02	0.07	0.10	0.13	0.25	0.02
$\boldsymbol{p}^*(9) = 0.9$							
θ	0	$\frac{1}{6}$	$\frac{1}{3}$	$\frac{1}{2}$	$\frac{2}{3}$	$\frac{5}{6}$	1
κ_a	1.10	1.20	1.10	2.60	1.40	1.90	1.40
$\lvert\bar{\mathfrak{p}}(8) - \boldsymbol{p}^*(8)\rvert$ (%)	22.50	31.13	22.50	11.70	22.37	24.05	37.00
MAD($\mathfrak{p}(8)$) (%)	0.34	4.12	0.34	9.19	5.06	3.76	1.17
var($\mathfrak{p}(8)$) (%)	0.03	0.22	0.03	1.37	0.30	0.36	0.14

Table E.11.: Statistics of $\boldsymbol{p}(8)$ using the standard algorithm for the 9 parameter case with 1000 drawn samples for varying height of the lower muscle $\boldsymbol{p}^*(9)$ and thickness of the surrounding tissue layer θ in the settings from Section 6.3.5 with $\boldsymbol{p}^*(4) = \frac{\pi}{4}$

$\boldsymbol{p}^*(9) = 0.1$							
θ	0	$\frac{1}{6}$	$\frac{1}{3}$	$\frac{1}{2}$	$\frac{2}{3}$	$\frac{5}{6}$	1
κ_a	2.10	2.50	2.50	2.70	3.10	3.20	2.40
$\lvert\bar{\mathfrak{p}}(8) - \boldsymbol{p}^*(8)\rvert$ (%)	0.60	1.08	1.12	1.59	1.43	1.42	1.27
MAD($\mathfrak{p}(8)$) (%)	0.59	0.95	0.97	0.93	0.92	1.59	1.64
var($\mathfrak{p}(8)$) (%)	0.01	0.02	0.02	0.02	0.02	0.09	0.10
$\boldsymbol{p}^*(9) = 0.3$							
θ	0	$\frac{1}{6}$	$\frac{1}{3}$	$\frac{1}{2}$	$\frac{2}{3}$	$\frac{5}{6}$	1
κ_a	1.80	2.30	1.70	1.90	2.20	1.50	1.60
$\lvert\bar{\mathfrak{p}}(8) - \boldsymbol{p}^*(8)\rvert$ (%)	1.48	2.17	2.54	3.42	3.40	4.95	3.65
MAD($\mathfrak{p}(8)$) (%)	0.82	0.74	0.93	1.09	2.38	3.61	4.93
var($\mathfrak{p}(8)$) (%)	0.02	0.02	0.03	0.06	0.13	0.28	0.48
$\boldsymbol{p}^*(9) = 0.5$							
θ	0	$\frac{1}{6}$	$\frac{1}{3}$	$\frac{1}{2}$	$\frac{2}{3}$	$\frac{5}{6}$	1
κ_a	2.30	1.70	1.90	1.60	1.50	1.50	1.50
$\lvert\bar{\mathfrak{p}}(8) - \boldsymbol{p}^*(8)\rvert$ (%)	1.49	2.63	4.13	13.01	1.79	2.48	4.75
MAD($\mathfrak{p}(8)$) (%)	0.88	2.32	3.75	1.19	1.04	0.97	4.67
var($\mathfrak{p}(8)$) (%)	0.06	0.09	0.22	0.03	0.04	0.06	0.29
$\boldsymbol{p}^*(9) = 0.7$							
θ	0	$\frac{1}{6}$	$\frac{1}{3}$	$\frac{1}{2}$	$\frac{2}{3}$	$\frac{5}{6}$	1
κ_a	2.30	2.00	2.10	1.70	1.60	1.60	2.10
$\lvert\bar{\mathfrak{p}}(8) - \boldsymbol{p}^*(8)\rvert$ (%)	1.35	2.38	6.33	4.59	9.09	33.05	38.86
MAD($\mathfrak{p}(8)$) (%)	1.05	1.12	2.28	1.71	2.62	4.53	2.62
var($\mathfrak{p}(8)$) (%)	0.07	0.04	0.14	0.06	0.13	0.32	0.13
$\boldsymbol{p}^*(9) = 0.9$							
θ	0	$\frac{1}{6}$	$\frac{1}{3}$	$\frac{1}{2}$	$\frac{2}{3}$	$\frac{5}{6}$	1
κ_a	1.60	2.30	2.40	1.40	2.40	2.10	1.50
$\lvert\bar{\mathfrak{p}}(8) - \boldsymbol{p}^*(8)\rvert$ (%)	4.90	4.51	5.41	27.83	8.46	10.41	32.11
MAD($\mathfrak{p}(8)$) (%)	2.26	3.83	2.99	0.56	7.31	7.62	5.17
var($\mathfrak{p}(8)$) (%)	0.12	0.32	0.20	0.05	0.93	1.01	0.34

Table E.12.: Statistics of $\boldsymbol{p}(8)$ using the standard algorithm for the 9 parameter case with 1000 drawn samples for varying height of the lower muscle $\boldsymbol{p}^*(9)$ and thickness of the surrounding tissue layer θ in the settings from Section 6.3.5 with $\boldsymbol{p}^*(4) = \frac{3\pi}{4}$

$\boldsymbol{p}^*(9) = 0.1$							
θ	0	$\frac{1}{6}$	$\frac{1}{3}$	$\frac{1}{2}$	$\frac{2}{3}$	$\frac{5}{6}$	1
κ_a	2.80	3.60	3.00	3.10	3.40	2.90	2.70
$\lvert\bar{\mathfrak{p}}(8) - \boldsymbol{p}^*(8)\rvert$ (%)	0.72	1.41	2.58	2.09	1.93	2.13	3.93
MAD($\mathfrak{p}(8)$) (%)	0.68	0.78	1.31	1.26	1.21	1.16	3.82
var($\mathfrak{p}(8)$) (%)	0.01	0.02	0.09	0.07	0.07	0.06	0.26
$\boldsymbol{p}^*(9) = 0.3$							
θ	0	$\frac{1}{6}$	$\frac{1}{3}$	$\frac{1}{2}$	$\frac{2}{3}$	$\frac{5}{6}$	1
κ_a	2.30	2.20	1.80	1.90	2.50	1.80	1.60
$\lvert\bar{\mathfrak{p}}(8) - \boldsymbol{p}^*(8)\rvert$ (%)	0.81	2.24	2.40	5.69	5.71	3.69	4.26
MAD($\mathfrak{p}(8)$) (%)	0.90	1.56	1.52	6.71	6.05	4.68	4.22
var($\mathfrak{p}(8)$) (%)	0.02	0.08	0.08	0.69	0.57	0.43	0.39
$\boldsymbol{p}^*(9) = 0.5$							
θ	0	$\frac{1}{6}$	$\frac{1}{3}$	$\frac{1}{2}$	$\frac{2}{3}$	$\frac{5}{6}$	1
κ_a	3.10	1.80	0.50	1.80	1.50	1.70	2.00
$\lvert\bar{\mathfrak{p}}(8) - \boldsymbol{p}^*(8)\rvert$ (%)	1.71	6.22	15.23	8.37	1.79	2.78	4.75
MAD($\mathfrak{p}(8)$) (%)	1.38	0.84	0.12	2.11	1.36	1.38	4.25
var($\mathfrak{p}(8)$) (%)	0.10	0.04	0.01	0.07	0.06	0.10	0.28
$\boldsymbol{p}^*(9) = 0.7$							
θ	0	$\frac{1}{6}$	$\frac{1}{3}$	$\frac{1}{2}$	$\frac{2}{3}$	$\frac{5}{6}$	1
κ_a	2.80	2.30	2.80	1.50	2.20	2.10	1.70
$\lvert\bar{\mathfrak{p}}(8) - \boldsymbol{p}^*(8)\rvert$ (%)	2.50	3.26	7.67	16.02	9.35	48.80	41.70
MAD($\mathfrak{p}(8)$) (%)	1.29	2.44	4.24	2.45	3.62	5.41	1.38
var($\mathfrak{p}(8)$) (%)	0.11	0.17	0.48	0.11	0.19	0.60	0.11
$\boldsymbol{p}^*(9) = 0.9$							
θ	0	$\frac{1}{6}$	$\frac{1}{3}$	$\frac{1}{2}$	$\frac{2}{3}$	$\frac{5}{6}$	1
κ_a	1.60	1.50	1.70	1.50	1.40	1.70	1.50
$\lvert\bar{\mathfrak{p}}(8) - \boldsymbol{p}^*(8)\rvert$ (%)	26.47	7.91	10.38	39.08	37.15	33.31	31.77
MAD($\mathfrak{p}(8)$) (%)	0.83	0.90	5.77	1.39	4.59	1.67	2.83
var($\mathfrak{p}(8)$) (%)	0.05	0.06	0.37	0.15	0.30	0.14	0.22

Table E.13.: Statistics of $\boldsymbol{p}(9)$ using the standard algorithm for the 9 parameter case with 1000 drawn samples for varying height of the lower muscle $\boldsymbol{p}^*(9)$ and thickness of the surrounding tissue layer θ in the settings from Section 6.3.5 with $\boldsymbol{p}^*(4) = 0$

$\boldsymbol{p}^*(9) = 0.1$							
θ	0	$\frac{1}{6}$	$\frac{1}{3}$	$\frac{1}{2}$	$\frac{2}{3}$	$\frac{5}{6}$	1
κ_a	1.40	1.80	1.90	2.40	1.70	2.00	1.50
$\lvert\bar{\mathfrak{p}}(9) - \boldsymbol{p}^*(9)\rvert$ (%)	11.41	3.00	3.78	4.46	2.90	2.93	2.68
MAD($\mathfrak{p}(9)$) (%)	3.65	1.72	2.39	1.39	1.77	1.58	1.67
var($\mathfrak{p}(9)$) (%)	0.18	0.05	0.07	0.03	0.05	0.06	0.05
$\boldsymbol{p}^*(9) = 0.3$							
θ	0	$\frac{1}{6}$	$\frac{1}{3}$	$\frac{1}{2}$	$\frac{2}{3}$	$\frac{5}{6}$	1
κ_a	1.50	1.60	1.40	1.20	1.30	1.40	1.30
$\lvert\bar{\mathfrak{p}}(9) - \boldsymbol{p}^*(9)\rvert$ (%)	3.72	1.86	12.80	13.50	10.47	0.69	9.16
MAD($\mathfrak{p}(9)$) (%)	3.75	4.83	4.73	3.52	4.88	1.05	3.01
var($\mathfrak{p}(9)$) (%)	0.25	0.41	0.47	0.27	0.31	0.03	0.18
$\boldsymbol{p}^*(9) = 0.5$							
θ	0	$\frac{1}{6}$	$\frac{1}{3}$	$\frac{1}{2}$	$\frac{2}{3}$	$\frac{5}{6}$	1
κ_a	2.40	0.40	1.00	1.50	1.40	1.10	0.90
$\lvert\bar{\mathfrak{p}}(9) - \boldsymbol{p}^*(9)\rvert$ (%)	12.17	20.65	21.40	19.25	12.60	14.42	33.18
MAD($\mathfrak{p}(9)$) (%)	4.46	1.98	0.97	1.58	4.26	3.90	2.02
var($\mathfrak{p}(9)$) (%)	0.38	0.11	0.07	0.10	0.40	0.25	0.26
$\boldsymbol{p}^*(9) = 0.7$							
θ	0	$\frac{1}{6}$	$\frac{1}{3}$	$\frac{1}{2}$	$\frac{2}{3}$	$\frac{5}{6}$	1
κ_a	2.20	1.00	1.00	0.50	0.80	1.90	1.80
$\lvert\bar{\mathfrak{p}}(9) - \boldsymbol{p}^*(9)\rvert$ (%)	0.16	16.97	18.93	19.43	19.40	19.33	19.20
MAD($\mathfrak{p}(9)$) (%)	5.79	1.40	0.65	0.62	0.34	0.36	0.47
var($\mathfrak{p}(9)$) (%)	0.40	0.05	0.03	0.01	0.01	0.02	0.02
$\boldsymbol{p}^*(9) = 0.9$							
θ	0	$\frac{1}{6}$	$\frac{1}{3}$	$\frac{1}{2}$	$\frac{2}{3}$	$\frac{5}{6}$	1
κ_a	1.10	1.20	1.10	2.60	1.40	1.90	1.40
$\lvert\bar{\mathfrak{p}}(9) - \boldsymbol{p}^*(9)\rvert$ (%)	32.53	32.21	32.53	21.14	39.64	27.14	37.66
MAD($\mathfrak{p}(9)$) (%)	1.04	2.82	1.04	3.00	1.55	1.76	2.34
var($\mathfrak{p}(9)$) (%)	0.11	0.16	0.11	0.19	0.18	0.16	0.19

Table E.14.: Statistics of $\boldsymbol{p}(9)$ using the standard algorithm for the 9 parameter case with 1000 drawn samples for varying height of the lower muscle $\boldsymbol{p}^*(9)$ and thickness of the surrounding tissue layer θ in the settings from Section 6.3.5 with $\boldsymbol{p}^*(4) = \frac{\pi}{4}$

$\boldsymbol{p}^*(9) = 0.1$							
θ	0	$\frac{1}{6}$	$\frac{1}{3}$	$\frac{1}{2}$	$\frac{2}{3}$	$\frac{5}{6}$	1
κ_a	2.10	2.50	2.50	2.70	3.10	3.20	2.40
$\lvert\bar{\mathfrak{p}}(9) - \boldsymbol{p}^*(9)\rvert$ (%)	8.89	6.68	5.64	5.44	4.15	6.51	4.88
MAD($\mathfrak{p}(9)$) (%)	3.68	2.45	4.04	1.96	3.21	4.62	1.38
var($\mathfrak{p}(9)$) (%)	0.19	0.12	0.20	0.06	0.12	0.28	0.03
$\boldsymbol{p}^*(9) = 0.3$							
θ	0	$\frac{1}{6}$	$\frac{1}{3}$	$\frac{1}{2}$	$\frac{2}{3}$	$\frac{5}{6}$	1
κ_a	1.80	2.30	1.70	1.90	2.20	1.50	1.60
$\lvert\bar{\mathfrak{p}}(9) - \boldsymbol{p}^*(9)\rvert$ (%)	5.96	11.35	14.60	0.39	0.83	4.27	10.83
MAD($\mathfrak{p}(9)$) (%)	6.99	10.74	6.56	3.28	2.61	4.33	3.84
var($\mathfrak{p}(9)$) (%)	0.69	1.37	0.70	0.13	0.15	0.30	0.26
$\boldsymbol{p}^*(9) = 0.5$							
θ	0	$\frac{1}{6}$	$\frac{1}{3}$	$\frac{1}{2}$	$\frac{2}{3}$	$\frac{5}{6}$	1
κ_a	2.30	1.70	1.90	1.60	1.50	1.50	1.50
$\lvert\bar{\mathfrak{p}}(9) - \boldsymbol{p}^*(9)\rvert$ (%)	11.11	22.29	21.57	22.73	28.95	14.53	28.15
MAD($\mathfrak{p}(9)$) (%)	10.17	0.92	1.58	1.45	3.36	3.35	10.07
var($\mathfrak{p}(9)$) (%)	1.24	0.04	0.09	0.09	0.26	0.17	1.24
$\boldsymbol{p}^*(9) = 0.7$							
θ	0	$\frac{1}{6}$	$\frac{1}{3}$	$\frac{1}{2}$	$\frac{2}{3}$	$\frac{5}{6}$	1
κ_a	2.30	2.00	2.10	1.70	1.60	1.60	2.10
$\lvert\bar{\mathfrak{p}}(9) - \boldsymbol{p}^*(9)\rvert$ (%)	11.33	5.56	18.24	19.14	18.23	18.78	19.39
MAD($\mathfrak{p}(9)$) (%)	6.86	6.73	1.34	0.74	2.67	0.71	0.51
var($\mathfrak{p}(9)$) (%)	0.63	0.64	0.06	0.04	0.18	0.03	0.02
$\boldsymbol{p}^*(9) = 0.9$							
θ	0	$\frac{1}{6}$	$\frac{1}{3}$	$\frac{1}{2}$	$\frac{2}{3}$	$\frac{5}{6}$	1
κ_a	1.60	2.30	2.40	1.40	2.40	2.10	1.50
$\lvert\bar{\mathfrak{p}}(9) - \boldsymbol{p}^*(9)\rvert$ (%)	27.44	14.45	16.35	42.65	17.99	20.75	38.26
MAD($\mathfrak{p}(9)$) (%)	1.57	3.23	3.06	1.59	6.08	3.48	2.58
var($\mathfrak{p}(9)$) (%)	0.09	0.16	0.20	0.22	0.74	0.35	0.21

Table E.15.: Statistics of $\boldsymbol{p}(9)$ using the standard algorithm for the 9 parameter case with 1000 drawn samples for varying height of the lower muscle $\boldsymbol{p}^*(9)$ and thickness of the surrounding tissue layer θ in the settings from Section 6.3.5 with $\boldsymbol{p}^*(4) = \frac{3\pi}{4}$

$\boldsymbol{p}^*(9) = 0.1$							
θ	0	$\frac{1}{6}$	$\frac{1}{3}$	$\frac{1}{2}$	$\frac{2}{3}$	$\frac{5}{6}$	1
κ_a	2.80	3.60	3.00	3.10	3.40	2.90	2.70
$\lvert\bar{\mathfrak{p}}(9) - \boldsymbol{p}^*(9)\rvert$ (%)	8.02	8.51	5.17	4.53	4.57	6.15	7.66
MAD($\mathfrak{p}(9)$) (%)	3.22	3.54	4.43	3.31	2.82	3.07	2.30
var($\mathfrak{p}(9)$) (%)	0.12	0.16	0.24	0.16	0.11	0.13	0.07
$\boldsymbol{p}^*(9) = 0.3$							
θ	0	$\frac{1}{6}$	$\frac{1}{3}$	$\frac{1}{2}$	$\frac{2}{3}$	$\frac{5}{6}$	1
κ_a	2.30	2.20	1.80	1.90	2.50	1.80	1.60
$\lvert\bar{\mathfrak{p}}(9) - \boldsymbol{p}^*(9)\rvert$ (%)	4.51	5.49	4.53	12.63	4.70	9.13	0.85
MAD($\mathfrak{p}(9)$) (%)	5.19	3.83	5.12	9.24	5.00	5.09	3.20
var($\mathfrak{p}(9)$) (%)	0.44	0.25	0.31	1.21	0.37	0.40	0.15
$\boldsymbol{p}^*(9) = 0.5$							
θ	0	$\frac{1}{6}$	$\frac{1}{3}$	$\frac{1}{2}$	$\frac{2}{3}$	$\frac{5}{6}$	1
κ_a	3.10	1.80	0.50	1.80	1.50	1.70	2.00
$\lvert\bar{\mathfrak{p}}(9) - \boldsymbol{p}^*(9)\rvert$ (%)	10.62	20.88	2.65	22.63	33.26	30.92	31.76
MAD($\mathfrak{p}(9)$) (%)	3.39	0.77	0.51	1.38	2.23	5.60	3.94
var($\mathfrak{p}(9)$) (%)	0.39	0.04	0.03	0.08	0.24	0.51	0.32
$\boldsymbol{p}^*(9) = 0.7$							
θ	0	$\frac{1}{6}$	$\frac{1}{3}$	$\frac{1}{2}$	$\frac{2}{3}$	$\frac{5}{6}$	1
κ_a	2.80	2.30	2.80	1.50	2.20	2.10	1.70
$\lvert\bar{\mathfrak{p}}(9) - \boldsymbol{p}^*(9)\rvert$ (%)	21.87	29.37	17.63	18.49	18.48	19.20	19.12
MAD($\mathfrak{p}(9)$) (%)	3.76	8.40	2.79	1.89	1.79	0.69	0.58
var($\mathfrak{p}(9)$) (%)	0.35	1.20	0.16	0.11	0.12	0.01	0.02
$\boldsymbol{p}^*(9) = 0.9$							
θ	0	$\frac{1}{6}$	$\frac{1}{3}$	$\frac{1}{2}$	$\frac{2}{3}$	$\frac{5}{6}$	1
κ_a	1.60	1.50	1.70	1.50	1.40	1.70	1.50
$\lvert\bar{\mathfrak{p}}(9) - \boldsymbol{p}^*(9)\rvert$ (%)	25.36	21.15	27.81	41.99	35.61	34.63	26.02
MAD($\mathfrak{p}(9)$) (%)	1.11	0.53	3.36	1.85	3.02	1.55	1.36
var($\mathfrak{p}(9)$) (%)	0.08	0.04	0.18	0.23	0.22	0.14	0.12

Bibliography

[1] H. M. Adorf. "Hubble Space Telescope image restoration in its fourth year". In: *Inverse Problems* 11.4 (1995), pp. 639–653. DOI: 10.1088/0266-5611/11/4/003.

[2] C. D. Aliprantis and K. Border. *Infinite dimensional analysis. A Hitchhiker's Guide*. 3rd ed. Springer Berlin Heidelberg, 2006. DOI: 10.1007/978-3-662-03961-8.

[3] M. Bachmayr and R. Schneider. "Iterative Methods Based on Soft Thresholding of Hierarchical Tensors". In: *Foundations of Computational Mathematics* 17.4 (2017), pp. 1037–1083. DOI: 10.1007/s10208-016-9314-z.

[4] A. B. Bakushinsky, M. Y. Kokurin, and A. Smirnova. *Iterative methods for ill-posed problems: An introduction*. Inverse and ill-posed problems series 54. De Gruyter, 2011. DOI: 10.1515/9783110250657.

[5] T. Bayes and R. Price. "LII. An essay towards solving a problem in the doctrine of chances. By the late Rev. Mr. Bayes, F. R. S. communicated by Mr. Price, in a letter to John Canton, A. M. F. R. S". In: *Philosophical Transactions of the Royal Society of London* 53 (1763), pp. 370–418. DOI: 10.1098/rstl.1763.0053. eprint: https://royalsocietypublishing.org/doi/pdf/10.1098/rstl.1763.0053.

[6] L. Borcea. "Electrical impedance tomography". In: *Inverse Problems* 18.6 (2002), R99–R136. DOI: 10.1088/0266-5611/18/6/201.

[7] P. Brémaud. *Probability Theory and Stochastic Processes*. Springer International Publishing, 2020. DOI: 10.1007/978-3-030-40183-2.

[8] A. P. Calderón. "On an inverse boundary value problem". In: *Computational and Applied Mathematics* 25 (2006), pp. 133–138.

[9] J. D. Carroll and J.-J. Chang. "Analysis of individual differences in multidimensional scaling via an n-way generalization of "Eckart-Young" decomposition". In: *Psychometrika* 35.3 (1970), pp. 283–319. DOI: 10.1007/BF02310791.

[10] E. Chauvet, O. Fokapu, and D. Gamet. "Inverse problem in the surface EMG: a feasibility study". In: vol. 2. 2001, pp. 1048–1050. DOI: 10.1109/IEMBS.2001.1020368.

[11] P. Chen, U. Villa, and O. Ghattas. "Hessian-based adaptive sparse quadrature for infinite-dimensional Bayesian inverse problems". In: *Computer Methods in Applied Mechanics and Engineering* 327 (2017). Advances in Computational Mechanics and Scientific Computation—the Cutting Edge, pp. 147–172. DOI: https://doi.org/10.1016/j.cma.2017.08.016.

[12] P. R. Conrad, Y. M. Marzouk, N. S. Pillai, and A. Smith. "Accelerating Asymptotically Exact MCMC for Computationally Intensive Models via Local Approximations". In: *Journal of the American Statistical Association* 111.516 (2016), pp. 1591–1607. DOI: 10.1080/01621459.2015.1096787.

[13] S. L. Cotter, G. O. Roberts, A. M. Stuart, and D. White. "MCMC Methods for Functions: Modifying Old Algorithms to Make Them Faster". In: *Statistical Science* 28.3 (2013), pp. 424–446.

[14] T. Cui, G. Detommaso, and R. Scheichl. *Multilevel Dimension-Independent Likelihood-Informed MCMC for Large-Scale Inverse Problems*. 2019. arXiv: 1910.12431 [stat.CO].

[15] T. Cui, K. Law, and Y. Marzouk. "Dimension-independent likelihood-informed MCMC". In: *Journal of Computational Physics* 304 (2014). DOI: 10.1016/j.jcp.2015.10.008.

[16] W. Dahmen, R. DeVore, L. Grasedyck, and E. Süli. "Tensor-Sparsity of Solutions to High-Dimensional Elliptic Partial Differential Equations". In: *Foundations of Computational Mathematics* 16.4 (2016), pp. 813–874. DOI: 10.1007/s10208-015-9265-9.

[17] M. Dashti and A. M. Stuart. "The Bayesian Approach to Inverse Problems". In: *Handbook of Uncertainty Quantification*. Ed. by R. Ghanem, D. Higdon, and H. Owhadi. Cham: Springer International Publishing, 2017, pp. 311–428. DOI: 10.1007/978-3-319-12385-1_7.

[18] P. Diaconis. "The Markov Chain Monte Carlo Revolution". In: *Bulletin of the American Mathematical Society* 46 (2009), pp. 179–205. DOI: 10.1090/S0273-0979-08-01238-X.

[19] J. Dick, F. Y. Kuo, and I. H. Sloan. "High-dimensional integration: The quasi-Monte Carlo way". In: *Acta Numerica* 22 (2013), pp. 133–288. DOI: 10.1017/S0962492913000044.

[20] T. J. Dodwell, C. Ketelsen, R. Scheichl, and A. L. Teckentrup. "A Hierarchical Multilevel Markov Chain Monte Carlo Algorithm with Applications to Uncertainty Quantification in Subsurface Flow". In: *SIAM/ASA Journal of Uncertainty Quantification* 3.1 (2015), pp. 1075–1108. DOI: 10.1137/130915005.

[21] K. van den Doel, U. M. Ascher, and D. K. Pai. "Computed myography: three-dimensional reconstruction of motor functions from surface EMG data". In: *Inverse Problems* 24.6 (2008). DOI: 10.1088/0266-5611/24/6/065010.

[22] K. van den Doel, U. M. Ascher, and D. K. Pai. "Source localization in electromyography using the inverse potential problem". In: *Inverse Problems* 27.2 (2011), p. 025008. DOI: 10.1088/0266-5611/27/2/025008.

[23] S. Dolgov, K. Anaya-Izquierdo, C. Fox, and R. Scheichl. "Approximation and sampling of multivariate probability distributions in the tensor train decomposition". In: *Statistics and Computing* 30.3 (2020), pp. 603–625. DOI: 10.1007/s11222-019-09910-z.

[24] O. Dössel. *Bildgebende Verfahren in der Medizin. Von der Technik zur medizinischen Anwendung*. 2nd ed. Springer Vieweg, Berlin, Heidelberg. DOI: 10.1007/978-3-642-54407-1.

[25] R. Douc, E. Moulines, P. Priouret, and P. Soulier. *Markov Chains*. Springer International Publishing, 2018. DOI: 10.1007/978-3-319-97704-1.

[26] E. R. Dougherty. *Random Processes for Image and Signal Processing*. Vol. PM44. SPIE PRESS Monograph. SPIE Publications, 1998. DOI: 10.1117/3.268105.

[27] S. Duane, A. Kennedy, B. J. Pendleton, and D. Roweth. "Hybrid Monte Carlo". In: *Physics Letters B* 195.2 (1987), pp. 216–222. DOI: https://doi.org/10.1016/0370-2693(87)91197-X.

[28] M. Eigel, M. Marschall, and R. Schneider. "Sampling-free Bayesian inversion with adaptive hierarchical tensor representations". In: *Inverse Problems* 34.3 (2018). DOI: 10.1088/1361-6420/aaa998.

[29] N. Emamy, P. Litty, T. Klotz, M. Mehl, and O. Röhrle. "POD-DEIM Model Order Reduction for the Monodomain Reaction-Diffusion Sub-Model of the Neuro-Muscular System". In: *IUTAM Symposium on Model Order Reduction of Coupled Systems, Stuttgart, Germany, May 22–25, 2018*. Ed. by J. Fehr and B. Haasdonk. Cham: Springer International Publishing, 2020, pp. 177–190. DOI: 10.1007/978-3-030-21013-7_13.

[30] H. W. Engl, M. Hanke, and A. Neubauer. *Regularization of Inverse Problems*. Vol. 375. Springer series in mathematics and its applications. Springer Netherlands, 2000.

[31] C. Gans. "Fiber Architecture and Muscle Function". In: *Exercise and Sport Sciences Reviews* 10.1 (1982), pp. 160–207.

[32] S. Geman and D. Geman. "Stochastic Relaxation, Gibbs Distributions, and the Bayesian Restoration of Images". In: *IEEE Transactions on Pattern Analysis and Machine Intelligence* PAMI-6.6 (1984), pp. 721–741. DOI: 10.1109/TPAMI.1984.4767596.

[33] P. Georg et al. "Low-rank Tensor Methods for Markov Chains with Applications to Tumor Progression Models". In: (2020). Forthcoming.

[34] C. J. Geyer. "Introduction to Markov Chain Monte Carlo". In: *Handbook of Markov Chain Monte Carlo*. Ed. by S. Brooks, A. Gelman, G. L. Jones, and X.-L. Meng. 1st ed. Chapman and Hall/CRC, 2011, pp. 3–48. DOI: 10.1201/b10905-2.

[35] G. H. Golub and U. von Matt. "Tikhonov regularization for large scale problems". In: *Scientific Computing*. Ed. by G. H. Golub, S. H. Lui, F. T. Luk, and R. Plemmons. Springer, 1997, pp. 3–26.

[36] L. S. Graham and D. Kilpatrick. "Estimation of the Bidomain Conductivity Parameters of Cardiac Tissue From Extracellular Potential Distributions Initiated by Point Stimulation". In: *Annals of Biomedical Engineering* 38.12 (2010), pp. 3630–3648. DOI: 10.1007/s10439-010-0119-y.

[37] L. Grasedyck. "Hierarchical Singular Value Decomposition of Tensors". In: *SIAM Journal on Matrix Analysis and Applications* 31.4 (2010), pp. 2029–2054. DOI: 10.1137/090764189.

[38] L. Grasedyck and C. Löbbert. "Distributed hierarchical SVD in the Hierarchical Tucker format". In: *Numerical Linear Algebra with Applications* 25.6 (2018). DOI: 10.1002/nla.2174.

[39] H. Haario, E. Saksman, and J. Tamminen. "Adaptive proposal disctribution for random walk Metropolis algorithm". In: *Computational Statistics* 14 (1999), pp. 375–395. DOI: 10.1007/s001800050022.

[40] H. Haario, M. Laine, A. Mira, and E. Saksman. "DRAM: Efficient adaptive MCMC". In: *Statistics and Computing* 16.4 (2006), pp. 339–354. DOI: 10.1007/s11222-006-9438-0.

[41] H. Haario, E. Saksman, and J. Tamminen. "An adaptive Metropolis algorithm". In: *Bernoulli* 7.2 (2001), pp. 223–242. DOI: bj/1080222083.

[42] W. Hackbusch. *Tensor Spaces and Numerical Tensor Calculus*. Vol. 42. Springer series in computational mathematics. Heidelberg: Springer, 2012. DOI: 10.1007/978-3-642-28027-6.

[43] W. Hackbusch and S. Kühn. "A New Scheme for the Tensor Representation". In: *Journal of Fourier Analysis and Applications* 15.5 (2009), pp. 706–722. DOI: 10.1007/s00041-009-9094-9.

[44] J. Hadamard. "Sur les problèmes aux dérivées partielles et leurs signification physique". In: *Princeton University Bulletin* 13.4 (1902), pp. 49–52.

[45] P. C. Hansen. "Analysis of Discrete Ill-Posed Problems by Means of the L-Curve". In: *SIAM Review* 34.4 (1992), pp. 561–580. DOI: 10.1137/1034115.

[46] R. Harshman. "Foundations of the PARAFAC procedure: Models and conditions for an "explanatory" multi-model factor analysis". In: *UCLA Working Papers in Phonetics*. 1970, pp. 1–84.

[47] W. K. Hastings. "Monte Carlo sampling methods using Markov chains and their applications". In: *Biometrika* 57.1 (1970), pp. 97–109. DOI: 10.1093/biomet/57.1.97. eprint: https://academic.oup.com/biomet/article-pdf/57/1/97/23940249/57-1-97.pdf.

[48] T. Heidlauf. *Chemo-Electro-Mechanical Modelling of the Neuromuscular System*. PhD Dissertation CBM-01. University of Stuttgart, 2015.

[49] S. Heinrich. "Multilevel Monte Carlo Methods". In: *Large-Scale Scientific Computing* 2179 (2001), pp. 58–67. DOI: 10.1007/3-540-45346-6_5.

[50] V. H. Hoang, C. Schwab, and A. M. Stuart. "Complexity analysis of accelerated MCMC methods for Bayesian inversion". In: *Inverse Problems* 29.8 (2013). DOI: 10.1088/0266-5611/29/8/085010.

[51] A. L. Hodgkin and A. F. Huxley. "A quantitative description of membrane current and its application to conduction and excitation in nerve". In: *The Journal of Physiology* 117.4 (1952), pp. 500–544. DOI: https://doi.org/10.1113/jphysiol.1952.sp004764.

[52] D. T. Hristopulos. *Random Fields for Spatial Data Modeling*. Springer Netherlands, 2020. DOI: 10.1007/978-94-024-1918-4.

[53] T. Hytönen, J. van Neerven, M. Veraar, and L. Weis. *Analysis in Banach Spaces*. Vol. 63. Ergebnisse der Mathematik und ihrer Grenzgebiete, 3. Folge / A series of Modern Surveys in Mathematics. Springer International Publishing, 2016. DOI: 10.1007/978-3-319-48520-1.

[54] H. L. III. *Medical Imaging*. Health and Medical Issues Today. ABC-CLIO, Incorporated, 2010.

[55] J. Kaipio and E. Somersalo. *Statistical and computational inverse problems*. Vol. 160. Applied mathematical sciences. Springer, 2005. DOI: 10.1117/3.268105.

[56] B. Kaltenbacher, A. Neubauer, and O. Scherzer. "Iterative Regularization Methods for Nonlinear Ill-Posed Problems". In: *Iterative Regularization Methods for Nonlinear Ill-Posed Problems* (2008). DOI: 10.1515/9783110208276.

[57] S. Kirkpatrick, C. D. Gelatt, and M. P. Vecchi. "Optimization by Simulated Annealing". In: *Science* 220.4598 (1983), pp. 671–680. DOI: 10.1126/science.220.4598.671.

[58] C. S. Klein, G. D. Marsh, R. J. Petrella, and C. L. Rice. "Muscle fiber number in the biceps brachii muscle of young and old men". In: *Muscle & Nerve* 28.1 (2003), pp. 62–68. DOI: 10.1002/mus.10386.

[59] A. Klenke. *Wahrscheinlichkeitstheorie*. Applied mathematical sciences. Springer Berlin Heidelberg, 2013. DOI: 10.1007/978-3-642-36018-3.

[60] T. G. Kolda and B. W. Bader. "Tensor Decompositions and Applications". In: *SIAM Review* 51.3 (2009), pp. 455–500. DOI: 10.1137/07070111X.

[61] D. Kressner and C. Tobler. "Algorithm 941: htucker—A Matlab Toolbox for Tensors in Hierarchical Tucker Format". In: *ACM Transactions on Mathematical Software* 40.3 (2014), pp. 1–22. DOI: 10.1145/2538688.

[62] D. Kressner and C. Tobler. "Low-Rank Tensor Krylov Subspace Methods for Parametrized Linear Systems". In: *SIAM Journal on Matrix Analysis and Applications* 32.4 (2011), pp. 1288–1316. DOI: 10.1137/100799010.

[63] D. Kressner and A. Uschmajew. "On low-rank approximability of solutions to high-dimensional operator equations and eigenvalue problems". In: *Linear Algebra and its Applications* 493 (2016), pp. 556–572. DOI: 10.1016/j.laa.2015.12.016.

[64] A. Kukush. "Measurement Error Models". In: *International Encyclopedia of Statistical Science*. 2011, pp. 795–798. DOI: 10.1063/1.1699114.

[65] C. L. Lawson and R. J. Hanson. *Solving Least Squares Problems*. Society for Industrial and Applied Mathematics, 1995. DOI: 10.1137/1.9781611971217.

[66] D. V. Lindley. *Bayesian statistics: a review*. CBMS-NSF Regional Conference Series in Applied Mathematics. Society for Industrial Mathematics, 1987.

[67] Y. Liu et al. "Three-Dimensional Innervation Zone Imaging from Multi-Channel Surface EMG Recordings". In: *International Journal of Neural Systems* 25.06 (2015). PMID: 26160432. DOI: 10.1142/S0129065715500240.

[68] B. Lobo, C. Hermosa, A. Abella, and F. Gordo. "Electrical impedance tomography". In: *Annals of Translational Medicine* 6.2 (2018). DOI: 10.21037/atm.2017.12.06.

[69] Y. Marzouk and D. Xiu. "A Stochastic Collocation Approach to Bayesian Inference in Inverse Problems". In: *PRISM: NNSA Center for Prediction of Reliability, Integrity and Survivability of Microsystems* 6 (2009). DOI: 10.4208/cicp.2009.v6.p826.

[70] R. Merletti and D. Farina. *Surface Electromyography: Physiology, Engineering and Applications*. 2016, pp. 1–570. DOI: 10.1002/9781119082934.

[71] L. Mesin. "Real time identification of active regions in muscles from high density surface electromyogram". In: *Computers in Biology and Medicine* 56 (2015), pp. 37–50. DOI: https://doi.org/10.1016/j.compbiomed.2014.10.017.

[72] N. Metropolis, A. W. Rosenbluth, M. N. Rosenbluth, and A. H. Teller. "Equation of State Calculations by Fast Computing Machines". In: *The Journal of Chemical Physics* 21.6 (1953), pp. 1087–1092. DOI: 10.1063/1.1699114.

[73] K. S. Miller. "On the Inverse of the Sum of Matrices". In: *Mathematics Magazine* 54.2 (1981), pp. 67–72. DOI: 10.2307/2690437.

[74] M. Mordhorst, T. Heidlauf, and O. Röhrle. "Predicting electromyographic signals under realistic conditions using a multiscale chemo–electro–mechanical finite element model". In: *Interface Focus* 5.2 (2015). DOI: 10.1098/rsfs.2014.0076.

[75] M. Mordhorst, T. Strecker, D. Wirtz, T. Heidlauf, and O. Röhrle. "POD-DEIM reduction of computational EMG models". In: *Journal of Computational Science* 19 (2017), pp. 86–96. DOI: 10.1016/j.jocs.2017.01.009.

[76] F. Natterer. "Regularisierung schlecht gestellter Probleme durch Projektionsverfahren". In: *Numerische Mathematik* 28 (1977), pp. 329–341. DOI: 10.1007/BF01389972.

[77] R. M. Neal. "MCMC using Hamiltonian dynamics". In: *Handbook of Markov Chain Monte Carlo*. Ed. by S. Brooks, A. Gelman, G. L. Jones, and X.-L. Meng. 1st ed. Chapman and Hall/CRC, 2011, pp. 113–162. DOI: 10.1201/b10905-6.

[78] M. Nelson. "Electrophysiological Models". In: *Databasing the brain* (2005), pp. 285–301.

[79] J. R. Norris. *Markov Chains*. Cambridge Series in Statistical and Probabilistic Mathematics. Cambridge University Press, 1997. DOI: 10.1017/CBO9780511810633.

[80] A. O'Hagan. "Probabilistic uncertainty specification: Overview, elaboration techniques and their applications to a mechanistic model of carbon flux". In: *Environmental Modelling & Software* 36 (2012), pp. 35–48. DOI: 10.1016/j.envsoft.2011.03.003.

[81] M. van Oijen. *Bayesian Compendium*. 1st ed. Cham: Springer, 2020. DOI: 10.1007/978-3-030-55897-0.

[82] S. Oladyshkin, F. Mohammadi, I. Kroeker, and W. Nowak. "Bayesian3 Active Learning for Gaussian Process Emulator Using Information Theory". In: *Entropy* 22.8 (2020). DOI: 10.3390/e22080890.

[83] A. J. Pullan, L. K. Cheng, and M. L. Buist. *Mathematically Modeling the Electrical Activity of the Heart*. WORLD SCIENTIFIC, 2005. DOI: 10.1142/5859.

[84] C. E. Rasmussen. "Gaussian Process to Speed up Hybrid Monte Carlo for Expensive Bayesian Integrals". In: *Bayesian Statisitacs* 7 (2003), pp. 651–659.

[85] S. Reuschen, T. Xu, and W. Nowak. "Bayesian inversion of hierarchical geostatistical models using a parallel-tempering sequential Gibbs MCMC". In: *Advances in Water Resources* 141 (2020). DOI: https://doi.org/10.1016/j.advwatres.2020.103614.

[86] M. Richey. "The Evolution of Markov Chain Monte Carlo Methods". In: *The American Mathematical Monthly* 117.5 (2010), pp. 383–413. DOI: 10.4169/000298910X485923.

[87] O. Röhrle, J. B. Davidson, and A. J. Pullan. "Bridging Scales: A Three-Dimensional Electromechanical Finite Element Model of Skeletal Muscle". In: *SIAM Journal on Scientific Computing* 30.6 (2008), pp. 2882–2904. DOI: 10.1137/070691504.

[88] A. Rörich, T. A. Werthmann, D. Göddeke, and L. Grasedyck. "Bayesian inversion for electromyography using low-rank tensor formats". In: *Inverse Problems* (2021). DOI: https://doi.org/10.1088/1361-6420/abd85a.

[89] P. Rosenfalck. "Intra- and extracellular potential fields of active nerve and muscle fibres: A physico-mathematical analysis of different models". In: *Acta Physiologica Scandinavica. Supplementum* 321 (1969), pp. 1–168.

[90] D. Rudolf and B. Sprungk. "On a Generalization of the Preconditioned Crank-Nicolson Metropolis Algorithm". In: *Foundations of Computational Mathematics* 18 (2018), pp. 309–343. DOI: 10.1007/s10208-016-9340-x.

[91] Y. Saad. *Iterative Methods for Sparse Linear Systems*. 2nd ed. Society for Industrial and Applied Mathematics, 2003. DOI: 10.1137/1.9780898718003.

[92] R. Scheichl, A. M. Stuart, and A. L. Teckentrup. "Quasi-Monte Carlo and Multilevel Monte Carlo Methods for Computing Posterior Expectations in Elliptic Inverse Problems". In: *SIAM/ASA Journal on Uncertainty Quantification* 5.1 (2017), pp. 493–518. DOI: 10.1137/16M1061692.

[93] C. Schillings and C. Schwab. "Sparse, adaptive Smolyak quadratures for Bayesian inverse problems". In: *Inverse Problems* 29.6 (2013). DOI: 10.1088/0266-5611/29/6/065011.

[94] C. Schillings, B. Sprungk, and P. Wacker. "On the convergence of the Laplace approximation and noise-level-robustness of Laplace-based Monte Carlo methods for Bayesian inverse problems". In: *Numerische Mathematik* 145 (2020). DOI: 10.1007/s00211-020-01131-1.

[95] O. H. Schmitt. "Biological Information Processing Using the Concept of Interpenetrating Domains". In: *K. N. Leibovic (eds) Information Processing in the Nervous System* (1969), pp. 325–331. DOI: 10.1007/978-3-642-87086-6_18.

[96] L. F. Shampine and M. W. Reichelt. "The Matlab ODE Suite". In: *SIAM Journal on Scientific Computing* 18.1 (1997). DOI: 10.1137/S1064827594276424.

[97] P. R. Shorten, P. O'Callaghan, J. B. Davidson, and T. K. Soboleva. "A mathematical model of fatigue in skeletal muscle force contraction". In: *Journal of Muscle Research and Cell Motility* 28.6 (2007), pp. 293–313. DOI: 10.1007/s10974-007-9125-6.

[98] V. de Silva and L.-H. Lim. "Tensor Rank and the Ill-Posedness of the Best Low-Rank Approximation Problem". In: *SIAM Journal on Matrix Analysis and Applications* 30.3 (2008), pp. 1084–1127. DOI: 10.1137/06066518X.

[99] A. M. Stuart. "Inverse problems: A Bayesian perspective". In: *Acta Numerica* 19 (2010), pp. 451–559. DOI: 10.1017/S0962492910000061.

[100] J. Taylor. *An Introduction to Error Analysis: The Study of Uncertainties in Physical Measurements*. ASMSU/Spartans.4.Spartans Textbook. University Science Books, 1997.

[101] L. Tierney. "Markov Chains for Exploring Posterior Distributions". In: *The Annals of Statistics* 22.4 (1994), pp. 1701–1728.

[102] L. Tierney and A. Mira. "Some adaptive Monte Carlo methods for Bayesian inference". In: *Statistics in Medicine* 18 (1998), pp. 2507–2515. DOI: https://doi.org/10.1002/(SICI)1097-0258(19990915/30)18:17/18<2507::AID-SIM272>3.0.CO;2-J.

[103] A. N. Tikhonov and V. Y. Arsenin. *Solutions of ill-posed problems*. V. H. Winston & Sons, 1977.

[104] C. R. Vogel. *Computational Methods for Inverse Problems*. Vol. 23. Frontiers in applied mathematics. Philadelphia: SIAM, 2002. DOI: 10.1137/1.9780898717570.

[105] S. J. Vollmer. "Dimension-Independent MCMC Sampling for Inverse Problems with Non-Gaussian Priors". In: *SIAM/ASA Journal on Uncertainty Quantification* 3.1 (2015), pp. 535–561. DOI: 10.1137/130929904.

[106] H. Yang and A. Veneziani. "Efficient estimation of cardiac conductivities via POD-DEIM model order reduction". In: *Applied Numerical Mathematics* 115 (2017), pp. 180–199. DOI: 10.1016/j.apnum.2017.01.006.